PhD-FSTC-2016-08
The Faculty of Sciences, Technology and Communication

DISSERTATION

Defense held on 26/02/2016 in Luxembourg

to obtain the degree of

DOCTEUR DE L'UNIVERSITÉ DU LUXEMBOURG EN SCIENCES DE L'INGÉNIEUR

by

Alvaro Antonio ESTUPINAN DONOSO

Born on 25/12/1978 in Cali-Colombia

A DISCRETE-CONTINUOUS APPROACH TO MODEL POWDER METALLURGY PROCESSES

Dissertation defense committee

Dr.-Ing. Bernhard Peters, dissertation supervisor
Professor, Université du Luxembourg (LU)

Dr. Ralph Useldinger
Manager Group Analytics and Fundamental R&D, CERATIZIT Luxembourg S.à r.l. (LU)

Dr.-Ing. Manfred Greger, Chairman
Professor, Université du Luxembourg (LU)

Dr. Frankie Hippe
R&D Engineer, CERATIZIT Luxembourg S.à r.l. (LU)

Dr.-Ing. Florian Hoffmann, Vice Chairman
R&D Engineer, INUTECH GmbH (DE)

University of Luxembourg
PhD-FSTC-2014-04
The Faculty of Sciences, Technology and Communication

A Discrete-Continuous Approach to Model Powder Metallurgy Processes

Alvaro Antonio ESTUPINAN DONOSO

Submitted in partial fullfillment of the requirements for the degree of
DOCTEUR DE L'UNIVERSITÉ DU LUXEMBOURG
EN SCIENCES DE L'INGÉNIEUR, January 2016

Summary

In Powder Metallurgy (PM), is observed a close relationship between the powder grain size and the properties of the sintered alloys: the lower the original pure-metal grain size and the narrower its distribution the higher the mechanical properties that a sintered alloy may achieve. Thus, one topic of major interest for PM is to effectively and accurately control the grain size of the metallic powder.

One of the most common materials employed within the PM industry is tungsten carbide (WC), one of the hardest material made by man. Tungsten carbide grain size characteristics are governed by the size of the employed tungsten metal powder. Tungsten is industrially produced by hydrogen reduction of tungsten oxides; during such a heterogeneous reduction, the build-up of tungsten crystals is driven by the participating conversion mechanisms. Extensive empirical research has found that the solid structure formation is influenced by the reaction kinetics, the gas phase transport, the reduction temperature and the powder bed depth. During the course of industrial reduction of tungsten oxides, hydrogen diffuses into the powder bed, reacts with the oxides and, as gas product, water vapour exits from the powder bed into the gas flow. Hydrogen-flow does not only drive the reduction process, but it also helps to remove the formed water vapour. Retention of water vapour within the bed is a non desirable phenomenon since water vapour may react with the existing oxides and result in the formation of volatile compounds (e.g. $WO_2(OH)_2$). Such volatiles are transported to different localities and further deposited in lower oxides. This transport and deposition mechanism is believed to be directly responsible for abnormal tungsten grain growth.

In the past, thorough studies have revealed empirical tools to investigate into the complex phenomena involved in tungsten oxides reduction. However, the detailed mechanisms occurring upon the interaction between gaseous and solid phases is still not well understood. Therefore, the aim of this doctoral research is to deliver a multiscale and multi-physics simulation framework that helps understanding the mingled phenomena involved in the tungsten oxide powder reduction at the onset of the tungsten metal formation. With the developed discrete-continuous model, based on an eXtended Discrete Element Method (XDEM) approach, concentration and flow of gas species as well as heat and mass transfer phenomena occurring during the process can be investigated. The developed approach treats the solid phase, represented by particles, and the fluid phase as two distinguished phases that are coupled through heat, mass and momentum transfer. Moreover, the solid feedstock is discretized in single entities and the interaction with and through the surrounding gas phase is modeled in an Eulerian approach with a variant of Navier-Stokes equations for compressible fluids in porous media. Hence, XDEM predictions include detailed information about temperature and species distributions that allow determining

local and instantaneous states for, both, solid and gaseous phases. Two different kinetic mechanisms describe solid state conversion. Namely, volatilization and deposition of tungsten oxides/metallic tungsten; where grain size information is provided by a deterministic model supported by the kinetics of the linked reactions.

The large amount of entities to be solved upon powder applications make difficult to employ conventional discrete element techniques at industrial scales. Nevertheless, this problem is dealt with by the introduction of a new concept, the Agglomerated Particle Method (APM), that represents all the particles in a same neighborhood receiving the same boundary conditions in a sole effective entity. Thus, the numerical technique solves the problem for industrial scale reactors at feasible time and lower computational costs.

Isothermal and non-isothermal predictions, for the reduction of tungsten trioxide, were compared to experimental data from literature and the results agreed to a high degree of accuracy. Non-isothermal experiments from an industrial facility were employed to validate grain size and reduction progress predictions under industrial conditions. Thus, the accuracy and the quality of the herein presented results show that the proposed model can provide decisive breakthroughs for the powder metallurgy industry.

Dedication

This dissertation is lovingly dedicated to my family. Their support, encouragement, and constant love have brought me here.

I'm a success today because I had a friend who believed in me and I didn't have the heart to let him down.

Abraham Lincoln

Acknowledgements

The achievement of this work was only possible thanks to the excellent management approach, support and constant feedback of my mentor Prof. Bernhard Peters. Thanks to his valuable advice my knowledge and ideas were better structured. I am especially grateful to him for making me to develop my career into a different and challenging path pointing to Doctor of Philosophy qualifications.

I would like to thank Dr. Ralph Useldinger and Dr. Frankie Hippe (CERATIZIT Luxembourg S.à r.l.) for welcoming me in this Powder Metallurgy world. I acknowledge gratefully their performed experiments and the long discussions that were a key part of this research. I am also greatly thankful to Prof. Manfred Greger for his highly appreciated comments and revisions all along my doctoral training. I am greatly indebted towards Dr. Florian Hoffmann, whose guidance and support throughout my whole PhD study, and before, has helped me in gaining knowledge in basics of computational mechanics.

I would like to sincierely thank all my colleagues at the University of Luxembourg especially Xavier Besseron for his aid in increasing the performance of the solver. Amir Houshang Mahmoudi for the fruitful modeling discussions. I would also like to thank Suresh Kumar Kannan, Mark Michael, Mohammad Mohseni, Andrew Ignatenko, Anas Obeidat, Maryam and Mehdi Baniasadi, Yu-Chung Liao, Gabriele Pozzetti, Edder Rabadan as well as Pascal Loew for their support, friendship and nice discussions during my stay at the University of Luxembourg. Very special thanks to Alina Gritsenko for all the help and commitment to this work. Additional thanks to Diana Aleksandrova and André Wilmes for all the invested time in reading and correcting my publications. I would also like to thank all the students and visitors, at the *LuXDEM research center*, that have contributed to my personal and professional enrichment. Special thanks to Edoardo Copertaro for the excellent work and dedication to our cooperation.

Many thanks to the *RUES* administrative assistants, Simone Drees and Annabella Simon, who frequently went out of their way to help me out with organizational difficulties.

Last, but not least, I would like to thank my family members especially my wife Diana, parents and parents in law for supporting me in all the decisions that I have made and this PhD would not have been possible without their support and sacrifices.

Contents

List of Tables

List of Figures

Table of Symbols

Latin Symbols

Symbol	Unit	Meaning
A	m^2	area
c_i	mol/m^3	molar concentration of species i
$c_{p,i}$	J/kgK	specific heat capacity at constant pressure for species i
$c_{v,i}$	J/kgK	specific heat capacity at constant volume for species i
d	m	diameter
d_p	m	pore diameter
D	m	diameter
D_P	m	particle diameter
D_{ij}	m^2/s	molecular binary diffusion coefficient of species i in species j
e	J	internal energy
E_a	J/mol	activation energy
$\vec{F}$	N	force vector
$\vec{F}_\phi$	-	flux vector
g	m/s^2	gravity
$\Delta_r G$	J/mol	Gibbs free energy of reaction
H	m	height
$\Delta_r H^{298K}$	J/mol	standard enthalpy of reaction at 298 K

Symbol	Unit	Meaning
k_0,k_f,k_b	-	kinetic frequency factor; k_0 general, k_f forward reaction, k_b backward reaction
K	m^2	permeability
K_{eq}	-	equilibrium constant
L	m	length
L_{char}	m	characteristic length
m	kg	mass
$\dot{m}$	kg/s	mass flow rate
$\dot{m}''$	kg/m^{2}s	mass flux
M_i	kg/mol	molar mass of species i
n	-	a positive integer
$\vec{n}$	-	normal vector
N	-	a positive integer
p	Pa	pressure
O	m^2	surface
O_{sp}	m^2	specific inner surface of a porous particle
$\dot{q}''$	W/m^2	heat flux
Q_V	-	volumetric source term
Q_S	-	surface source term
r	m	radius; radial coordinate
r	mol/m^{3}s	reaction rate
R	m	radius, outer radius
R	-	reduction degree
$\mathcal{R}$	J/molK	universal gas constant
R_v	J/kgK	specific gas constant
S	m^2	surface area
t	s	time
T	K	temperature
u_g	m/s	gas phase velocity
v	m/s	velocity

Symbol	Unit	Meaning
V	m^3	volume

Greek Symbols

Symbol	Unit	Meaning
∂	-	Differential operator
∇	-	Nabla operator
Δ	-	difference
α	W/m^2K	heat transfer coefficient
β	m/s	mass transfer coefficient
γ	-	interpolation coefficient
Γ	-	diffusion coefficient
ϵ_B	-	bed porosity
ϵ_P	-	porosity within a porous particle
η	-	volume fraction
ϑ	°C	temperature
λ	W/mK	heat conductivity
μ_i	kg/ms	dynamic viscosity of species i
ν_i	-	stoichiometric coefficient for reactant i
ξ	-	mass fraction
ρ	kg/m^3	density
ρ_g	kg/m^3	density of gaseous phase
ρ_i	kg/m^3	partial density of species i
ρ_p	kg/m^3	density of a particle
σ	$Js^{-1}m^{-2}K^{-4}$	Boltzmann constant

Symbol	Unit	Meaning
τ	-	tortuosity
$\vec{\tau}$	N/m^2	fluid viscous shear tensor
ϕ	-	intensive fluid property
Φ	-	extensive property
$\dot{\omega}$	mol/m^3s	reaction source term

Dimensionless numbers

Symbol	Name	Meaning
Da	Damkoehler number	$\frac{\text{chemical reaction rate}}{\text{convective mass flow rate}}$
Ma	Mach number	$\frac{\text{fluid velocity}}{\text{speed of sound}}$
Nu	Nusselt number	$\frac{\text{convective heat flux}}{\text{conductive heat flux in fluid}}$
Pe	Peclet number	$\frac{\text{advective mass flux}}{\text{diffusive mass flux}}$
Pr	Prandtl number	$\frac{\text{viscous diffusion rate}}{\text{thermal diffusion rate}}$
Re	Reynolds number	$\frac{\text{inertia force}}{\text{viscous force}}$
Sc	Schmidt number	$\frac{\text{viscous (momentum) diffusion rate}}{\text{molecular (mass) diffusion rate}}$
Sh	Sherwood number	$\frac{\text{convective mass transfer coefficient}}{\text{diffusive mass transfer coefficient}}$
Th	Thiele number	$\frac{\text{chemical reaction rate}}{\text{diffusive mass flow rate}}$

Acronyms and Abbreviations

Abbreviations	Meaning
AP	Agglomerated Particle
APM	Agglomerated Particle Method
APT	Ammonium Paratungstate
CFD	Computational Fluid Dynamics
CNT	Classical Nucleation Theory
CVT	Chemical Vapour Transport
CVD	Chemical Vapour Deposition
DEM	Discrete Element Method
DPM	Discrete Particle Method
PM	Powder Metallurgy
PPB	Powder Packed Bed
REV	Representative Elementary Volume
RPM	Representative Particle Method
SEM	Scanning Electron Microscopy
TBO	Tungsten Blue Oxide
TKD	Tetrakaidecahedra
WO_X	Tungsten oxides
XDEM	eXtended Discrete Element Method

Chapter 1

Introduction

You can never cross the ocean until you have the courage to lose sight of the shore.

C. Columbus

The Powder Metallurgy (PM) industry began an important industrial age of hardmetals with the discovery of cemented carbides. "Harder" metals allowed wear pieces to be replaced less often, to reduce energy usage, to drill more easily into the earth's crust in order to reach fuel resources, to build more resistant armors and more proficient weapons. Since then, mankind is in a constant search to obtain more optimal carbide materials in a more efficient manner.

The most common cemented carbide, tungsten carbide (WC), consists of tungsten, carbon and cobalt powders. Any other metal does not equal the quality characteristics of tungsten carbide. Its greatest virtue being its capacity to retain its strength at high temperatures. Concerning hardness, tungsten carbide is still one of the hardest materials made by man. During sintering of WC, the average grain size increases. Small grains may dissolve and larger grains grow resulting in a stepwise increase of the average grain size. According to the sintering conditions, the grains tend to grow differently and some individual grains may even grow to an uncommon large size compared to the average grain size. These abnormalities are devastating for the quality of the final tungsten made products. The powder characteristics significantly influence the properties of the subsequent PM operations (e.g. pressing, sintering or metalworking). It is believed that the WC grain size and grain distribution are the two parameters that affect the most the mechanical properties of cemented carbides, because abnormally large grains act as initiation points for breakage [2]. The WC grain sizes and size distribution are essentially determined by the grain size and grain size distribution (GSD) of the employed tungsten powder [1, 3]. One of the major challenges in the cemented carbide technology is to control the GSD of the metallic powder effectively and accurately [4].

Tungsten, as pure element, never occurs by itself in nature, it is always found in oxidized forms. Even after being concentrated by complicated processes from reluctant ores, it is still tied to oxygen. Tungsten trioxide is commonly obtained and must be further reduced for final use in the hard metal industry. Thus, a full understanding of the irregularities in the starting raw materials and a deeper knowledge of the chemical and physical processes arising during the subsequent transformations are mandatory in order to increase the quality of final tungsten products.

According to the World Tungsten Report of November 2013, production of tungsten has struggled to supply the demand growth in recent years. China continues dominating about 90% of the world production, which reached nearly 80.000 tons in 2013. The majority of the worldwide production takes place in push type furnaces. During the process, tungsten oxide (WO_X) layers, varying from few mm up to some cm, are deposited in containers so-called boats, then the powder containers are pushed in stages through a furnace in corrosion-resistant steel tubes at specific intervals of time. Multi-tube furnaces (sev-

eral tubes arranged rows) are frequently in use today. According to the literature, it is presumed that the process is carried out in a laminar flow of hydrogen with a temperature range of 750 − 1200 °C [1, 5]. Besides driving the reaction rate, the hydrogen-flow transports the produced water vapour out of the bed. The manufacturing parameters influence the quality of the produced tungsten powder; such quality depends on different characteristics as listed next:

Technological properties
- fluidity
- compaction
- density

Physical properties
- grain size
- grain size distribution
- agglomeration
- porosity
- grain shape

Chemical properties
- purity
- oxygen content
- humidity

Globally, the quality of the reduced tungsten powder is governed by the prescribed humidity and temperature of the process [1, 6, 7, 8, 9, 10, 11]. However, these two parameters depend on numerous factors such as the height and morphology of the initial oxide powder beds, the flow of the feedstock, the direction and flow of the reducing agents, the dew point, etc. In principle, low temperature and low water concentrations may be employed to promote formation of small grains. Nevertheless, low water vapour partial pressure is difficult to achieve under industrial conditions due to the considerable amounts of water formed and retained in the powder bed during the course of the reduction.

Researchers have identified two different reduction mechanisms occurring in the hydrogen reduction of tungsten oxides. Those mechanisms are named accordingly to the main gaseous element produced by the reactions; the *oxygen transport*, or direct, mechanism and the *tungsten transport* mechanism. Thus, during the conversion from tungsten oxides to lower oxides, reduction through Chemical Vapour Transport (CVT) may also occur. The latter is enhanced under wet atmospheres and is responsible for the final powder size characteristics [6, 7, 8, 12, 13]. While CVT reinforces grain growth, nucleation is attributed to the direct reduction mechanism [1]. For both cases, direct reduction and reduction through CVT, the water to hydrogen partial pressures ratio as well as the temperature drives the reaction progress [1, 8, 12, 14, 15, 16]. Hence, the individual tungsten grains formed during reduction are a result of the oxygen transport mechanism and the grain growth results from the tungsten transport mechanism. The latter is responsible for the final powder metal characteristics. Due to the water vapour concentrations, the two mechanisms may also be referred to as “dry” mechanism and “wet” mechanism.

In order to study heterogeneous reduction processes, such as the WO_X industrial reduction described earlier, scientists have developed models to help the understanding and to try to control the phenomena. The first heterogeneous reduction models assumed simple

laws for the temporal reduction progress. Many researchers established these models by monitoring the mass loss of samples undergoing reduction over time. As an example, McKewan [17] discovered a linear dependency of the reduction progress of iron oxides with time. However, a more recent investigation points out that such a reduction process is more complex and depends, in addition to the temperature range, on several factors such as the samples composition, porosity, composition of the reducing gas, intra-particles porosity or even on the geometrical arrangement of particles. More complete, but yet empirical, models rely on theoretical diffusion equations described in terms of temperature, time, diffusion-path lengths, and oxide bulk density to predict the extent of heterogeneous reactions. However, such models are impractical and industrial production today is still predominantly based on empirical knowledge [5]. In 1993, pursuing thermogravimetric observations, Bustnes et al. [18] successfully modeled the WO_3 to W reduction time by assuming a homogeneous hydrogen propagation through an "unpacked-bed". More recently, Harboury et al. [15] confirmed the observations by Bustnes et al. And, under the same research for energy storage, Milshtein et al. [19] proposed a simple model to estimate the volumetric production rate of H_2 occurring all along tungsten oxidation. Harboury et al. [15] and Milshtein et al. [19] reported that the increase in feedstock height increases the error of their predictions. Nonetheless, the above-mentioned models are not suitable for setups offering considerable resistance to gaseous products evacuation such as occurring in industrial reduction. Due to the height of the employed powder beds, industrial reduction conditions present a heterogeneous distribution of species and a significant retention of gaseous products.

Taking into consideration the state of the art on tungsten production under factory conditions, there is still a lack of comprehensive models accounting for the involved, and strongly coupled, phenomena (e.g. fluid transport, diffusion of gaseous species out of/into the powder particles, heat transfer and heat generation/consumption, kinetics of the phase formation, nucleation and grain growth). Moreover, the limited number of numerical studies on the reduction of powder-oxides obstruct the task of implementing and comparing new modeling approaches [20]. Industrial production today is still based on empirical knowledge supported by in-depth understanding of the basic aspects governing the reduction process [5].

One plausible solution to study all the variables involved in the complex WO_3 to W-reduction process consists in combining continuous and discrete approaches. Such a concept is covered by the recently structured numerical framework XDEM (eXtended Discrete Element Method) [21, 22]. With the increase of computational power over the last decades, the way was paved for the exploration of numerous numerical techniques such as the coupling of Discrete Element Method (DEM) with Computational Fluid Dynamics (CFD). The combination of these two methods allows to obtain the advantages

of both consolidated techniques [23]. As originally developed by Cundall and Strack [24], DEM simulates the dynamics and micro-mechanics of granular materials, and, CFD is widely accepted for representing problems involving fluid flow. The eXtended Discrete Element Method have successfully been used to model heat transfer and mass transfer during water removal of packed beds [25, 26, 27]. Hoffmann [28] studied the complex process of iron oxides reduction by using the same Euler-Lagrange approach. Moreover, biomass pyrolysis and combustion processes have been studied by means of XDEM technique [29, 30, 31, 32]. Martin et al. [33] used Discrete Element Methods to model metallic powder sintering. Despite the fact that nucleation has not been properly considered, the grain growth simulations in [33] show a promising path to predict powder metallurgy processes. Estupinan et al. [34, 35] employed a XDEM single particle approach to model WO_3 reduction. In [36, 37, 38] predictions for a powder bed of tungsten trioxide were compared to isothermal and non-isothermal observations; and the results showed excellent agreement.

The goal of this thesis is to develop a valuable numerical tool to investigate in detail the temporal and spacial thermochemical conversion as well as the gaseous species transport arising in the course of industrial reduction of tungsten ores. Hence, this research relies on XDEM as a new and a comprehensive technique to represent the different thermochemical processes as well as the fluid flow involved in the industrial reduction of tungsten oxides. Herein, powder packed beds (PPB) of WO_3 particles are represented by an ensemble of discrete-particles experiencing thermochemical conversion in hydrogen atmospheres. The flow through the void space of the PPB is modeled as a flow through a porous media. Fluid fields are described by solving the respective differential conservation equations and the particles' properties are also solved by conserving quantities that yields, both, a spatial and temporal internal distribution of temperature and species. The chemical conversion of WO_3-particles to pure-tungsten is described by oxygen and transport reduction mechanisms, as documented by Lassner and Schubert [1]. The formation of volatile compounds (e.g. $WO_2(OH)_2$) is accounted for, and therefore, nucleation and grain growth via Chemical Vapour Transport are taken into consideration.

Thesis structure

This document is structured as follows:

- In chapter 2, an overview of the theoretical foundations considered in this thesis are presented. A summary of the main powder metallurgy processes introduces the chapter. Section 2.2 reviews the tungsten element and its chemical production. Moreover, the tungsten oxides reduction mechanisms and the intermediate species proceeding during such a process will be explored. In section 2.3, the main aspects, special considerations and the state of the art of heterogeneous reactions modeling for Powder Packed Beds (PPB) are summarized.

- Chapter 3 introduces the general concept employed in this work to model the technical reduction of tungsten oxides. The chapter presents a review on studies related to this work and exposes the versatility of the employed approach.

- Chapter 4 describes the multiscale mathematical formulation employed in this work to numerically reproduce the industrial conversion of tungsten trioxide particles into metallic tungsten. Section 4.1.2 outlines the governing conservation equations that describe the temporal and spacial thermochemical state of single particles within PPBs. And, section 4.1.3 describes the penetration and transport of gaseous species to and along the PPB, as well as, the coupling between solid and fluid phases.

- Chapter 5 presents a detailed validation of the different phenomena involved in PPBs. Thus, chapter 5 proves that the developed model can be seen as a general approach to represent the complex powder oxides reduction process. This chapter is based on the publications performed during this study.

- Chapter 6 presents the industrial scale results of this research; where, new insights into the tungsten oxide reduction process are presented and discussed. The interactions of heat transfer, mass transfer and heterogeneous reactions of single particles as well as the PPB conversion are analyzed in detail. Moreover, predictions for tungsten grain size, under both conditions, dry and humid, are compared to industrial experiments performed at CERATIZIT Luxembourg S.à r.l.

- Finally, the conclusions and future work of this framework are summarized in chapter 7.

Chapter 2

Background

Contents

If the facts don't fit the theory, change the facts.

A. Einstein

2.1 Powder Metallurgy

Powder Metallurgy (PM) is a material-processing technique in which, with the influence of pressure and heat, metallic granular materials are consolidated to semi-finished and finished metal products. Powder metallurgy techniques, to a certain extent, offer flexibility and possibilities to control composition and microstructure of the final PM products. The annual industrial market demand for PM products is very high. For instance, the PM industry has estimated sales of $5 billion in North America [39] and the annual worldwide metal powder production exceeds 700000 tons [39]. PM is international in scope with growing industries in all of the major industrialized countries.

Different materials are processed with PM techniques, for instance: iron and steel, aluminum, copper alloys, titanium alloys, tungsten carbide. The so-called hardmetals, and most precisely cemented carbides or tungsten carbide (WC), are materials of particular importance for the PM industry [3]. Within this dissertation, WC is taken as an example of the materials employed within PM processes. Thus, this document refers to hardmetal or carbide processes when referring to Powder Metallurgy.

Long before ancient artisans learned how to melt and cast iron PM was practiced. Around 1906, many attempts were made regarding the manufacture of the lighting filaments by powder metallurgy process. But finally, the development was attributed to W.D. Coolidge, who took his patent in 1909 [40], although, Henri Moisson had already produced W_2C in an electric-arc furnace developed by himself during the 19^{th} century [3].

At the beginning of the 20^{th} century, the German Gaslighting Company carried out research to produce the required tungsten wire for electric light bulbs using cast tungsten carbide instead of costly diamond as drawing dies. An important role in the early development was played by Karl Schröter who was working in the electrical section of the "Deutschen Gasglühlicht Aktiengesellschaft" company. His work gave birth to the idea of replacing the expensive diamond-wire drawing dies by other materials. Nevertheless, in view of the earlier reports by Skaupy on the development of hardmetals, it seems that Schröter was not the only inventor [3]. At about the same time a patent appeared for the production of small WC spheres, by Conell, which could be used as a substitute for rubies in clocks. Lohmann, from the Metal Forming Company in Essen, was granted a patent for a process of production of large pieces of any desired shape in pure tungsten or molybdenum carbide as well as a mixture of the two for use as tools of any kind [3].

Schröter improved the production of carbide by carburizing very fine tungsten powder in an atmosphere of water vapour enriched with coal gas or benzene vapour [3]. The second step was to mix the carbide powder with powder of a lower melting point auxiliary metal such as iron, nickel, or cobalt. Subsequently, the mixture was compressed and then

sintered. Following this work, the patent, which is today acknowledged as the basic hardmetal patent, was granted to Schröter in 1925. However, Skaupy, who was Schröter's superior, claimed to have suggested using iron group metals such as nickel and cobalt. *"The main features of the obtained carbide were high hardness, adequate toughness, good hot hardness and elevated temperature strength properties to resist plastic deformation" [3].*

During the first decades after hardmetals appeared on the market, further development was mostly done on an empirical basis, but only in recent decades, it has been complemented by scientific work.

According to the old nomenclature, hardmetals are divided into cast and sintered hardmetals. The first consist of primarily mono-tungsten carbide crystallites in a eutectic matrix of Co, Ni, and/or Fe with W_2C as well as small quantities of molybdenum, tantalum, and chromium carbides. Hardmetals of this kind are melted in a carbon-arc furnace or in a high frequency furnace at 2900-3000 °C and casted into graphite molds. Conversely, for the second type, sintering takes place below the melting point of the carbide, but in the presence of a liquid phase. Common components of this kind of hardmetal are cobalt and/or nickel as binder and tungsten carbide, titanium carbide, tantalum carbide, vanadium carbide, and/or chromium carbide as hard phases. Alongside cast and sintered hardmetals exist the cermets, which were originally materials, in which ceramic particles were embedded in a metal matrix [3]. Hardmetals currently available on the market have reached a high level of performance, and their development is in the direction of still finer grained material and further improvement and broadening of the existing types of cermet.

About 67% of the total hardmetal is used for metal-cutting tools followed by application in mining, oil drilling, and tunneling with 13%, wood-working with 11%, and construction industry with 9%. In view of the increasing importance of sintered hardmetals, the quality demand on raw materials becomes increasingly higher. Consequently, the suppliers of these raw materials need to emphasize the trend to more intensive control of their production processes that will lead to increasingly upgrading the reproducibility of the property profile of their end products.

2.1.1 Starting materials

The starting materials for hardmetals industry generally consist of hard-metallic carbides such as mono-tungsten carbide (WC), titanium carbide (TiC), tantalum carbide (TaC), as well as mixed carbides (W, Ti)C, (W, Ti, Ta)C and a metallic binder phase, both in the form of powder. Tungsten carbide is one of the hardest metallic composites, so far made use of by man, and the most widely used hard material. Hence, the process of carburizing tungsten metal is of major significance.

During carburization of tungsten metal, the tungsten powder is mixed with pure carbon black and then heated. The reaction occurs under hydrogen or in vacuo and the heating processes may take place in carbon tubes within induction furnaces. The carburization temperature is adjusted according to the purity and particle size of the metal powder used, as well as to the properties required for the carbide. Tungsten carbide grain sizes and size distribution is essentially determined by the grain size and grain size distribution (GSD) of the tungsten powder used [1, 3]. Thus, one of the major problems in cemented carbide technology is to effectively and exactly control the GSD of the metallic powder [4].

A high-purity tungsten powder with a purity of 99.9% is used as starting material for tungsten carbide production, and therefore, tungsten ores are considered the head of hardmetal processes. During the 1950s PM industry made a remarkable change in the highly pure starting trade oxide material. The traditional, heretofore used, tungstic acid (H_2WO_4) was replaced by Tungsten Blue Oxide (TBO) or yellow tungsten oxide (WO_3) [41]. The reason of this change remains unclear.

2.2 Tungsten review

2.2.1 Tungsten in history

In the beginning, tungsten was known as wolfram, named after its precursor mineral the wolframite; from the German words "wolf" and"rahm" (lupi spuma). Peter Woulfe manifested, in 1779, the possibility that wolframite might contain a yet unknown substance. Similarly, in 1781 Carl Wilhelm Scheele concluded that "Scheelite" contained limestone and a new "tungstic acid" that could be transformed into a new metal [42]. However, it was only in 1783, in Spain, that the De Elhuyar brothers obtained the new metal by reducing an acid from wolframite [1, 13]. They named it wolfram. However, some years later Scheele and Bergman gave the current name tungsten, derived from the Swedish words "tung", meaning heavy, and "sten", meaning stone [43].

In 1890, during an attempt to reproduce diamonds Henry Moisson discovered the tungsten carbide. On the next thirty years, tungsten carbide was mostly used in high-speed steel cutting tools production.

In 1903 Just and Hanamann produced the first tungsten filaments for incandescent lamps with a very expensive and complicated procedure, but the filaments were replaced by carbon filament due to their simple production and lower energy consumption. In 1909, W.D. Coolidge developed a new technology to produce ductile tungsten wire. The technique would give birth to a large-scale powder metallurgy process [1].

Tungsten played an important role in 1913, before World War I had begun. The Germans were using tungsten on high-speed cutting tools. Their tungsten was useless tungsten that the British were selling because they did not have use for tungsten and it was considered waste while also disturbing the extraction of tin. The Germans were increasing their munitions output more than that of the Allies. Later the Allies found out that it was because of the tungsten ore coming from the British mines [42].

During World War II, the Germans had a tungsten carbide armor piercing shell. Tungsten was used in 15000 different types of war items in World War II. To produce it, Germany had acquired nearly the entire world supply of tungsten ore. It took two years before the Allies came up with similar technology and a quantity sufficient to defeat the Germans [42].

2.2.1.1 Importance of tungsten nowadays

Tungsten is used in a wide range of fields; as a pure metal, as carbide and in its oxides form. Seventy to eighty percent of all tungsten materials are produced via PM techniques.

Sustainable energy sources with low CO_2 is a major challenge for the future. The development of fission nuclear reactors worldwide seem to be a viable alternative. Nevertheless, a number of technical challenges, such as material selected to be in contact with the plasma inside the fusion reactor have to be addressed before the commercialization of that technology [44]. Tungsten based products, due to their high stability at high temperatures, are the most promising candidates for such an application [44].

The element tungsten has a density equal to that of gold, thus, tungsten is used in jewelry as an alternative to gold or platinum with hypo-allergenic and scratching resistant properties. Because of its high atomic number, tungsten is commonly chosen for stationary and rotating anodes of X-ray tubes used in medical diagnosis giving an excellent X-ray output. Tungsten oxides are used as pigments in ceramic glazes and calcium/magnesium tungstates are widely used in fluorescent lighting. Tungsten is still used as the preferred material of the filament in "halogen lamps". The halogens are included to prevent the tungsten filament from degrading the lamps and in order to avoid wall-blackening and more energy efficiency than standard incandescent light bulbs. Tungsten composites produced by coating methods are believed to be great candidates for aerospace material requiring high heat resistance [45].

Tungsten and tungsten chemicals are highly used as catalysts in modern days [12, 46], some of these catalysts help to reduce environmentally harmful byproducts, such as sulfur and nitrogen compounds. Emerging applications include fuel cell catalyst support, where tungsten is a promising replacement for high surface area activated carbon [46].

Recently, Harboury et al. [15] and Milshtein et al [19] proposed an energy storage and recovery approach by using a W/WO_3 redox system. Their system attempts to store energy employing tungsten metal by reducing the tungsten oxide with hydrogen. Thereafter, the steam and heat resulting from fuel-cells operation is used to re-oxidise the metal and recover the hydrogen.

Nowadays, tungsten nano-whiskers are of special interest because of their distinctive characteristics that could be exploited for various applications, such as gas and humidity sensors, optical devices, electro-chromatic windows, catalysts, etc. [12].

Irrefutably, the main use of tungsten is as WC (tungsten carbide) for the production of hardmetals; this is the scope of this contribution. Among within several pieces, WC is mainly employed for knives for drills, wear-resistant abrasives and cutters, milling and circular saws, .

2.2.2 Tungsten production

Industrial production of pure tungsten occurs almost exclusively under hydrogen atmospheres. The reduction of tungsten oxides with carbon oxides was performed in earlier years; today, however, it is employed for direct carburization process (direct production of tungsten carbides) [1, 5].

Nowadays, tungsten is primarily obtained from wolframite (Fe,Mn)WO_4, and Scheelite, also known as tungstone or hardstone $CaWO_4$, making them the most important tungsten ores. The largest deposits are located in China, the former USSR, South Korea, Australia, Burma, and Canada. Some small reserves are found in Portugal, Austria, Bolivia, and Peru.

From wolframite processing are obtained the almost pure end products Ferberite ($FeWO_4$) and Hubnerite ($MnWO_4$) which occur rarely in nature. Scheelite is generally contaminated with calcium molybdate ($CaMoO_4$), where in some cases copper is substituted for calcium. The upgrading and processing of the ores and the preliminary separation of impurities, such as tin, silicon, arsenic, phosphorus, and molybdenum, is done by expensive physical methods such as gravity separation, magnetic means, and/or flotation [3]. After a separation process, the resulting sodium tungstate solution is still contaminated with small quantities of tramp elements which were contained in the original material. The impurities are removed in a two-stage purification process via specific chemical additions that convert them into insoluble compounds. This then undergoes a final treatment with aqueous ammonia, where tungsten-free extraction medium is recirculated while the aqueous ammonium tungstate solution may be further purified and finally evapourated. The result is a difficult-to-dissolve ammonium tungstate, or so-called ammonium paratungstate (APT), with chemical formula $(NH_4)_{10}W_{12}O_{41} \cdot 5H_2O$. In some cases, a resulting by-product ammonia/steam mixture is burnt polluting the environment.

Once the above mentioned ores containing tungsten have been mined and purified, the ore is crushed, roasted, cleaned and then treated with several alkalis until obtaining tungsten trioxide, which is further reduced to pure tungsten.

In the hardmetal industry, APT or TBO have been the most common intermediate traded materials. Hereafter, such intermediate materials may be referred to as “raw” materials, since they are considered the starting point for the technical reduction of WO_X.

2.2.2.1 Ammonium Paratungstate

Ammonium Paratungstate is a crystallized powder, which presents crystal size ranges between 30 and 100 μm. It presents mainly faceted crystals and only few inter-grown or agglomerates, as shown in fig. 2.2.1. Agglomerates are understood as coarse accumulations of grains or particles. A common grain size distribution of a commercial APT is shown in fig. 2.2.2.

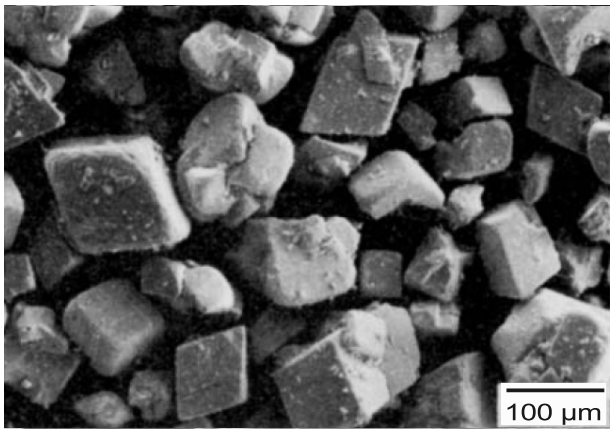

Figure 2.2.1: Common APT grain size distribution. Source: [1].

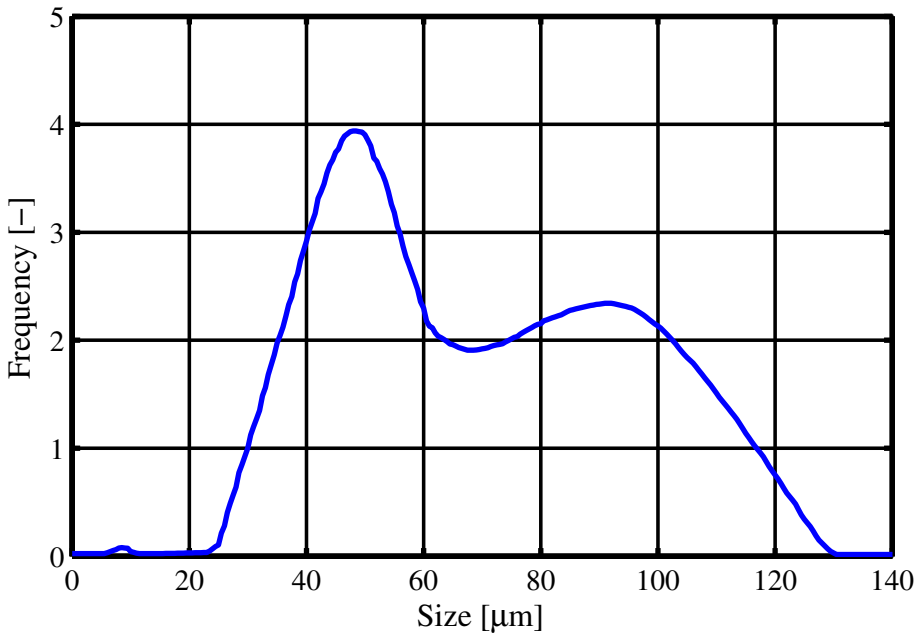

Figure 2.2.2: Common APT grain size distribution. Source: [1].

The ammonium paratungstate is commonly traded as a standard intermediate product and is offered in different grades depending on its purity and particle size. Purity depends on how reliably the crystallisation is controlled as well as on the associated purification steps [3, 47].

After a subsequently roasting the APT is converted to tungsten oxide(s). In a rich air-flow, yellow tungsten oxide (WO_3) is formed. If the roasting is done in absence of air and/or in a H_2 reducing atmosphere the so-called TBO is obtained [41].

Even though APT is the most traded tungsten source and more than 90% of the W powders produced today are derived from APT, it is always processed down to WO_{3-x} prior to reduction into tungsten metal [48].

2.2.2.2 Tungsten Blue Oxide (TBO)

The tungsten blue oxide is not a standard defined product, its chemical and physical properties vary depending on production conditions and the equipment used. The calcination conditions to produce the APT determine the quality of the obtained TBO.

The relative amounts of the different compounds of TBO depend on the calcination parameters, meaning: temperature, heating time, composition and pressure of atmosphere, mass of APT flow with time, gas flow, layer height in the boat [49]. These are compounds with approximate ratios $WO_{2.98}$ to $WO_{2.72}$, that is to say having no exact stoichiometric composition. The decomposition generally takes place in the temperature range of 500 to 700 °C. Under more reductive conditions, meaning under exclusion of air and with a higher gas flow, even traces of WO_2 and W-β can be present. Pusher-furnace-derived TBO particles may present differences between individual particles depending on their position in the powder layer, whereas the product of rotary furnaces is more homogeneous [41].

The obtained oxide compounds are usually pseudo-morph to APT [50], meaning they keep the APT size and shape, but they are built of very small grains. Figure 2.2.3 shows an example of a TBO particle, the pseudo-morph particle conserves its precursor's shape and size (fig. 2.2.1).

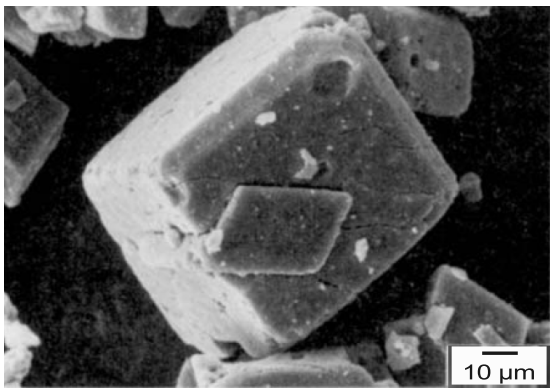

Figure 2.2.3: SEM micro-graph example of a TBO particle. Source: [1].

Metallic tungsten powder is synthesized in rotary furnaces or pusher furnaces, with temperatures ranging from 750 - 1200 °C. The push-type furnaces are preferred by the PM industry; where the synthesis process is always carried out in a flow of hydrogen [5].

2.2.2.3 Push-type furnace

A push-type furnace, for powder metallurgy, is a continuous furnace through which the material proceeds in boats. Iron alloys high in Ni and Cr, TZM (molybdenum alloy with Ti, Zr, and C) or pure tungsten boats, are charged with tungsten oxide powder layers varying from a few mm up to some cm, then pushed in stages through a furnace in corrosion-resistant steel tubes at specific intervals of time. By introducing a new boat into the tube, the boats in front are pushed forward by the length of the introduced boat.

Hydrogen in excess is applied either co- or counter-current to the tungsten flow direction. The range varies between 2.5 and 40 times stoichiometric. The hydrogen not only drives the reduction process, but also helps to remove the formed water vapour. The exiting wetted-H_2 is dried to a pre-set dew point and re-circled into the furnace.

In this type of furnace, the reduction process is frequently carried out in one step, while a staged reduction is preferred in some cases.

2.2.2.4 Powders characterization

A correct powder characterization can lead to better powder understanding and control, but this is not always an easy task. There are different ways and methods to characterize powders, more specifically tungsten powders, the most relevant techniques are documented in annex A.

When referring to powders different size-scales definitions for the single entities may appear, the following list distinguishes some of the size terminology employed in PM:

Particle: is also understood as an agglomerated of grains commonly of the same material. It is small enough in size to not consider it as a bulk, but composed of one or several grains.

Grain: is understood as a volume of a material within which the crystal structure and the orientation of the crystals is same. A single grain can be composed of several crystals.

Crystal: is understood as a solid body for which its primary entities (e.g. atoms, molecules or ions) are highly ordered in a microscopic structure. Moreover, a crystallite is understood as the size of a single crystal inside a grain or particle. Polycrystalline materials are composed of several crystallites.

2.2.3 The element tungsten

The element tungsten, also known as wolfram, is a metallic transition element which can be considered as a rather inert metal [1]. The element tungsten is well known for, among other properties, presenting the highest melting point of all metals, this being the most prominent characteristic in regard to all applications as a refractory metal. Table 2.2.1 summarizes the main atom-related characteristics of tungsten.

Table 2.2.1: Tungsten's properties [1, 51].

Atomic number	74	
Period	VI	
Group	6 (IUPAC proposal 1985)	
Average relative atomic mass	183.85 ± 0.03	
Atomic radius	Metallic	137.0 pm (coordination number 8)
	Covalent	125.0 pm (single bond; valence 6) 121.0 pm (double bond; valence 6)
Ionization potential	7.98 eV	
Electron affinity ($M \rightarrow M^-$)	0.816 ± 0.008 eV	
Number of known isotopes	35 (including isomers)	
Half-life	few milliseconds to more than 200 days	

Tungsten exists in both α and β crystalline forms. W-α presents a body-centered cubic structure and is the most stable form [1]. W-β is metastable, but can coexist with the α phase, at least partially, during low-temperature hydrogen reduction of tungsten oxides, tungsten bronzes or ammonium paratungstate. Several coexisting elements such as P, As, Al, K promote W-β formation and have stabilizing effects at higher temperatures [52].

The manufacturing parameters will influence the quality of the produced tungsten powder; such a quality depends on its physical, mechanical, thermal and chemical properties.

Table 2.2.2: Tungsten's elastic properties [1].

E = 90 - 410	GPa, Young's modulus
G = 156 - 177	GPa, Shear modulus
K = 305 - 310	GPa, Bulk modulus
v = 0.28 - 0.30	−− , Poisson's ratio
Compressional modulus	
$L = (5.2415 \times 10^{12}) - (3.7399 \times 10^{8})T - (4.598 \times 10^{4})T^2$	

2.2.3.1 Physical properties

Tungsten is a hard steel grey metal that could be brittle and hard to work. However, in a pure state, it could become malleable enough to be easily worked [53]. It has the highest melting point (3422 °C), the lowest vapour pressure, the highest tensile strength and the lowest coefficient of thermal expansion of any pure metal [45].

The density of tungsten is one of the highest densities among all metals. Measured densities of sintered materials may vary significantly, because full density is only achieved after heavy working. For instance, the range found in literature for W- α are 16.74 ± 0.6 g/cm^3 (at melting temperature) to 19.254 ± 0.005 g/cm^3 (at ambient temperature). And about 19 ± 0.1 g/cm^3 for W- β . Common tungsten exhibits point defects (vacancies, self interstitial atoms, impurity atoms), line defects (dislocations), plane defects (stacking faults, grain boundaries, twins), and volume defects (clusters, voids and bubbles, segregations, micro-cracks). Even the purest and long-time annealed tungsten always contains lattice defects. The concentration of defects depends on the temperature and the deformation of the material, as well as on its purity [1].

Regarding elasticity, at least at a/below room temperature, tungsten behaves nearly isotropically. The elastic constants for polycrystalline tungsten at 20 °C are given in table 2.2.2.

At low temperatures, if subjected to tensile stresses, tungsten behaves brittle when loading. This behavior changes above a certain transition temperature (e.g. 200-300 °C) [1]. The range of temperature depends on mechanical, structural, and chemical conditions. It is believed that brittleness is due to the weakness of the grain boundaries; this leads to initiation of cracking of tungsten materials. Firstly it was thought that cracking occurred along grain boundaries, but later, a high percentage trans-granular fracture was also noticed. Today, it is possible to determine fractures by looking at deformation history, purity, and stress state [1].

When grain growth occurs, the internal grain boundary surface is reduced and consequently the concentration of the grain boundary impurities rises. Since the grain bound-

aries are stronger when the segregations are distributed on a larger area, the ductility decreases [4]. Nowadays, the brittle-to-ductile transition is believed to occur in two phases [1]:

- grain interior: 30 - 40 °C
- grain boundaries: 280 - 330 °C

2.2.3.2 Mechanical properties

The mechanical properties of polycrystalline tungsten are highly influenced by its microstructure and purity.

Tungsten microstructure, depending on the type of preparation (e.g. powder metallurgy, arc cast, electron beam melted, zone refined, chemical vapour deposition) and depending on the subsequent working (e.g. deformation, annealing, recrystallization) influences the mechanical properties in a broad range. However, in PM processing, the microstructure can be regulated to a certain extent by affecting sintering conditions, the intermediate and final annealing processes. Hence, crystal sizes and shapes can be influenced in the course of production [3].

Impurities influence the structure of the hardmetals produced by sintering to high density in a number of ways. The influence on the final product of even the smallest amount of impurity can, during the pre-sintering stage, be substantially greater than that of variation of the carbide particle size and size distribution. As a result, different levels of coarseness can be observed in the sintering of tungsten carbide [3].

2.2.3.3 Thermal properties

Table 2.2.3 sums up the thermal properties of pure tungsten. Full details are available in [1].

Table 2.2.3: Tungsten's thermal properties.

Melting point	3422 °C
Boiling point	5700 ± 200 °C
Critical temperature	13400 ± 140 K
Critical pressure	(3.37 ± 0.85) x 10^8 Pa
Critical density	4.31 g/cm^3

Tungsten's heat capacity C_p varies considerably with temperature. Figure 2.2.4 shows the heat capacity values for low as well as for high temperatures.

From the data in fig. 2.2.4 the polynomial expression representing C_p (J/molK) writes

$$C_p = 22.78 + 0.0043T + 8 \times 10^{-7}T^2 - 8 \times 10^{-10}T^3 + 2 \times 10^{-13}T^4 \quad (2.2.1)$$

However, within the temperature range of hardmetal production, a linear approximation (eq. (2.2.2)) is favored instead of the above-presented eq. (2.2.1), namely

$$C_p = 22.72 + 0.0045T \quad (2.2.2)$$

The diffusion process is characterized by the diffusion coefficient D, which is equally temperature dependent. At certain temperature T, this temperature dependency is commonly expressed by an Arrhenius law as

$$D = D_0\, e^{-\frac{Q}{R}T} \quad (2.2.3)$$

where the constant D_0 is commonly expressed in cm^2/s, Q (kJ/mol) is the activation enthalpy and R is the molar gas constant. Polycrystalline tungsten in PM is the most important form of the metal and the most frequently used. For polycrystalline tungsten $D_0 = 54\ \mathrm{cm}^2/\mathrm{s}$ and $Q = 504$ kJ/mol, whereas for tungsten single crystals $D_0 = 42.8\ \mathrm{cm}^2/\mathrm{s}$ and $Q = 640$ kJ/mol [1]. Nevertheless, self-diffusion parameters are influenced by the impurities in the diffusion zone, which attract vacancies disturbing the diffusion process. This effect is higher at low temperatures and vanishes above 2316 °C.

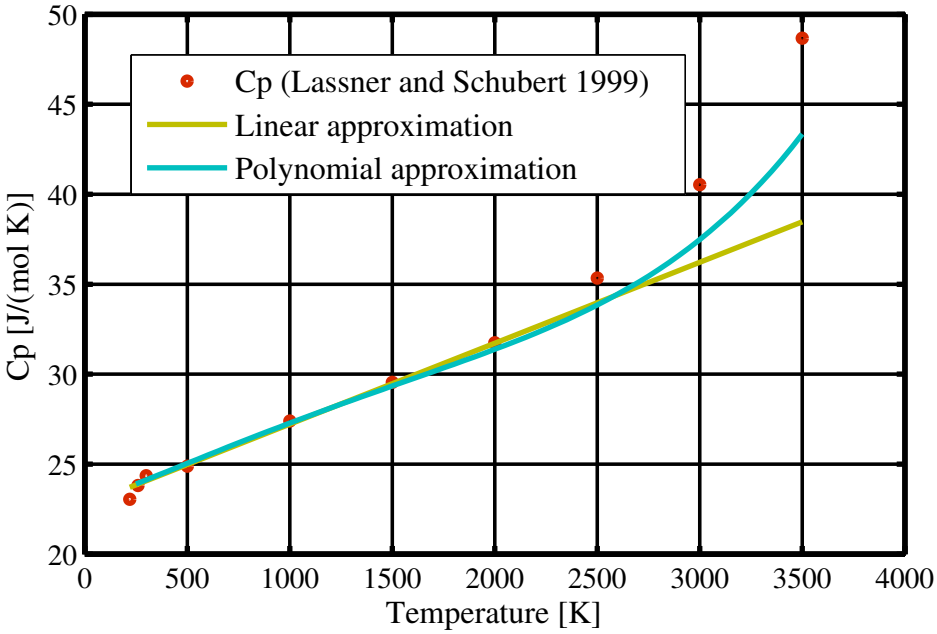

Figure 2.2.4: Tungsten heat capacity (C_p) versus temperature.

Schubert et al. [48, 54] found that below 2100 °C, grain boundary diffusion is the dominant mechanism in polycrystalline tungsten. Activation enthalpies between 377 and 460 kJ/mol were measured.

Tungsten's thermal diffusivity at ambient temperature is about 0.662 cm^2/s, decreasing to 0.246 cm^2/s at the melting point. Thermal conductivity coefficient λ is about 1.75 W/cmK at room temperature. Figure 2.2.5 show typical λ values of tungsten. Figure 2.2.5 includes a comparison against a polynomial approximation for the data presented in [1].

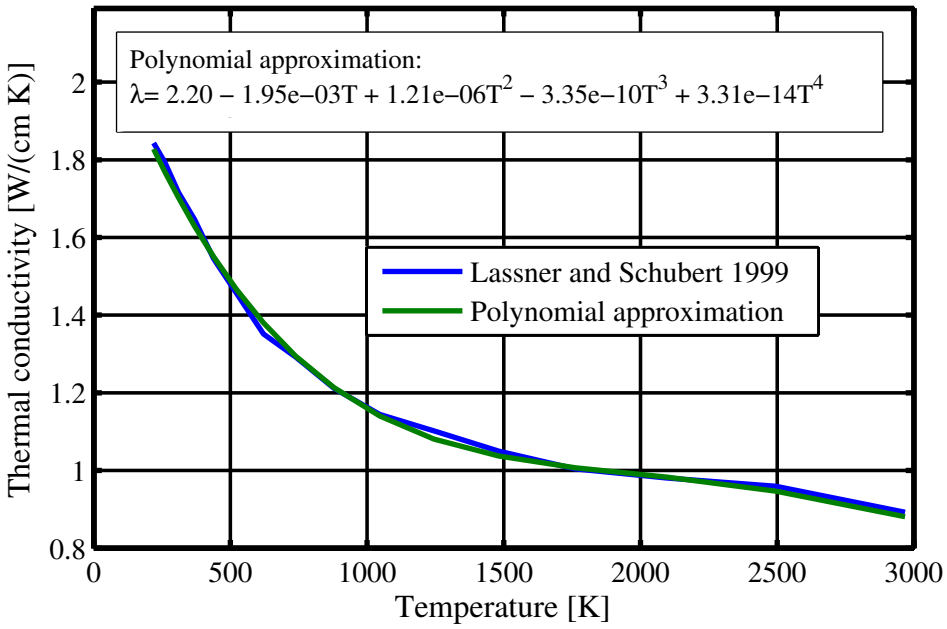

Figure 2.2.5: Tungsten's thermal conductivity coefficient (λ) versus temperature.

2.2.3.4 Chemical properties

"Tungsten is stable to mineral acids in the cold and is only slightly attacked at higher temperatures. Nevertheless, it reacts with numerous elements and chemical compounds" [1]. For instance, it can be strongly attacked by fluorine. Below 1000 °C it dissolves in alkali solutions containing oxidizing agents, in hydrofluoric-nitric acid mixtures and nitrohydrochloric acid (aqua regia) [1].

Tungsten is compatible with most ceramics and glasses up to high temperatures and shows good resistance to many molten metals. Above 1000 °C, reactions with carbon or carbon-containing compounds are possible. This type of reactions are important in the preparation of tungsten carbide:

Carbon monoxide. Between 80 and 200 °C, tungsten hexacarbonyl forms. At about 550 °C nano-crystalline powders start to carburize. From 1000 °C upward, bulk tungsten is carburized:

$$xW + 2CO \rightarrow W_xC + CO_2 \qquad (x = 1, 2) \tag{2.2.4}$$

Carbon dioxide. CO_2 acts as an oxidizing agent at high temperatures and, depending on temperature and partial pressure, lower or higher tungsten oxides are formed:

$$xW + yCO_2 \rightarrow W_xO_y + yCO \tag{2.2.5}$$

Reaction of tungsten with oxygen

The most common formal oxidation state of tungsten is +6, but it shows oxidation states from +6 to −2 [12]. There are many non-stoicheiometric compounds particularly in its oxides forms (e.g. $WO_{2.9}$, $WO_{2.72}$).

Tungsten behaves stable in dry and humid air only at moderate temperature [1, 55]. Its oxidation starts at about 400 °C. The resulting oxide layer is not dense, thus no protection against further oxidation is provided. The oxidation rate increases rapidly after 700 °C. Above 700 °C, sublimation of the oxide starts, resulting in ruinous oxidation of the metal [1]. The high sensitivity against oxidation is its biggest disadvantage. As a result, high temperature applications are contract to a protective atmosphere or vacuum [55].

Warren et al. [56] reviewed the W oxidation in dry and humid atmospheres by means of electron spectroscopy for chemical analysis. It was shown that tungsten oxidation starts at room temperature. Despite the fact that their study was concentrated in temperatures below 500 °C, the review showed that tungsten oxidation at high temperatures is closely related to temperature and to oxygen partial pressure.

The oxygen partial pressure in the powder bed is determined by room temperature and the dew point. Depending on the oxidation conditions various intermediate tungsten oxides such as $WO_{2.9}$, $WO_{2.72}$, WO_2 may appear during the oxidation process [42, 55].

Absorption: At low temperature (i.e. < 0 °C), oxygen is adsorbed molecularly, but at room temperature this adsorption is a precursor state to atomic adsorption. A covered surface shows an ordered oxygen superstructure. If the temperature is increased, a more extensive coverage occurs and oxide-like structures are formed. The surface layer can be described as adsorbed oxide [1].

Diffusion: Oxygen diffuses from the surface into the crystal lattice forming a bcc (α) solid solution. The solubility is very low. Calculated diffusion coefficients at 1700 °C are given

as $D = 10^{-7}$ and $D = 3 \times 10^{-8}$ to $D = 5 \times 10^{-8}$ cm^2/s for polycrystalline tungsten [1].

Permeation: Lassner et al. [1] found the next relation for the diffusion of oxygen through PM tungsten in the temperature range 1950-2300 °C:

$$P = 380\, e^{-\frac{-38100}{R}T}, \quad [\mathrm{mm^3O_2/(cm^2 atm^{1/2} min)}] \tag{2.2.6}$$

where P denotes the permeation coefficient and T is the temperature in K.

Reaction of tungsten with water

Industrial tungsten production is commonly performed in the absence of O_2. However, as further described, H_2O is present in the system, and therefore, it is important to consider the reaction of tungsten with water.

The main equation for the reaction involved is

$$\mathrm{W} + x\mathrm{H_2O} \rightleftarrows \mathrm{WO}_X + x\mathrm{H_2} \tag{2.2.7}$$

Water starts reacting with tungsten below the boiling point. In principle, water acts as an oxidizing agent. According to Warren et al. [56], WO_2 and WO_3 are formed by:

$$\mathrm{W} + 2\mathrm{H_2O} \rightleftarrows \mathrm{WO_2} + 2\mathrm{H_2} \tag{2.2.8}$$

$$\mathrm{W} + 3\mathrm{H_2O} \rightleftarrows \mathrm{WO_3} + 3\mathrm{H_2} \tag{2.2.9}$$

Warren et al. [56] also showed that reaction with water vapour or humid air 60-95% relative humidity, at 20-500 °C, causes a WO_3 layer formation. The thickness of the resulting layer increases with humidity. The reaction rate is related to the temperature and the $[H_2O]/[H_2]$ partial pressure ratio. The high partial pressure of water or hydrogen drives the reaction in a particular direction.

Posterior investigations by Sabourin and Yetter [57], confirmed that all known tungsten oxides formation depend on p_{H_2O}/p_{H_2} ratio and temperature. Conversely, maintaining both these parameters at low values yields WO_2 formation. Increasing both parameters results in higher oxides formation (e.g. $WO_{2.72}$, $WO_{2.9}$, WO_3).

At temperatures above 600 °C, the so-called Chemical Vapour Transport (CVT) process starts with $WO_2(OH)_2$ or $WO_3 \cdot H_2O$, a gaseous transport agent between the transformation steps [1, 12]. Thus, a volatilization of tungsten with water occurs forming hydrated tungsten oxides that are convected into the flowing atmosphere [58]. Several authors have studied this mechanism. Greene and Finfrock [58] studied the tungsten vapourization by measuring the weight loss of tungsten rods in flowing steam between 700 °C and

1350 °C. In a similar study, Sabourin and Yetter [57, 59], employed 200 µm tungsten foils to perform heterogeneous oxidation in a H_2O/H_2 atmosphere. Some authors propose correlations for vapourization rates $k[\ s^{-1}]$ which depend on water vapour concentration in the form of the following power law

$$k = Ae^{-E_a/(RT)} {P_{H_2O,torr}}^n \tag{2.2.10}$$

where the equation parameters A, E_a as well as the temperature range are indicated in table 2.2.4.

Table 2.2.4: Review of tungsten volatilization rates in the presence of water vapour.

A	E_a [kcal/mol]	n [-]	T range [K]	Reference
6.805	-48.9	1.00	1323 - 1723	[60]
1.137×10^{-3}	-22.7	1.00	1723 - 1923	[60]
1.886	-47.2	1.00	1073 - 1623	[58]
7.595	-48.1	1.00	1073 - 1973	[61]
10	-48.0	0.80	1960 - 2290	[62]
6.595	-51.0	0.83	1473 - 1973	[59]

The volatilization of tungsten, tungsten oxides as well as the reactions involved are further reported in section 2.2.4.2.

Tungsten trioxide (WO_3) reduction sequence

The industrial reduction of WO_{3-X} to W powder by hydrogen is considered a well established process, in which empirical knowledge has allowed the production of fine metallic-W powders [5, 63, 64]. Commercial tungsten raw concentrates contain 65-78% WO_3, and therefore, tungsten trioxide is the head of the reduction sequence in this review.

The hydrogen reduction of tungsten trioxide, described by the elementary expression $WO_3 + 3H_2 \rightarrow W + 3H_2O$, is indeed a rather heterogeneous process. As described in fig. 2.2.6, the reduction process is not only a direct conversion from oxide to metal, but several solid and gaseous intermediates may arise. The formation transport and deposition of gaseous forms of tungsten (tungsten volatiles) are responsible for the final powder grain size characteristics [1, 6, 7, 8]. Yuping et al. [9] investigated the effects of the hydrogen dew point and the flow of blue tungsten oxide reduction. Although they had not found vapour phases, they documented the influence of the reductive-atmosphere on the different paths. In a similar approach Zhiqiang et al. [10, 11] studied the effect of humidity on the dynamic process at low temperature. They found that the initial oxide form was strongly affecting the process [11]. However, both, investigations by Yuping et al. [9] and Zhiqiang et al. [10, 11], agree that temperature is the most important parameter promoting the reduction process.

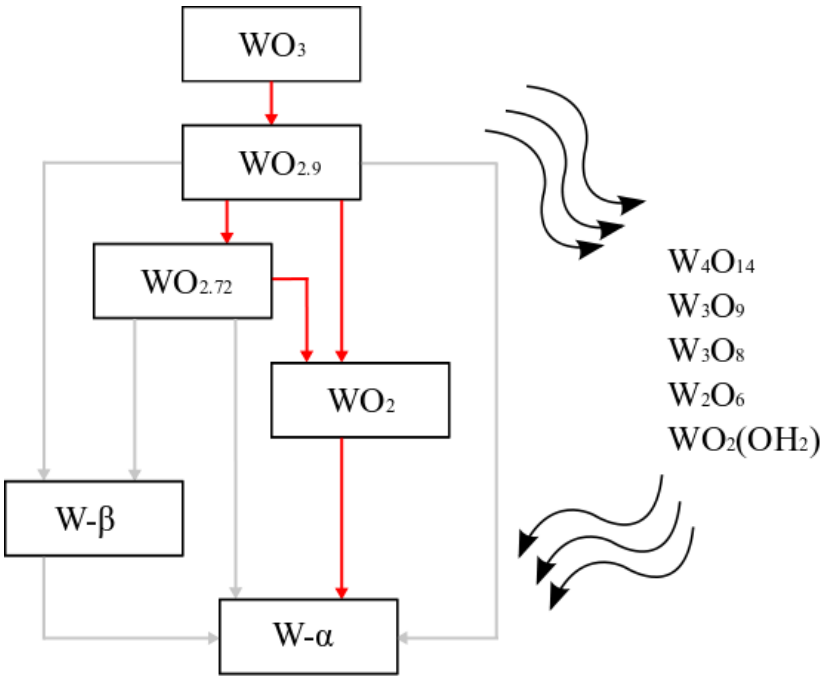

Figure 2.2.6: Reduction paths and the intermediate species involved in the hydrogen reduction of tungsten trioxide. While the boxes contain the solid species, the cloud lists the gaseous species. The red lines represent the main transition paths.

A comprehensive review of the applicable literature concerning the physical chemistry of tungsten was published by Lassner and Schubert[1]; but additional details may be found in [65].

2.2.4 Reduction of tungsten trioxide into pure tungsten

According to the investigations on the field, two mechanisms explain the technical hydrogen reduction of tungsten oxides. The first dominates the reaction course under atmospheres with a lower water vapour content and is known as dry mechanism, direct mechanism or oxygen transport mechanism. The second is important under the presence of water vapour and is known as wet mechanism, CVT mechanism or tungsten transport mechanism. Which of the two mechanisms dominates the course of the reduction is regulated by the interaction among temperature, dew point, hydrogen flow, and the kinetics of the new phase formation. The latter deserves deeper consideration, and therefore, is discussed in the next subsections 2.2.4.1 and 2.2.4.2.

2.2.4.1 Oxygen transport mechanism

The oxygen transport mechanism is also called *Diffusion in Solid State* or *Direct Reduction mechanism*. Here the reduction takes place by direct removal of oxygen from the solid phases, where oxygen is 'transported' out of the system in the form of water vapour [35]. When the reduction is governed by this mechanism, the reduced metal particles remain pseudo-morphous to the starting oxide [6, 50, 66]. Thus, the powder morphology of elemental raw powder is maintained after the reduction process. The reduced powder consist of small W metal grains within a large agglomerate forming a polycrystalline metal sponge as depicted in figs. 2.2.7 and 2.2.8, the finer the crystal size, the higher the strength of these agglomerated particles. The reactions usually occur at temperatures below 750 °C.

The commonly accepted solid oxides intermediates and the sequence occurring upon reduction under industrial conductions is described in the following eqs. (2.2.11) to (2.2.14)

$$WO_3(s) + 0.1H_2(g) \rightleftarrows WO_{2.9}(s) + 0.1H_2O \tag{2.2.11}$$

$$WO_{2.9}(s) + 0.18H_2(g) \rightleftarrows WO_{2.72}(s) + 0.18H_2O \tag{2.2.12}$$

$$WO_{2.72}(s) + 0.72H_2(g) \rightleftarrows WO_2(s) + 0.72H_2O \tag{2.2.13}$$

$$WO_2(s) + 2H_2(g) \rightleftarrows W(s) + 2H_2O \tag{2.2.14}$$

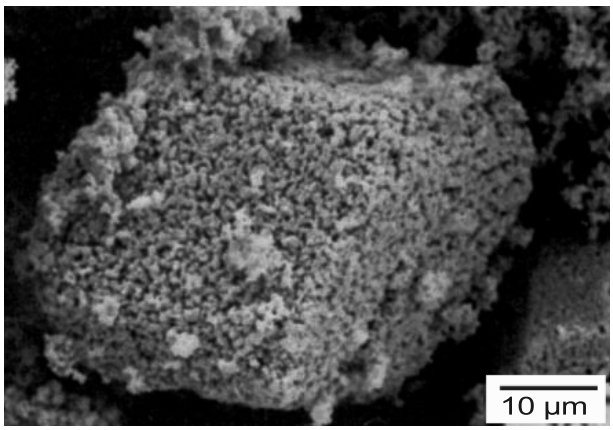

Figure 2.2.7: SEM micro-graph example of a reduced tungsten metal agglomerate. Reduction governed by oxygen transport. Source: [1].

Thermodynamic and kinetic considerations

A basic understanding of the process is provided by the thermodynamic study of the phase equilibria during the chemical reactions outlined in eqs. (2.2.11) to (2.2.14).

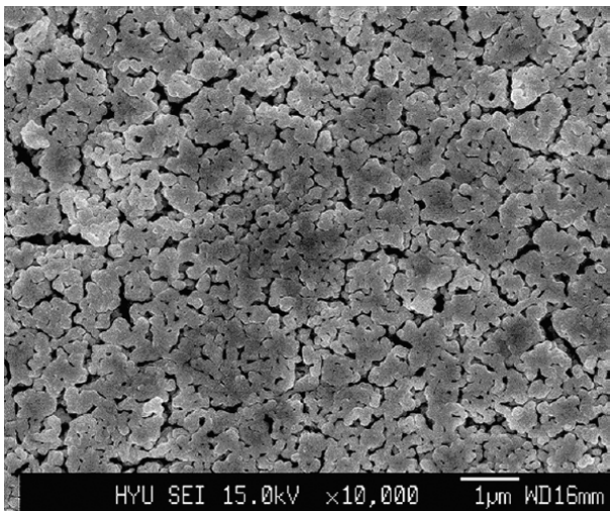

Figure 2.2.8: SEM micro-graph example of a reduced tungsten metal (as supplied). Reduction governed by oxygen transport. Source: [66].

Figure 2.2.9 and table 2.2.5 depict the stability regions of the oxides. The equilibrium expressions have been determined from experimental observations of temperature and the p_{H_2O}/p_{H_2} ratio, of the different steps of eqs. (2.2.11) to (2.2.14). The diagram suggests that all the solid phases can be obtained by processing WO_3 or W under the respective equilibrium temperature and humidity conditions.

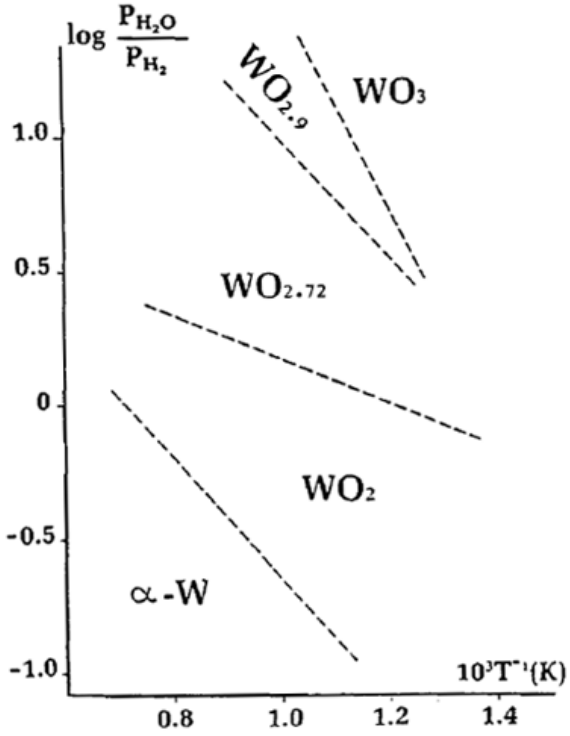

Figure 2.2.9: Equilibrium diagram for the W-O-H system. Source: [1].

Today, W-β is well accepted as a transient as well as metastable and is, therefore, not present in the equilibrium phase relations of table 2.2.5.

Table 2.2.5: Accepted equilibrium constants of the direct reduction mechanism [1].

$K_{eq} = e^{A_{eq}/T+B_{eq}}$, [-]		
Step	A_{eq} $[K]$	B_{eq} $[-]$
$WO_3 \leftrightarrow WO_{2.9}$	- 8933.6	12.35
$WO_{2.9} \leftrightarrow WO_{2.72}$	- 4952.6	7.2062
$WO_{2.72} \leftrightarrow WO_2$	- 1858.4	2.2631
$WO_2 \leftrightarrow W$	- 5143.7	3.647

Wu Xiang-Wei et al. [8] found that among these phase transitions, the first three transitions, $WO_3 \rightarrow WO_{2.9}$, $WO_{2.9} \rightarrow WO_{2.72}$, and $WO_{2.72} \rightarrow WO_2$, proceed very fast, and therefore, the reduction rate is limited mainly by the $WO_2 \rightarrow W$ path.

Thin layers of fine powder particles of WO_3 have been used in different studies to investigate the reduction kinetics by means of thermogravimetric techniques. These techniques allow determining reduction parameters such as activation energies and pre-exponential factors for modeling the extend of the reaction's evolution. Activation energies and pre-exponential factors are the model parameters of the reaction rates, which can be characterized as function of a rate constant that follows an Arrhenius equation. In the last years, thermogravimetric observations have proved the consistency of the kinetic parameters documented by Lassner and Schubert [1]. This data will be further presented in section 4.1.2.2.

2.2.4.2 Tungsten transport mechanism

Referred to earlier as *Chemical Vapour Transport*, in this mechanism, $WO_2(OH)_2$ (tungstic acid vapour) together with other formed volatile tungsten compounds, are responsible for the tungsten transport between various intermediate transformation steps [5, 67]. However, equilibrium calculations included in [1] show $WO_2(OH)_2$ as the most volatile Tungsten Oxide Hydrate (TOH), and the other volatile compounds could be considered negligible.

With fig. 2.2.10, Schulmeyer and Ortner [68] described the steps of a particle transformation under a Chemical Vapour Transport mechanism. The figure may schematically represent the main steps that a tungsten oxide particle undergoes during the tungsten vapour mechanism:

- The volatilization of WO_X (S1 in fig. 2.2.10) with water vapour forms $WO_2(OH)_2$ (TP1 in fig. 2.2.10) in a surface reaction.
- Nuclei are build up according to nucleation processes.
- Transport of the tungsten oxide hydrate.
- $WO_2(OH)_2$ is reduced at the surface of the existing tungsten oxide/metal nuclei (S2 in fig. 2.2.10).
- Grains, or nuclei, growth by the deposition of $WO_2(OH)_2$.

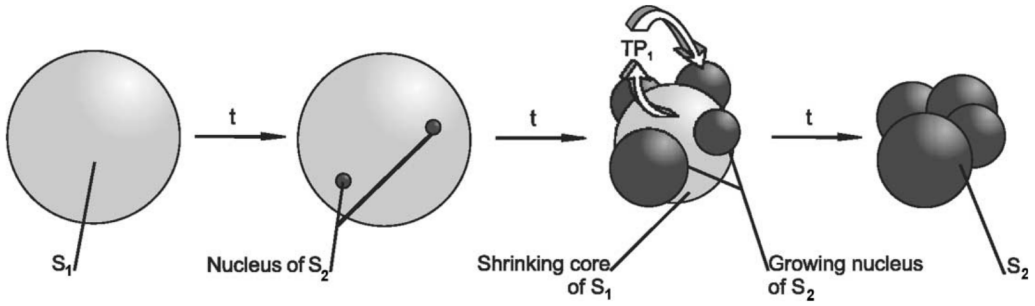

Figure 2.2.10: Graphical representation of a CVT transformation. Source: [68].

When tungsten transport occurs, changes in the morphology of the solid phases appear [6, 12, 48, 66]. Bigger tungsten crystals (ranging from 1 to several μm) grow individually (fig. 2.2.11a). This type of agglomeration is looser than the pseudo-morphous described earlier and takes place mainly under wet reduction conditions. On the other hand, if the reduction occurs under wet conditions and high temperature inter-growing crystals results (fig. 2.2.11b).

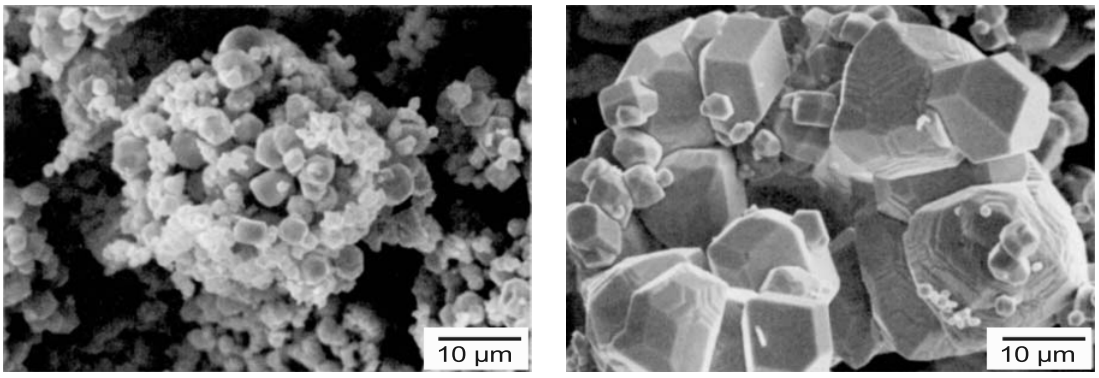

(a) Reduction under dry H2 **(b)** Reduction under wet H2

Figure 2.2.11: SEM micro-graph example of reduced tungsten metal (as supplied). In both cases the reduction was influenced by CVT. Source: [1].

Tungstic acid vapour formation

The presence of $WO_2(OH)_2$ (tungstic acid vapour), during the WO_X reduction process, was first proven in 1963 by Glemser et al. [63] by means of mass spectroscopy.

When the reduction, or oxidation process, show an apparent increase in vapour pressure at high temperatures a reaction between tungsten oxides or metallic tungsten and H_2O occurs. As a product the volatile $WO_2(OH)_2$ is formed [1, 48, 64]. Despite today's discussion on tungsten reduction mechanisms, many authors have agreed on the dominance of the transport of tungsten through the gas phase by the volatile oxide hydrate. In industrial tungsten metal production, the oxide hydrate is considered as the main agent responsible for reduction of tungsten oxide [7, 14, 41, 59, 67, 69].

"Under near equilibrium conditions the tungsten may be transported three times via the vapour phase before it is reduced to the metal" [1]:

$$WO_3(s) + H_2O(g) \rightleftarrows WO_2(OH)_2(g) \tag{2.2.15}$$

$$\frac{1}{2}W_{20}O_{58}(s) + 11H_2O(g) \rightleftarrows 10WO_2(OH)_2(g) + H_2(g) \tag{2.2.16}$$

$$W_{18}O_{49}(s) + 23H_2O(g) \rightleftarrows 18WO_2(OH)_2(g) + 5H_2(g) \tag{2.2.17}$$

$$WO_2(s) + 2H_2O(g) \rightleftarrows WO_2(OH)_2(g) + H_2(g) \tag{2.2.18}$$

$$W(s) + 4H_2O(g) \rightleftarrows WO_2(OH)_2(g) + 3H_2(g) \tag{2.2.19}$$

Greene [58] suggested that as the tungsten oxides were hydrated by the water vapour to $WO_2(OH)_2$, it entered a water vapour boundary layer where it immediately condensed back to tungsten-oxide during a cooling step. Similarly, Lassner and Schubert [1] estimated that volatiles are fast deposited on the next available sites. However, Matviichuk et al. [70] found that the tungstic acid vapour travels distances of up to 50 cm before condensation.

Thermodynamic and kinetic considerations

In the past, the equilibrium constants K_{eq} for the current mechanism were investigated and established. Recent thermodynamic calculations, performed by Matviichuk et al. [70], are in accordance with earlier researches. Thus, the tungsten transport mechanism can be understood as a thermodynamically well-known mechanism. Table 2.2.6 outlines the equilibrium constants of the different steps involved in the process.

Even though the thermodynamics of this wet mechanism are defined, the kinetics of the different steps of the mechanism are unknown. Volatiles, such as $WO_2(OH)_2$, are deposited as soon as they are produced [1], and therefore, the short half-life of the volatile

species present in the mechanism impede the task of measuring their production or consumption rate. Thus, defining the kinetics of the volatilization and deposition reactions (eqs. (2.2.15) to (2.2.19)) remains a challenge for physicists and engineers. In addition, $WO_2(OH)_2$ is still not a well-known species and the lack of its physical characterization is still considered a source of errors within predictive models.

2.2.5 Nucleation and crystal growth phenomena

Phase nucleation is the first step when a new phase is formed during a reduction process.

Oxygen transport mechanism dominates the low-temperature reduction of tungsten oxides, and no significant grain coarsening is observed during this sequence. Moreover, the the pores of the oxides may increase [48, 54]. The lower the humidity the higher is the nucleation rate and therefore the lower is the growth of the individual grains, which result in smaller average grain sizes. The contrary also applies, during high humidity few nuclei are formed leading to a coarse product. Freshly generated tungsten metal nuclei are active sites onto which volatiles are deposited. Thus, tungsten transport mechanisms may lead to pronounced grain growth [6, 7, 8, 14].

Lassner et al. [1] found that particle coarsening occurs via a vapour phase, leading to the evaporation of smaller grains as well as the growth of the larger grains in a similar process to an Ostwald ripening.

The height and porosity of the powder layer determine the diffusion of gases from and through the bed. Hence, the water vapour arising during the reactions may be concentrated within the layer favoring grain growth by CVT.

Table 2.2.6: Equilibrium constants of the tungsten transport mechanism extracted from literature.

$$K_{eq} = e^{A_{eq}/T + B_{eq}}$$

Step	A_{eq} [K]	B_{eq} [-]	Reference
$WO_2(OH)_2 \leftrightarrow WO_3$	20096.82	-9.44	Glemser [71], Haubner [65]
$WO_2(OH)_2 \leftrightarrow WO_{2.9}$	197175.27	-86.82	Haubner [65]
$WO_2(OH)_2 \leftrightarrow WO_{2.72}$	307268.39	-109.67	Haubner [65]
$WO_2(OH)_2 \leftrightarrow WO_2$	17783.28	-6.32	Haubner [65]
$WO_2(OH)_2 \leftrightarrow W$	13447 ± 852	-2.8 ± 0.53	Belton and McCarron [72]
$WO_2(OH)_2 \leftrightarrow W$	10347.13	-0.92	Haubner [65]

2.2.5.1 Considerations to reduce W powder size and size distribution

Polycrystalline tungsten produced during industrial processing may have a broad size distribution, high degree of particle agglomeration and high reactivity [48]. As long as the temperature and the powder layer height are kept low while a high and dry reductive gas flow is granted, fine powders can be easily produced [48, 54]. Under such conditions the reduction proceeds mainly via the direct $WO_3 \rightarrow WO_{2.9} \rightarrow$W-$\beta \rightarrow$W-$\alpha$ reaction path. However, this is not always possible during industrial reduction. During technical reduction, the high powder bed exerts a high-diffusion resistance to the formed water removal from the layer. The layer humidity provide the conditions for tungsten vapour transport reactions to occur during the reduction sequence. Increasing the hydrogen flow in high layer beds (up to cm), will only affect the rate of water removal from the uppermost part of the layer, letting the reactions inside the layer remain diffusion-controlled. Hence, the powder layer height and its porosity become of crucial importance on the retention of the reaction water since diffusion resistance drives a dynamic humidity level within the layer. This results in a significant influence on the reduction path, reduction rate, nucleation and grain growth conditions, where not only W grain size is affected, but also size distribution, morphology, agglomeration, apparent density, and compatibility.

The grain size distribution is predominantly influenced by the powder layer height. The growth conditions are different over the boat. For instance the humidity is higher in the interior and decreases when approaching the surface. Hence, larger grain-sized particles appear inside the layer, while smaller grain-sized particles are found at surface-neighboring areas.

To reduce the above effect during industrial reduction low layers may be employed, but this solution reduces the production capacity. Nevertheless, the low production capacity can be compensated, to a certain extent, by using multiple boats.

Co-current instead of counter-current hydrogen flow favors a more uniform size distribution as reported by Zhengji [50, 73]. In addition, below 0.5 µm the powders may be pyrophoric and, co-current hydrogen flow seems to be the most effective method to avoid the burning of such powders. Nevertheless, industrial reduction usually applies a counter-current hydrogen flow direction [5].

Table 2.2.7 summarizes the general rules to reduce W grain size during the reduction process, nonetheless, during technical reduction, this may not be strictly respected. By selection of the appropriated reduction parameters, the mean particle size can be varied between 0.1 and 0.15 µm.

Table 2.2.7: Considerations to obtain a small W powder grain size.

Reducing agent related	WO_X related	Energy related
Dry hydrogen High hydrogen flow rate Low dew point Co-current flow	Small powder layer height High porosity Low oxide powder feed	Low temperature

Inhibitors or dopants may be added at primary stages in order to favor evenly distributed and/or to attenuate grain growth [48, 74]. In addition, a humid atmosphere can be granted in order to obtain a uniform grain growth along the bed and, consequently, a uniform size distribution may be achieved. Moreover, Kim et al. [66] found that the particle size of the reduced metal phase can be strongly influenced by an earlier ball-milling treatment of the raw WO_3 powder.

Another technique to reduce grain size is high-energy mechanical milling (MM). With this technique particles in the micro-scale are milled and fractured onto the nano-scale. The resulting powders have sizes below 20 nm. However, milling produces contamination from the wear of equipment and media [44].

Certain trace elements, such as Li, Na, K, Mn, Fe, Co or Ni, improve the reduction rate during the $WO_2 \rightarrow$W, stage while others, such as B, Al or Cr retard it. Crystal growth can be significantly stimulated by alkali metals, whereas Co, Al, V, Cr may reduce, or even suppress it. Ardestani et al. [69] propose copper acting as a barrier for formation and transportation of volatile $WO_2(OH)_2$.

Grain growth via CVT mechanism may be attenuated, or even avoided, by affecting the reduction parameters (e.g. depth of the boats, humidity, temperature, partial pressure ratio). For instance, different approaches, such as the reduction in a vertical tube reactor of Kamberovi et al.[16], successfully produced fine tungsten powders at high temperatures without the presence of $WO_2(OH)_2$. Lackner et al. [6] showed a different tungsten oxide reduction mechanism/apparatus (with temperatures from 800 to 1100 °C) that contradicted the industrial reduction in a powder bed and was, thus, not affected by the CVT-mechanism.

Wu [14] proposed a short-range CVT mechanism, in which $WO_{2.72}$, also called TVO (Tungsten Violet Oxide), is used as initial oxide. It is clear that the oxygen content of $WO_{2.72}$ is lower than its precursors, hence, the water vapour formed during further reduction is less. Nevertheless, the size of $WO_{2.72}$ nano-tubes is still determining the W grain size.

2.3 A survey on Powder Metallurgy processes modeling

2.3.1 Overview

In PM processes, a series of heterogeneous reactions take place. Heterogeneous reactions play a significant role in the extraction of pure metals from their ores states, as well as in a larger number of industrial applications such as combustion of solid fuels. Thus, the reduction of metallic oxides into pure metals is performed by applying a reducing gas, commonly hydrogen or carbon monoxide, over a granular feedstock of metallic oxides. Understanding the thermo-chemical processes and the interaction phenomena within these industrial reactors is crucial for accurate predictions that will lead to stable operation, lower energy consumption, higher efficiency, homogeneous products, etc. An extensive review on modeling of heterogeneous reactions was documented by Hoffmann [28] and an excellent theoretical background on heterogeneous reactions can be found in Szekely, Evans and Yong Sohn [75].

The production of steel powders for PM applications has been modelled by Sato et al. [20] via a pure continuous approach implemented in Fluent [76]. The study was concentrated on gas species transport along a push type furnace and a simple heterogeneous reaction accounting for H_2O was documented.

Martin et al. [33] used a variant of the Discrete Element Method to model the free sintering of metallic powders. They introduced a simple coarsening/anisotropic shrinkage model to simulate densification rates and compare it with experimental data.

2.3.2 Review on tungsten oxides reduction modeling

Harboury et al. [15], modelled the WO_3 to W reduction rate by assuming uniform hydrogen distribution in an "unpacked bed", but, their lumped model was accurate only for low layers with a height < 1.5 mm.

Sha et al. [77] developed a general computational model, which can be used for calculation and graphical visualization of the standard Gibbs free energy changes and equilibrium constants for most reactions and phase transitions in chemical reactions of metallurgy processes. They employed the scheme represented by eqs. (2.2.11) to (2.2.14). The resulting thermodynamic data, accounting for the different species involved on reactions eqs. (2.2.11) to (2.2.14), is collected in table 2.3.1

Table 2.3.1: Thermodynamic data of substances in reactions eqs. (2.2.11) to (2.2.14) [77].

Substance	ΔH^0_{298} [kcal/mol]	$C_p = a + bT + cT^{-2} + dT^2$ [cal/molK]				T range [K]
		a	$b \times 10^{-3}$	$c \times 10^{-5}$	$d \times 10^{-6}$	
$WO_{3(s)}$	-201.460	20.950	3.864	-4.182	0	298 - 1050
		19.348	3.913	0	0	1050 - 1745
$H_{2(g)}$	0	4.044	14.689	0.141	-19.015	298 - 400
		6.759	0.100	0.196	0.351	400 - 1600
$WO_{2.9(s)}$	-196.000	21.347	2.757	-4.672	0	298 - 2000
$H_2O_{(g)}$	-57.798	8.023	-1.004	0	3.528	298 - 600
		5.227	5.392	2.029	-0.956	600 - 1600
$WO_{2.72(s)}$	-186.700	20.196	2.911	-4.323	0	298 - 2000
$WO_{2(s)}$	-140.940	18.503	-1.675	-4.420	2.119	298 - 1997

2.3.2.1 Considerations to model WO_X reduction into metallic tungsten

In order to overpass the uncertainty existing on the industrial reduction of tungsten oxides, some outcomes have to be considered and measures to reduce its impact have to be taken. The following factors are of particular interest.

Temperature: As reviewed by Lassner [41], literature values for temperature measurements *"can be misleading because some are related to the real temperature of the powder layer, while others are furnace temperatures measured at the wall of the heating compartment or tube" [41]*. Thus, in order to validate predictions of numerical models, experimental data must include a detailed description of the temperature measurements.

Kinetics: Many discrepancies among peer-reviewed articles are found on the kinetics, composition, and structure of the tungsten oxide formation, and this restrict the tungsten redox phenomenon study.

The kinetics of the WO_3 volatilization may be obtained from Matviichuk [70] observations. Nevertheless, due to the non-homogeneity of his experiment, intrinsic kinetic data may not be obtained without the help of comprehensive models involving transport phenomena. It has to be pointed out that Matviichuk's data [70] is the only available research providing kinetic information to model the process of volatilization of WO_3.

Particle size: Short diffusion paths along small particles may allow the reducing agents to reach the entire inner surface more easily. Turkdogan et al. [78] observed that, for small iron oxide particles, the time to complete the reduction under H_2 process is independent of the particle size. However, due to the dense nature of WO_3 particles and as documented

in [28, 78], diffusion processes and kinetics of the reaction at the pore walls (or reaction sites) do contribute to the thermo-chemical conversion of single WO_3 particles. This fact was separately observed by Harboury et al.[15] and Bustnes et al. [18]. They probed that the size of the particles influence the time of the reduction of WO_3.

Particle splitting: Figure 2.2.3 shows a TBO micro-image which predominantly kept the shape of its precursors APT crystals. Some existing cracks on the surface may influence a split along these cracks favoring the gas circulation during the subsequent reduction [6, 50].

Chapter 3

eXtended Discrete Element Method

I start where the last man left off.

T.A. Edison

In order to predict the complex phenomena occurring during the hydrogen reduction of WO_X, this study relies on a multi-physics numerical framework, referred to as eXtended Discrete Element Method (XDEM). In XDEM the numerical research is focused on the thermal conversion of powder matters. As presented by Peters et al. [79], and graphically summarized in fig. 3.1, XDEM extends the dynamics of particles described by the classic Discrete Element Method (DEM) (Cundall et al. [24]) by supplementary properties such as the thermodynamic state or stress/strain for each individual particle [79, 80]. In addition, the concept involves heat and mass interaction of single particles with its environment by linking, both, continuous and discrete approaches. Hence, XDEM augments the classic DEM by providing information on the thermodynamic state of particles.

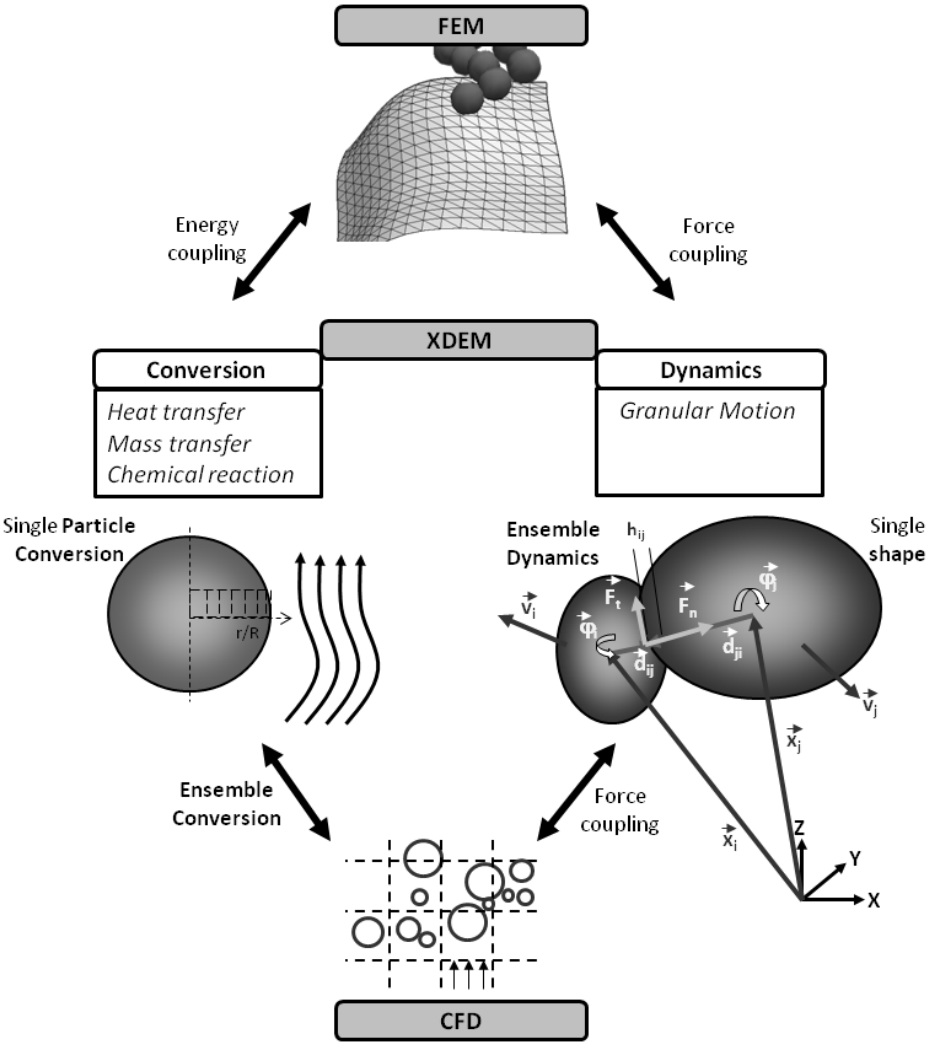

Figure 3.1: Graphical representation of XDEM and its couplings. Source [28].

This numerical framework has successfully been used in different industrial applications. Michael et al. [81] coupled it to the continuous Finite Element Analysis (FEA) in order to predict the interaction of tires with snow particles. Peters [30, 31, 32] and Mahmoudi et al. [29] employed XDEM techniques to model the pyrolysis and combustion of biomass materials. Predictions for heat transfer and mass transfer during water removal of packed beds were validated by Estupinan et al. [25], Peters et al. [26] and Mahmoudi et al. [27] were performed under the XDEM concept. Ashraf et al. [82] has coupled CFD to DEM to investigate numerically crystal dynamics in an existing pilot-scale batch crystallizer; this research yielded a detailed description of crystal dynamics considering a four-way coupling. Heterogeneous reductions occurring in packed beds of metallic oxides were predicted by Hoffmann [28] with a high degree of accuracy. Due to the metal oxide reduction reactions modeling introduced by Hoffmann, his work [28] is a valuable reference for metal oxides reduction modeling such as the one presented in this work.

This study generated intermediate publications in which XDEM was successfully presented as a novel approach for thermochemical conversion on powder metallurgy. Estupinan et al. [34, 35] used a single XDEM particle model to validate the direct reduction of tungsten trioxide particles. XDEM predictions were compared to experimental data of powder packed beds (PPB) undergoing decarbonation [36] to validate the approach at a micro-particle scale. In Estupinan et al. [38], the isothermal reduction of a PPB of tungsten trioxide was predicted under dry atmospheres. The non-steady reduction of tungsten trioxide in hydrogen atmospheres was presented by Estupinan et al. [37], whose results are included in chapter 5. Thus, it is believed that the proposed numerical technique can be employed to predict the spatial and temporal evolution of tungsten powder production and the intermediate species appearing during processes.

Chapter 4

Numerical model

Contents

There is no unique picture of reality.

S. Hawking

4.1 Multiscale modeling

4.1.1 Overview

Multiscale modeling attempts to couple the models of different time and length scales to describe processes from theoretical foundations. Different scale-ranges are found in powder metallurgy, from the atomic level to the plant level. Not surprisingly, the industrial reduction of tungsten oxide into metallic tungsten is considered as a multiscale problem. For several decades the multiscale reduction model showed on fig. 4.1.1, indirectly proposed by Haubner [65], has been employed to explain the complexity of the reduction process. Nevertheless, Haubner's model has never been translated into a comprehensive mathematical model, and as introduced in chapter 2, only few lumped models or empirical correlations describe parts of the process.

The goal of this multiscale model is to combine all the scales listed hereafter to describe the industrial reduction of tungsten oxides process.

Molecular scale Rate constants, activation energies, heat of adsorption or heat capacities, as well as nucleation and grain growth rates are provided by atomistic models. Such models are the input of a molecular scale, consisting of surface processes and/or chemical reactions [83].

Particle scale The transport phenomena inside particles in combination with the kinetics of the molecular scale and crystallization processes are described by one-dimensional conservation equations. Thus, the approach yields distribution of species, temperature and morphology within particles. This concept has been consolidated as an accurate representation for similar problems over the last two decades [28, 31, 84].

Powder layer, or powder packed bed (PPB) scale It is to be understood as an accumulation of particles; where neighbor particles as well as boundaries and particles exchange heat fluxes by conduction and radiation. The fluid phase filling the void space between particles is treated as a compressible, multicomponent continuum exchanging energy and mass with the PPB.

Furnace scale According to Haubner [65], this scale is the input of the system. Set points for temperature, reacting agents flow as well as material inflow are applied to the system following industrial rules in order to control the process.

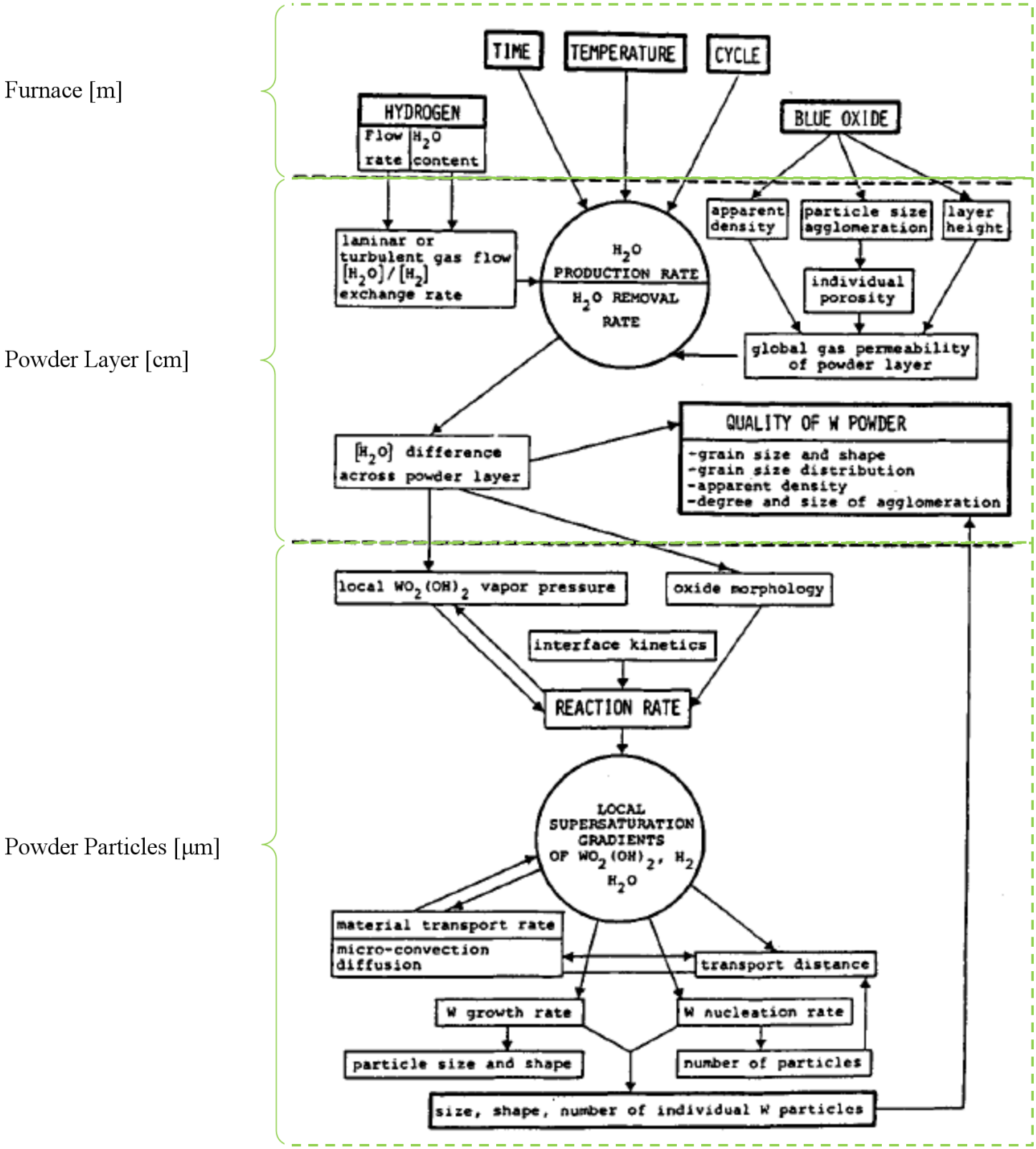

Figure 4.1.1: The different length scales of the industrial reduction of tungsten oxides. Source: [65].

Since the molecular scale is considered in the particle model and the furnace scale is explicitly given as an input, the particle scale and the PPB scale can be understood as the core of the numerical model presented in this chapter.

The current multiscale process involves multiple phases such as the solid oxides and the reducing gases and gaseous products. The solid phase is characterized by a porous media on two scales: WO_X particles exhibit an internal pore structure [1, 16, 85] and PPBs exhibit void spaces on a much larger scale; in which, energy, mass and momentum transport occurs. The mathematical foundation to write the governing equations of the treated transport phenomena has extensively been studied and documented by many authors [28, 83, 86, 87, 88]. This thesis collects these mathematical formulation in appendix B for reference purposes.

4.1.2 Powder particle scale

The smallest representative unit of a heterogeneous reduction, such as the herein presented, is the interaction of a single powder particle with the fluid stream. Thus, this section describes the thermochemical conversion of single powder particles. The conversion of more complex assemblies of particles is subsequently described in section 4.1.3. At the powder particle scale, the mathematical model describing the thermochemical conversion of single particles is based on the following statements [21]; which are applied according to the conservation equation theory described in appendix B.2:

- One-dimensional and transient conservation equations characterize energy and mass transport within each particle. According to Man and Byeong [84], this is an accurate approach for the scale of the treated problems.
- Each particle is discretized in Cartesian, cylindrical or spherical coordinates systems according to its geometry.
- Particles are assumed as porous and uniform material with properties changing along a representative length scale.
- Particles are considered to consist of liquid, solid and gas phases.
- An important quantity to characterize the void space, or available space for gaseous species, of a discrete particle is the porosity ϵ_P. It is defined as the ratio of the porous volume, occupied by gaseous species V_g, to the volume of the particle V_P ($\epsilon_P = V_g/V_P$). The remaining space is fully occupied by liquid and solid species, which are assumed to reduce/increase the porosity according to its production/consumption.

- Morphology changes are accounted for by the evolution of porosity and particles size.
- Gas is transported by diffusion and convection within the particle-pore space.
- The inertial terms of the momentum equation for the gas flow is neglected due to the very small pore diameter [89].
- Gaseous species are treated as ideal gases.
- Inside the particles, solid and gaseous species are in local thermal equilibrium. This assumption is based on the Peclet number (ratio of conduction to convection heat transfer rates) assessment effectuated by Peters [31] and Kansa et al. [89].
- Heat transfer occurs by conduction and radiation between neighbor particles.
- Heat and mass transfer from fluid to particles are represented through boundary conditions specified by the surrounding gas and the surface conditions of the particle.
- Convective heat transfer coefficients are estimated from Nusselt number semi-empirical correlation for mono-disperse and naturally arranged packed beds [90].
- Reaction kinetics are described by intrinsic rate modeling for equilibrium reactions according to [28].
- The sum of all particle processes represents the entire process.
- Particle cracking is not considered in this study. Nevertheless, it is believed that cracking effects may be captured by the intra-particle porosity.

According to the statements above, conservation equations for species, mass, energy and momentum are solved to determine the state variables distributions over time and space within the particles.

4.1.2.1 Discrete particle conservation equations

Linear momentum conservation According to Hoffmann [28], for particles with a microscopic pore structure the porous medium can be solved as a homogeneous system. Thus, due to the very low Reynold numbers observed in powder systems, a one-dimensional form of Darcy's law can be employed, namely

$$-\frac{\partial \langle p \rangle}{\partial x} = \frac{\mu_g \epsilon_p}{K} \langle u_g \rangle \tag{4.1.1}$$

where $\langle p \rangle$ and $\langle u_g \rangle$ extrinsic phase-averaged pressure and velocity respectively. μ_g denotes the dynamic viscosity and K represents the permeability of the porous particle.

Mass conservation The mass balance of the gas phase within the pores of a particle is based on eq. (B.3.30); where the intrinsic density $\langle\rho_g\rangle^g$ of the gas can be computed by the sum of all the species' partial densities, present in the gas phase, as

$$\langle\rho_g\rangle^g = \sum_i \langle\rho_{i,g}\rangle^g \tag{4.1.2}$$

The source term of eq. (B.3.30), accounting for gas mass consumption or production by chemical reactions, is obtained by the sum of mass production or consumption rates of the individual species.

Gaseous species conservation The one-dimensional balance of an individual specie i within the pores of a given particle is described by

$$\frac{\partial(\epsilon_p\langle\rho_{i,g}\rangle^g)}{\partial t} + \frac{1}{r^n}\frac{\partial}{\partial r}\left(r^n\langle\rho_{i,g}\rangle^g\langle u_g\rangle\right) = \frac{1}{r^n}\frac{\partial}{\partial r}(r^n D_i\epsilon_p\frac{\partial}{\partial r}\langle\rho_{i,g}\rangle^g) + \epsilon_p\sum_k \dot{\omega}_{k,i,g} \tag{4.1.3}$$

where $\dot{\omega}_{k,i}$ denotes the source term accounting for the consumption or generation of species i; which result from reaction k. $\langle\rho_{i,g}\rangle$ represents the intrinsic partial density of the specie i, $\langle u_g\rangle$ denotes the extrinsic velocity and D_i is the molecular diffusion coefficient. Equation (4.1.3) is conveniently written to be represented on different coordinates systems. Thus, the particle geometry can be chosen to be an infinite plate $n = 0$, infinite cylinder $n = 1$ or a sphere $n = 2$.

Species transport is assumed to occur by advection and molecular diffusion. An effective diffusion coefficient is determined to account for diffusion in a porous particle. Moreover, a binary diffusion coefficient of gas species includes morphology effects via tortuosity τ and porosity ϵ_p as

$$D_{ij,\text{eff}} = D_{ij}\frac{\epsilon_p}{\tau} \tag{4.1.4}$$

The diffusion coefficients D_{ij} may be affected by temperature changes. Thus, a temperature dependence is introduced as

$$D_{ij}(T) = D_{ij}^{273\text{ K}}\left(\frac{T}{273\text{ K}}\right)^{1.5} \tag{4.1.5}$$

If a Knudsen diffusion is accounted for then the effective diffusion coefficient is obtained from

$$\frac{1}{D_{\text{eff}}} = \frac{1}{D_{ij,\text{eff}}} + \frac{1}{D_{\text{Kn,eff}}} \tag{4.1.6}$$

The Knudsen diffusion coefficient, $D_{\text{Kn,eff}}$, is calculated according to Bird et al. [88]

$$D_{\text{Kn,eff}} = d_p \sqrt{\frac{8RT}{9\pi M_i}} \frac{\epsilon_p}{\tau} \tag{4.1.7}$$

where d_p characterizes the pore diameter and M_i represents the molar mass of the diffusing species.

Equation of state Assuming the gas as a perfect gas in thermodynamic equilibrium, the equations of state as a function of the two state variables temperature T and gas density ρ are given as

$$p = \rho R_v T \qquad \text{and} \qquad h = c_p T \tag{4.1.8}$$

If the mass fractions and molecular weights of the individual gaseous species are accounted for, then the density of the gas phase may be obtained as

$$\langle \rho_g \rangle^g = \frac{\langle p_g \rangle^g}{R \langle T \rangle \sum_i \frac{\xi_i}{M_i}} \tag{4.1.9}$$

Liquid and solid species conservation The mass balance of liquid and solid species i is based on the following chemical conversion rates $\dot{\omega}_k$ [28]

$$\frac{\partial \rho_{i,\text{liquid}}}{\partial t} = \sum_k M_i \cdot \dot{\omega}_{k,i,\text{liquid}} \tag{4.1.10}$$

$$\frac{\partial \rho_{i,\text{solid}}}{\partial t} = \sum_k M_i \cdot \dot{\omega}_{k,i,\text{solid}} \tag{4.1.11}$$

where $\dot{\omega}_{k,i,liquid/solid}$ is the rate of consumption or generation of the liquid/solid species i resulting from reaction k.

Energy conservation For the energy balance of the particle local thermal equilibrium between the gas phase, the liquid and the porous solid is assumed. This can be justified by the negligible thermal mass (ρc_p) of the gas phase compared to the liquid and solid phases. Hence, heat transported through bulk motion of gaseous species within the pore space is neglected. Therefore, the energy equation is based on the homogeneous model for a porous medium as described in appendix B.3.3 and writes as:

$$\frac{\partial \langle \rho c_p T \rangle}{\partial t} = \frac{1}{r^n} \frac{\partial}{\partial r} \left(r^n \lambda_{\text{eff}} \frac{\partial \langle T \rangle}{\partial r} \right) + \sum_{k=1}^{l} \dot{\omega}_k H_k \tag{4.1.12}$$

where λ_{eff} is an effective thermal conductivity calculated according to [28]. The source term, denoted by $\dot{\omega}_k H_k$, represents the heat released/consumed by the chemical reaction k,where the corresponding enthalpy is characterized by H_k.

Boundary Conditions Initial and boundary conditions are required in order to solve the presented conservation equations. Due to the possible geometries considered by the model (sphere, infinite cylinder or infinite plate), a symmetric boundary condition are applied to the center of particles

$$-\lambda_{\text{eff}} \frac{\partial \langle T \rangle}{\partial r}\bigg|_{r=0} = 0 \tag{4.1.13}$$

$$-D_i \frac{\partial \langle \rho_{i,g} \rangle^g}{\partial r}\bigg|_{r=0} = 0 \tag{4.1.14}$$

while for the surface the following relations apply for energy transfer and mass transfer respectively

$$-\lambda_{\text{eff}} \frac{\partial \langle T \rangle}{\partial r}\bigg|_{r=R} = \alpha(T_R - T_\infty) + \dot{q}''_{\text{rad}} + \dot{q}''_{\text{cond}} \tag{4.1.15}$$

$$-D_i \frac{\partial \langle \rho_{i,g} \rangle^g}{\partial r}\bigg|_{r=R} = \beta_i(\langle \rho_{i,g} \rangle^g - \rho_{i,\infty}) + \dot{m}''_{i,g} \tag{4.1.16}$$

where α and β denote the heat and mass transfer coefficients, T_∞ represents the local ambient temperature, T_R indicates the particle temperature at the surface, $\rho_{i,\infty}$ denotes the gas partial density of the species i in ambient gas and $\langle \rho_{i,g} \rangle^g$ is the partial density of species i at the surface of the particle. $\dot{m}''_{i,g}$ accounts for the mass fluxes from the environment. Radiative heat transfer with the surroundings and/or conductive heat transfer by physical contact with neighbors is accounted for through the heat fluxes ($\dot{q}''_{\text{rad}}$, $\dot{q}''_{\text{cond}}$) in eq. (4.1.15). These heat fluxes are computed according to Peters [31] as follows

$$\dot{q}''_{p,\text{rad}} = \sum_{j=1}^{M} F_{p\to j}\sigma \left(T_p^4 - T_j^4\right) \tag{4.1.17}$$

$$\dot{q}''_{p,\text{cond}} = \sum_{j=1}^{N} \frac{1}{\frac{1}{\lambda_p} + \frac{1}{\lambda_j}} \frac{T_p - T_j}{\Delta x_{p,j}} \tag{4.1.18}$$

where $F_{p\to j}$ is the view factor between particle p and its neighbor j and λ is the thermal conductivities of the different particles.

The exchange of species with the ambient gas depends on the direction of the gas flow in the pores of the surface of the particle. This exchange is characterized by the term $\dot{m}''_{i,g}$

in eq. (4.1.16) and is computed as

$$\dot{m}''_{i,g} = \begin{cases} \langle \rho_{i,g} \rangle^g \langle u_g \rangle & \text{if } \langle u_g \rangle > 0 \\ -\rho_{i,\infty} \langle u_g \rangle & \text{if } \langle u_g \rangle \leq 0 \end{cases} \tag{4.1.19}$$

The transfer coefficients α and β in eqs. (4.1.15) and (4.1.16) are calculated according to empirical correlations established for different geometries and flow conditions at the particle surface. More information about suitable relations for spherical particles immersed in a laminar fluid can be found in [25, 27, 28, 88].

Different techniques to calculate transfer coefficients exist. However, empirical correlations for Nusselt (heat transfer) or Sherwood (mass transfer) numbers are commonly employed, namely

$$\alpha = \mathrm{Nu} \frac{\lambda_f}{D_p} \tag{4.1.20}$$

$$\beta = \mathrm{Sh} \frac{D_{ij}}{D_p} \tag{4.1.21}$$

According to preliminary numerical studies within this work, the Achenbach correlation is chosen due to its wide range of applicability [28]. According to Achenbach's work [91] the convective heat transfer coefficient can be estimated by

$$\mathrm{Nu},\, \mathrm{Sh} = \left[\left(1.18 \mathrm{Re}_p^{0.58}\right)^4 + \left(0.23 \mathrm{Re}_h^{0.75}\right)^4 \right]^{1/4} \tag{4.1.22}$$

where Re_p denotes the particle Reynolds number and Re_h denotes the hydraulic Reynolds number, which are defined as

$$\mathrm{Re}_p = \frac{\langle \rho_f \rangle^f \epsilon_f \langle v_f \rangle^f D_p}{\mu} \tag{4.1.23}$$

$$\mathrm{Re}_h = \frac{\mathrm{Re}_p}{(1 - \epsilon_f)} \tag{4.1.24}$$

The employed transfer coefficients only apply for vanishing advective fluxes. If advective fluxes out of and/or into the particle become important, mass transfer coefficients have to be corrected. For instance according to the Stefan correction [31, 88], the corrected coefficient may be deduced as

$$\beta = \frac{\dot{m}''_g}{\exp(\dot{m}''_g / \beta_0) - 1} \tag{4.1.25}$$

while heat transfer coefficient also have to be corrected. Similarly, according to the Ackermann correction [31, 88], the corrected coefficeint may be computed as

$$\alpha = \frac{\dot{m}''_g \, c_{p,g}}{\exp(\dot{m}''_g \, c_{p,g}/\alpha_0) - 1} \tag{4.1.26}$$

where $\dot{m}''_g$ is the mass flux (mass flow across a unit area).

The corrected coefficients above are larger than the coefficients of the film theory for advective flows on the outer direction a particle and smaller for the opposite case [31, 28].

4.1.2.2 Chemical reactions

In section 4.1.2.1, the choice of conservation equations describing the different transport phenomena were presented. This section describes the mathematical expressions governing the chemical conversions occurring at the particle scale. The rate laws for the production or consumption of the species involved in the tungsten oxide reduction mechanisms of sections 2.2.4.1 and 2.2.4.2 are formally described.

The oxygen transport mechanism as well as the tungsten transport mechanism concern equilibrium or reversible reactions, which may be represented by

$$\sum_{i=1}^{N} \nu'_i \, R_i \;\rightleftharpoons\; \sum_{j=1}^{M} \nu''_j \, P_j \tag{4.1.27}$$

where N denotes the number of reactants R_i, M denotes the number of products P_j and $\nu_{i/j}$ represents the absolute values of the corresponding stoichiometric coefficients [92].

$$\omega = -\frac{1}{\nu'_i}\frac{dc_i}{dt} = \frac{1}{\nu''_j}\frac{dc_j}{dt} \tag{4.1.28}$$

The actual reaction rate ω may depend on species concentrations, the available reactive surface O_{sp} and the temperature; so that in general $\omega = f(c_i, c_j, O_{sp}, T, \ldots)$. Thus, an Arrhenius law is employed to describe the temperature dependency of the reaction rate as

$$k(T) = k_0 \, e^{\left(\frac{-E_a}{RT}\right)} \tag{4.1.29}$$

where $k(T)$ represents the temperature dependent rate coefficient, k_0 referred to as frequency factor and E_a denotes the activation energy [92].

Following a general heterogeneous reduction model presented in [28], the forward and backward reaction rates of a reversible reaction are hereafter described as

$$r_f = k_f(T) \cdot \prod_{i=1}^{N} c_{R_i}^{\nu_i'} \tag{4.1.30}$$

$$r_b = k_b(T) \cdot \prod_{j=1}^{M} c_{P_j}^{\nu_j''} \tag{4.1.31}$$

If thermodynamic equilibrium is reached, namely $r_f = r_b$, then an equilibrium constant $K_{\mathrm{eq,c}}$, representing the thermodynamically equilibrium state, can be obtained as

$$K_{\mathrm{eq,c}}(T) = \frac{k_f(T)}{k_b(T)} = \frac{\prod_{j=1}^{M} c_{\mathrm{eq},P_j}^{\nu_j''}}{\prod_{i=1}^{N} c_{\mathrm{eq},R_i}^{\nu_i'}} \tag{4.1.32}$$

The equilibrium constant can be expressed in terms of the partial pressures of the gaseous species involved in the reactions. Assuming ideal gases, concentration based equilibrium constant $K_{\mathrm{eq,c}}(T)$ and pressure based equilibrium constant $K_{\mathrm{eq,p}}(T)$ may be related as

$$K_{\mathrm{eq,p}}(T) = \frac{\prod_{j=1}^{M} p_{\mathrm{eq},P_j}^{\nu_j''}}{\prod_{i=1}^{N} p_{\mathrm{eq},R_i}^{\nu_i'}} = K_{\mathrm{eq,c}}(T) \cdot (RT)^{(\sum \nu_j'' - \sum \nu_i')} \tag{4.1.33}$$

Consequently, the reaction rate of a species k, involved in an equilibrium reaction at temperature T, may be represented by the following differential relation

$$\frac{dc_k}{dt} = k_f(T) \cdot \left(\nu_k' \cdot \prod_{i=1}^{N} c_{R_i}^{\nu_i'} - \frac{\nu_k''}{K_{\mathrm{eq,c}}(T)} \cdot \prod_{j=1}^{M} c_{P_j}^{\nu_j''} \right) \tag{4.1.34}$$

Oxygen transport mechanism modeling The staged direct reduction of tungsten oxides into metallic tungsten, described in section 2.2.4.1 and schematically represented by fig. 4.1.2, is represented by equilibrium reactions competing for the available species. Thus, the mathematical relation of eq. (4.1.34) is used to represent each of the reactions participating in the mechanism.

On one hand, the activation energies employed in this direct mechanism have been well studied and documented [15, 18, 65, 93, 94, 95, 96]. On the other hand, there are no reports on frequency factor values. Frequency factors are parameters that may capture

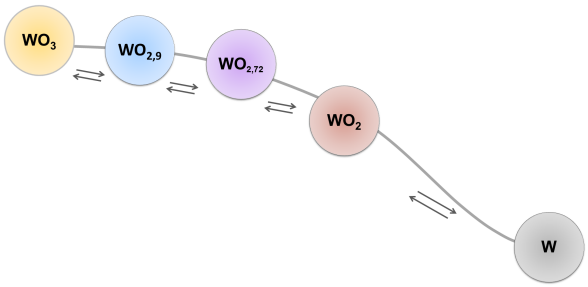

Figure 4.1.2: Direct reduction sequence. Source: [35].

the physical and geometrical characteristics on the mathematical description (e.g. surface area of the adsorbent, linear or power law temperature dependence, diffusion effects). One advantage of the proposed model is that all aspects of fluid transport, gas penetration into the bed, gas diffusion in the pores of particles and chemical reaction are considered. Thus, it leaves no scope for assuming diffusion-limiting or reaction-limiting processes. The frequency factors employed for this mechanism were deduced according to eq. (4.1.34) and the mass change curves documented by Bustnes et al.[18] and Haboury et al.[15]. The kinetic parameters describing the reaction rate employed in this model are gathered in table 4.1.1 and comparative kinetic models are documented [6].

Table 4.1.1: Kinetic parameters of the direct reduction mechanism.

Step	E_a [kJ/mol]	$k_o \times 10^5$ [m/s]	Reference
$WO_3 \leftrightarrow WO_{2.9}$	92.00	2.0	[1]
$WO_{2.9} \leftrightarrow WO_{2.72}$	70.45	4.0	[15, 18]
$WO_{2.72} \leftrightarrow WO_2$	69.94	3.7	[15, 18]
$WO_2 \leftrightarrow W$	84.21	1.7	[15, 18]

During direct reduction, the reduced metal-particles remain pseudo-morphous to the initial WO_X-particle [6, 50, 66]. Thus, the powder morphology of elemental raw powder is maintained even after completion of the reduction process. Hence, as shown in fig. 4.1.3, $WO_{3\text{-}X}$-particles keep their initial-size during the reduction process, but vary in porosity and total surface area.

Tungsten transport mechanism modeling. The Chemical Vapour Transport (CVT) steps, occurring in the tungsten transport mechanism, are assumed as reversible reactions. In a CVT process species in a gaseous state are deposited only into existing solid nuclei according to the kinetics of the reaction. Thus, as in the direct reduction model, the reactions involved in this mechanism can be represented by eq. (4.1.34).

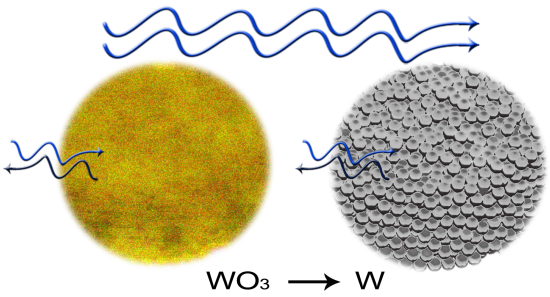

Figure 4.1.3: Morphology changes upon direct reduction. Source: [35].

The kinetics of this mechanism are still unknown. Nevertheless, it has to be pointed out that this mechanism is an intermediate step occurring within the before-presented direct reduction mechanism; and therefore, the kinetics of this tungsten transport mechanism (table 4.1.1) has to be consistent with the direct ones. In section 6.1, the kinetic parameters for the volatilization and further deposition of WO_X will be presented as one contribution of this dissertation.

4.1.2.3 Nucleation and grain growth

The formation of a new phase in gas-solid reactions goes through different steps: mass transfer of reactants from the gas phase to the solid surface, adsorption on the surface, surface diffusion, surface reaction, nucleation of solid product and desorption of gaseous products from the surface to the bulk of the gas phase [97]. In this section, nucleation and posterior grain growth are introduced in detail.

In order to study nucleation and grain growth occurring during reduction of WO_3 to W in a H_2 atmosphere, a direct symbolic reduction step is assumed

$$WO_n(s) + \zeta H_2(g) \leftrightarrows WO_{n-x}(s) + \zeta H_2O(g) \tag{4.1.35}$$

and a CTV (Chemical Vapour Transport) symbolic reduction step

$$WO_n(s) + \zeta H_2O(g) \leftrightarrows WO_2(OH)_2(g) + \xi H_2(g) \tag{4.1.36}$$

$$WO_2(OH)_2(g) + \zeta H_2(g) \leftrightarrows WO_{n-x}(s) + \xi H_2O(g) \tag{4.1.37}$$

where ζ and ξ represent the symbolic stoichiometric coefficients and n and $n-x$ denote the initial oxide number and the reduced oxide respectively. In principle, the above reactions are applicable to all the WO_3 reduction steps.

Nucleation This is a highly studied topic. However, there is still a lack of detailed information about nucleation processes during gas-solid reactions [97]; and therefore, remains a very active research. The models, commonly used in transport phenomena, adequately describe gas-solid reactions for coarse grain materials, but the majority of these models do not describe/include the nucleation process. More advanced models include the effects of grain growth, but consider an arbitrary and/or constant initial grain "germs" for nucleation [98, 99, 100]. More comprehensive models predict the initial number of nuclei by employing statistical functions which depend on the reduction rate and/or the kinetics of the reaction by considering a given number of formed nuclei based on empirical correlations [101]. Avrami [102] found that considering a constant rate of nucleation may be contradictory to experimental facts in many cases.

Most of the above referred models are based on the assumption that particles are spherical, thus, ignoring the prismatic characteristic of the grain and with this the actual particle surface. TC-PRISMA models [103], which extend the classical nucleation theory (CNT) [103], consider that all grains are equally large tetrakaidecahedra (TKD, fig. 4.1.4) and in addition, implement three different models for grain growth in conjunction with conservation equations for mass and continuity. Nevertheless the application does not seem to be ready for the industrial WO_3 reduction simulation because of the huge amount of particles to be solved. As reviewed by R. German [100], the TKD grain shape is a good approximation for W-powders.

Nucleation occurs when, by changes of external parameters (e.g temperature or pressure), a metastable phase is converted to a more stable one. Nuclei formation is usually classified into primary and secondary nucleation. Within primary nucleation, spontaneous formation of crystals from clear supersaturated solutions appear. Primary nucleation is subdivided into homogeneous and heterogeneous nucleation. Within secondary nucleation a large number of crystals are already present. Although some mechanisms have been proposed for secondary nucleation, only empirical correlations are available to correlate the rate of nucleation and the operating conditions [104].

In homogeneous nucleation, the birth of nuclei implies the formation of an interface at the boundaries of a new phase, and therefore, a high driving force is required. Heterogeneous nucleation appears on phase boundaries or whenever impurities are present and therefore it requires a much lower driving force than homogeneous nucleation.

The probability that nucleation starts by a heterogeneous gas-solid surface reaction is thus much higher than that of it starting by a homogeneous gas-gas reaction. This, due to the presence of dislocations, grain boundaries, edges, and corners in the existing solid WO_X crystals. In addition, a nucleus most probably appears at one facet of the WO_X grain [64]. The currently proposed model, following the studies realized by Haubner, Schubert and

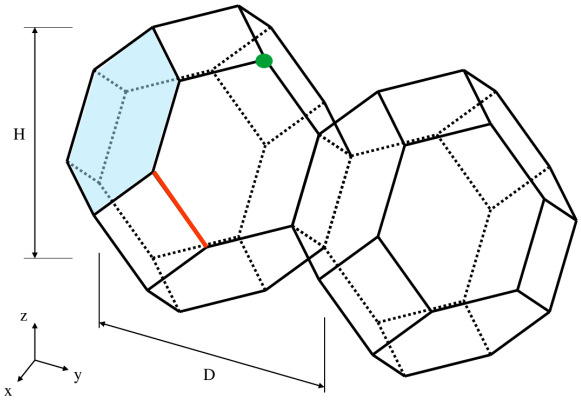

Figure 4.1.4: Tetrakaidecahedron approximation of W grains [103]. A classic TKD has 14 faces (blue), 36 corners (green) and 24 edges (red).

Lassner [64, 63], only considers heterogeneous nucleation. However, nucleation foundations are described by the homogeneous nucleation theory, and therefore it is convenient to understand it before describing heterogeneous nucleation processes.

Homogeneous nucleation At present, the process by which a stable nucleus is created in a homogeneous fluid remains uncertain [105]. However, it can be treated as a stochastic process.

Classic Nucleation Theory (CNT) introduces a free energy barrier (ΔG^*) and a critical nuclei size (r^*). The nuclei with size larger than the critical size "have more chances of survival". The free energy barrier is equal to the maximum point of the sum of the excess of energy between the particle-fluid phase boundary and the volume excess free energy [47, 103, 105, 106]. A graphical description is presented in fig. 4.1.5.

In this regard, by maximising

$$\Delta G = 4\pi r^2 \sigma + \frac{4}{3}\pi r^3 \Delta G_V \tag{4.1.38}$$

the expressions for the critical size and critical free energy are obtained

$$r^* = \frac{-2\sigma}{\Delta G_V}, \ (\Delta G_V < 0) \tag{4.1.39}$$

$$\Delta G^* = \frac{4\pi r^{*2}\sigma}{3} = \frac{16\pi\sigma^3}{3\Delta G_V^2} \tag{4.1.40}$$

where σ is the surface energy or inter-facial tension and ΔG_V is the Gibbs energy change

of the transformation per unit of volume. Moreover, $\Delta G_V = \Delta G^{n\to(n-x)}/V^{(n-x)}$, where $V^{(n-x)}$ is the molar volume of the new "$(n-x)$" phase.

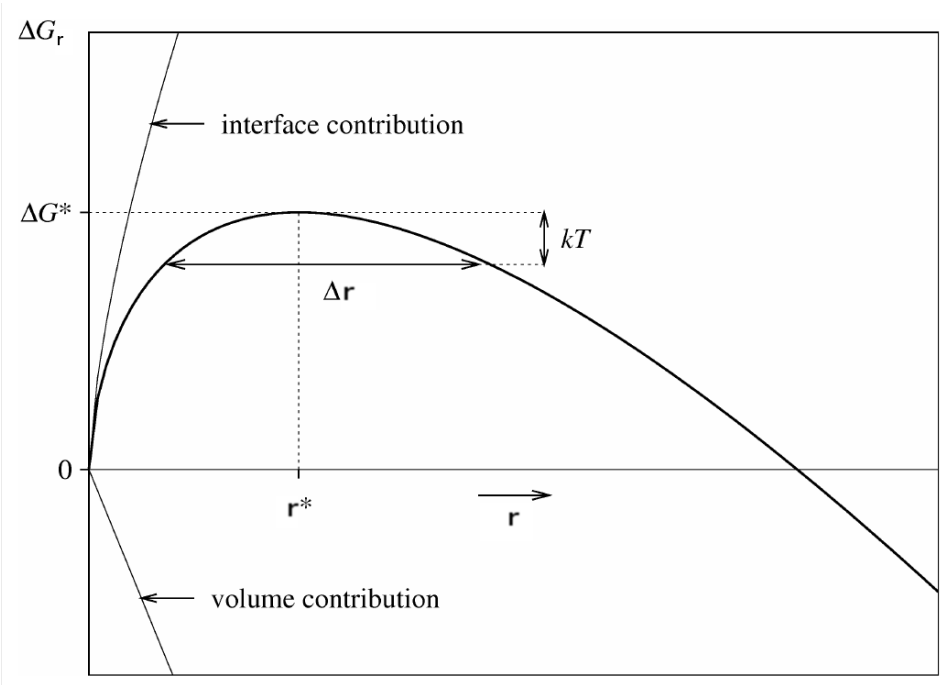

Figure 4.1.5: Variation of the nuclei formation free energy ΔG_r with the nuclei size r. The size interval Δr characterizes the energy profile around the critical size, hence it may be related to the Zeldovich factor. Source: [106].

The constituted nuclei in the close range of the critical size may be unstable, meaning that if a germ is formed it may tend to dissolve.

Nucleation rate Once the system fluctuations have overcome the critical point, meaning that ΔG^* is high enough when compared to $\kappa_B T$, then CNT assumes that a steady-state has been reached and that the formed nuclei with sizes larger than r^* will continue to grow. Consequently, the rate at which a stable nuclei is created is expressed as [105, 106]

$$J_{ss} = \beta^* Z N_0 e^{\left(-\frac{\Delta G^*}{\kappa_B T}\right)} \tag{4.1.41}$$

where κ_B represents the Boltzmann constant, β^* denotes the rate at which a critical nucleus grows, N_0 represents the number of usable sites accessible to nuclei per unit volume (e.g $N_0 = 1$ when all the lattice sites can receive a nucleus) and Z characterizes the Zeldovich factor which is introduced to describe system fluctuations according to the thermodynamics of the process. The Z factor quantifies the probability of a nucleus

slightly larger than r^* passing back across the barrier and re-dissolving into the matrix. In other words, the value of Z characterizes the flatness of the energy profile around the critical size [106].

$$Z = \frac{V^{(n-x)}}{2\pi N_A r^{*2}} \sqrt{\frac{\sigma}{\kappa_B T}} \tag{4.1.42}$$

where T is the absolute temperature and N_A is the Avogadro number.

Using the previous result, a time dependent nucleation rate $J(t)$ can be defined as [105]

$$J(t) = J_{ss} e^{-\frac{t_{inc}}{t}} \tag{4.1.43}$$

where t_{inc} denotes the so called incubation time for establishing steady-state nucleation conditions. In this study, the t_{inc} definition obtained by E. Clouet [106] is adopted, namely

$$t_{inc} = \frac{\pi^3}{4Z^2\beta^*} \tag{4.1.44}$$

Heterogeneous nucleation Haubner et al [64] concluded in their nucleation analysis that individual $WO_{n\text{-}x}$ grains will heterogeneously nucleate when the $[H_2]/[H_2O]$ ratio (η_H) approaches equilibrium concentrations for the direct $WO_n \rightarrow WO_{n\text{-}x}$ reduction. That is:

- A direct reaction, as described by eq. (4.1.35), starts. Consequently, as result a pseudomorphous new phase and water vapour are produced.
- The locally produced $H_2O(g)$ increases η_{H_2O}.
- A higher η_{H_2O} will favor reaction (4.1.36).
- WO_X is dissolved on one side according to reaction (4.1.37).

In a first step, the next concepts may be established by using the first PRISMA-TC heterogeneous nucleation model [103]. For this, all the equations of section 4.1.2.3 remain the same, but the available nucleation sites and the nucleation energy are different.

An effective surface energy is assumed for each possible nucleation site. The number of nucleation sites will depend on the shape and the size of the WO_X grains. To a first estimation, all the grains contained along a particle are assumed to be equally sized TKD with H characterizing the distance between one pair of square faces and D representing

the distance between the two other pairs, as shown in fig. 4.1.4. For the grain boundary area, the edge length and the corner, the following densities are defined

$$\text{(grain boundary area)}, \quad \rho_2 = \frac{6\sqrt{1+2A^2}+1+2A}{4A} D^{-1} \tag{4.1.45}$$

$$\text{(grain edge length)}, \quad \rho_1 = 2\frac{\sqrt{2}+2\sqrt{1+A^2}+}{A} D^{-2} \tag{4.1.46}$$

$$\text{(grain corner)}, \quad \rho_0 = \frac{12}{A} D^{-3} \tag{4.1.47}$$

where $A = H/D$ is the grain aspect ratio or elongation degree (e.g. $A = 1$ for non elongated grains). If the boundary thickness is presumed equal to an atomic layer, then the available nucleation sites can be obtained by

$$N_i = \rho_i \left(\frac{N_A}{V_n} \right)^{i/3} \tag{4.1.48}$$

where $i = 2, 1, 0$ for area, edge and the corner respectively.

Similarly to eq. (4.1.48), the number of nucleation sites at the dislocations can be calculated by

$$N_d = \rho_d \left(\frac{N_A}{V_n} \right)^{1/3} \tag{4.1.49}$$

Some heterogeneous models are based on the Avrami investigations [102]. He observed that the new phase is nucleated by "germ" nuclei which already existed in the precursor phase, meaning that, each "germ" nuclei is a nucleation site for the new "(n-x)" phase. Thus, Avrami's models can be seen as a particular case where one old grain may generate one new phase grain.

4.1.2.4 Grain growth

Local concentration gradients and the diffusion rate of volatiles control the final growth of W grains. Over humid conditions, CVT governs the growth of the $WO_{n\text{-}x}$ grain according to the deposition reaction (4.1.37), as the CVT reactions (4.1.37, 4.1.36) are expected to proceed much more rapidly than the direct reaction (4.1.35).

Contrary to the approach by Vetter et al. [107], the growth rate, given by the reaction rate of eq. (4.1.37), is not directly coupled to the nucleation rate. This is because during nucleation the supersaturation ($C_{WO_2(OH)_2}$) is only consumed by homogeneous nucleation, which is neglected by the current model.

When oxygen transport mechanism dominates the WO_X reduction process no significant grain coarsening occurs because of the absence of supersaturation. Moreover, as the theory predicts, the surface area of the porous oxide is maintained or even increased.

Grain size distribution (GSD) Grain growth depends on the local conditions at the interior of particles undergoing conversion. Different sizes of grains appear due to gradients of temperature, humidity and volatiles. Consequently, a GSD is present within a particle, as defined in section 2.2.2.4, and characteristics such as the internal porosity and/or mean grain size within the particle are affected. Thus, the effects of GSD are taken into account when solving the conservation equations of section 4.1.2.1.

4.1.3 Powder layer scale

During the industrial production of metallic tungsten, rectangular shaped containers are filled with powder particles up to several centimeters. The containers, industrially known as boats, are introduced into push-type furnaces, in which a flow of hydrogen is applied as a reducing agent. Thus, in principle, the process is not too distant from larger scale studies on thermal conversion of packed beds interacting with continuous phases. Packed bed modeling has been used to solve many challenging problems in engineering, for instance as described in [25, 28, 29, 31, 83, 108, 109]. Despite the high size scale difference between these packed bed studies and the current PPB one, the Eulerian technique and the conservation equations employed to resolve fluid phases remain the same. The modeling technique represents the fluid through packed beds as a flow traversing a porous media, as defined by Faghri and Zhang [86]. Thus, the model accounts for a solid matrix with void spaces for which a compressible fluid is passing through. Fluid and solid phases are allowed to exchange energy and mass by convection.

According to the above description and taking into account the mathematical foundation explained in appendix B the conservation equations for the fluid phase are summarized in table 4.1.2.

Table 4.1.2: Conservation equations of the continuous fluid phase.

Continuity conservation equation

$$\frac{\partial}{\partial t}\left(\epsilon_f \langle\rho_f\rangle^f\right) + \vec{\nabla}\cdot\left(\epsilon_f \langle\rho_f\rangle^f \langle\vec{v}_f\rangle^f\right) = \dot{m}'''_{s,f} \tag{4.1.50}$$

Momentum conservation equation

$$\begin{aligned}\frac{\partial}{\partial t}\left(\epsilon_f \langle\rho_f\rangle^f \langle\vec{v}_f\rangle^f\right) + \vec{\nabla}\cdot\left(\epsilon_f \langle\rho_f\rangle^f \langle\vec{v}_f\vec{v}_f\rangle^f\right) = \\ \vec{\nabla}\cdot\left(\epsilon_f \langle\vec{\tau}'_f\rangle^f\right) - \frac{\mu_f}{K}\epsilon_f^2 \langle\vec{v}_f\rangle^f - C\langle\rho_f\rangle^f \epsilon_f^3 |\langle\vec{v}_f\rangle^f| \langle\vec{v}_f\rangle^f\end{aligned} \tag{4.1.51}$$

$$K = \frac{D_P^2 \epsilon_f^3}{150(1-\epsilon_f)^2} \tag{4.1.52}$$

$$C = \frac{1.75(1-\epsilon_f)}{D_P \epsilon_f^3} \tag{4.1.53}$$

Energy conservation equation

$$\begin{aligned}\frac{\partial}{\partial t}\left(\epsilon_f \langle\rho_f\rangle^f \langle h_f\rangle^f\right) + \left(\epsilon_f \langle\rho_f\rangle^f \langle\vec{v}_f h_f\rangle^f\right) = \\ \frac{\partial\langle p_f\rangle}{\partial t} + \epsilon_f \cdot \langle\vec{v}_f\rangle^f \cdot \vec{\nabla}\langle p_f\rangle + q'''_{s,f}\end{aligned} \tag{4.1.54}$$

Species conservation equation

$$\frac{\partial}{\partial t}\left(\epsilon_f \langle\rho_{f,i}\rangle^f\right) + \nabla\cdot\left(\epsilon_f \langle\rho_{f,i}\rangle^f \cdot \langle V_f\rangle^f\right) = \sum_{i=1}^{M} m'''_{s,f,i} \tag{4.1.55}$$

4.1.3.1 Continuous and discrete phases 4-way coupling

In this subsection, the energy and mass exchange between the mesh-based Eulerian fields and the particle-based Lagrangian quantities is explained. Within this text, a continuous and discrete phases 4-way coupling is to be understood as the dual interaction between continuous and discrete phases for energy and mass transfer. It means a 2-way conversation for energy transfer and a 2-way conversation for mass transfer.

Section 4.1.2.1 introduced the boundary conditions for particles, which are also employed to couple continuous to discrete phases. The other part of this dual exchange (discrete to continuous coupling) is modeled as a convective transport in which the source terms of eqs. (4.1.50), (4.1.54) and (4.1.55) are calculated by following the film theory [28]. The above-listed conservation equations present a volumetric source term that mathematically favors the coupling from the discrete phase to the continuous phase. Thus, the source

magnitudes are computed from the difference between the values of fluid and particle's surface of the conserved properties scaled by an adequate transfer coefficient.

Thus, the volumetric source term in the energy equation (4.1.54) takes the form

$$\vec{q}'''_{s,f} = \sum_{j=1}^{N} \left\langle \frac{A_{p,j}}{V_{\text{REV}}} \alpha_j \left(T_{p,j} - T_f\right) \right\rangle \tag{4.1.56}$$

where A_p is the surface area of the particle, α the heat transfer coefficient and N accounts for all the contributing particles N in a representative elementary volume (REV), as described in appendix B.3.

Analog to the energy equation, the intensity of mass exchange of species i between a particle and the gas phase, denoted by $m'''_{p,f,i}$, adopts the form

$$A_p \beta_i \left(\langle \rho_{p,i,g} \rangle^g - \rho_{f,i}\right) + A_p \cdot m''_{p,i,g} = \dot{m}'''_{p,f,i} V_{\text{REV}} \tag{4.1.57}$$

where β describes the mass transfer coefficient , while the particle quantities in the above equation correspond to those described in eq. (4.1.16). For N particles in a REV, the following holds

$$\dot{m}'''_{s,f,i} = \sum_{j=1}^{N} \left(\dot{m}'''_{p,f,i}\right)_j \tag{4.1.58}$$

The sum of all species mass source terms M yields the overall fluid mass volumetric source term in eq. (4.1.50), that is

$$\dot{m}'''_{s,f} = \sum_{i=1}^{M} \sum_{j=1}^{N} \left(\dot{m}'''_{s,f,i}\right)_j \tag{4.1.59}$$

The heat and mass transfer coefficient calculation have been previously described in section 4.1.2.1. The coefficients are employed to evaluate the convective boundary conditions of a single particle by using local gas properties in the REV.

4.1.3.2 Powder layer void fraction and total solid surface area

The intrinsic characteristics of the powder layer are calculated from the properties of the individual particles. The bed void fraction, denoted ϵ_b, is computed according to the position and the volume of the particles. The N particles contributing to the solid volume

fraction of a given REV, are determined and included into the void fraction as:

$$\epsilon_b = \frac{1}{V_{\text{REV}}} \sum_{j=1}^{N} \eta_{j,\text{REV}} V_{p,j} \tag{4.1.60}$$

where $\eta_{j,\text{REV}}$ is the fraction of volume that particle j contributes to the given REV.

The mean particle diameter $\overline{D}_p$ can be calculated from the total average surface area $\overline{S}_{\text{REV}}$ of all N particles contributing to the REV as

$$\overline{S}_{\text{REV}} = \frac{1}{N} \sum_{j=1}^{N} A_{p,j} \tag{4.1.61}$$

$$\overline{D}_p = \sqrt{\frac{\overline{S}_{\text{REV}}}{\pi}} \tag{4.1.62}$$

where the quantities $\overline{D}_p$ and $\overline{S}_{\text{REV}}$ are required characteristics to calculate the bed permeability K of eq. (4.1.52) and the drag coefficient C of eq. (4.1.53).

4.2 Model implementation

4.2.1 Introduction to the employed framework

The computational implementation of the complex model described in this chapter is described in this section. Within the XDEM multi-physics model framework, the Discrete Particle Method (DPM) developed by Peters [31, 110] was employed for particles undergoing thermochemical conversion. Conversely, a multi-phase OpenFOAM solver for porous media was modified to resolve the fluid phases on the atmosphere of the reduction reactors.

Figure 4.2.1 exemplifies the XDEM framework implemented on the hydrogen reduction of a sample of tungsten trioxide. In the figure, the previously described discrete and continuous models can be identified.

4.2.2 Discrete Particle Method (DPM)

In contrast to continuum approaches that average over an ensemble of particles in space, in the Discrete Particle Method (DPM), particles are discretized as individual entities with motion and thermochemical conversion attached to them. Thus, particle-based Lagrangian quantities are resolved for each single particle [31].

In DPM two main simulation modules are available: The motion of granular material is dealt within the *Dynamics module*, while the thermo-chemical conversion occurs in the *Conversion module*. The software supports direct coupling with external software such as DiffPack Langtangen [111] for Finite Element Analysis (FEA) or OpenFOAM [112] for Computational Fluid Dynamics (CFD), in addition to other computational tools. However, DPM simulations in a decoupled mode are also supported.

4.2.2.1 Dynamics module

This module, as the classic representation of DEM, describes the trajectories of particles in a system.

Preparation of numerical samples

Even thought, the WO_3 particles can be considered as “stationary” during is industrial conversion to metallic tungsten, this motion module is employed to accurately predict the

arrangements of particles in a natural form. Positioning of the particles, within the emulated container, affects the reduction progress because it directly influences the porosity of the bed and consequently the flow of gaseous products. With a natural position of particles inside containers physical effects, such as the wall effect, are accounted for. Thus, in this work, the reactors are naturally filled by gravity deposition following Michael [113]. A graphical representation of wall effect is further depicted in appendix C-fig. C.3.2.

Moreover, the advanced partner detection models, implemented within the dynamics module, are employed during the initialization of "static" simulations to find radiation and conduction neighbors.

4.2.2.2 Conversion module

Derived from the motion module concept, the same discrete particle representation accounts for the thermochemical conversion of particles within the software. Hence, temperature, species distributions and morphological changes at the intra-particle level can be predicted. In this module, each particle/entity may be considered to consist of different phases such as solid, liquid, gas or inert material; for which diffusion within the void volume is accounted for.

4.2.3 OpenFOAM multi-phase solver for porous media

The conservation equations (section 4.1.3), describing transport of gaseous species, are implemented as a standalone application in OpenFOAM. The solver is based on the flexible PIMPLE (PISO-SIMPLE) solution for time-resolved and pseudo-transient simulations allowing equation under-relaxation and ensuring the convergence of all the equations at each time-step [112]. OpenFOAM is a versatile open source CFD software package with a large of users from both commercial and academic sectors [112].

The coupling between discrete and continuous phases is performed by an external interface that transfers the exchange terms, described in section 4.1.3.1, between Eulerian and Lagrangian fields of the continuous phase and the particles phase respectively.

Chemical reactions in the fluid phase are accounted for by a thermochemical derived solver implemented in the solver developed for this work. Moreover, the interaction between solid continuous bodies, e.g. losses through walls or heating devices, and fluid as well as particle phases are supported by a conjugated heat transfer concept. In which a derived implementation of the so-called *chtMultiRegionFoam* solves the heat conduction equation in solids as proposed by Carslaw et al. [114].

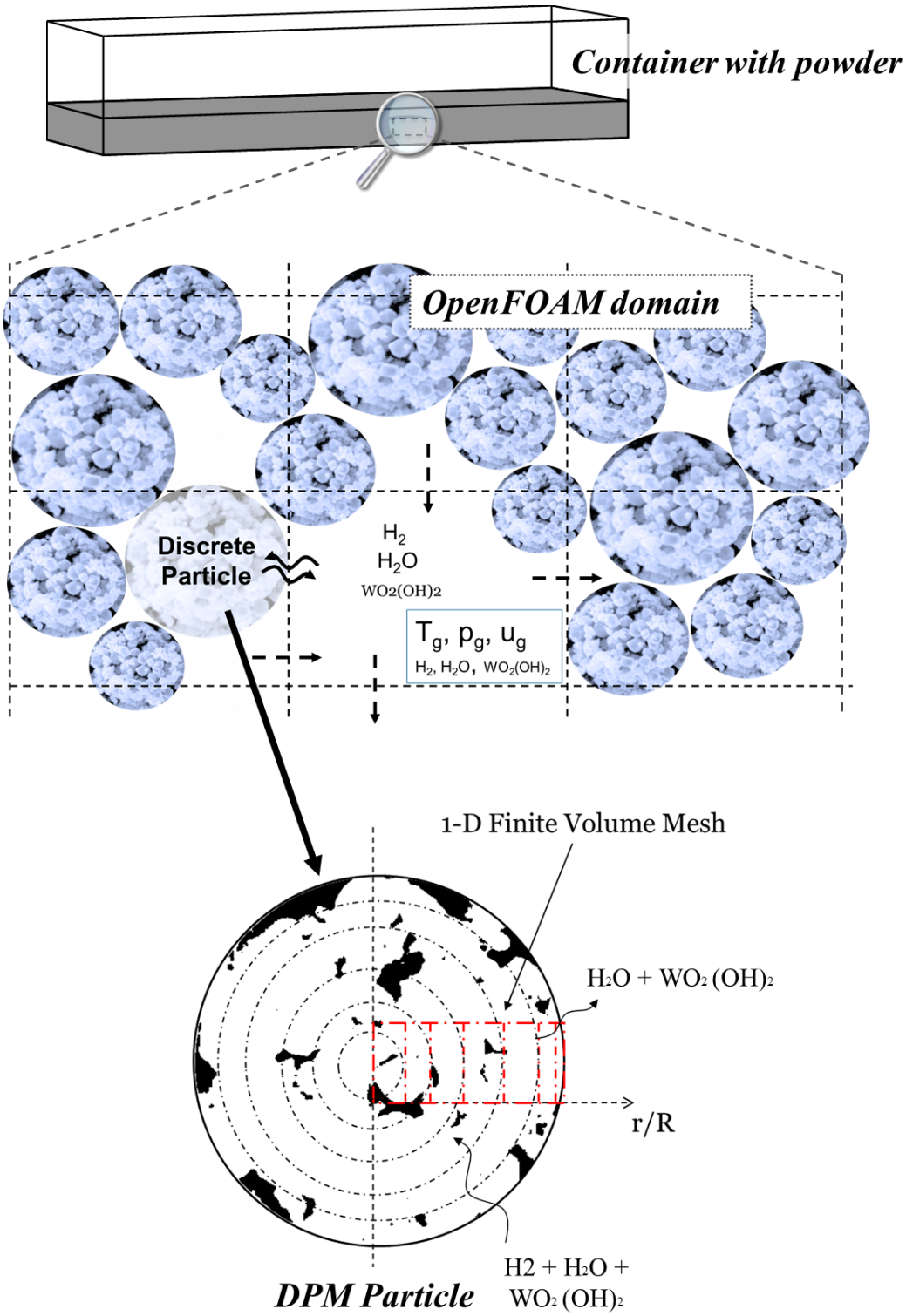

Figure 4.2.1: Graphical representation of the XDEM as implemented for the reduction of WO_3 by hydrogen.

4.2.4 Numerical techniques to reduce CPU time

4.2.4.1 Reducing the number of particles

A numerical treatment of each tungsten oxide particle is not feasible due to a too high number of particles (e.g. 10^{12}). However, from numerical observations with lower number of particles some reasonable assumptions can be drawn. It is anticipated that the gradients concerning the thermodynamic state of each particle vary both moderately and smoothly for particles in the same "neighborhood", or unit cell. This means that differences in temperature or composition of particles in a considered spatial domain do not vary significantly. This is guaranteed for mono-dispersed particles under the same boundary conditions. Thus, the solution of all the particles within a "neighborhood" can be computed with an unique estimate. However, these methods may lose accuracy and/or morphology change information of particles, which, however, does not significantly affect the overall accuracy. Moreover, if the size of the unit cells are of the same order of magnitude than the size of the actual particles, then nor the morphology neither the accuracy are compromised.

Two reducing strategies that lower the number of particles, or entities to be computed are the Representative Particle Method (RPM) [108] and the Agglomerated Particle Method (APM). The latter method has also been presented for coarse-graining or upscaling small particles into larger meso-particles for fastening classic DEM simulations [115].

4.2.4.2 Representative Particle Method

As depicted in fig. 4.2.2, the entire space is divided into sub-domains, of which, each is attached to a representative particle, for which the state is predicted by XDEM techniques. The thermodynamic state of these representative particles thus represents the state of all particles occupying the sub-domains. This technique is widely employed by many researchers dealing with discrete element techniques. Nevertheless, the Representative Particle Method (RPM) was formally documented by Zobel [108].

All the other particles within the finite volume are assumed to obey the same characteristics as the representative one [83, 108]. Thus, all the particles within a finite volume have the same surface temperature and therefore the energy fluxes by conduction and net radiation within a finite volume is null. Gradients of energy may be observed in particles located at the boundaries of the finite volumes, but, particles in this region are not resolved. Therefore, RPM does not account for the energy transport within the solid phase. In addition, the method does not account for inhomogeneities, such as wall effects, which certainly influence the response of the flow.

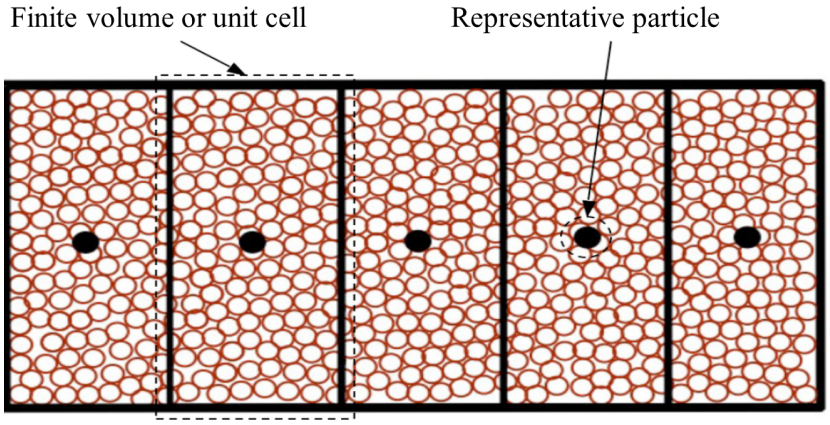

Figure 4.2.2: A visual representation of the representative particle method. Source: [108].

4.2.4.3 Agglomerated Particle Method

The APM is based on the principle of the so-called Population Balance Method, as described by Marshall and Li [116], where an agglomeration or parcel of particles is replaced by a single effective particle (mesoparticle).

In the herein proposed method, the entire space is divided into sub-domains, of which, each is solved as an agglomeration of particles (AP) within a unit cell. The thermochemical state of each AP is predicted by eXtended Discrete Element Method techniques implemented in DPM. The single particle model implementation described in section 4.1.2 and implemented in DPM holds, however, modifications for the intra-particle porosity and the total surface area of the AP have to be applied as follows.

Shape: If one conveniently chooses the AP to adopt the size of a cell of a structured mesh based domain (e.g. unit cell equal to a CFD cell), or an integer multiple of it, then the most suitable shape of meso-particles are cuboids. Thus, an agglomerated particle can be seen as a cubic porous sponge, as shown in fig. 4.2.3.

The morphology evolution of the actual, or original, particles may be captured by combining the RPM with the current method. While the APM solves appropriately the thermochemical conversion, the RPM yields morphological changes.

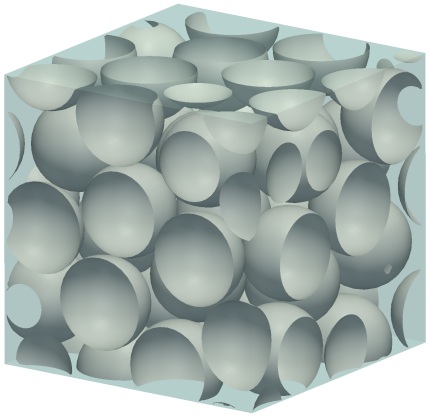

Figure 4.2.3: Visual illustration of an agglomeration of particles within a unit cell.

Porosity: The AP particles can be considered to have an empty space characterized by the ratio of the empty volume between particles contained within the unit cell and the apparent volume of the agglomerated (V_{Ucell}) or unit cell. Hence, the porosity of an AP can be expressed as

$$\epsilon_{AP} = 1 - \frac{\Sigma V_{P_i}}{V_{Ucell}} \tag{4.2.1}$$

where ϵ_{AP} is the porosity of the agglomerated or macro-porosity and V_P is the volume of original particles within the unit cell.

Original DPM particles are considered to be porous with a void space characterized by ϵ_P. Consequently, the effective porosity in terms of ϵ_P and ϵ_{AP} can be obtained as:

$$\epsilon_{eff} = 1 - (1 - \epsilon_{AP})(1 - \epsilon_P) \tag{4.2.2}$$

The effective porosity calculated from eq. (4.2.2) is employed during intra-particle calculations according to section 4.1.2, whereas ϵ_{AP} is employed in geometrical calculations such as contact surface, total surface area, total solid volume, etc.

The kinetics of heterogeneous reactions is highly influenced by surface area on which the reactions are taking place. Such a reactive-surface, or intrinsic surface, is also computed by considering the new effective porosity.

Conduction area: From fig. 4.2.3, it is possible to observe that an AP, due to its cubical shape, can be chosen to be in perfect contact to other APs. Nevertheless, as shown in fig. 4.2.4, the conduction area between adjacent AP, as well as at the interior of the AP, is lower than the area of a face of the cubical shape. The actual conduction area of a group of common particles is smaller than that of the unit cell face. Therefore, the contact area, or solid surface, of an AP has to be corrected. A viable solution is to relate the area of a plain face A_{face} to the void fraction of the agglomerated particle. Thus, assuming a uniform porosity through all the unit cell, it can be easily proven that the area exposed to contact A_{AP_c} can be calculated as

$$A_{AP_c} = A_{face}(1 - \epsilon_{AP}) \tag{4.2.3}$$

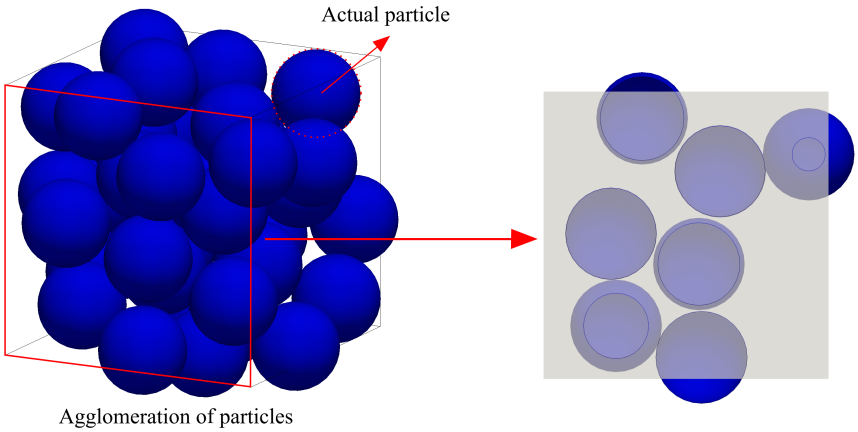

Figure 4.2.4: Contact surface of an agglomeration of particles. The intersection between the faces of the AP and actual particles, on the right side of the figure, estimates the conduction area of the APs.

Total surface area: An agglomerate particle, generally, represents an ensemble of polydisperse particles as schematized on fig. 4.2.5. In order to continue the applicability of the PPB model, developed in section 4.1.3, the total surface area as well as a mean radius characterizing the AP have to be redefined.

Assuming the size distribution of the contained particles to be expressed as

$$\chi_1 r_1,\ \chi_2 r_2,\ \ldots, \chi_i r_i,\ \ldots,\ \chi_n r_n \tag{4.2.4}$$

where r_i is the radius of the class i and χ_i is the weight of the class i defined by:

$$\chi_i = \frac{n_{P_i}}{n_{Ptotal}} \tag{4.2.5}$$

with n_{Pi} defining the number of particles of the class i and n_{Ptotal} the total number of

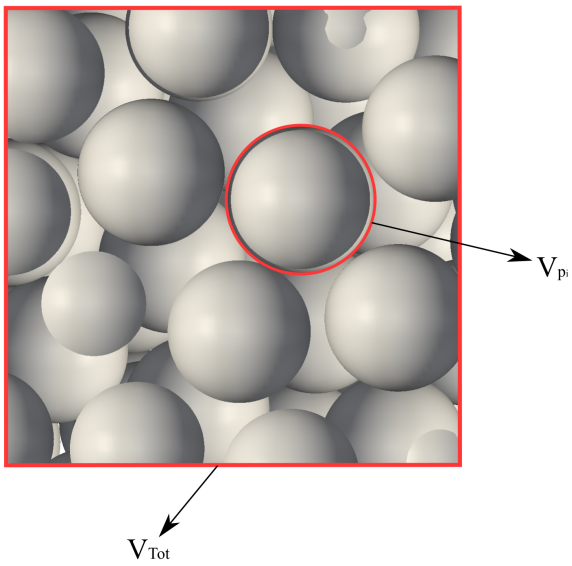

Figure 4.2.5: Agglomerated particle representing an ensemble of polydisperse particles. V_{Tot} and V_P denote total volume of the unit cell and volume of a single particle respectively.

particles contained in the agglomerated particle $S_{AP_{total}}$. The total surface area of the polydisperse particles contained in the unit cell is

$$S_{AP_{total}} = 4\pi(n_{P_1}r_1^2 + n_{P_2}r_2^2 + \cdots + n_{P_n}r_n^2) \tag{4.2.6}$$

Since the number of particles per class may be an unknown quantity, it is more convenient to write eq. (4.2.6) in terms of its class weights. Thus, from eq. (4.2.6) and eq. (4.2.5) the following is deduced

$$\begin{aligned} S_{AP_{total}} &= 4\pi\, n_{Ptotal}(\chi_1 r_1^2 + \chi_2 r_2^2 + \cdots + \chi_n r_n^2) \\ &= 4\pi\, n_{Ptotal} \sum_{i}^{n} \chi_i r_i^2 \end{aligned} \tag{4.2.7}$$

Similarly the volume of the particles contained in the unit cell $V_{AP_{total}}$ can be expressed as

$$V_{AP_{total}} = \sum_{i}^{k} V_{p_i} = \frac{4}{3}\pi\, n_{Ptotal} \sum_{i}^{k} \chi_i r_i^3 \tag{4.2.8}$$

Finally, rearranging and from eqs. (4.2.2), (4.2.7) and (4.2.8), the total surface area can be written in terms of known quantities, namely the size distribution of the contained particles, the bed porosity and the unit cell (AP) volume.

$$S_{AP_{total}} = 3\,V_{Ucell}\,(1-\epsilon_{AP})\,\frac{\sum \chi_i r_i^2}{\sum \chi_i r_i^3} \tag{4.2.9}$$

4.2.4.4 Parallelization

DPM include a parallel simulation driver used to distribute sub-domains, of a given DPM simulation, into different executions that are solved simultaneously. Distributed executions provide two main benefits. Firstly, the particles are distributed over the memory of all computing nodes, thus allowing for simulations involving a larger number of particles that would not fit in the memory of one single machine. Secondly, because most of the computation within a time step are independent, the simulation can be executed in parallel among all the nodes of a cluster, and thus reduce the total time of the simulation. Parallelization is based on the classical scheme of domain decomposition which relies on three main concepts: The simulation domain corresponds to the space that contains all particles. Cells of fixed size correspond to regular subdivisions of the domain. A subdomain or partition is a set of cells which is assigned to a given node [28, 113]. More details on the parallelization of XDEM approaches are described by Besseron et al. [117].

In addition to the before-described sub-domains distribution, the individual mathematical solution of particles may be achieved in a multi-threaded mode. Hence, particle integrations are forked to a specified number of slave threads allocated to different processors.

Chapter 5

XDEM model validation

Contents

If you're going through hell, keep going.

W. Churchill

5.1 Validation of packed beds undergoing heat-up

Within this validation, the accuracy of predictions for the flow through a packed bed of metallic particles as well as its further thermal interaction are shown. Detailed validations, at single particle level as well as on differently arranged packed-beds, were carried out and good agreement was achieved between experimental data and predictions. An extract of this research was documented in:
[25], Estupinan Donoso AA, Hoffmann F, Peters B, eXtended Discrete Element Method Used for Convective Heat Transfer Predictions, International Review of Mechanical Engineering 7 (2) (2013) 328–336.
The full description of the validation cases and the heat-up results are reported in appendix C.

5.2 Validation of a Powder Packed Bed (PPB) undergoing thermochemical conversion

The aim of this research was to examine the ability of the model formulation to reproduce the experimental thermochemical conversion of powder materials. Due to the uncertainty about the kinetics of the tungsten oxide reduction mechanisms, a first approach was to validate the concept with materials on a similar scale than WO_X powders, but with a consolidated reaction kinetic. The validation results were documented in:
[36], Copertaro E, Chiariotti P, Estupinan Donoso AA, Peters B, Revel GM, A Discrete-continuous Approach to Describe CaCO3 Decarbonation in Non-steady Thermal Conditions, Powder Technology 275 (2015) 131–138.

The research addressed the problem of the numerical prediction of heat propagation and chemical conversion of the material bed in cement kilns for clinker production. The XDEM software platform was successfully applied to the prediction of the calcination process in non-steady thermal conditions, involving a small sample of calcium carbonate in powder state. Predictions were validated with the experimental data documented by Gieorgieva et al. [118], where conduction with the solid walls played a major role in the process, similar to the presented upon thermochemical conversion of tungsten powders.

The parameters of the numerical model are summarized in table 5.2.1.

The validation of the numerical model for PPB undergoing thermochemical conversion was performed by comparison between the experimental thermogravimetric (TG) curves and predictions for mass loss. The employed kinetic parameters were obtained from

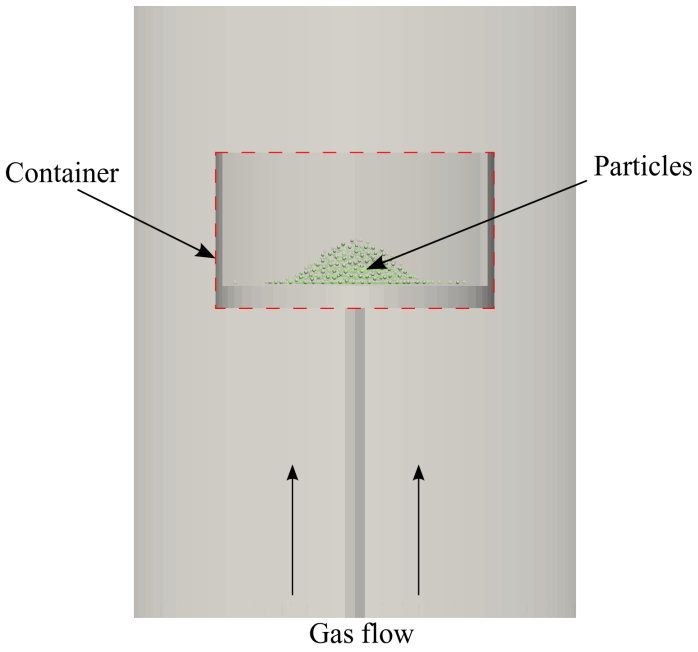

Figure 5.2.1: Geometry of the numerical model [36].

Gieorgieva [118], namely the pre-exponential factor is 7.41×10^{16} [1/min], activation energy is 325.1 [kJ/mol]. Experimental and numerical thermogravimetric curves are documented in figs. 5.2.2a to 5.2.2d. The experimental and numerical TG curves exhibit the same trend upon heating rate change. Thus, an excellent agreement between the experimental and the numerical data was found.

Table 5.2.1: Experimental setup of a undergoing thermochemical conversion [118].

Fluid properties:		
Volumetric flow	25	cm^3/min
Composition		
N_2	99.99	%
Solid phase properties:		
Total mass	5	mg
Composition		
$CaCO_3$	100	%
Crucible size:		
Height	3	mm
Diameter	6	mm

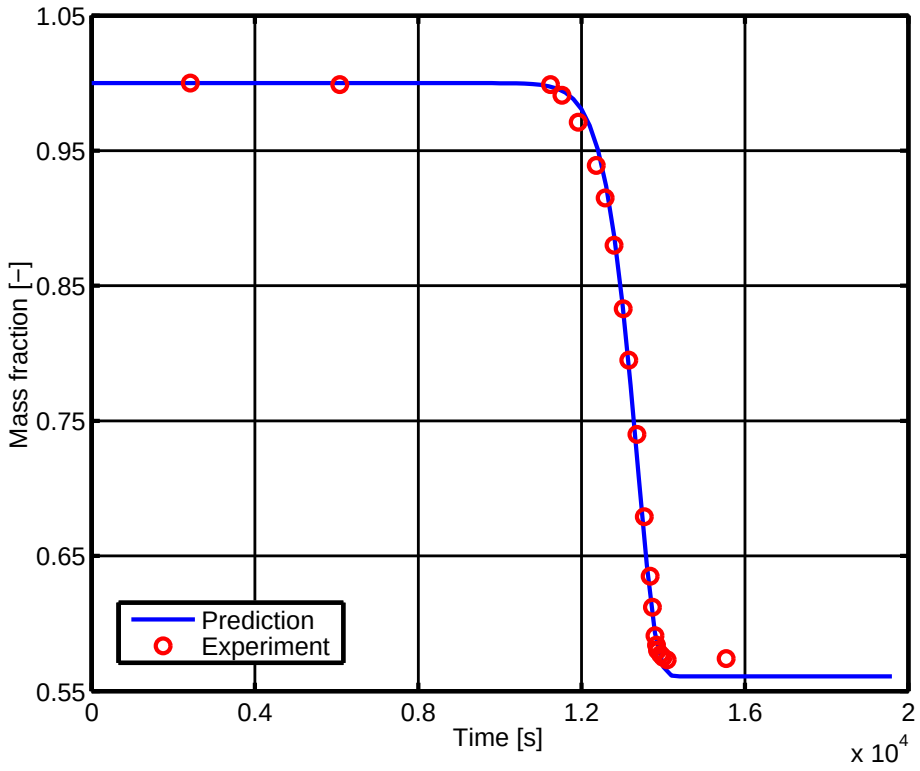

(a) XDEM validation for PPB undergoing thermochemical under a heating rate of 3 °C/min.

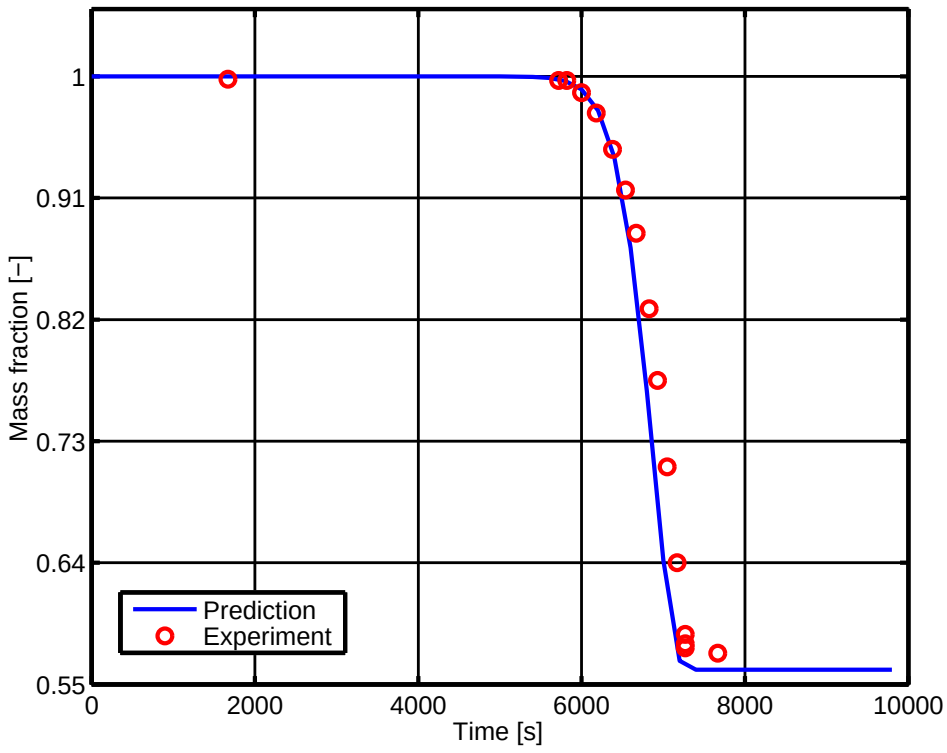

(b) Validation at 6 °C/min.

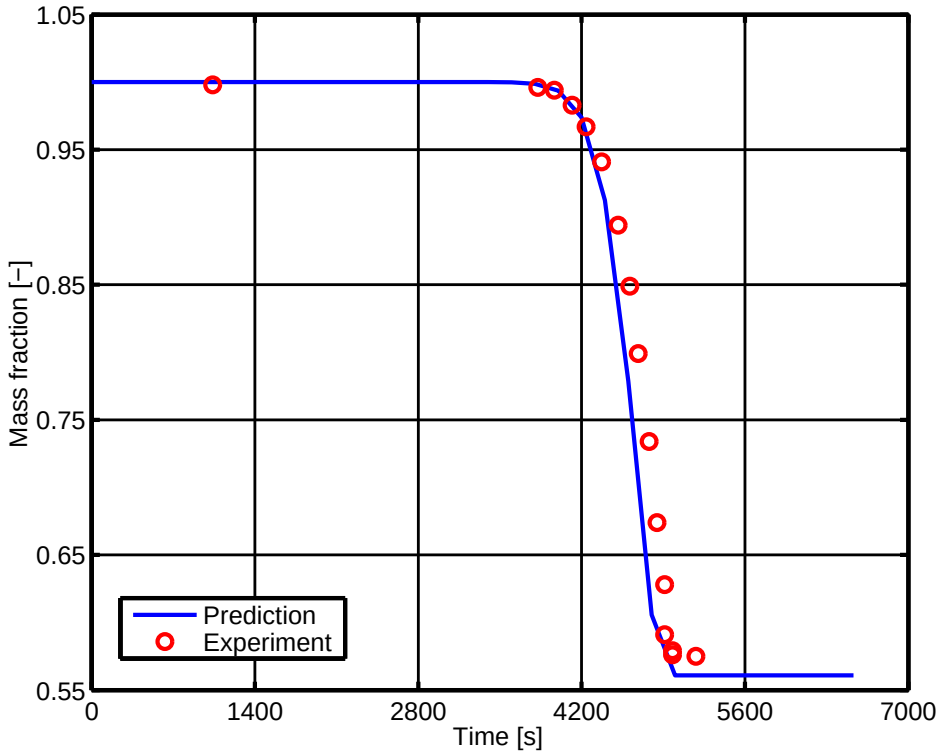

(c) Validation 9 °C/min.

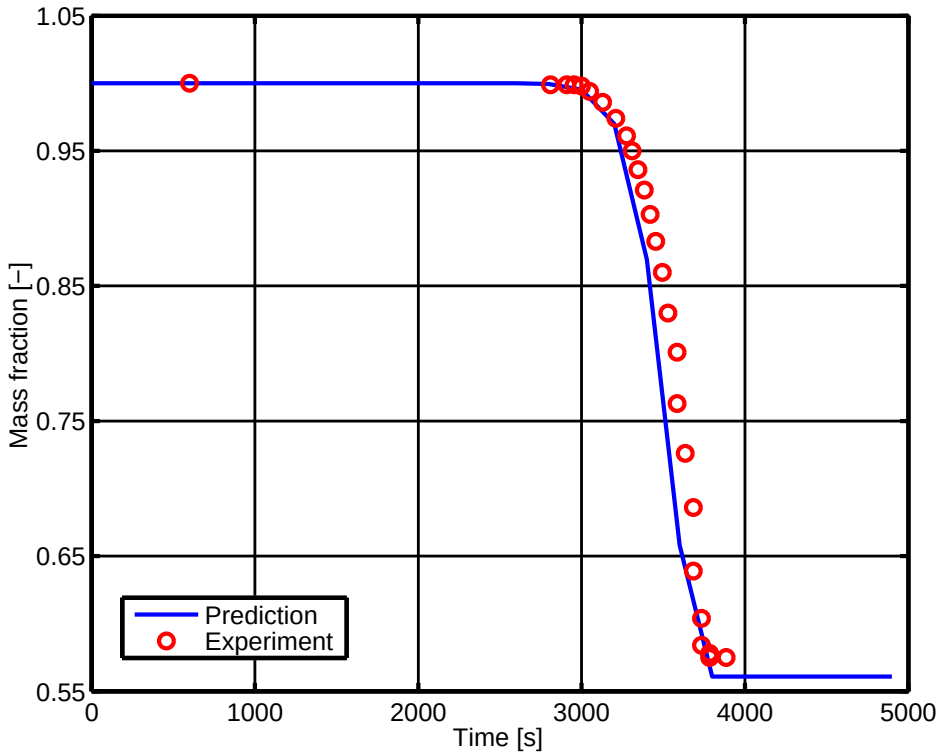

(d) Validation 12 °C/min.

Figure 5.2.2: Comparison of numerical predictions [36] with experimental data [118].

5.3 Isothermal reduction of WO_3 in dry-H_2 atmospheres

5.3.1 Overview

This section is a compilation based on the following publications:
[35], Estupinan Donoso AA, Peters B, XDEM Employed to Predict Reduction of Tungsten Oxide in a Dry Hydrogen Atmosphere, International Journal of Refractory Metals and Hard Materials 49 (March) (2015) 88–94.

[38], Estupinan Donoso AA, Peters B, XDEM Used for Predicting Tungsten-Oxide Reduction, in: Prof. Eugeny Kenig (Ed.), Computer Aided Process Engineering (CAPE) Forum 2015, Paderborn, DE, 2015, pp. 43–52.

5.3.2 Isothermal reduction of WO_3 under homogeneous conditions

Within this validation, XDEM based predictions are compared to the experimental data from isothermal reduction studies. Harboury et al. [15] and Bustnes et al. [18] employed 99.8% pure WO_3-powder to investigate the kinetics of the hydrogen reduction of tungsten trioxide, with the parameters as shown in table 5.3.1. Nitrogen was used to heat up the samples until the reduction temperature was reached, then the reducing-gas, a mixture of Argon/Hydrogen (95/5), was introduced. The experiments were repeated at 750 °C, 800 °C, 850 °C, and 900 °C. The mass loss history was monitored with a computer at intervals of 1 s. More details about the experimental setup are documented in [15].

An alumina crucible of 5.58 mm diameter and 3.58 mm height containing up to 0.6 mm (46 mg) of WO_3-particles was used to study the effect of the temperature on the reduction kinetics.

Uniformly sized spherical particles of 15 µm diameter were assumed according to the above-described experimental setup. In addition, due to the low layer height and the fluid flow, it is assumed that the produced water is driven out of the powder bed fast enough to keep a dry atmosphere. Given these conditions, the model was prepared for simulation of the different experiments [15] under the assumption that the reducing gas was uniformly distributed all around the bed. According to the current experimental setup, it can be assumed that the reducing agents are always available and the produced gases are fast-driven out of the system. Therefore, there is no need to account for gas

transport at the bed scale; nevertheless, the effect of gas transport will be discussed in the following section 5.3.3.

Figure 5.3.1 summarizes the comparison of the XDEM predictions with experiments obtained after reducing a 0.6 mm bed height of WO_3-particles. The dimensionless mass loss represents the ratio current-mass/initial-mass. On fig. 5.3.1, it can be distinguished two of the four slope-changes that point the formation and reduction of the different oxide intermediates [15]:

- The inflection that appears close to 93.1% represents the dominance of the reduction from $WO_{2.72}$ to WO_2.
- And the last inflection, at 79.3% (reduction at 750 C^o), represents the full reduction from WO_2 into metallic tungsten.

The minor discrepancy on the accuracy of the curve at 750 °C is attributed to the fact that the model does not implement the step (shortcut) $WO_{2.9} \rightarrow WO_2$. This step appears upon reduction at temperatures below industrial range ($T \leq 750$ °C).

The model's response to temperature changes is shown by analyzing the different curves of fig. 5.3.1. It is observed how the reaction-rate increases upon an increase on the applied temperature.

The XDEM approach appears to accurately capture the complex phenomena involved in the reduction of WO_3 with a dry H_2 process. The employed reaction model does not bound the reactions to a finite temperature range, so different events can take place simultaneously.

Table 5.3.1: Experimental setup for Bustnes and Haboury et al' experimentation

Powder		
WO_3	99.9	%
Size	10 - 20	µm
Mass	46	mg
Powder bed porosity	0.56	–
Reducing gas		
H_2	99.9	%
Volumetric flow	100	ml/min
Crucible		
Diameter	5.58	mm
Filling-height	0.60	mm

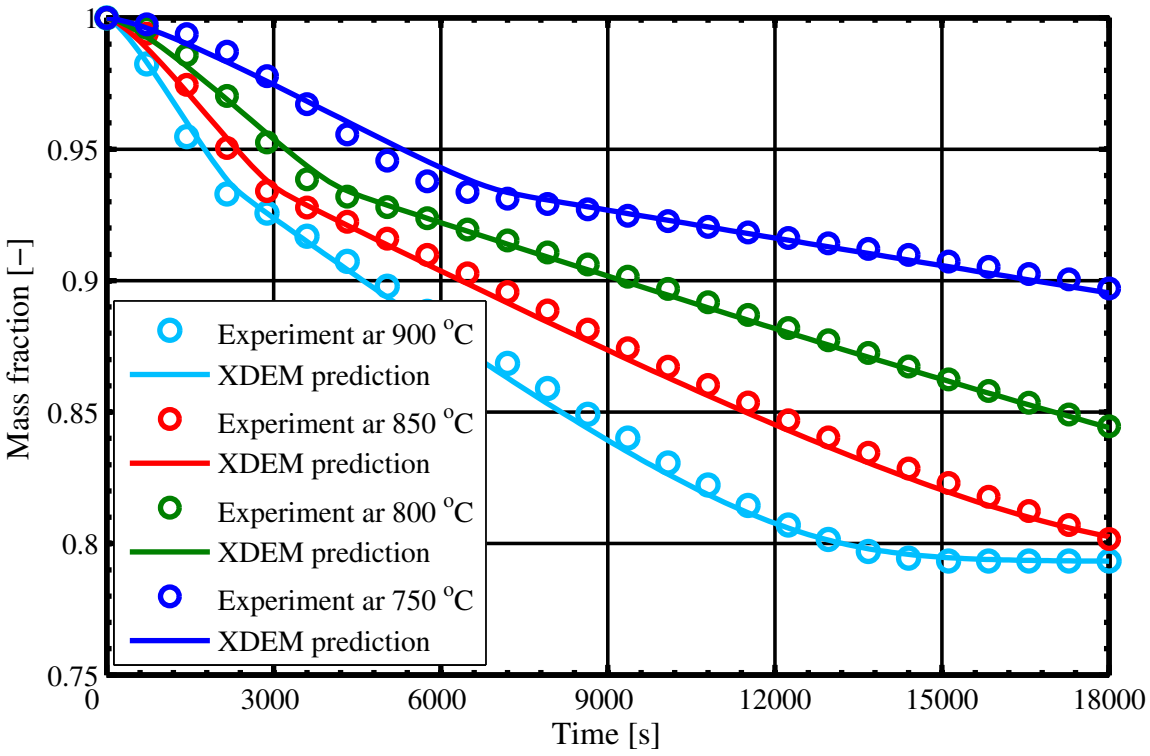

Figure 5.3.1: Isothermal reduction of WO_3 under dry atmospheres. Mass fraction predicted by XDEM-modelling and experiment measurements at different temperatures [35].

5.3.3 Isothermal reduction of WO_3 under the effect of gas transport

In the present validation case, a comprehensive and fully coupled XDEM model accounting for energy and mass transport in the gaseous phase, thermochemical conversion of solid species as well as mass and energy exchange with the solid matrix is presented. Predictions for the thermogravimetric reduction of tungsten oxides were conducted according to experimental data from Fouad et al. [95]. Therein, the authors placed 100 mg of tungsten trioxide into a metallic crucible immersed in a flowing hydrogen atmosphere. The following table 5.3.2 summarizes the experimental setup:

Due to the symmetry of the problem, axial symmetry boundary conditions and periodic boundary conditions for the fluid and solid phases, respectively, were applied. As schematized in fig. 5.3.2a, a wedge representing a quarter of the reactor was employed. In order to avoid the increase of void space around the inner walls, the full container was naturally filled up by gravity deposition and the particles out of the wedge were removed. Hence, as described in fig. 5.3.2b contrary to the crucible wall, there is not such a wall effect on the planes of symmetry. The void space, or porosity, is computed by taking into account the particle position and sizes within each CFD cell. Thus, the current approach

Table 5.3.2: Numerical setup for the isothermal reduction validation as reported by Fouad et al. [95].

Powder		
WO_3	99.9	%
Size	45 ± 3	µm
Mass	83.3	mg
Reducing gas		
H_2	99.9	%
Volumetric flow	1×10^{-6}	m^3/s
Reducing temperatures		
	640	°C
	710	°C
	740	°C

omits empirical correlations to estimate the void space between particles. Following the experimental setup in [95], the numerical setup considers a uniform initial temperature equal to the isothermal reduction temperature. In addition, because the crucible receives a constant energy flux from the heating elements, the temperature of the solid walls is assumed constant and equal to the reduction temperature.

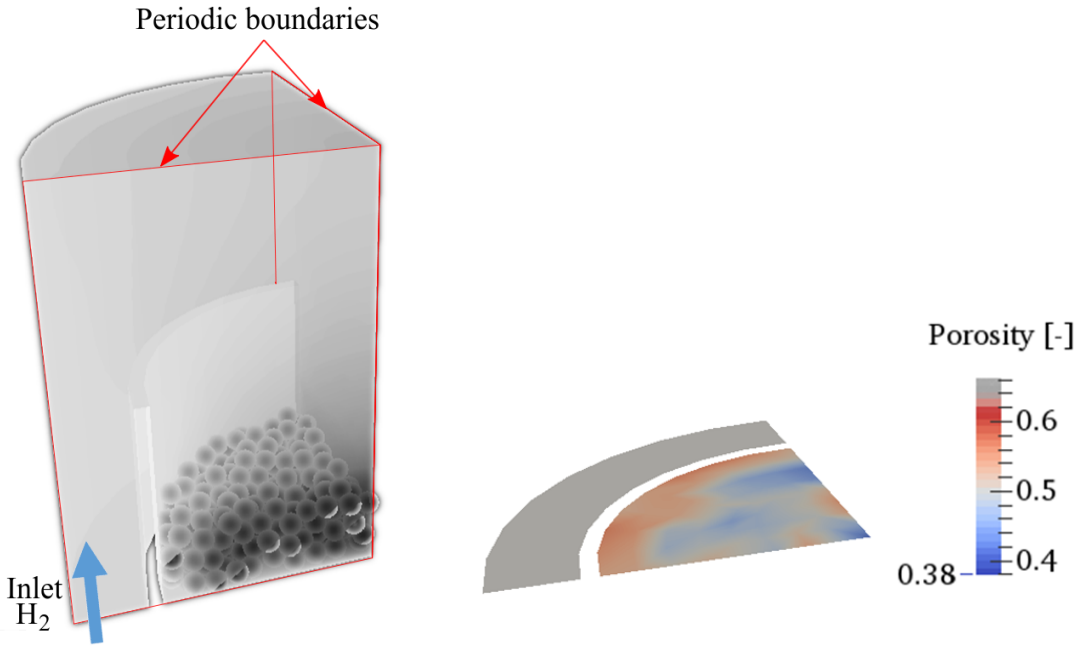

(a) Numerical setup of a quarter of a thermogravimetric reactor.

(b) Example of radial void space distribution at a given position within the powder bed.

Figure 5.3.2: Numerical setup for the validation case of the isothermal reduction of WO_3 under the effect of gas transport [36].

The tungsten oxide reduction is an endothermic process, meaning that particles absorb energy from the environment during the chemical conversion. The energy exchange process is clearly observed in fig. 5.3.3, where the lower temperature of fluid at the particles region is due to the energy absorbed by particles during conversion. Due to the low height of the sample, a quasi-homogeneous heat and mass transport is observed across the height of bed. However, a radial distribution of temperature and species may exist upon the course of the reactions, as shown in the lower edges of fig. 5.3.3a. The radial temperature gradient is mainly attributed to the radiation exchange of particles and the walls of the crucible as well as the energy consumed by reactions, as further explained.

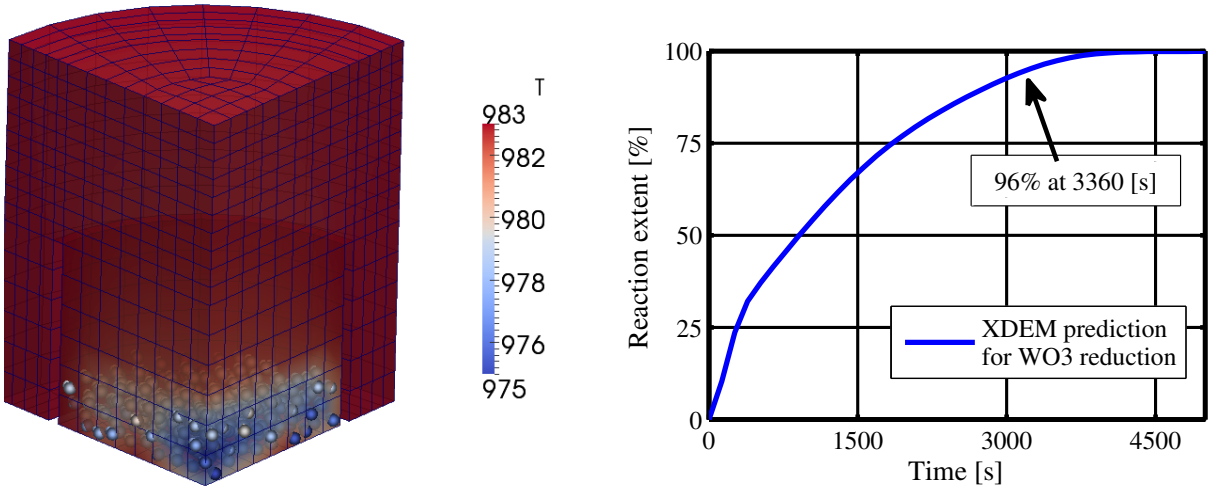

(a) Temperature distribution in fluid and particles at 3600 s.

(b) Reduction extent of a WO_3 sample with time.

Figure 5.3.3: Temperature in gas and solid phases for WO_3 reduction at 710 °C as well as the extent of the reaction [36].

Excellent agreement between experiments and XDEM predictions for mass lost, and full reduction time, during the thermochemical conversion of tungsten trioxide is described in fig. 5.3.4. When WO_3 is reduced below 750 °C, a shortcut, $WO_{2.9} \rightarrow WO_2$, appears. As pointed out in [35], when such a shortcut is not characterized and at reduction temperatures below 750 °C, discrepancies on the accuracy may be observed during the intermediate steps of the numerical predictions. However, this limitation is not affecting the total reduction time. Such a mechanism was not implemented because of the absence of kinetic information of the reaction. Moreover, this mechanism is considered out of the scope of the research since reduction temperatures below 750 °C are not practiced upon industrial reduction [5].

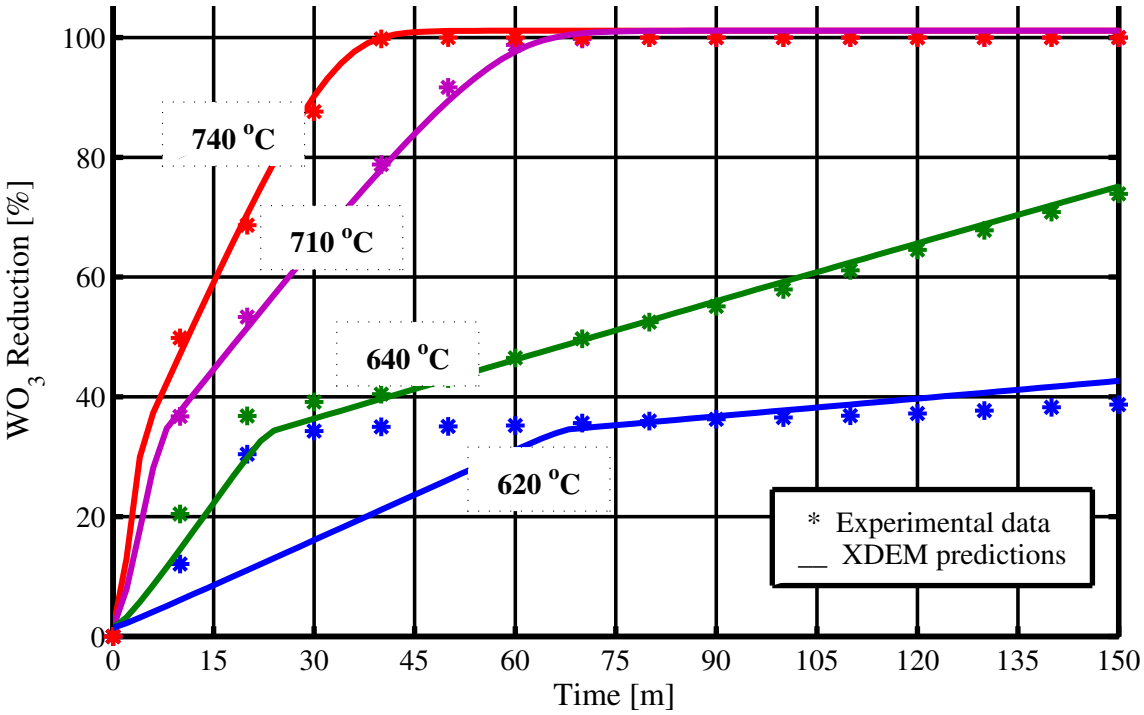

Figure 5.3.4: Isothermal reduction of WO_3 under dry atmospheres. Comparison of degree of WO_3 reduction as predicted by the XDEM [35] and the isothermal experimentation measurements by Fouad et al.[95].

5.3.4 Conclusions on the isothermal reduction validations

Different simulations, with different setups, were performed above to validate the ability of the model to reproduce the isothermal reduction of WO_3 in dry-H_2 atmospheres.

The numerical model was validated by comparison to isothermal thermogravimetric data. The results show the XDEM capacity to accurately predict the complex thermochemical process occurring in the course of dry hydrogen reduction of tungsten trioxide.

5.4 Non-isothermal reduction of tungsten trioxide under dry H_2-atmospheres

5.4.1 Introduction and model description

This section was extracted from:
[37], Estupinan Donoso AA, Peters B, Predicting Tungsten Oxide Reduction with the Extended Discrete Element Method, Advances in Powder Metallurgy & Particulate Materials (2015) 02.35–02.48.

For this validation case, predictions were conducted according to the experimental setup performed by Fouad et al. [93, 95]. According to the axial symmetry of the latter publication, symmetry plane and periodic boundary conditions for the continuous and solid solvers, respectively, were applied as a measure to save computational costs. Hence, as schematized in fig. 5.4.1, a representative section of the reactor was employed as a simplification of the full reactor. In order to avoid the increase of void space around the symmetry walls, a full crucible was filled up by gravity deposition and the particles located out of the wedge domain were removed. Hence, issues related to a "wall effect" are avoided on the planes of symmetry. According to the experiments [93, 95], the numerical setup assumes a uniform initial temperature. Moreover, the temperature of the solid walls was assumed to follow the reduction temperature. Walls radiate energy to particles as inferred from the experimental facility information. Reduction through Chemical Vapour Transport (CVT) takes place when the produced water is retained within the bed. However, in low WO_3 beds (< 1.2 mm) as employed in [95, 93], the presence of volatiles (e.g. $WO_2(OH)_2$) can be ignored because water leaves the system fast enough as not to allow the formation of volatiles. Therefore, grain-growth and other Chemical Vapour Transport effects are neglected within this study.

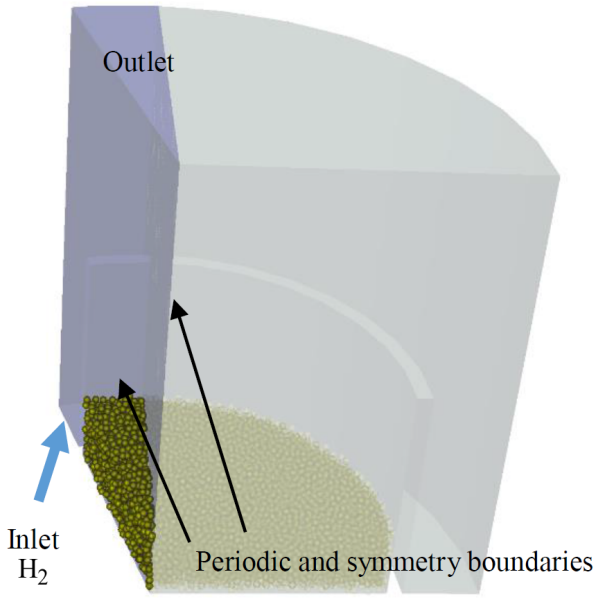

Figure 5.4.1: Thermogravimetry numerical setup. The purple wedge region, on the left side, is the considered simulation domain [37].

Particles are assumed to be spherical, but the actual irregular shape of the grains is covered by the spherisity term which corrects the geometrical properties (e.g. volume, surface) of the grains. The spherisity is estimated as the ratio of the surface area of spherical particles, with equal volume as the irregular particles, to the surface area of the irregular particles. More characteristics about the employed setup is collected in the

following table 5.4.1.

Table 5.4.1: Numerical setup for the non-isothermal reduction validation as reported in [95, 93]

Powder		
WO_3	99.9	%
Size	45 ± 3	µm
Mass	83.3	mg
Reducing gas		
H_2	99.9	%
Volumetric flow	5	ml/min
Crucible		
Diameter	6	mm
Height	3	mm
Wedge angle	15	°

5.4.2 Numerical predictions

To test the proficiency of the proposed method treating heterogeneous processes, such as the discussed in this section, XDEM predictions for mass loss in the course of the non-isothermal reduction of WO_3 were performed and compared with the experimental data, as graphically represented in fig. 5.4.2. While fig. 5.4.2a describes the actual transient comparison for mass loss, fig. 5.4.2b shows the evolution of the absolute error of the computation ($error = prediction - observation$). The mean deviation of the computation absolute error is found to be 0.3% of mass loss.

The XDEM accurately follows the inflections along the experimental curve with a high level of accuracy. The inflections yield information on the step of the reduction and the predominant intermediate oxides. However, the current model provides the exact development of the composition as described in section 4.1.2. Thus, fig. 5.4.3 shows the existing reaction overlaps, the one that was already described by Fouad et al. [95], who determined that the step $WO_3 \rightarrow WO_{2.72}$ was overlapped by the succeeding step $WO_{2.72} \rightarrow WO_2$.

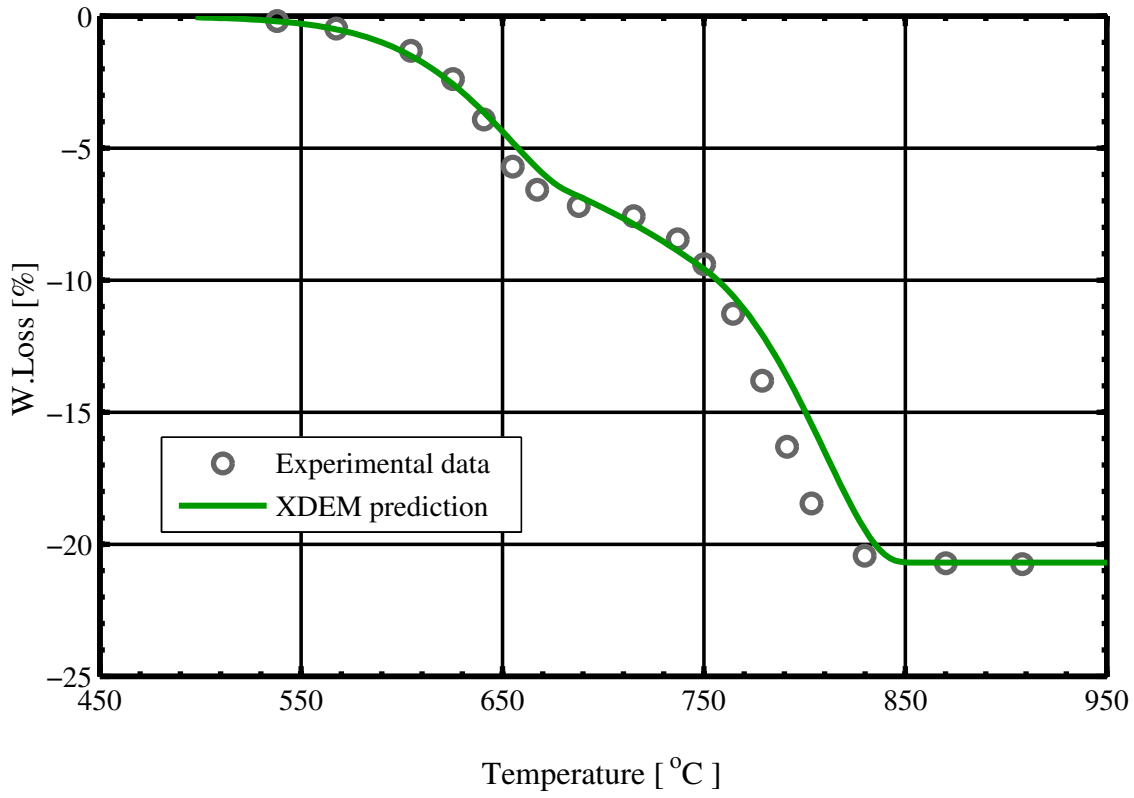

(a) Non-isothermal reduction of WO_3 under dry atmospheres. Comparison of thermogravimetric measurements [93] and XDEM predictions for mass loss progress [37].

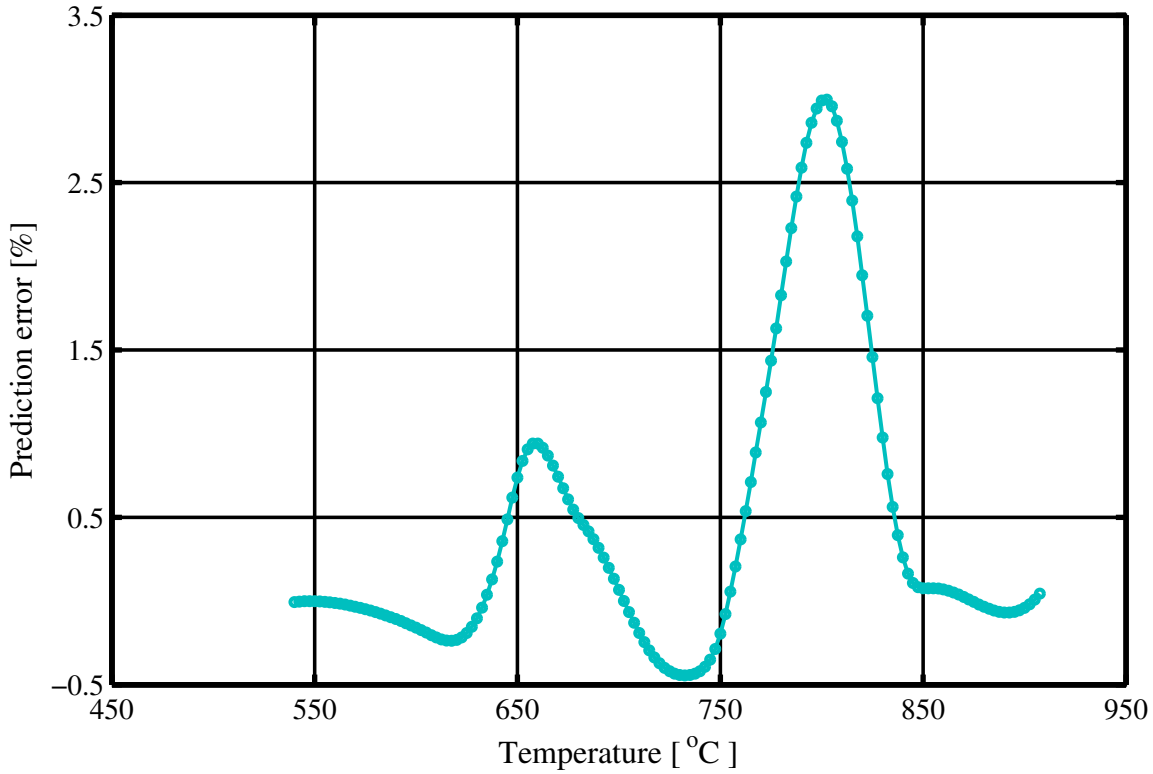

(b) Instantaneous absolute error of the computation ($error = prediction - observation$) [37].

Figure 5.4.2: Validation of XDEM predictions for the non-isothermal reduction of WO_3 at 0.25 °C/min in a hydrogen atmosphere and error analysis.

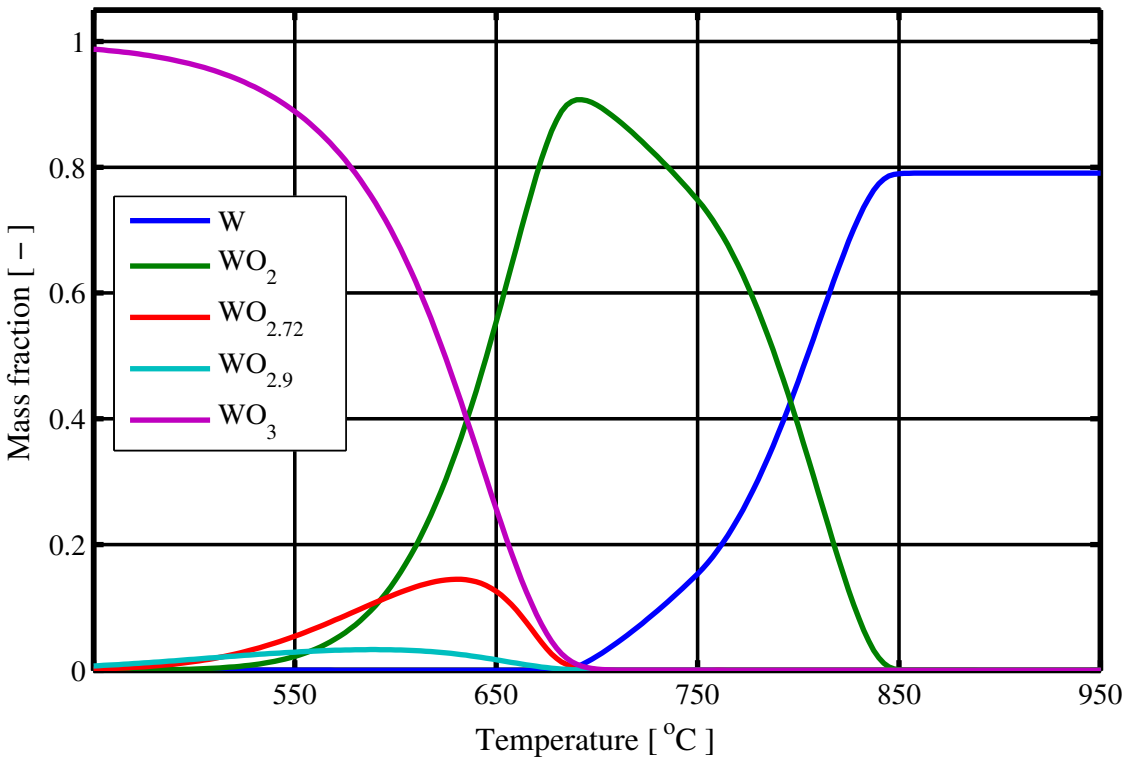

Figure 5.4.3: Non-isothermal reduction of WO_3 under dry atmospheres. Dimensionless total solid mass fraction according to XDEM predictions [37].

Figure 5.4.4 shows the tungsten formation along the radius at the bottom of the bed. For this, three particles were sampled, one located at the center of the crucible, one at the wall region and one between the two particles. The particles where chosen in this location to observe radial gradients within the solid matrix. It is shown that even in such a small geometry, tungsten formation is not uniform. With this geometry, particles at the wall region are reduced faster than at the center of the reactor. This is a consequence of a lower H_2 to H_2O ratio at the center of the container.

Similar to the observation of the solid species, it is possible to investigate the gaseous species inside particles as well as in the continuous domain, namely the furnace atmosphere. Figure 5.4.5 depicts the evolution of the instantaneous water vapour inside the bed compared to the total water vapour in the fluid phase. In addition, the transient change of gaseous products for the above-mentioned three monitored particles was used to investigate at the presence of gradients in the vapour quantities. Particles at the center of the reactor retain more gaseous products than those at the wall region. The qualitative correlation between figs. 5.4.6b and 5.4.6c and the trends of fig. 5.4.5 shows that water vapour in the fluid has the same behavior as the water inside particles. This indicates that gaseous products diffuse into the fluid phase at a high rate. The effect is stressed by the correlation of integral evolution of water vapour in the fluid and in the intra-particle (fig. 5.4.5). Hence, it was appropriated to neglect reduction trough CVT, because the

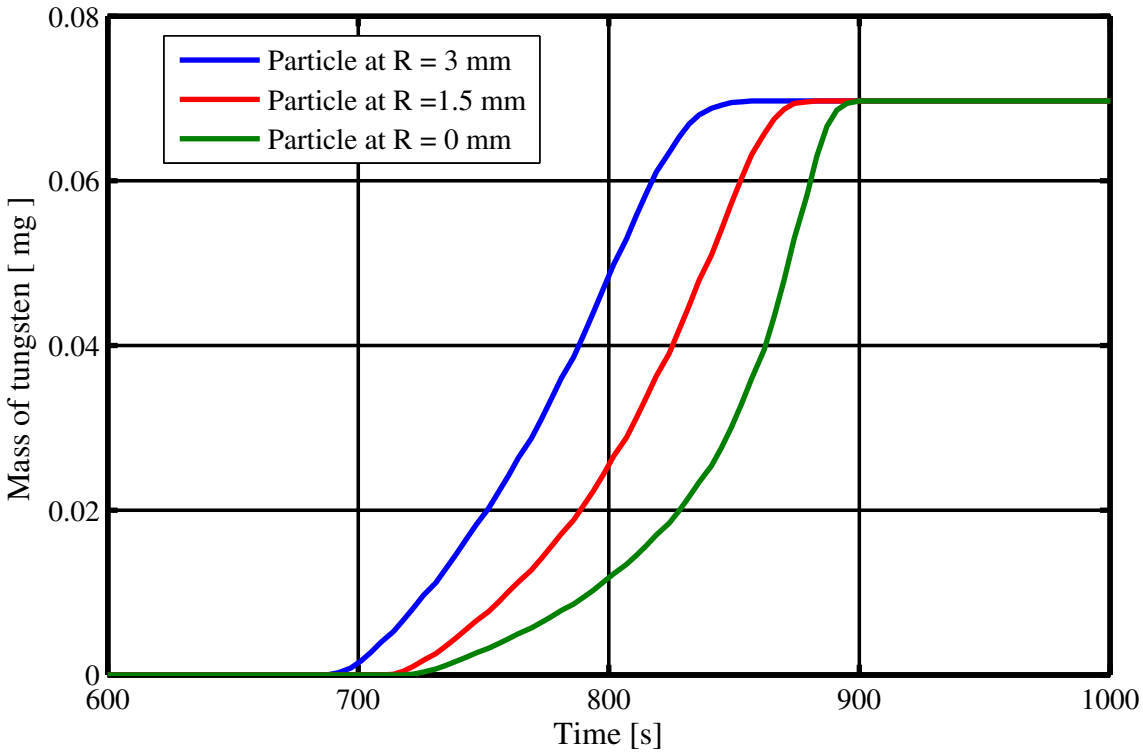

Figure 5.4.4: Non-isothermal reduction of WO_3 under dry atmospheres. Tungsten formation progress, per particle, along the radius of the sample holder as predicted by the proposed model formulation [37].

residence time of water vapour in the reaction sites is very short.

Figure 5.4.7 helps to better understand the trends obtained on the above described results. The high temperature at the wall region, transferred to particles by conduction, convection and radiation, considerably increases diffusion of gaseous species because of the power law temperature dependence. Moreover, due to the wall effect [25], the increase of void space at the wall region, as schematised in fig. 5.3.2b, facilitates the circulation of gaseous species. Figure 5.4.7 also shows the heat interaction between fluid and particles. In figs. 5.4.4 and 5.4.6c is described a faster reduction progress at the wall regions. In that region, energy is mainly provided by radiation from the walls. Particles, that are not in the walls vicinity, obtain its energy required to drive reactions mainly from convection. Such an energy consumption is reflected by heat transfer from the fluid phase as it can be visualized in fig. 5.4.6a.

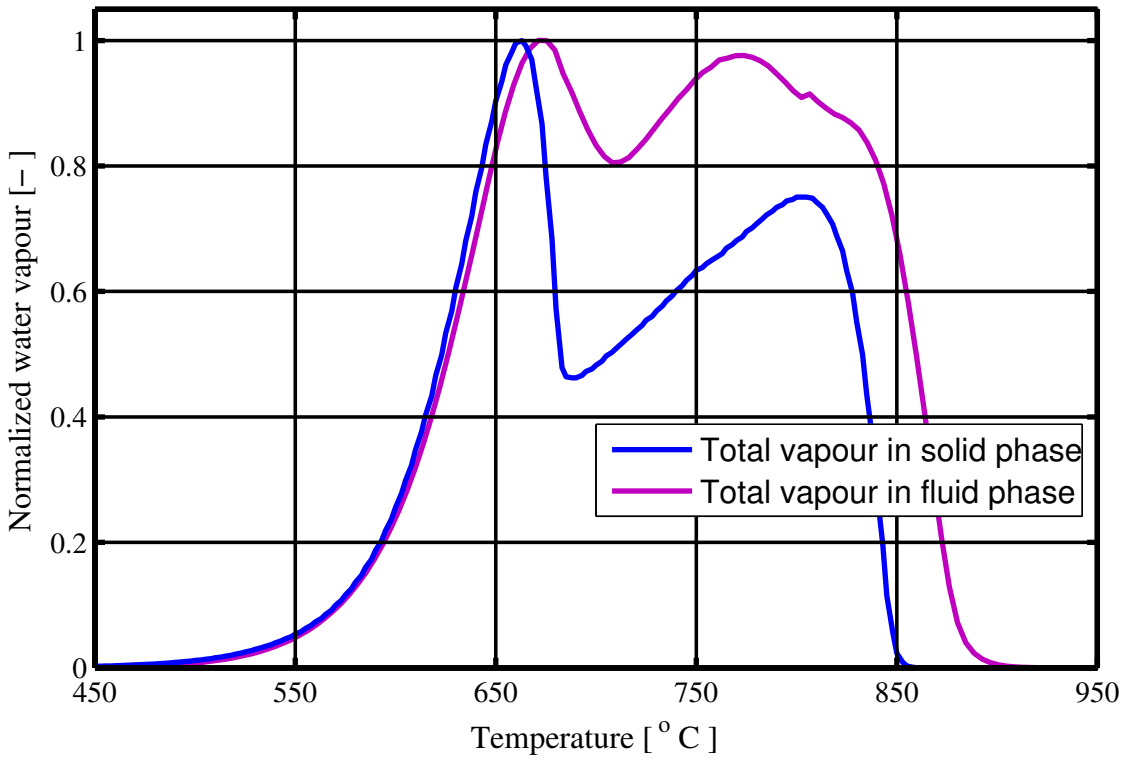

Figure 5.4.5: Dimensionless comparison of total water vapour in the fluid and inside of the powder bed. The actual values were normalized by their individual maximum value [37].

5.4.3 Discussion

In this study the transient comparison of total water vapour, in the solid and gaseous phases, suggests that inward and outward diffusion of gaseous species have no limiting effects on the reaction rate. One advantage of this comprehensive model formulation is that all aspects of fluid transport, gas penetration into the bed, gas diffusion in the pores of particles and chemical reaction are considered; and thus it leaves no scope for assuming diffusion-limiting or reaction-limiting processes. Moreover, the comprehensive results proof that the model is a valuable tool to investigate the transient and spatial advance of the reduction of tungsten trioxide processes, at both, microscopic and macroscopic levels.

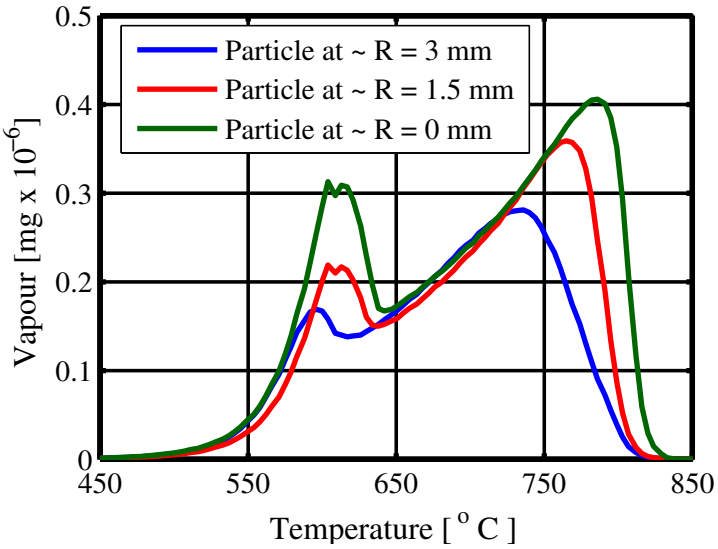

(a) Intra-particle water vapour evolution for the three sampled particles [37].

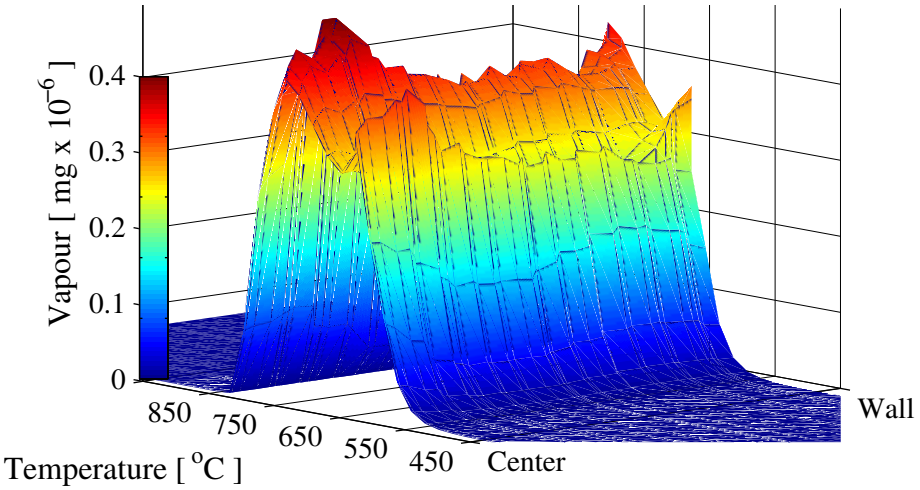

(b) 3D plot of local mass of water vapour inside particles over the crucible radius and time.

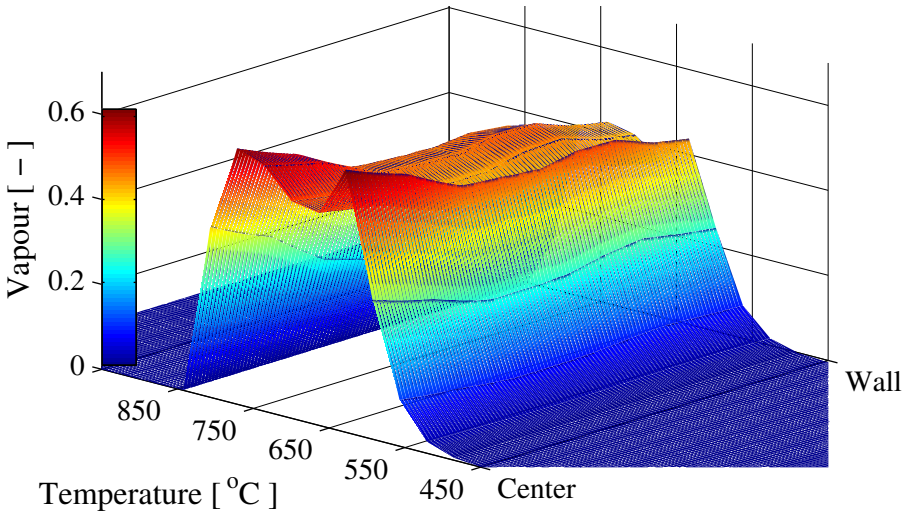

(c) 3D plot of mass fraction of water vapour in the fluid phase over crucible radius and time.

Figure 5.4.6: Non-isothermal reduction of WO_3 under dry atmospheres. Time evolution of the water vapour along the radius of the sample holder for discrete and continuous phases.

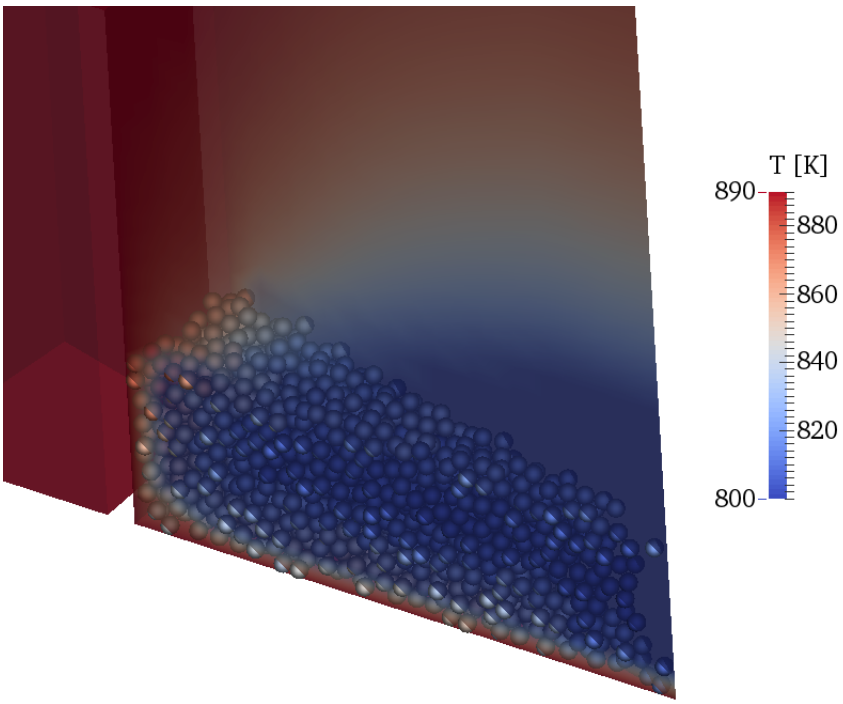

(a) 3D impression of the temperature fields inside the numerical crucible wedge.

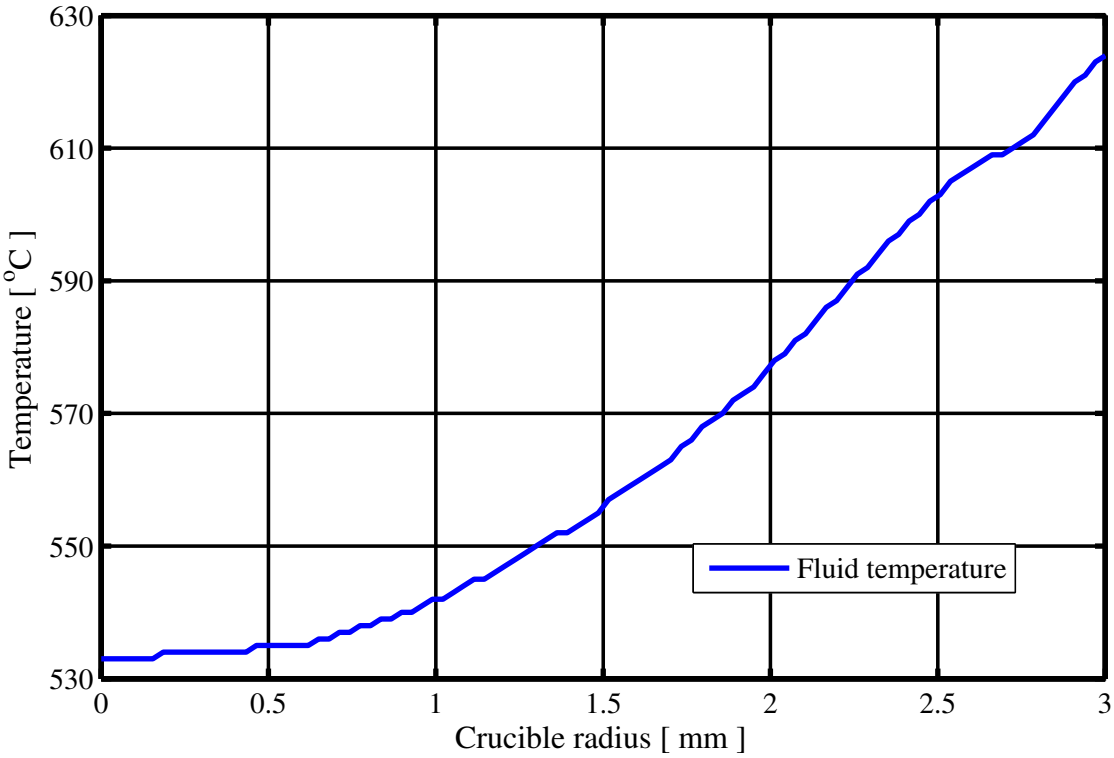

(b) Radial fluid temperature profile in the crucible.

Figure 5.4.7: Non-isothermal reduction of WO_3 under dry atmospheres. Radial temperature profiles in the solid and fluid phases at $t = 2400$ s [37].

5.5 Agglomerated particle method (APM) verification and validation

5.5.1 Agglomerated particle method introduction

In this section, the new approach developed within this research work was subjected to numerical verification and validation to asses its capacity to reduce computational costs without compromising the accuracy of the results. Verification and validation was performed for heat and mass transfer predictions of the APM. The agglomerated particle method (APM), as previously described in section 4.2.4.3, aims to solve a single set of equations for a group of particles under similar boundary conditions.

5.5.2 APM applied to packed beds undergoing drying

As a first validation, the novel technique was compared to experimental and numerical results of a packed bed of particles undergoing drying. Drying of solid beds involve different mechanisms for water vapor production than the observed in the hydrogen reduction of tungsten oxides. However, such a differences are basically reflected in the water vapour production rate. Assuming the same order of magnitude of vapour production rate, for both drying and WO_X reduction, the current case study is employed for numerical assessment of the APM because drying involves water vapour production and transport. As presented in section 2.2.4, vapour transport and production phenomena are considered of major importance upon the hydrogen reduction of tungsten oxides.

The test reactor Pantha, as described in appendix C.5, is commonly used by numerous researches [25, 29, 83, 108, 109, 119, 120] to examine the accuracy of numerical methods dealing with thermochemical conversion of packed beds (e.g. heating up, drying and pyrolysis). Thus, as documented in [27, 120], drying experimentation and fully resolved XDEM predictions as in [27] were employed for evaluation of the herein proposed agglomerated method.

The employed drying mechanism was exactly taken as [27, 120] in order to avoid introducing uncertainties into the comparison. Therefore, a discussion on the drying mechanism implemented for these simulations is out of the scope of this thesis. Following the investigation of Mahmoudi et al. [27], the heat sink model [119] of eq. (5.5.1) was implemented

for both, agglomerated and non-agglomerated, formulations. Namely,

$$\dot{w}_{H_2O} = \begin{cases} \frac{(T - Tevap)\rho\, c_p}{H_{evap}\ \delta t} & \text{if} \quad T \geq T_{evap} \\ 0 & \text{if} \quad T \leq T_{evap} \end{cases} \tag{5.5.1}$$

where ρ, c_p and H_{evap} denote the density and the thermal capacity of dry wood and water evaporation enthalpy, respectively. Within the model, water vapour inside the particle does not leave the particle instantaneously; vapour transfer is limited from the particle to the surrounding environment by the difference in vapour concentration inside the particle and environment. The heat available above the evaporation temperature T_{evap} is consumed by evaporation without distinguishing between bound and free water.

Figure 5.5.1, graphically represents the geometry employed for the verification of heat and mass transfer predictions of agglomerated particles (AP) undergoing drying. Details about the physical experiments are exhaustively documented in [27, 120] and a summary is presented in table 5.5.1. Figure 5.5.1a, depicts a fully resolved XDEM-particles setup involving 2667 particles, while fig. 5.5.1b is the corresponding reduced representation with 424 agglomerated entities. Since all the particles within a CFD-cell share the same boundary conditions, one AP per CFD-cell was chosen for this setup. In addition, properties such as the number of original particles per CFD-cell, cell-porosity and total surface of original particles per CFD-cell were averaged and associated with the corresponding entities. Thus, the characteristic bed properties of the porous medium were estimated based on the original particles position and size.

Table 5.5.1: Numerical properties, initial and boundary conditions used during Pantha experiments.

XDEM Pantha setup

Gas Phase: Air

$T_{fi_{max}}$	=	573	K	Maximal Inlet Temperature

Solid Phase

T_{p_o}	=	298	K	Initial temperature of particles
R	=	3.5	mm	Particle radius
ρ	=	750	kg/m^3	Density
c_p	=	2551.3	J/kgK	Specific heat
λ	=	0.1256	W/mK	Conductivity

Reactor's characteristics

D	=	40	mm	Diameter
H	=	210	mm	Height
$No._p$	=	2667		Number of particles

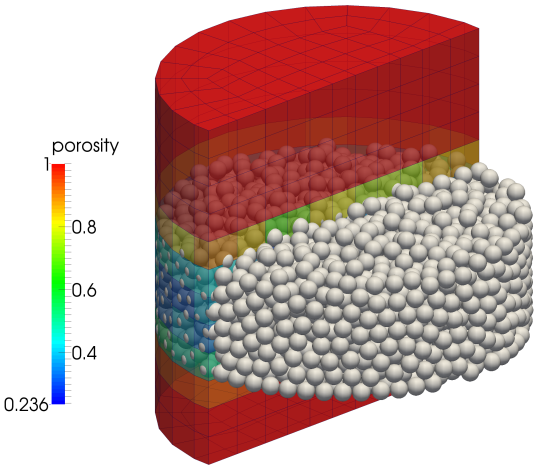

(a) Reactor with original particles.

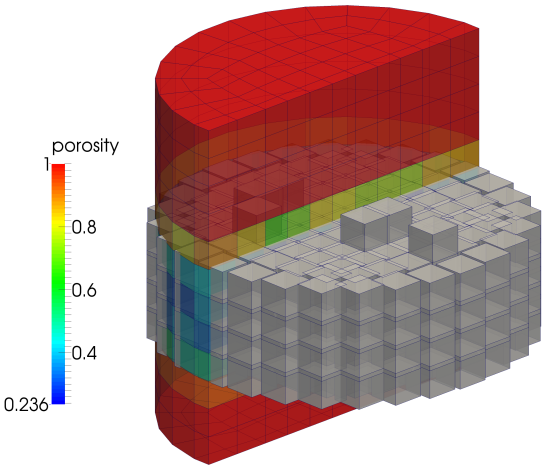

(b) Reactor with agglomerated particles.

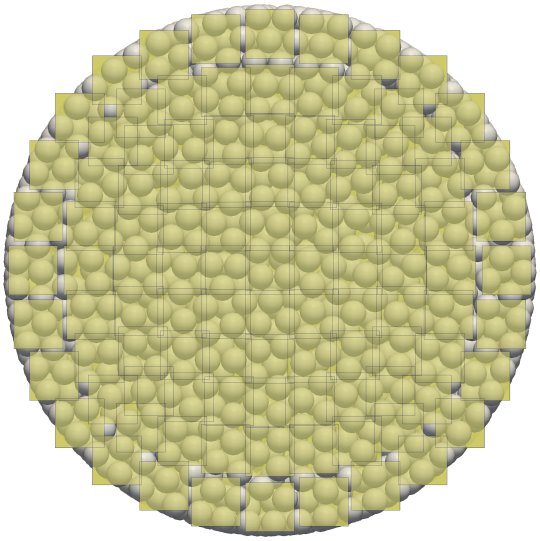

(c) Bottom view of the original particles mapped to their agglomerated particle representation.

Figure 5.5.1: Numerical representation of the Pantha reactor as set for drying predictions.

Figure 5.5.2 compares the dimensionless loss of water for the drying experiment and, both, APM simulation and the entirely solved particles simulation. Using the latter as reference, the mean APM prediction error over time is 0.24% with an standard deviation of 0.01%. Where the error is computed as the difference between the resolved and the APM predictions. The discussion on the deviation between predictions and measurements is out of the scope of this study; nevertheless, it is reported in [27].

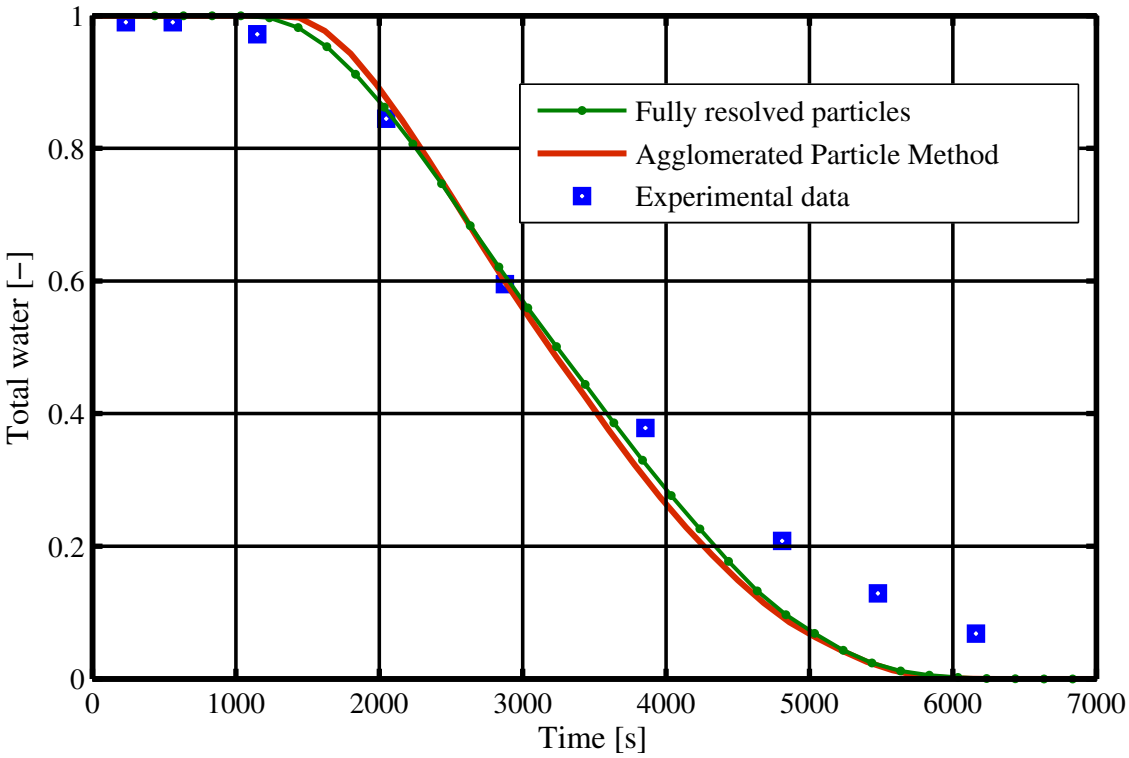

Figure 5.5.2: Dimensionless comparison of total water loss within the bed. The deviation between predictions and experiments are discussed by Mahmoudi et al. [27].

The equilibrium reactions considered during the WO_X conversion are directly influenced by the temperature. Thus, fig. 5.5.3a compares the average temperature predictions for APM and the entirely solved particles simulations. Figure 5.5.3b, describes the progression of the APM prediction error; with a mean value of 2.01 K.

The error in temperature predictions is explained by the shape and volume differences between agglomerated particles and CFD cells. APM particles are conveniently chosen as perfect cubes with equal size and mass (section 4.2.4.3). However, as shown in figs. 5.5.1a and 5.5.1b, CFD-cells are uneven hexahedrons with a varying number of particles in each. A more accurate solution can be achieved by reducing the size of agglomerates or/and by mapping the exact cell properties to the agglomerated particles according to their position within the bed. Nevertheless, the error was acceptable and did not influence the conversion predictions considerably. In the present case comparison, the APM solution was 5 times faster compared to the original XDEM prediction, which are in the order of few days when running in a single processor.

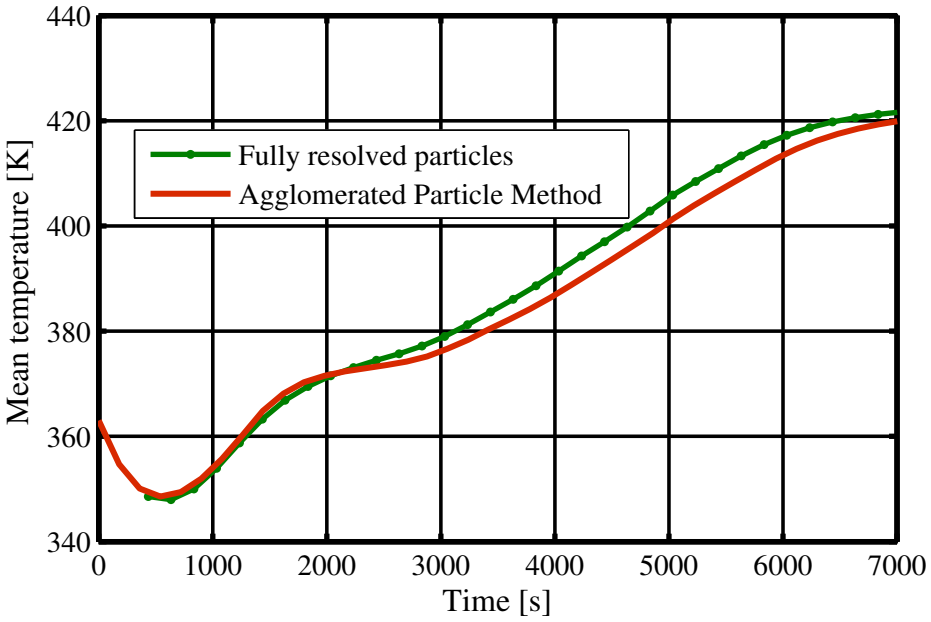

(a) Average bed temperature evolution of APM and fully resolved particles predictions.

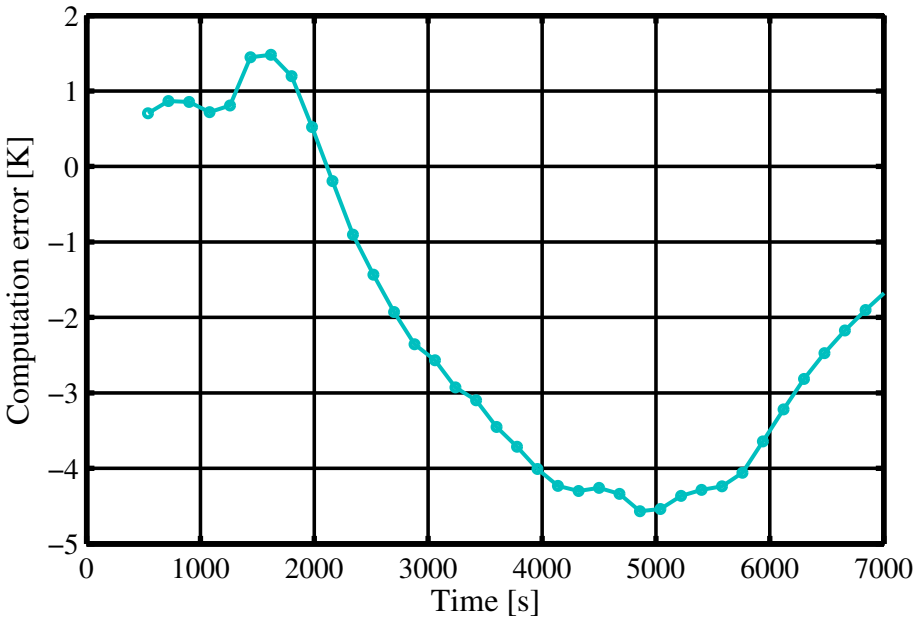

(b) Instantaneous APM-prediction error for the average temperature of the bed. The error indicates the deviation of APM from the fully resolved particle computations.

Figure 5.5.3: Temperature predictions comparison between APM and a fully resolved particle approach.

5.5.3 Hydrogen reduction of tungsten oxides

In this subsection, the accuracy of the APM upon the reduction of tungsten oxides is evaluated. A simple channel containing 910 WO_2 particles, with a diameter of 35.6 µm exposed to industrial reacting conditions, is employed as reference solution for this numerical verification. Figure 5.5.4 shows a graphical representation and table 5.5.2 summarizes the numerical setup of the proposed numerical verification.

Table 5.5.2: Numerical properties employed for the verification of APM upon hydrogen reduction of tungsten oxides.

Solid Phase: WO_2 particles

	Particles ensemble	APM	
T_{p_o}	1073	1073	K, Initial particles temperature
L	35.6	5×10^3	µm, Characteristic length
$No._p$	930	3	Number of particles per CFD cell
ϵ_{P_o}	0.2	0.62	−, Initial particle porosity

Gas Phase: 100% H_2

U_{f_i}	0.1	m/s, Inlet velocity
$T_{fi_{max}}$	1073	K, Inlet Temperature

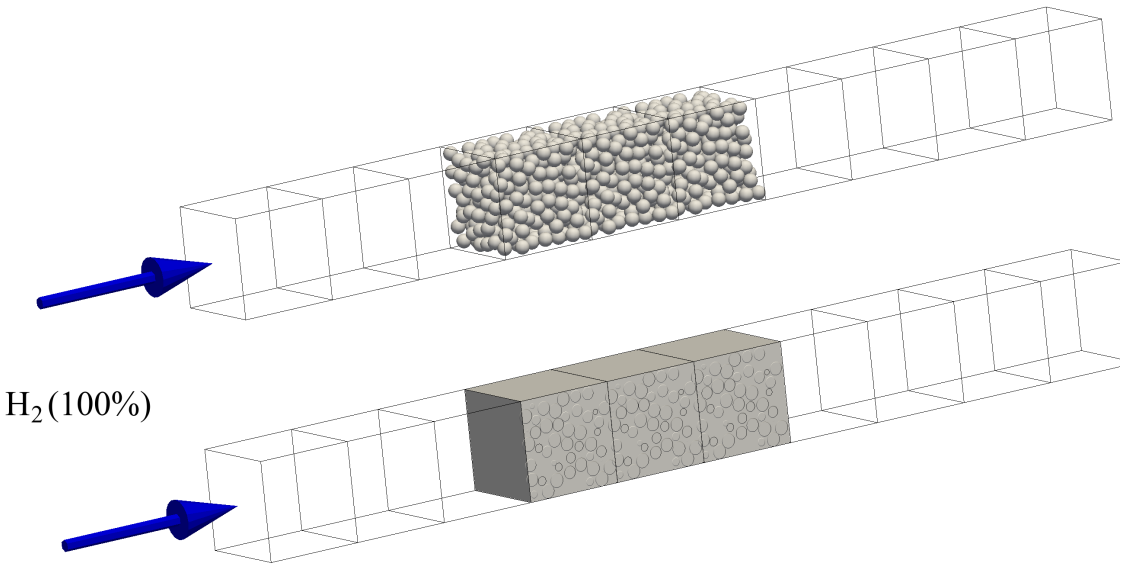

Figure 5.5.4: Numerical setup for verification of the APM employed applied to H_2 reduction of WO_2. The upper case is a CFD channel with fully resolved discrete entities and the lower case is the corresponding APM representation.

Figure 5.5.5 qualitatively compares both methods at different times, namely, fully resolved particle and the APM approaches. As expected, the reaction front proceeds from the inlet side and continues towards the outlet. After 700 s, vapour gradients are negligible and the tungsten concentration becomes uniform. In addition, the uniform solution of resolved particles within a same CFD-cell over time can be appreciated on the fully resolved case; this shows that, under the current case conditions the choice of agglomerated particle size seems to be adequate.

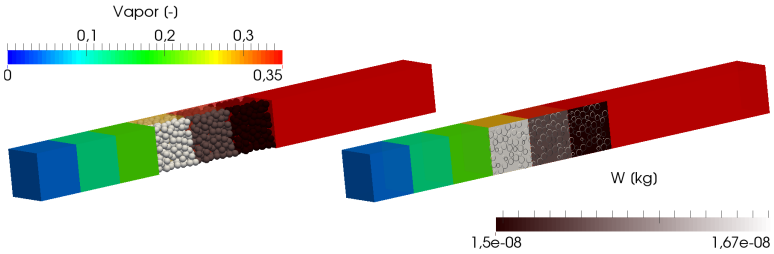

(a) Comparison of APM predictions at 10 s.

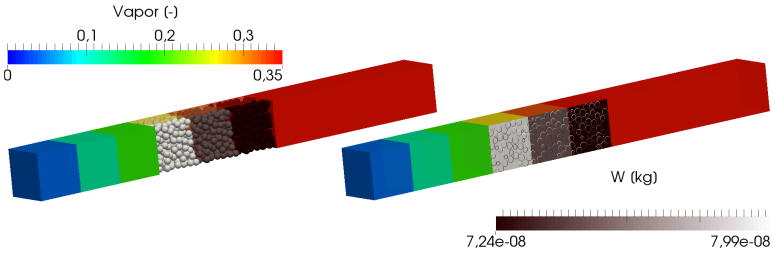

(b) Comparison of APM predictions at 50 s.

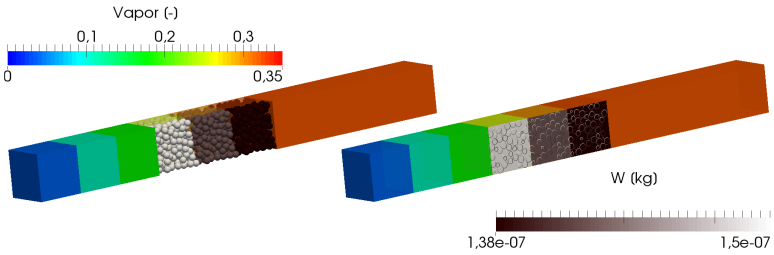

(c) Comparison of APM predictions at 100 s.

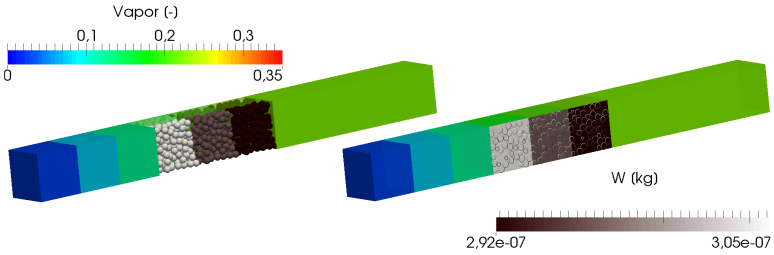

(d) Comparison of APM predictions at 250 s.

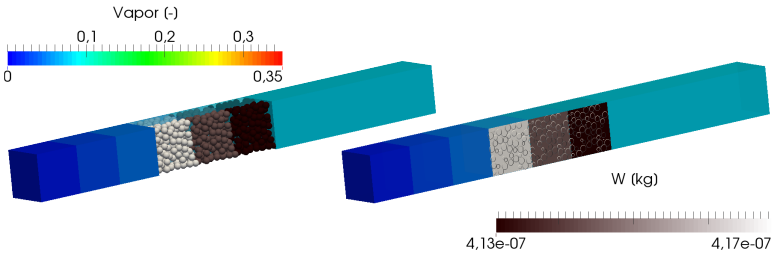

(e) Comparison of APM predictions at 500 s.

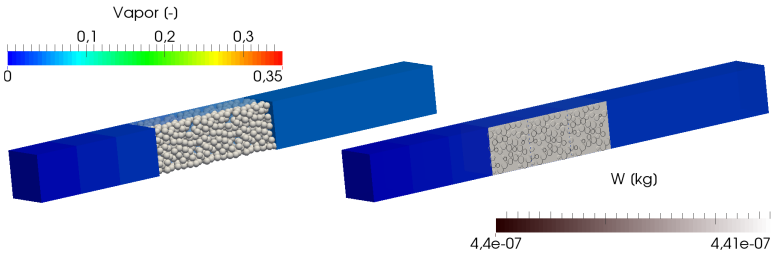

(f) Comparison of APM predictions at 700 s.

Figure 5.5.5: Comparison of numerical predictions for WO_2 reduction in a 1D channel. The upper-left scales indicate the mass fraction of water vapour in the fluid phase, while the bottom-right scale describe the total mass of tungsten in each unit cell.

Contrary to the cell geometry of the drying verification case, see section 5.5.2, in this setup all the cells are perfect cubes. Hence, bed properties were easily set to the APM case according to an exact property mapping from the unit cell generated by the original particles case. Thus, as shown in fig. 5.5.6, in this validation a higher level of accuracy is achieved for temperature predictions.

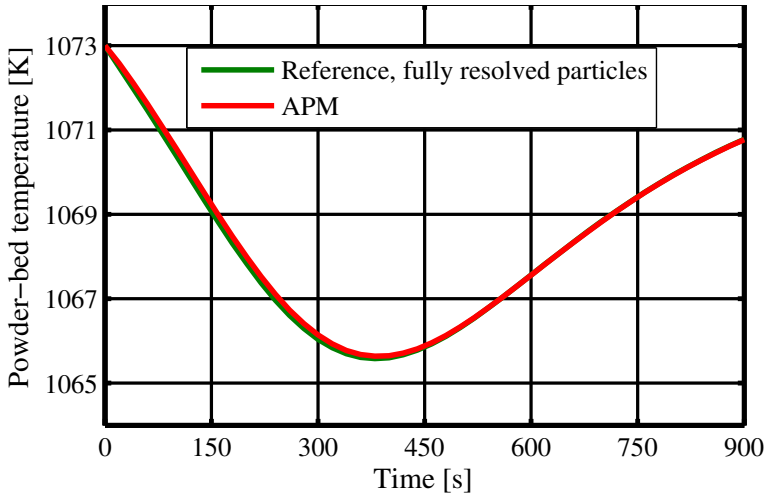

Figure 5.5.6: Numerical predictions for bed temperature during reduction of WO_2.

The complete reduction is achieved after 900 s when oxygen has been removed from the starting tungsten dioxide. As shown in fig. 5.5.7a, the two proposed methods converge to the same solution. Moreover, the APM transient solid species calculation is achieved with high degree of accuracy compared to the fully resolved particles (fig. 5.5.7b). Finally, it has to be stressed that, for the current verification, the agglomerated solution decreased more than 12 times the computational cost of the fully resolved XDEM prediction. The maximum APM-prediction relative error in fig. 5.5.7 is 0.4%, while the mean relative error is about 0.15%.

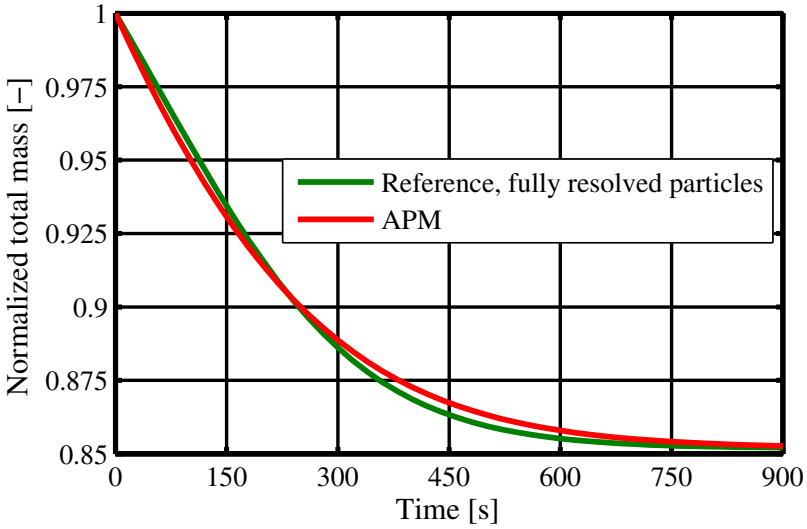

(a) Total mass vs time during reduction of WO_2 for APM and fully resolved approaches.

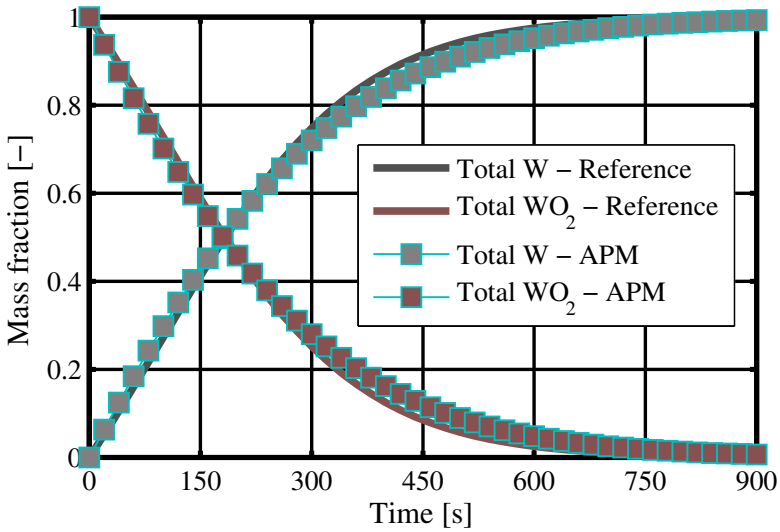

(b) Solid species mass vs time during reduction of WO_2 for APM and fully resolved approaches.

Figure 5.5.7: Comparison of numerical predictions for WO_2 reduction in a 1D channel.

5.5.4 Conclusions on the APM verification

The above documented results show the ability of the APM model to capture the details of drying for a random packed bed at a lower computational cost. Employing the novel technique for all particles within the bed in combination with an appropriate continuous model for the surrounding gas, enables the prediction of a process for an entire packed bed by summation of individual particle processes. Thus, under similar reducing conditions and as numerically proven in this section, the Agglomerated Particle Method (APM) can predict the hydrogen reduction of tungsten oxides with a confidence of more than 99%; taking as reference a conventional XDEM solution.

The choice of APM particles size is governed by the CFD-cell size and by the flow conditions; and therefore, as it can be observed from the above APM verifications and validation, a lower flow through the particles leads to bigger parcels of particles sharing the same boundary conditions. The bigger the parcels, the lower the number of APMs and the lower the computational costs that can be achieved.

Chapter 6

Predicting metallic tungsten production under industrial conditions

Contents

The best way to predict the future is to invent it.

A. Kay

6.1 Obtaining kinetic parameters of heterogeneous reactions

6.1.1 Introduction

In this section is presented a classical optimization problem, which consists of the estimation of the kinetic parameters that best fit experimental data for the *tungsten transport mechanism* of section 2.2.4.2. The final step during the tungsten oxide reduction (WO_2 to W) is recognized to be the dominant part of the WO_3 reduction processes. Thus, due to the impossibility of finding reliable information for the kinetics of volatilization and deposition of the different tungsten oxides, and assuming that the kinetic parameters of volatilization-deposition of metallic tungsten are known (table 2.2.4), the focus of this study is to determine the kinetic parameters for the volatilization/deposition of tungsten dioxide.

As described in section 4.1, and recalled by fig. 6.1.1, even if chemical reactions are taking place only at the surface of the particle pores, complex multiscale phenomena are involved during the heterogeneous reactions such as the tungsten oxide reduction. These mechanisms include property variations, complicated regions, combined transport mechanisms, chemical reactions, and varying boundary conditions. Therefore, obtaining kinetic data from such processes is considered a difficult task and has to be performed with the help of multiscale models like those proposed in this work.

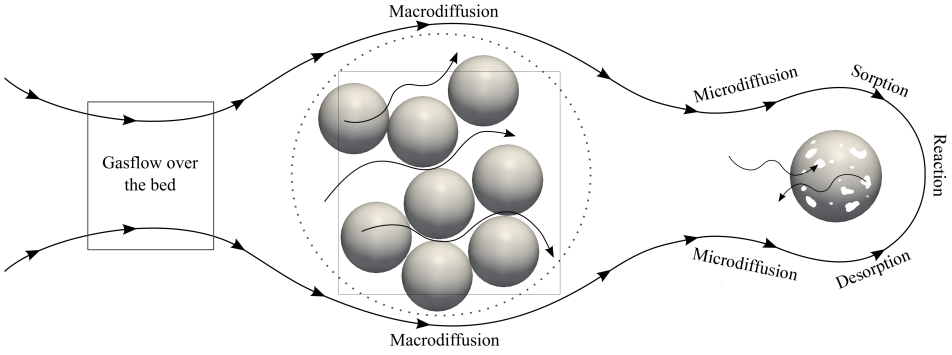

Figure 6.1.1: An overview of the phenomena involved in heterogeneous reactions.

6.1.2 XDEM employed to obtain the kinetic parameters of WO_2 volatilization

The *tungsten transport mechanism*, as modelled in section 4.1.2.2, is always coupled with the *oxygen transport mechanism*. Nevertheless, in the previous chapter it was proven that the total reduction may be modeled even if only the direct scheme is accounted for. Both schemes, direct reduction model or reduction through CVT model, are believed to produce the same results for the extent of the reduction. However, in order to model the morphological change of grains (section 4.1.2.3), grains nucleation (*oxygen transport mechanism*) is combined with the intermediate volatilization-deposition reactions accounting for grain growth. Thus, the XDEM reduction predictions reported in section 5.4, which employed only a direct scheme, are taken as the reference solution for the optimization problem. Consequently, consistency between reduction through the step represented by eq. (2.2.14) and through the intermediate scheme represented by eqs. (2.2.18) and (2.2.19) has to be granted.

Heuristic algorithms are commonly used to solve similar optimization problems and different studies have been carried out for the estimation of the kinetic parameters of chemical reactions. For instance, Cutillas-Lozano [121] evaluated several local and global search methods to determine the kinetic constants of complex chemical reactions in heterogeneous phases. Puxty et al. [122] proposed a tutorial to find kinetic data by employing differential equations, calculations of concentration profiles and using non-linear regression to fit the rate constants of the model to the measured multiwavelength data. In [123], an iterative methodology to determine kinetic parameters for simple chemical models and simple transport properties is also employed.

Despite the fact that evolutionary algorithms (EA) or genetic algorithms (GA) are highly used within optimization problems, a *simplex* algorithm, implemented in the Matlab optimization toolbox under the name of *fminsearch*, was employed in this work. The Nelder-Mead *simplex* algorithm, since its first publication in 1965, has become a widely used method for nonlinear unconstrained optimization [124]. The Nelder-Mead algorithm is very popular in the fields of chemistry, chemical engineering and medicine; where it is employed to estimate the parameters that diminish the error between predictive models and observations. The Nelder-Mead algorithm is a method that minimizes a real-valued function, known as objective function, $f(x)\,\mathrm{for\,x} \in \mathrm{R_n}$. [124]. In the first k^{th} iteration, $k \geq 0$, is set a "nondegenerate simplex" Δk, with its $n+1$, vertices pointing to R_n. Consecutively, the k^{th} iteration defines a set of $n+1$ vertices that generate a different "simplex" for the next iteration.

In general, in systems with a high dependency on the concentration of products (e.g. reversible systems), transport phenomena are of importance and have to be considered within the objective function. Herein the objective function is the prediction error between the reference and the "new " XDEM kinetic model coupled to a transport model describing flow, heat and mass transfer applied the experimental reactor described in section 5.4. In each k^{th} iteration, according to [124], a new set of kinetic parameters are evaluated to compare and try to minimize the error of transient mass loss predictions. Thus, the herein proposed method employs a robust and complete tool to determine kinetic parameters.

Figure 6.1.2 presents an example of the XDEM evaluations performed during the first part of the optimization processes. In the figure it is possible to observe how the optimization process tries to converge into a minimum prediction error. This first, or preliminary optimization is performed in shorter scales of time in order to find the best starting parameters-point. Subsequently, the optimization is completely run with the different starting points and the results of the best fitting are compared again to obtain the "best of the best" fitting; this can be understood as a comparison between local minimums. As a final result, fig. 6.1.3 compares the reference and the objective function evaluated with the obtained best parameters. After comparison, the "best of the best" parameter values, namely the pre-exponential factor and the activation energy, are reported as 8 [1/s] and 49.5 [kJ/mol], respectively.

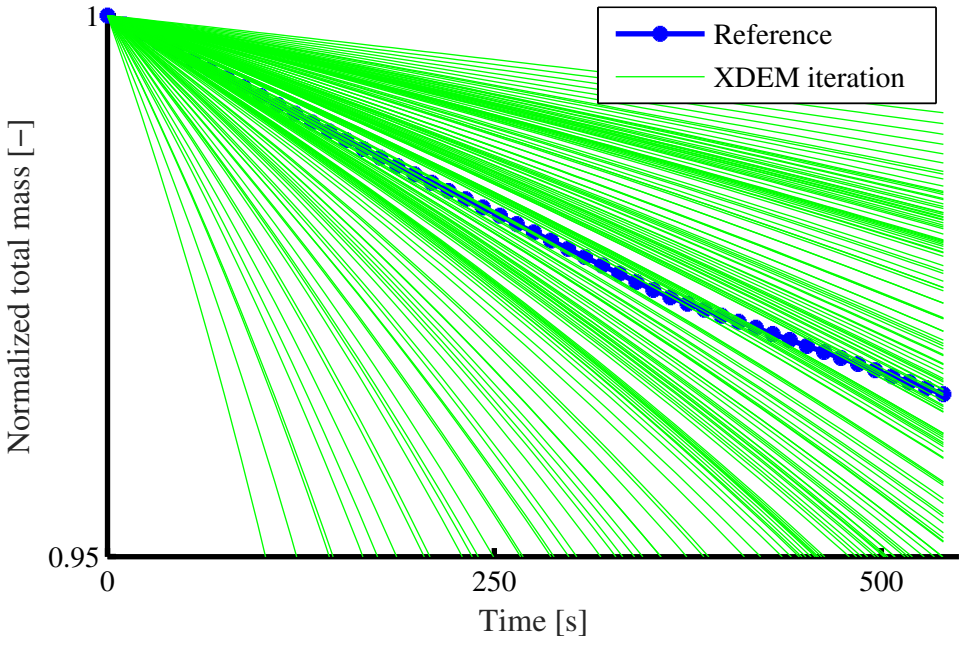

Figure 6.1.2: Example of preliminary Matlab-XDEM optimization routine to determine kinetic data. The green lines are single XDEM test-evaluations and the blue-doted line represent the reference value; which is the prediction in fig. 5.4.2a.

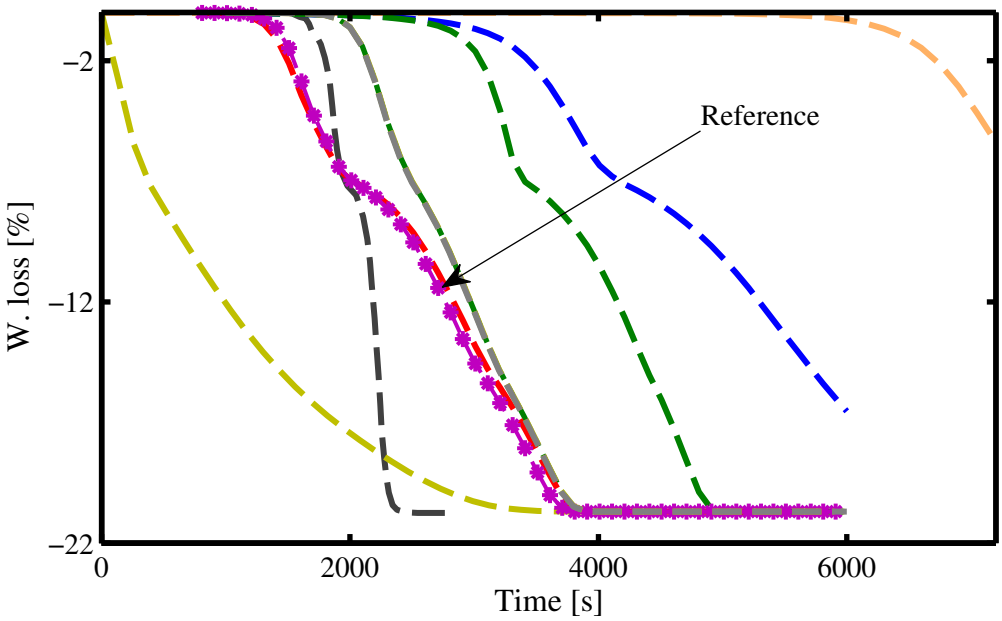

Figure 6.1.3: Comparison of reference solution (see fig. 5.4.2a) and evaluation of XDEM with best fitting values for weight loss. The doted line represent the reference solution and the dashed lines are the different XDEM evaluations. The red dashed line represent the XDEM prediction with the finally chosen parameters.

The kinetic parameters for the WO_2 volatilization have been obtained under the awareness of several uncertainties. Some of the major uncertainties are the $WO_2(OH)_2$ physical characterization and the kinetic parameters of the volatilization-deposition reaction of metallic tungsten; which, within this study was assumed as given factors but discrepancies exist about such a data [58]. Greene and Finfrock [58] conclude from their observation on vapourization of tungsten that, due to the complexity of the process, kinetic correlations for a given vapourisation process are more reliable than physical chemistry analysis. This can be interpreted as: the existing kinetic data for such a volatilization process may be unique to the given experimental conditions. For instance, Kilpatric and Lott [60] delivered data with half of the rate reported in [58]. Thus, the data employed and delivered, during this part of the work, has to be understood as non-definitive data and an exhaustive study into these volatilization-deposition processes is suggested to be conducted as future work. Nevertheless, it is believed to be in the orders of magnitude corresponding to the real intrinsic process. In addition, with the obtained parameters a more complete model to understand grain grow mechanisms is achieved. Hence, the employability of the XDEM for tungsten grain size prediction can be assessed.

6.1.3 Verification of kinetic parameters in the presence of water vapour

In order to evaluate the proposed kinetic data, numerical WO_3 isothermal reductions 1100 K were performed in the presence of a humid reducing gas (0.9/0.1 H_2/vapour). Hence, fig. 6.1.4 compares predictions for the humid-hydrogen reduction via direct mechanism or via the intermediate mechanism. The figure suggest a consistency between the different schemes for tungsten production.

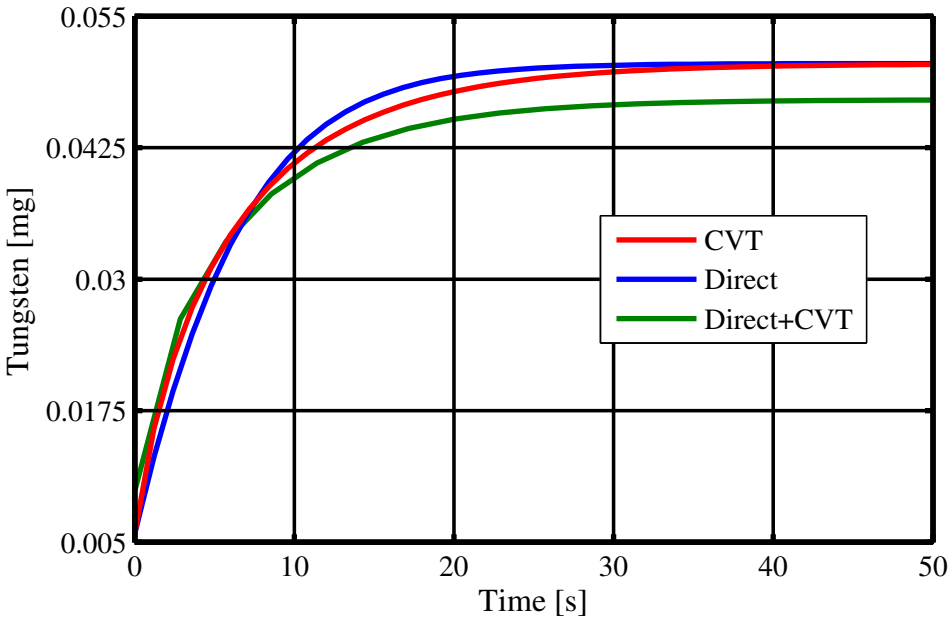

Figure 6.1.4: Isothermal formation of tungsten per particle under humid conditions through three different schemes.

The main purpose of describing the tungsten dioxide reduction via CVT is to capture morphology changes. Although closeness of the three different predictions of fig. 6.1.4, the following fig. 6.1.5 shows different radial distributions of porosity for the direct and the combined (direct + CVT) predictions. Thus, fig. 6.1.5 shows the instantaneous representation of the radial distribution of porosity inside a tungsten agglomerated particle after complete reduction.

As expected, in a direct reduction implementation case, there is no transport of tungsten atoms; and therefore, the tungsten distribution along the particle is uniform. When volatilization is present, tungsten atoms are transported in the form of gaseous compound across the particle. The highest impact on the morphology characteristics seems to occur when the two mechanisms are equally present. As depicted in fig. 6.1.6, the higher porosity at the surface of the particle could be attributed to a lower deposition rate of tungsten.

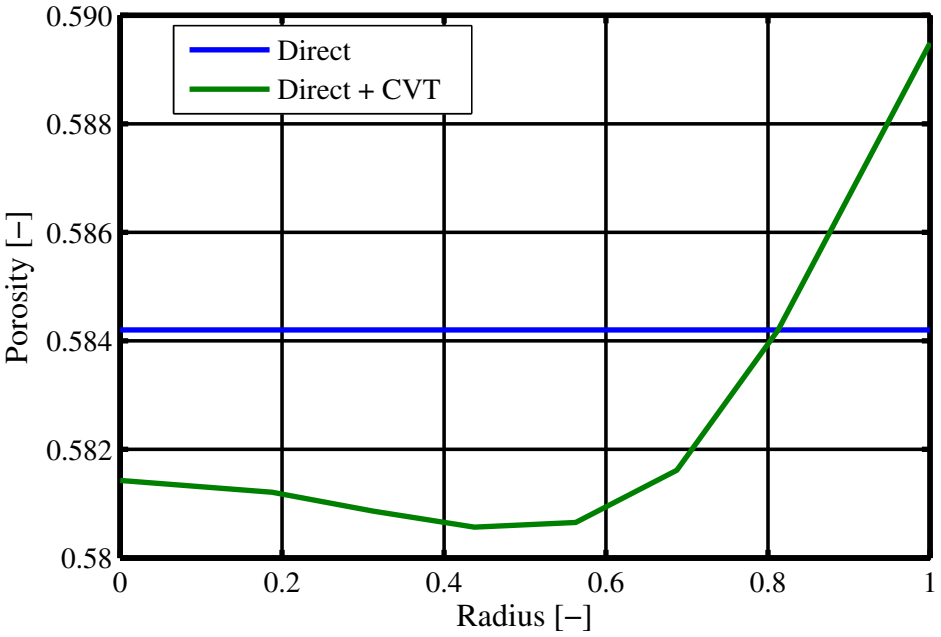

Figure 6.1.5: Intra-particle porosity after a complete tungsten dioxide reduction, following the two studied reduction schemes.

Otherwise, higher volatilization-deposition rates at the center of the particle are attributed to higher vapour concentrations.

Additionally, grain size prediction can also be obtained, but such predictions are documented in a further section 6.2.4.

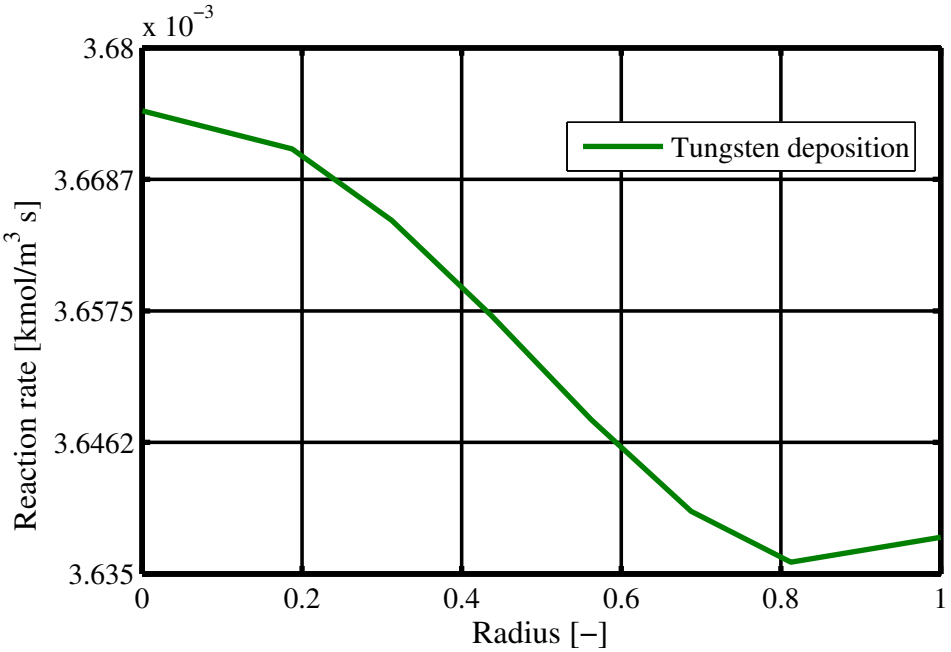

Figure 6.1.6: Instantaneous intra-particle profile of tungsten deposition at 50 s.

6.2 The hydrogen reduction of tungsten dioxide under industrial conditions

6.2.1 Introduction

The aim of this part of the investigation is to apply the XDEM model to the industrial reduction of tungsten dioxide. WO_2 is rarely traded as starting material for tungsten production; nevertheless, the reduction from $WO_2 \rightarrow W$ is the dominant step during tungsten production (section 2.2.2) and it is believed to govern the final tungsten powder grain size characteristics. Thus, in this section, predictions for tungsten dioxide reduction in a laboratory scale furnace is presented and discussed. Results are compared to experimental data obtained from the laboratory furnace located at the research facility of CERATIZIT Luxembourg S.à r.l.

6.2.2 Experimental description and numerical model

Figure 6.2.1 graphically depicts the internal dimensions of the furnace facility and the employed experimental boat. The internal radial-dimensions of the employed lab-furnace correspond to those of the push-type furnace of the production plant. The atmospheric conditions that powders experience along the production furnace are reproduced by an advanced control-software capable of varying the inlet gas flow and composition, internal temperature, pressure and humidity. Thus, the facility is capable of replicating almost all the eventualities that WO_X powders may undergo upon industrial reduction.

The powder employed for this part of the study, a blue/brown WO_2, was prepared by CERATIZIT Luxembourg S.à r.l. prior to the reduction experiments. Experiments were carried out intending to maintain a homogeneous reduction over the whole powder bed. For this, it was employed an acceptable amount of powder to produce reliable measurements and yet prescribe homogeneous conditions. Several preliminary experiments were performed to find out the region of the boat in which homogeneous reduction was possible. The homogeneous zones were identified after reduction by performing oxygen content measurement of the samples at different positions along the boats. As a result of these preliminary experiments, and as schematised in fig. 6.2.2, the sample powder was only located along less than half of the boat's length. This matches with a region where uniform temperature within the furnace was ensured. Each of the final experimental tests were repeated three times under non-isothermal conditions with similar heating rates but up to two different maximum temperatures. However, as shown in fig. 6.2.3 all the reduction experiments were carried out with the same temperature conditions because the complete

reduction was achieved before reaching the higher temperature. The experiments, were labeled as *Ref.289* and *Ref.293*, with maximum inlet temperature of 900 °C and 1000 °C respectively.

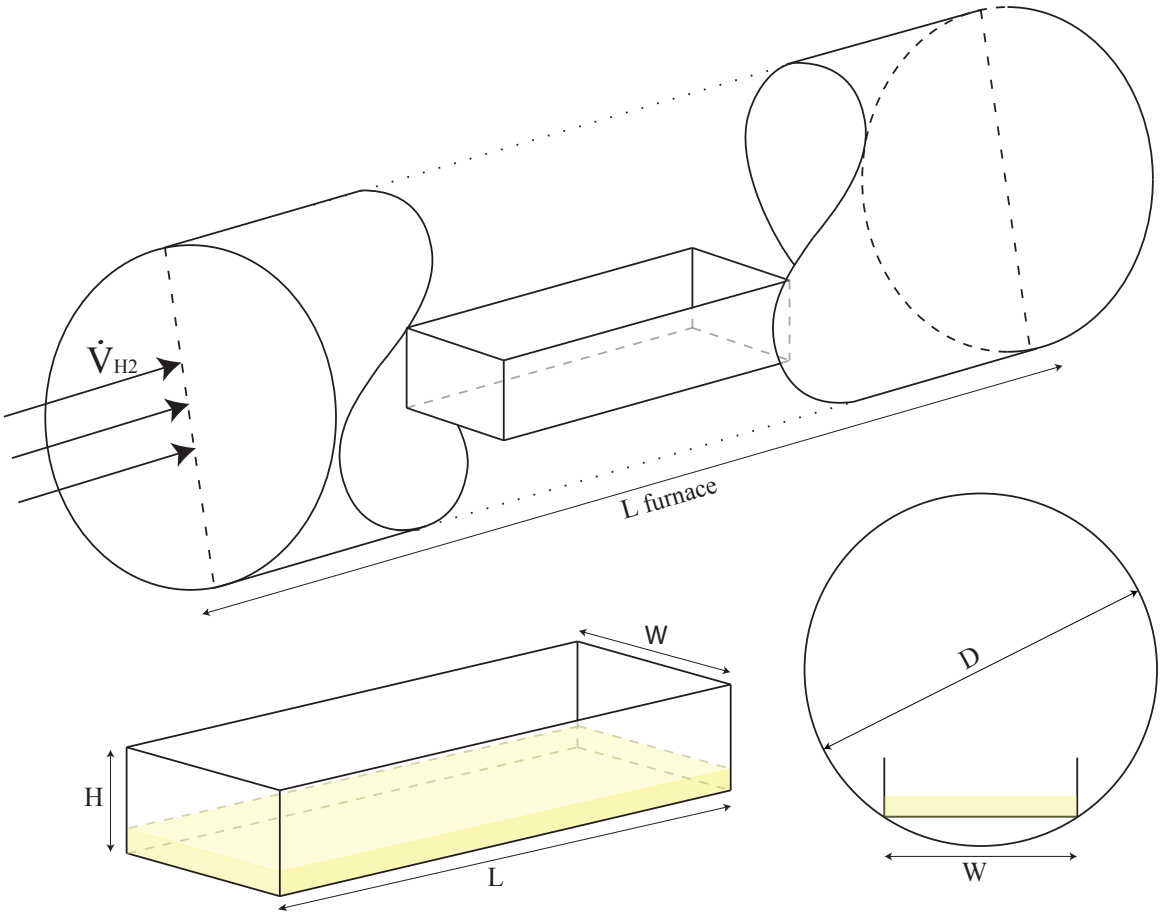

Figure 6.2.1: 3D graphical representation of furnace and experimental boat employed during WO_2 reduction experiments.

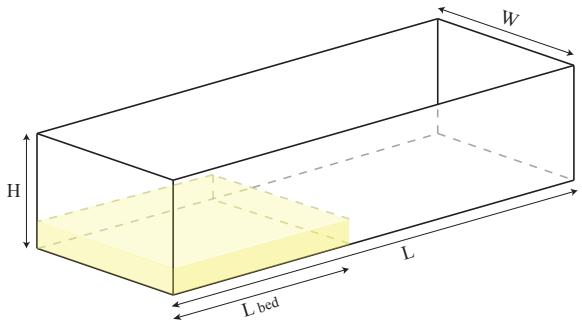

Figure 6.2.2: Experimental boat with powder.

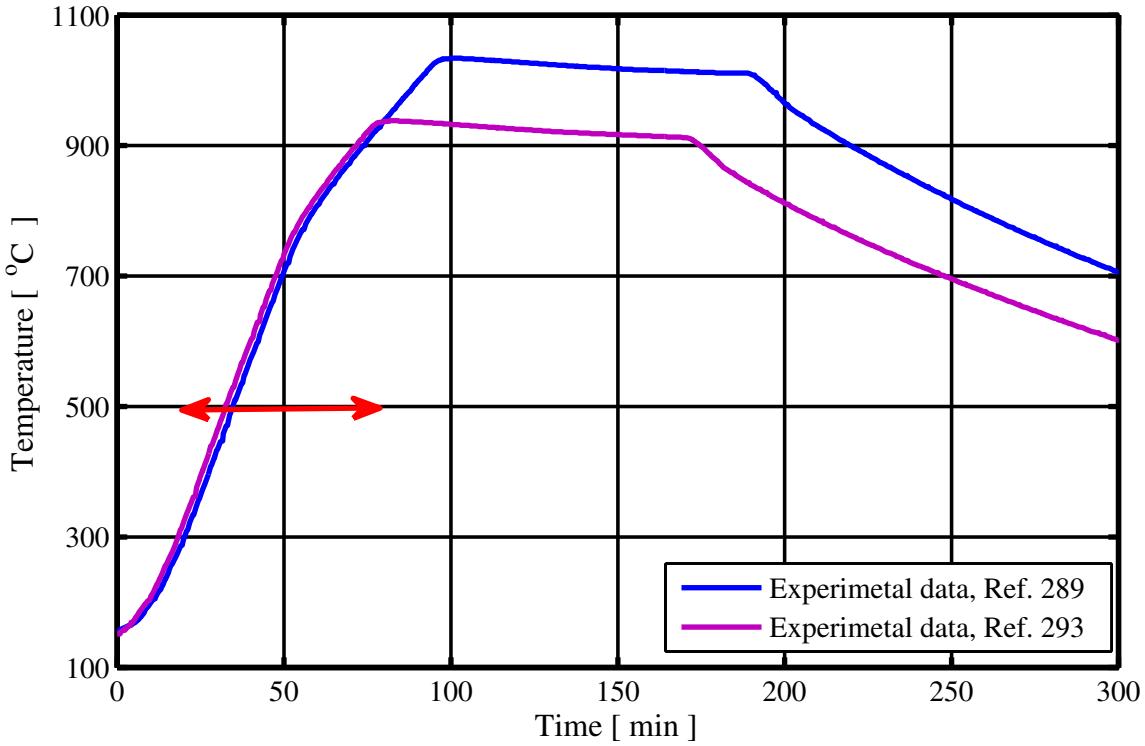

Figure 6.2.3: Time evolution of the inlet temperatures employed during the reduction experiments. The red double-arrow represents the range in which reductions were taking place.

Due to the exposed temperature conditions, one single simulation was performed for this part of the study because it was believed that both inlet temperature-curves (fig. 6.2.3) yield the same final results; a fact corroborated from experimental observations. Table 6.2.1 summarizes the experimental as well as the numerical setup of the above-mentioned experiments.

Table 6.2.1: Numerical properties selected during WO_2 reduction simulation.

Experimental boat setup

Gas Phase: 100% H_2				
T_f	=	fig. 6.2.3		Time varying inlet temperature
$\dot{V}$	=	15	Nm^3/s	Volumetric flow
Solid Phase: 100% WO_2				
m_o	=	50	g	Total initial mass
T_{p_o}	=	400	K	Initial temperature
R	=	35	µm	Original particle radius
L_{AP}	=	500	µm	Characteristic length (AP)
No_{AP}	=	388		Number of AP

These industrial scale simulations are performed by representing the whole problem with a slice, in the flow direction, of the geometry. The sliced setups were chosen in order to reduce computational costs and were supported by cold flow 3D simulations that showed a quasi-homogeneous flow in the crosscut plane of the boats.

6.2.3 Prediction of WO_2 reduction under industrial conditions

In order to understand the further described qualitative results, fig. 6.2.4 identifies the fluid and particles regions. The powder bed has visually been scaled 10 times in the frontal direction to provide better visualization of the powder region. Moreover, fig. 6.2.4 sketches the walls of the boat with a continuous line. The upper side has symmetry plane boundary condition (BC) applied, while the front and back planes are set as empty BC, and finally the left and right planes are inlet and outlet BC respectively.

The accuracy of the XDEM predictions for the bed temperature along the powder bed can be assessed by comparing it with direct temperature measurements. The observations of the powder temperature were achieved with an optical measurement instrument pointing to the surface of the powder bed. The experimental measurements as well as the corresponding XDEM predictions for the temperature of particles along the boat are reported in fig. 6.2.5. As it can be observed in fig. 6.2.5, the very low temperature gradients at the different locations demonstrate thermal homogeneity along the powder bed. Moreover, the comparison of the observations and the predictions in fig. 6.2.5 are in excellent agreement.

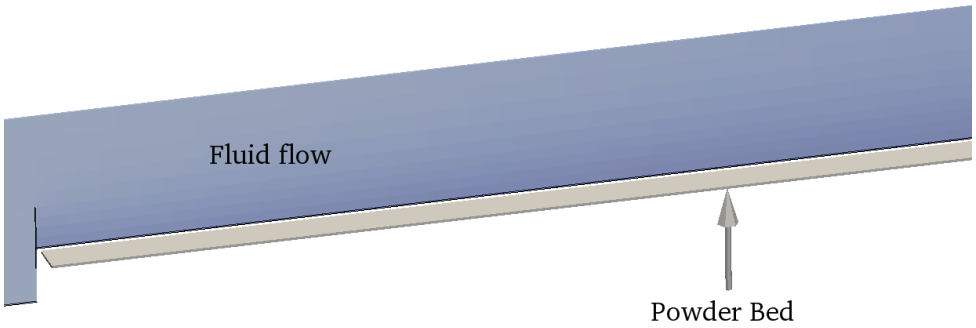

Figure 6.2.4: Numerical description of fluid and powder bed zones.

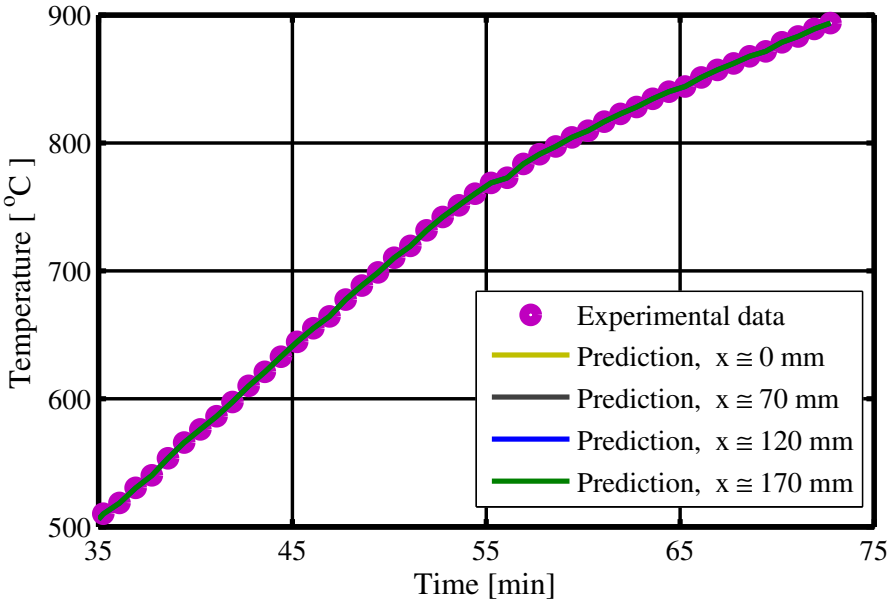

(a) Temperature comparison in the course of WO_2 reduction.

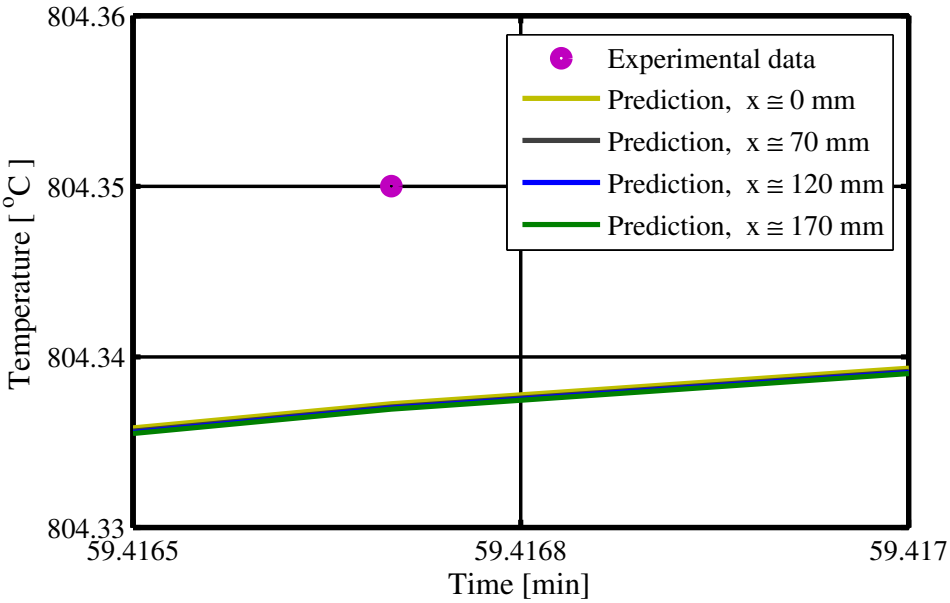

(b) Figure 6.2.5a is herein magnified at 59.4 s to observe the negligible gradients.

Figure 6.2.5: Measurement and predictions for bed temperature at different locations along the boat.

In fig. 6.2.6, especially in figs. 6.2.6c to 6.2.6e, a specific region of the bed in which the process proceeds differently than the rest of the bed is observed. A smooth reaction front starting at the beginning of the boat can be expected; nevertheless, the reaction front is affected due to the walls of the boat. These non-homogeneous profiles of figs. 6.2.6 and 6.2.7 can be qualitatively correlated to some examples of industrial reduction of TBO; where non-homogeneities are identified in the same region. Such a qualitative comparison will be discussed in the following section 6.3.

The non-uniformities are attributed to the vortex formed due to the flow resistance provided by the boat geometry to the direction of the reducing gas. A clear example of the vortex formed all along the reduction process is presented in fig. 6.2.8. There are no vortices present on the right side of the simulation because no walls were set on that side and the flow is well developed again. Despite the low profile of the employed experimental boats, a recirculation zone is present and is the direct responsible for non-homogeneity of the results (e.g. products concentration, tungsten grain size).

In figs. 6.2.9a and 6.2.9c, and more clearly in fig. 6.2.9 a small area in which the reduction starts at a higher rate is observed. This occurs due to the accumulation of the reducing gas that is brought by the vortex. However, as products start appearing, the same vortex seems to recirculate the product gases decreasing the H_2/H_2O ratio. This phenomenon generates a sort of shield that delays the reduction in the recirculation zone (see figs. 6.2.9c and 6.2.9d) until the product gases diffuse and hydrogen can continue the reduction of the remaining oxides.

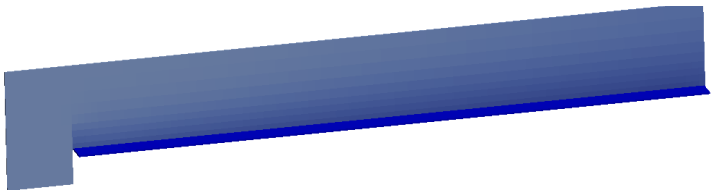

(a) Fluid temperature and tungsten production at 25 min.

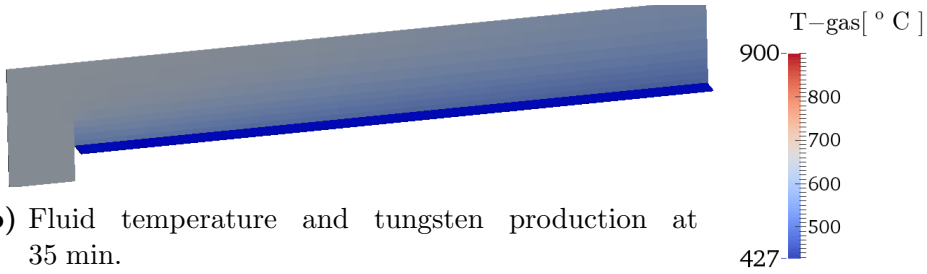

(b) Fluid temperature and tungsten production at 35 min.

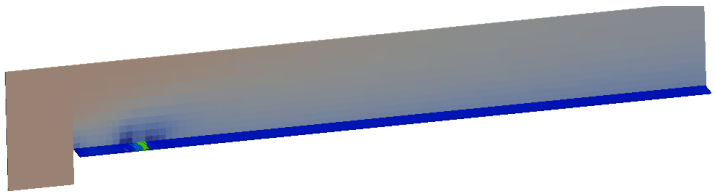

(c) Fluid temperature and tungsten production at 45 min.

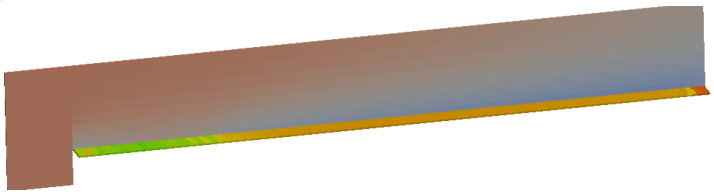

(d) Fluid temperature and tungsten production at 55 min.

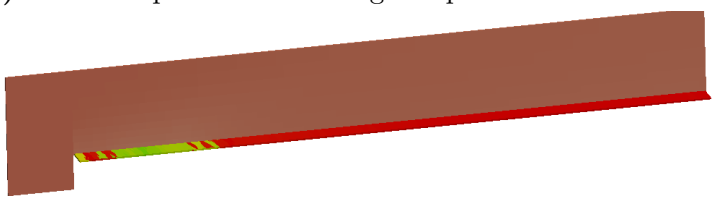

(e) Fluid temperature and tungsten production at 65 min.

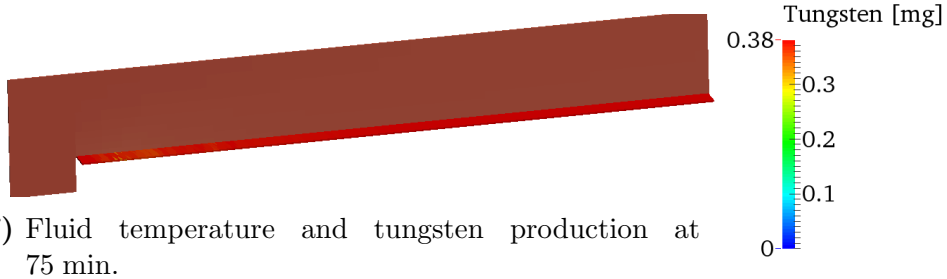

(f) Fluid temperature and tungsten production at 75 min.

(g) Fluid temperature and tungsten production at 85 min.

Figure 6.2.6: Fluid temperature and tungsten formation predictions during the industrial reduction of tungsten dioxide.

(a) Vapour in fluid and WO_2 at 25 min.

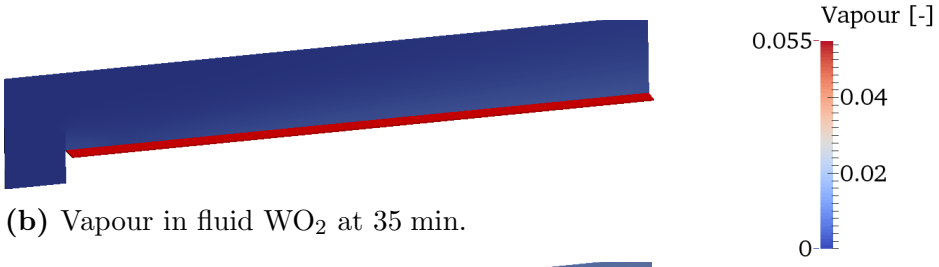

(b) Vapour in fluid WO_2 at 35 min.

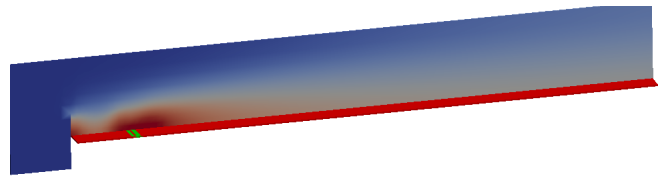

(c) Vapour in fluid and WO_2 at 45 min.

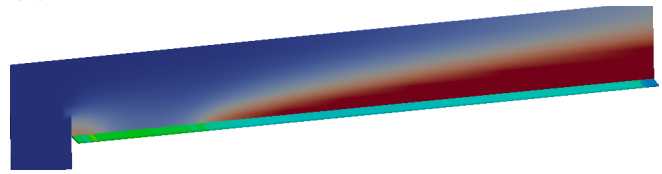

(d) Vapour in fluid and WO_2 at 55 min.

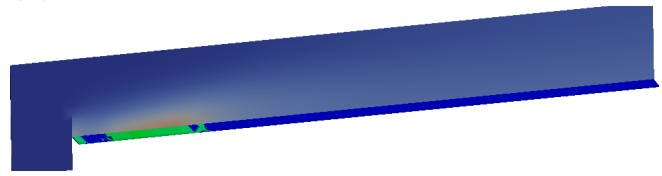

(e) Vapour in fluid and WO_2 at 65 min.

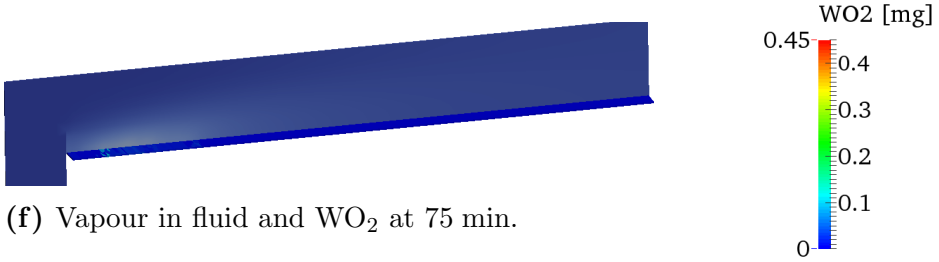

(f) Vapour in fluid and WO_2 at 75 min.

(g) Vapour in fluid and WO_2 at 85 min.

Figure 6.2.7: Water vapour in fluid phase and WO_2 consumption predictions during the industrial reduction of tungsten dioxide.

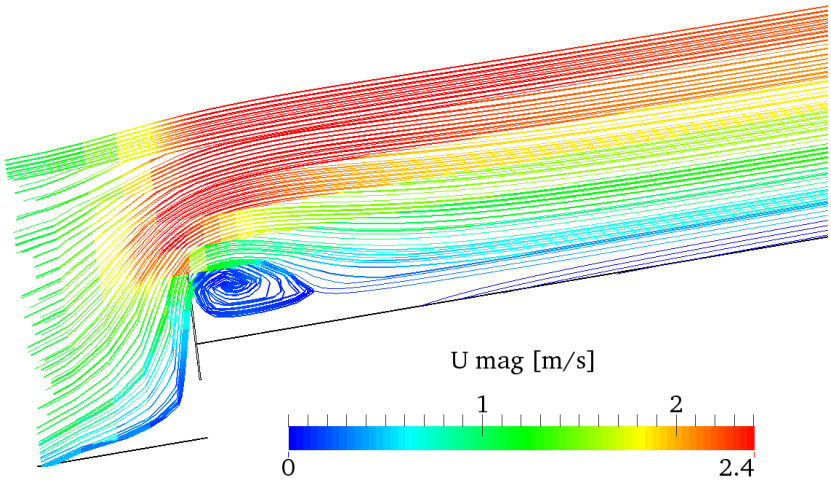

Figure 6.2.8: An illustration of the flow field as represented by streamlines during the process of hydrogen reduction of tungsten dioxide.

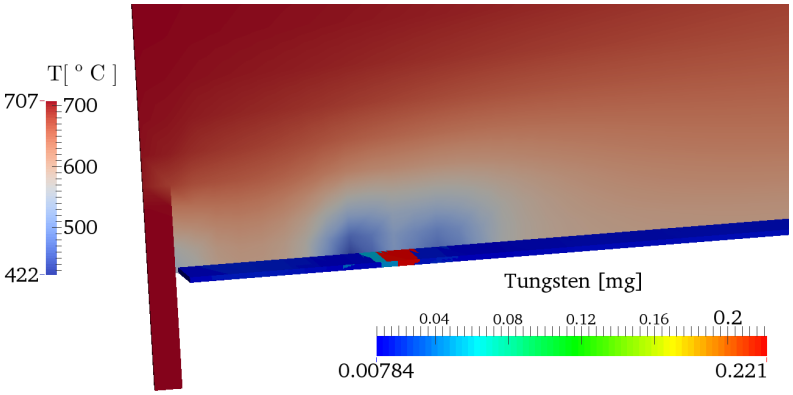

(a) Magnification of fig. 6.2.6c. Fluid temperature and tungsten production at 45 min.

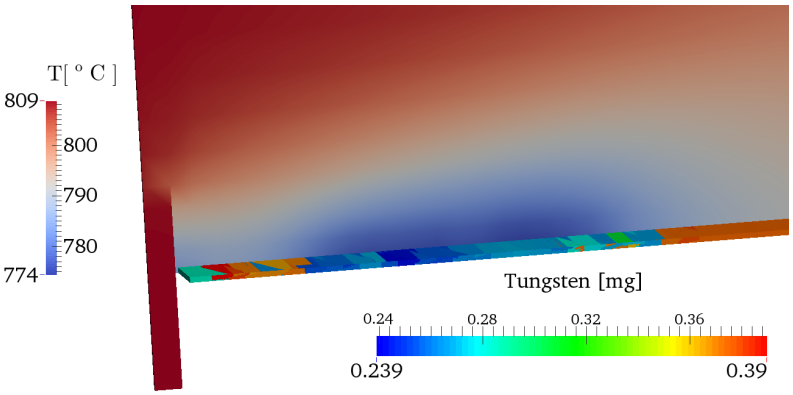

(b) Magnification of fig. 6.2.6e. Fluid temperature and tungsten production at 65 min.

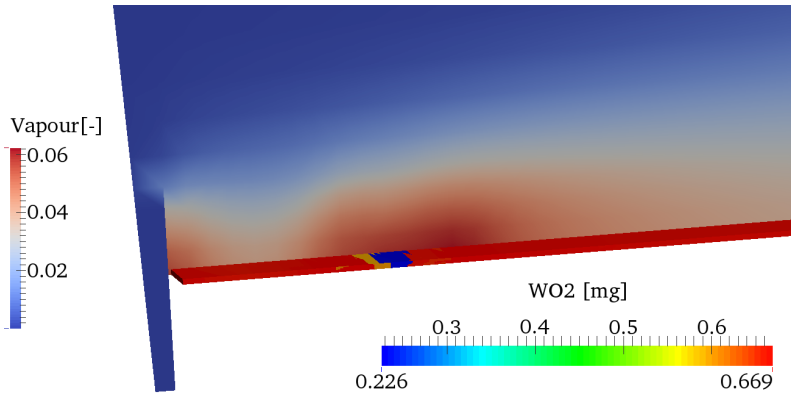

(c) Magnification of fig. 6.2.7c. Vapour in fluid and WO_2 at 45 min.

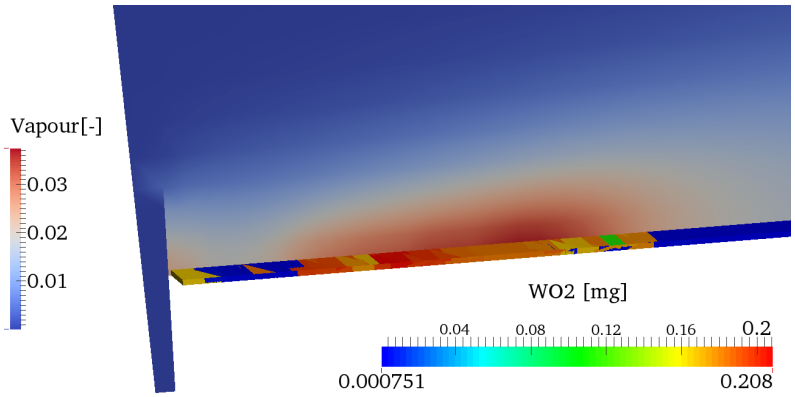

(d) Magnification of fig. 6.2.7e. Vapour in fluid and WO_2 at 65 min.

Figure 6.2.9: Magnification of interest zones during the industrial reduction of tungsten oxide.

A low water vapour retention is expected inside the furnace due to the low amount of employed powder. Hence, vapour measurements at the outlet of the furnace are believed to represent the reaction progress, to some extent, because it is assumed that water vapour leaves the powder bed as soon as it is produced. Figure 6.2.10 correlates predictions for vapour water content inside particles with the vapour partial pressure in the furnace, as calculated from the dew point measurements at the outlet of the furnace. The higher value of water vapour shown by the figure is consistent with the two dimensional representation of fig. 6.2.7d.

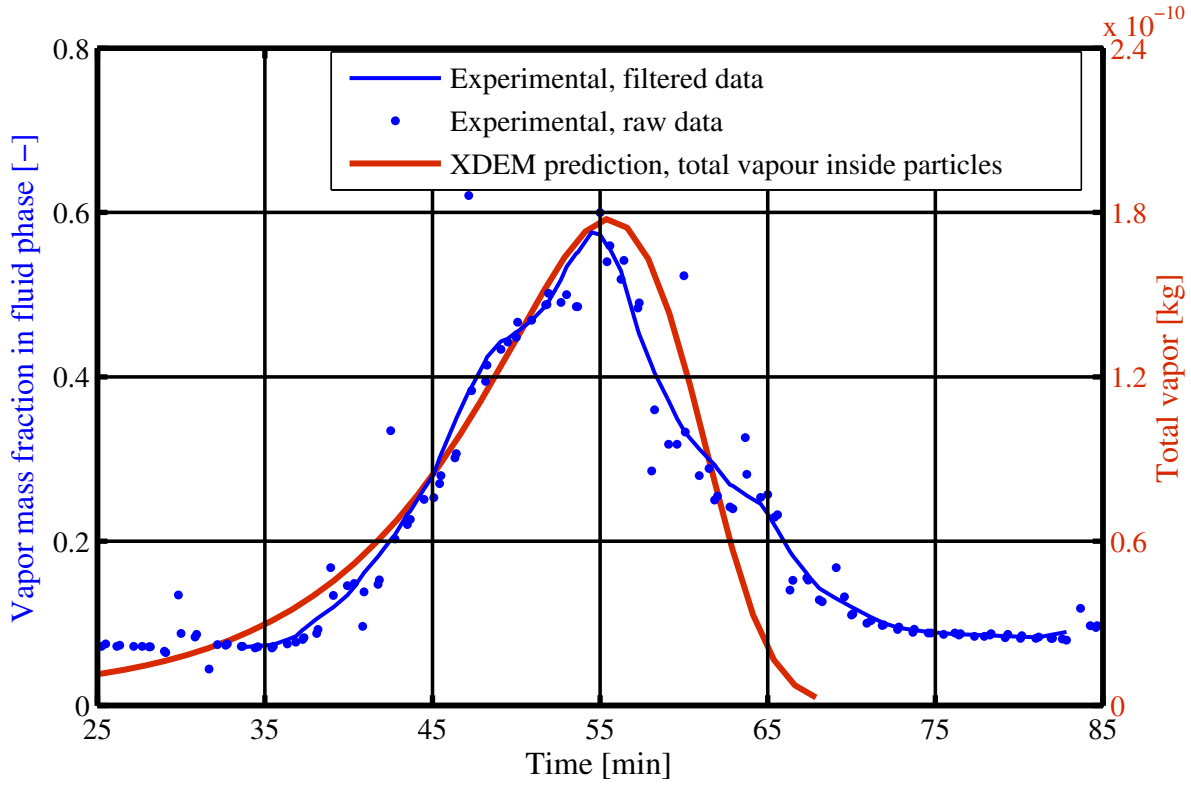

Figure 6.2.10: Comparison of water vapour within the powder bed and experimental measurements in gas outlet.

Dew point measurements on the outlet-gas can yield information of the progress of the reaction. Still, with the present reduction conditions, and due to the location of the measurement devices, a direct translation from the dew point to the water content is not evident. Following the advice of the constructor of the dew point sensor the following eq. (6.2.1) [125] was applied to estimate the water content at the outlet of the furnace. In the formula, dew point is directly related to the partial pressure of the water vapour contained in the gas, as

$$p_{\text{vapour}} = \left(1.0007 + 3.46 \times 10^{-6}\, p\right)\, 6.1121\, e^{\frac{17.502\, T_{DP}}{240.97 + T_{DP}}} \tag{6.2.1}$$

where p_{vapour} represents the water vapour partial pressure, p denotes the total pressure

in mbar and T_{DP} is the measured dew point. However, the formula is based on thermodynamics used for determining the dew point of hydrocarbons and, according to the constructor, *"it suffers from several sources of errors leading to different outputs for dew point" [126]*; and hence, the determination of water content in the furnace is impacted. Thus, fig. 6.2.10 must be seen more like a qualitative trend, which validates a quantitative time prediction for progression of the reaction as well as the total time of the reduction. Due to the impossibility on obtaining transient measurements of the consumption/formation of solid species, a quantitative comparison of the numerical model to the experimental data was let out of the scope.

From a qualitative point of view, the behavior of the predicted total vapour inside particles and the experimental measurements of fig. 6.2.10 are highly correlated. If dew point measurements are assumed as a close replica of the real reduction progress, then a *Pearson-r correlation coefficient* of 0.907, computed from the data represented in fig. 6.2.10, indicates that the XDEM prediction highly captures the reaction progress of WO_2 reduction under hydrogen atmospheres.

6.2.4 Predictions of grain size distributions under industrial conditions

Employing the kinetic model outlined in section 4.1.2.3 and previously summarized in fig. 2.2.10, predictions for grain size distribution (GSD) of each of the agglomerated particles were deduced. As any other process predicted by XDEM approaches, the sum of all the individual GSD represents the total GSD of the process. Figure 6.2.11, shows the individual GSD curves of all the agglomerated particles, where the individual distributions appear to coincide around the same grain diameter but with different distributions. This coincidence around the same mean size is due to the low bed height in the case; which provides a quasi-homogeneity that yield almost uniform nucleation conditions along the bed. The total gain size distribution is obtained by weighting the individual GSDs by the total tungsten contain in each AP

$$GDS = \frac{\sum GSD_i \times m_{W_i}}{\sum m_{W_i}} \tag{6.2.2}$$

where GSD_i and m_{W_i} denotes the grain size distribution and the tungsten mass of the agglomerated particle i, respectively.

Figure 6.2.12 shows the predicted total tungsten grain size distribution and compares it to the GSD measured from the experiment *Ref.293*. The comparison of the cumulative probability curves of fig. 6.2.12 shows an excellent agreement between prediction and

actual observations.

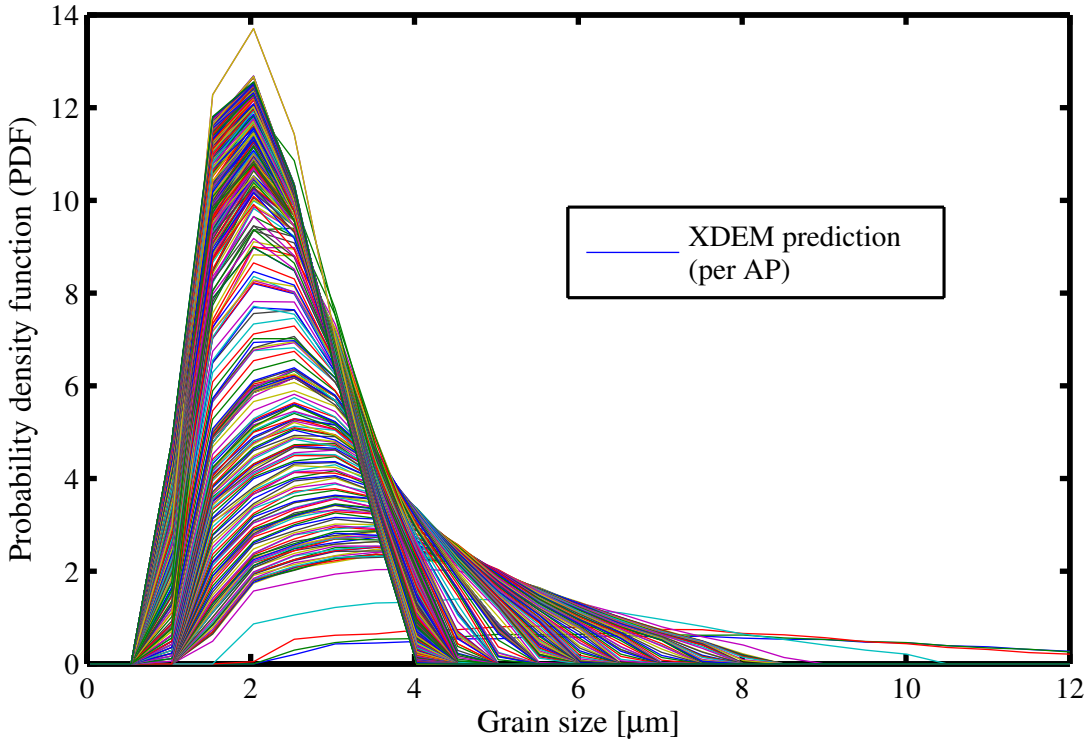

Figure 6.2.11: Grain size distribution of agglomerated particles. Each line represent the grain distribution at a given location of the bed.

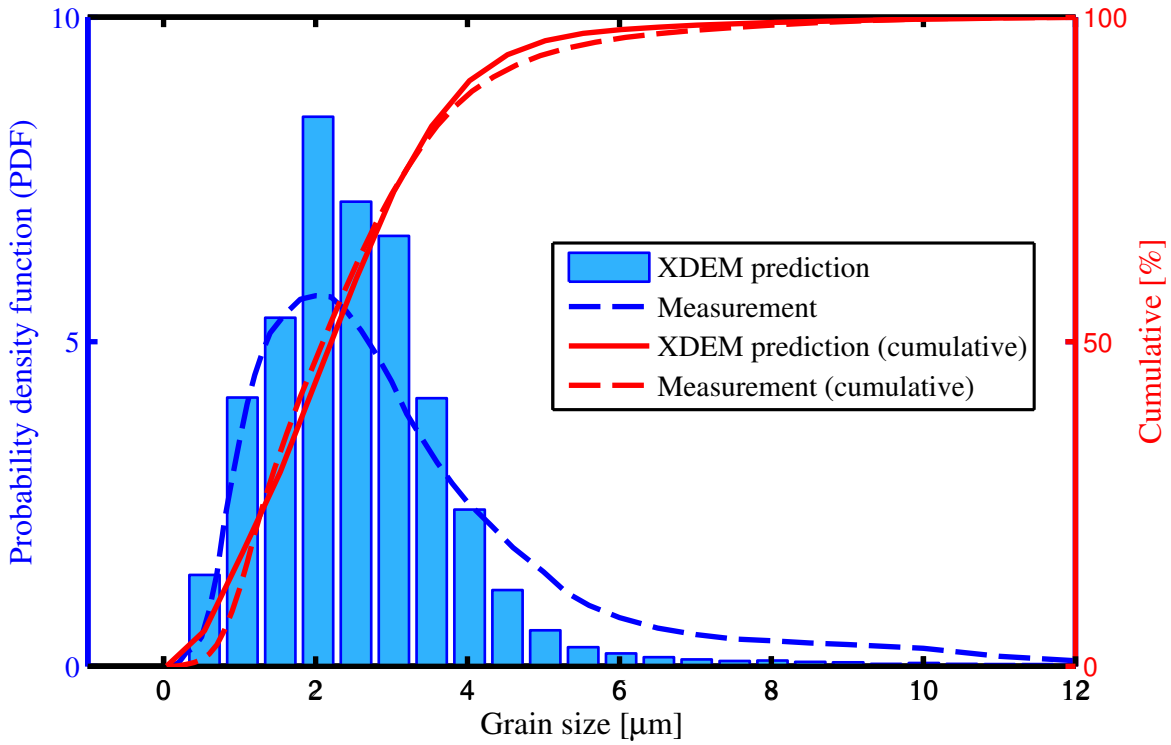

Figure 6.2.12: Grains size distribution predictions compared to experimental measurements for the non-isothermal reduction of WO_2 into metallic tungsten.

Since all instantaneous information for each particle is available during a numerical simulation, it is possible to study a chosen property in time and space. As an example, the map in fig. 6.2.13 describes the mean diameter of grains within an AP along the bed versus time. The right hand side of the figure gives an idea of the final distribution of particle sizes along the bed; information that is congruent with fig. 6.2.12. Figure 6.2.13 only shows the mean diameter of particles at specific positions without giving information of number of particles and/or a weighting function (e.g tungsten volume). Nevertheless, using the produced tungsten as a weighting function allows to perform more realistic predictions for GSD as shown in fig. 6.2.12. The time evolution of the produced tungsten in space is graphically described in fig. 6.2.13. Figure 6.2.13 also describes the evolution of the before-exposed region in which tungsten production is delayed due to the existing fluid vortex.

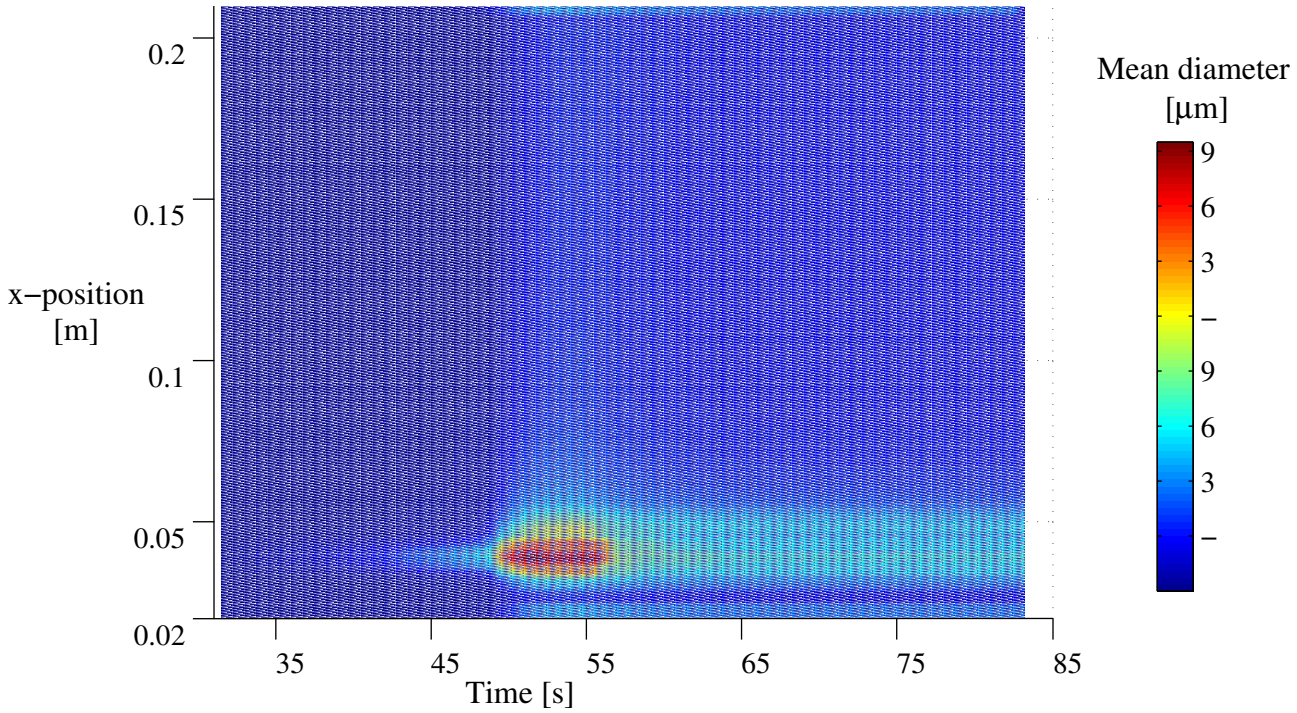

Figure 6.2.13: Time evolution map for the mean grain diameter along the powder bed.

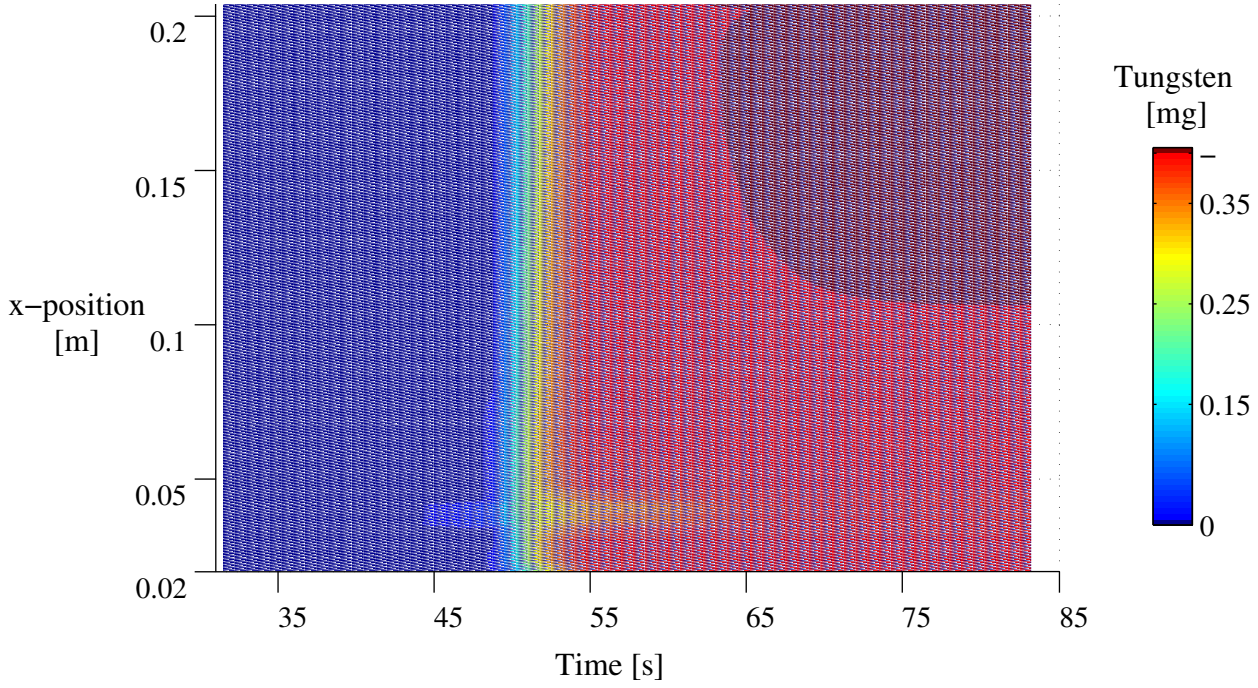

Figure 6.2.14: Time evolution map for the tungsten formation along the powder bed.

6.3 The hydrogen reduction of tungsten trioxide under industrial conditions

The results presented in this section are to be understood as an overview of the capacity of the proposed model to reproduce industrial conditions. A deeper analysis on the results

of this section is not presented due to the lack of data for comparison. In addition, due to the uncertainties in the employed data, any parametric study attempt would produce non reliable results and conclusions would be considered as conjectures.

As previously outlined in section 2.2.2, tungsten is industrially produced from ammonium paratungstate (APT). However, APT is always processed down to WO_{3-x}, or Tungsten Blue Oxide (TBO), prior to reduction into tungsten metal. Hence, WO_3 powder is considered as a starting material in this section, because it is at the head of the tungsten oxides chain.

The industrial reduction occurs in boats with higher walls than the ones previously employed in section 6.2. In order to get an overview of the model's applicability to the actual industrial conditions, a new simulation, employing an industrial boat geometry, was performed. Figure 6.3.1 shows the numerical domain representation of the herein treated case study.

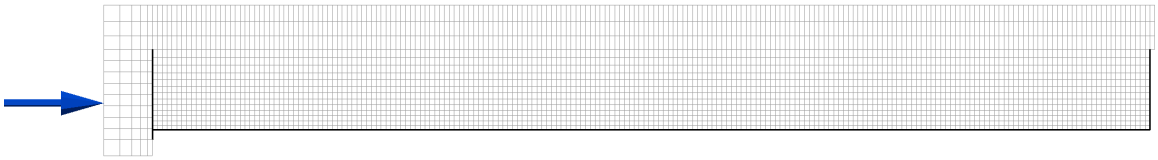

Figure 6.3.1: Numerical setup employed for the XDEM predictions of the industrial reduction of WO_3.

In this numerical case study, the boat was was filled up to 1 cm with WO_3 powder particles. The characteristics employed during this simulation are summarized in table 6.3.1.

Table 6.3.1: Numerical properties selected during WO_3 reduction simulation

Experimental boat setup				
Gas Phase: 100%, H_2/H_2O				
T_f	=	1000	°C	Temperature
$\dot{V}$	=	15	Nm^3/h	Volumetric flow
Solid Phase: 100% WO_3				
m_o	=	850	g	Total initial mass
T_{p_o}	=	1000	°C	Initial temperature
R	=	35	µm	Original particle radius
L_{AP}	=	1	mm	Characteristic length (AP)
No_{AP}	=	4100		Number of AP
Boat's characteristics: See fig. 6.2.2 .				
H_{powder}	=	10	mm	Powder bed height
L_{powder}	=	L_{boat}	mm	Powder bed length

Figure 6.3.2, exemplifies different stages of the industrial reduction of TBO-loaded boats after a programmed halt and cool down. The picture was obtained after extracting all the boats from the interior of the stopped industrial push-type furnace; which was undergoing TBO reduction. In the circled zone, an initial tungsten formation in the vortex zones is observed. Moreover, it is shown that on the frontal wall close-zones of the boats reaction proceeds slower than in the following region of the boat.

The above-mentioned vortex zones can be identified with the simulations performed in this section; hence, fig. 6.3.3 shows a vortex formation zone at the inlet region of the boat.

Figure 6.3.2 intends to present a qualitative, but realistic, comparison to an XDEM simulation. The conditions in which the experimentation was run are unknown. Nevertheless, the simulation was performed using the conditions of table 6.3.1, which describes characteristics close to the industrial conditions. Figure 6.3.4 presents the simulation results of tungsten trioxide undergoing reduction in a laminar stream of hydrogen. Figure 6.3.4 describes the reduction extend by total mass representation. The color-bar, for total mass representation, has been set close to the actual color change of tungsten oxides as described in [13]. Hence, it is possible to have a perception of the extent of the reduction. Moreover, the behavior of the produced vapour may also be observed in fig. 6.3.4. The simulation shows how water vapour accumulates in the corners of the boat. This singularity may re-oxidize, volatilize and redeposit the fresh formed tungsten grain into coarser grains. A clear fact is that the high vapour content at the corner of the boats delays reduction at those locations because it decreases the H_2 to H_2O ratio. The effect of such a delay can be observed in fig. 6.3.5, where the profile of the total formed tungsten is described.

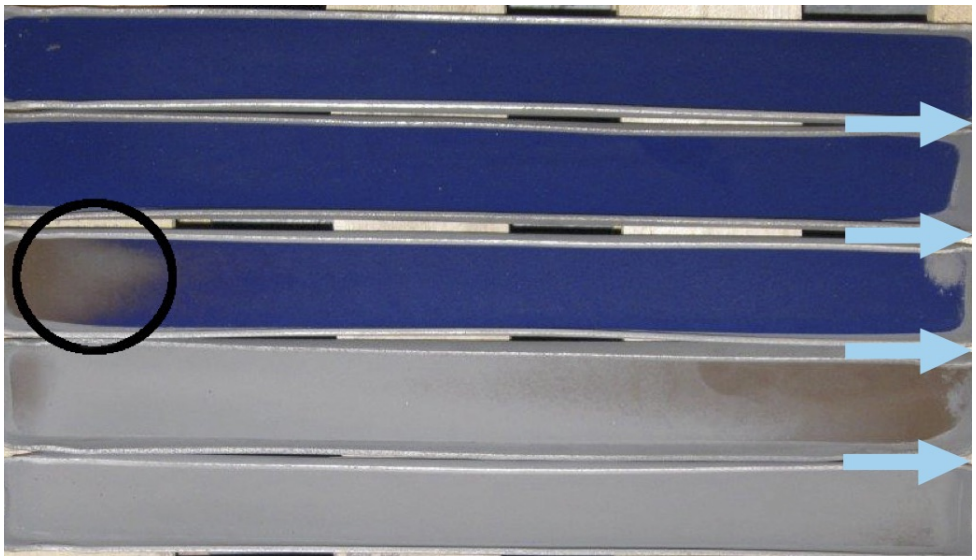

Figure 6.3.2: Non-homogeneities identified at the flow-front of the boats during industrial reduction of TBO. Source: CERATIZIT Luxembourg S.à r.l.

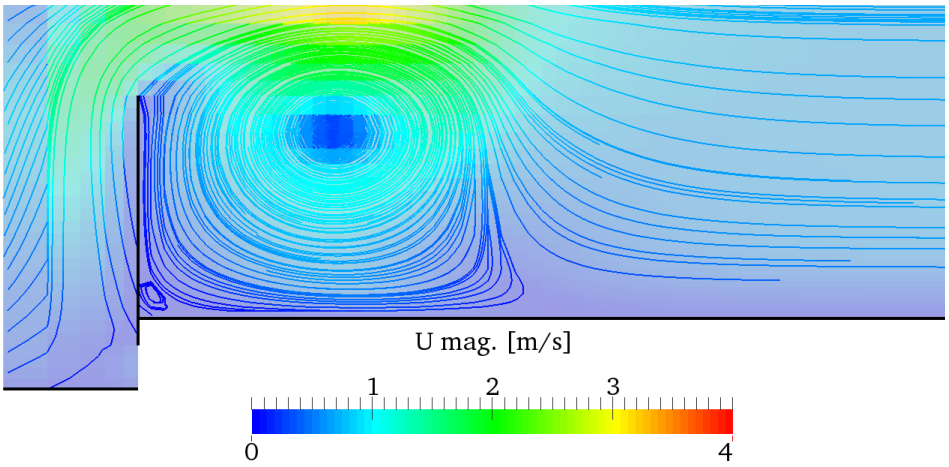

Figure 6.3.3: Example of a vortex formation at the corner of a boat employed for tungsten production as predicted using potential flow theory.

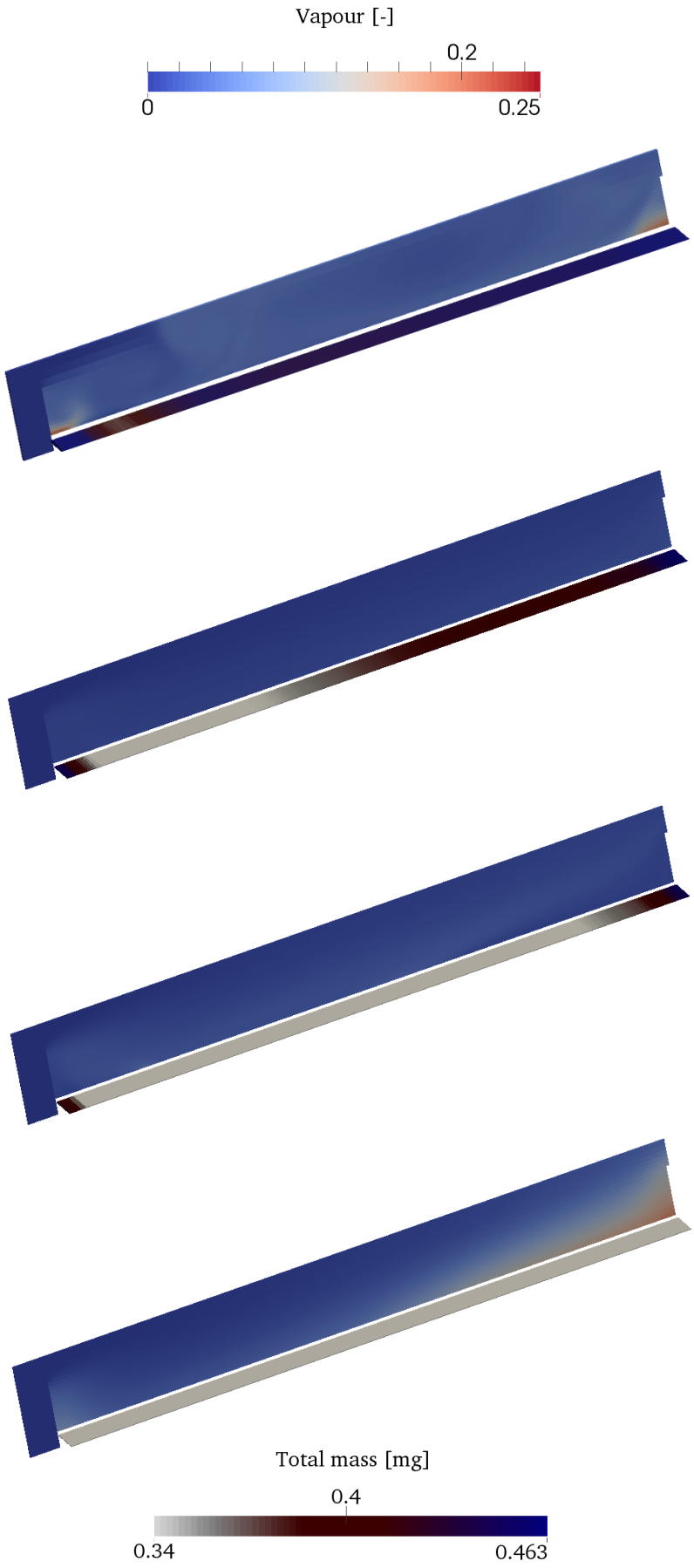

(a) 100 s.

(b) 350 s.

(c) 450 s.

(d) 550 s.

Figure 6.3.4: Water vapour and total mass of the powder bed, during the industrial reduction of WO_3, as predicted by XDEM.

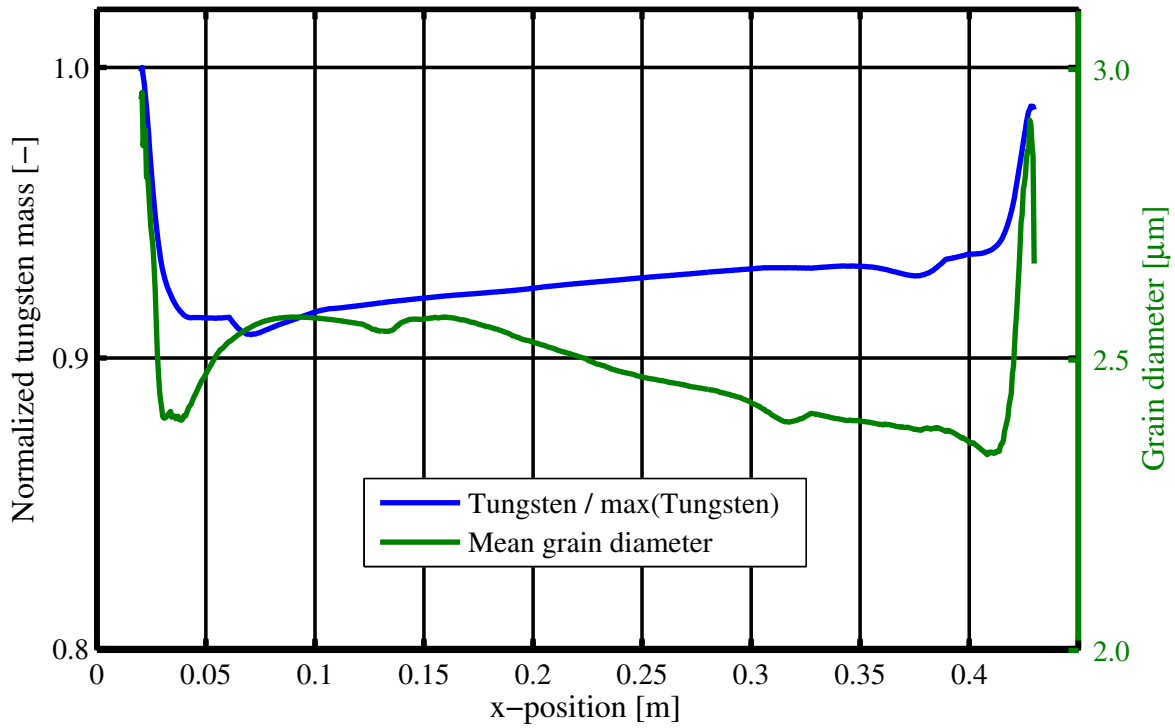

Figure 6.3.5: Predictions for tungsten content and grain diameter across a bed of powder after complete reduction from WO_3.

6.4 Conclusions on the prediction of industrial reduction of WO_X

As previously discussed in sections 6.2 and 6.3, the *Tungsten Transport Mechanism* combined with the direct reduction of tungsten dioxide offers a viable kinetic model to predict the grain size progression of tungsten powder production. This was proven by comparison of predictions with experimental data in section 6.2. It has to be reminded that the experimentation was performed under dry and quasi-homogeneous conditions; which are believed to have little influence on the volatilization and further grain growth. However, grain growth occurs and is reflected in the experimental as well as in the simulation results section 6.2.4.

The effect of humid atmospheres on grain size distribution was simulated by increasing the water vapour concentration at the inlet of the presented cases, but the results were not included into this work because of the lack of experimental data for accuracy assessment. Nevertheless, all the industrial simulation results show that the sharp corners of the boats directly influence the gas flow and, along with it, the grain growth.

Chapter 7

Conclusion and outlook

... and the cheese is eaten !

B. Peters

This research project was conducted to yield a multiscale and multi-physics simulation framework that helps understanding the complex phenomena involved in the tungsten oxide powder reduction at the onset of formation of tungsten metal.

Tungsten powder is employed in numerous applications for which the quality is governed by the tungsten grain size and its distribution. Hence, finding new WO_X reducing techniques is not anymore an exclusively experimental option involving complex and very expensive laboratories. The herein developed XDEM model represents an important advance in this direction. Due to the recent computational advances and this work, the hard metal industry can benefit from the first numerical tool of this type; which is capable of predicting the spatial, temporal and morphological progression of tungsten powder production and all the other thermochemical species of the processes.

The proposed numerical model, referred to as a multiscale model with focus on tungsten grain growth, employs and generates information at different size scales. At the molecular scale the tungsten oxide reduction processes are represented by two different kinetic mechanisms that describe the solid state conversion, volatilization and deposition of tungsten oxides and metallic tungsten. At a particle level, the predictions include detailed information about temperature and species distribution allowing determining local and instantaneous state. At the same level, grain size distribution is predicted by a deterministic model based on nucleation and volatilization/deposition reaction rates. At the powder bed scale the coupled CFD-DEM model gives information of concentration and flow of gaseous species and heat and mass transfer phenomena occurring during the process.

The reliability of the method was exhaustively tested by comparing predictions with several results from literature, which treat the hydrogen reduction of tungsten oxides at laboratory scale. Isothermal and non-isothermal experimentation was employed for validating the approach in both, qualitative and quantitative, forms. The predicted results were found to be in excellent agreement with the published data for mass loss upon reduction. Thus, it was shown that the XDEM model is a tool to investigate the transient and spatial progress of the reduction of tungsten oxide processes, at both, microscopic and macroscopic levels; which may be valuable for the PM industry.

The high correlation between industrial experiments and the simulations presented in section 6.2 proves that the model is capable of reproducing the complex phenomena appearing during the industrial production of tungsten powder. This fact is stressed by the excellent agreement for temperature prediction and observations performed upon the same study.

A clear advantage of the proposed model is that all aspects of fluid transport, gas penetration into the bed, gas diffusion in the pores of particles and chemical reaction are considered. The high level of the obtained and detailed information omits, to some extend, empirical correlations thereby making the model independent of any particular experimental conditions.

Heuristic algorithms were coupled to XDEM to obtain the missing link of the kinetic chain that represents the tungsten transport mechanism. In section 6.1, the applicability of the numerical tool with optimization algorithms to obtain the kinetics of the volatilization of tungsten oxides undergoing reduction was shown. The proposed multiscale and comprehensive model, in addition to fluid dynamics, takes into consideration the volatilization rate at the reaction sites of the porous oxide particles by including a micro-scale and an intrinsic reaction principle into the single particle model. Therefore, the kinetic parameters that are obtained with the help of XDEM may be assumed as it would be obtained from a reaction determining setup, in which the model parameters reflect the pure chemical dynamics of the process.

The uncertainty on the available kinetic parameters for tungsten volatilization is still a barrier for a reliable representation of the *Tungsten Transport Mechanism*. Therefore, results, for the reduction of tungsten trioxide under real industrial conditions, were presented more in a qualitative way that proofs the capacity of the model to deal with industrial WO_X reduction problems. Hence, the data employed and delivered, in this part of the work, has to be understood as a non-definitive data and it is suggested an exhaustive study into the volatilization-deposition processes in future work. Nevertheless, the herein presented results anticipate that the developed model may provide important breakthroughs for the powder metallurgy industry.

Recommendations for future work

In order to reduce computational costs, geometry simplifications, which neglect the effect of the front and back walls, were performed. Such simplifications were supported by cold flow 3D simulations. Nevertheless, it is believed that in the wall regions some higher concentrations of water vapour may occur and its impact should be evaluated. To reduce the high computational cost of a 3D simulation, the implementation of a full parallelization of the coupled CFD-DPM software is suggested.

The following are suggestions that have to be considered for further development and assessment of the nucleation and grain growth mechanism

- More experimental research has to be carried out to obtain complete information

that leads to more accurate kinetic parameters for the volatilization and deposition of tungsten oxides.

- Modeling and analyzing the impact of homogeneous nucleation, or nucleation proceeding directly from the gas phase.
- During reduction particles may grow and therefore local porosities may be affected. Thus, swelling and further rearrangement of particles is a phenomenon to evaluate.
- Study and evaluate stochastic models for describing nucleation phenomenon.

In order to reduce computational costs without sacrificing accuracy, a reduced method, herein named Agglomerated Particle Method was developed and successfully validated. Its implementation was possible due to the assumptions performed according to the nature of the treated processes. Nevertheless, it is believed that the novel technique could be extended to almost all the processes addressed by the eXtended Discrete Element Method. Thus, the following work packages are suggested for larger employability of the APM:

- In section 5.5.2 it was shown that the irregular shape of the CFD cells induce error in the predictions. Hence, different AP shapes have to be employed to solve larger variety of bed domains.
- In agglomerating or parceling methods, the volume change of the original particles (shrinkage/swelling) is lost. One viable solution to yield particle volume changes is to combine the presented APM with Representative Particle Methods.
- Common granular media applications, including powder metallurgy processes, may involve movement of particles. Thus, the dynamics of the agglomeration of particles or parcels of particles has to be studied for integrability with the current APM approach.
- Treatment of different materials within a same unit cell. The current reduced method considers an effective material per AP; however, different materials may be found in a parcel of particles.

Bibliography

[1] Lassner E, Schubert WD, Tungsten: Properties, Chemistry, Technology of the Elements, Alloys, and Chemical Compounds, 1st Edition, Plenum Publishers, 1999.

[2] Mannesson K, WC Grain Growth During Sintering of Cemented Carbides, Phd. dissertation, Royal Institute of Technology, Stockholm, Sweden (2011).

[3] EPMA (Ed.), Lectures on Powder Metallurgy of Hardmetals, European Powder Metallurgy Association, Shrewsbury, UK, 1995.

[4] Yamamoto H, The Relationship Between the Lattice Strains of WO3 and the Characteristics of W After Reduction., Nippon Tungsten Review 9 (1976) 1–7.

[5] Luidold S, Antrekowitsch H, Hydrogen as a Reducing Agent: State-of-the-art Science and Technology, J Miner Met & Mater Soc 2 (June) (2007) 20–27.

[6] Lackner A, Filzwieser A, Paschen P, Köck W, On the Reduction of Tungsten Blue Oxide in a Stream of Hydrogen, International Journal of Refractory Metals and Hard Materials 14 (1996) 383–391.

[7] Venables D, Brown M, Reduction of Tungsten Oxides with Hydrogen and with Hydrogen and Carbon, Thermochimica acta 285 (1996) 361–382.

[8] Wu XW, Luo JS, Lu BZ, Xie CH, Pi ZM, Hu Mz, Xu T, Wu GG, Yu ZM, Yi DQ, Crystal Growth of Tungsten During Hydrogen Reduction of Tungsten Oxide at High Temperature, Transactions of Nonferrous Metals Society of China 19 (2009) 785–789.

[9] Yuping N, Daixuan S, The Reduction Mechanism of Blue Tungsten Oxide by Hydrogen, Modern Developments in Powder Metallurgy 17 (1985) 15–19.

[10] Zhiqiang Z, Chungliang Q, Enxl W, Yuhua C, PM Research Institute, H2-Reduction Dynamics of Different Forms of Tungsten Oxide, International Journal of Refractory Metals and Hard Materials (1988) 57–60.

[11] Zou Z, Wu E, Tan A, Qian C, Formation of Tungsten Blue Oxide and its Hydrogen Reduction, 11 th International Plansee Seminar'85, (1985) 337–348.

[12] Williamson E, Yao N, Tungsten Oxide Nanorods: Synthesis, Characterization and Application, Nanotechnology in Catalysis 9 (2007) 115–137.

[13] Weil M, Schubert WD, The Beautiful Colours of Tungsten Oxides, Tungsten (2013) 1–12.

[14] Wu C, Preparation of Ultrafine Tungsten Powders by In-situ Hydrogen Reduction of Nano-needle Violet Tungsten Oxide, International Journal of Refractory Metals and Hard Materials 29 (6) (2011) 686–691.

[15] Haboury R, Pal U, Zink P, Gopalan S, Basu S, Study of an Energy Storage and Recovery Concept Based on the W/WO3 Redox Reaction: Part I. Kinetic Study and Modeling of the WO3 Reduction Process for Energy Storage, Metallurgical and Materials Transactions B 43 (4) (2012) 1001–1010.

[16] Kamberovic Z, Raic K, Filipovic M, Andic Z, Korac M, The Mechanism and Kinetics of the Tungsten (VI)-Oxide Rreduction in a Vertical Tube Reactor, Metalurgia International 17 (2012) 8–13.

[17] McKewan WM, Kinetics of Iron Oxide Reduction, Transactions of the Metallurgical Society of AIME (1960) 2–8.

[18] Bustnes JA, Sichen DU, Seetharaman S, Application of a Nonisothermal Thermogravimetric Method to the Kinetic Study of the Reduction of Metallic Oxides: Part II. A Theoretical Treatment of Powder Bed Reduction and its Application to the Reduction of Tungsten Oxide by Hydrogen, Metallurgical Transactions B 24 (3) (1993) 475–480.

[19] Milshtein JD, Gratz E, Basu SN, Gopalan S, Pal UB, Study of the Two-step W/WO3 Solar to Fuel Conversion Cycle for Syngas Production, Journal of Power Sources 236 (2013) 95–102.

[20] Sato I, Obana I, Nakamura N, A Numerical Analysis of Reducing Gas in the Reduction Furnace of Steel Powder, in: MPIF (Ed.), International Conference on Powder Metallurgy & Particulate Materials, APMI international, San Diego, 2015, p. 9.

[21] Peters B, The eXtended Discrete Element Method (XDEM) for Multi-physics Applications, Scholarly Journal of Engineering Research (2013) 1–20.

[22] Peters B, Besseron X, Estupinan Donoso AA, Hoffmann F, Michael M, Mahmoudi AH, Enhanced Thermal Process Engineering by the eXtended Discrete Element Method (XDEM), Universal Journal of Engineering Science (2013) 139–145.

[23] Adema A, Yongxiang Y, Rob B, Discrete Element Method-Computational Fluid Dynamics Simulation of the Materials Flow in an Iron-making Blast Furnace, ISIJ Int 50 (2010) 954–961.

[24] Cundall PA, Strack ODL, A Discrete Numerical Model for Granular Assemblies, Geotechnique 29 (1979) 47–65.

[25] Estupinan Donoso AA, Hoffmann F, Peters B, eXtended Discrete Element Method Used for Convective Heat Transfer Predictions, International Review of Mechanical Engineering 7 (2) (2013) 328–336.

[26] Peters B, Besseron X, Estupinan Donoso AA, Hoffmann F, Michael M, Mahmoudi AH, The eXtended Discrete Element Method (XDEM) Applied to Drying of a Packed Bed, IFRF Journal (2013) 1–12.

[27] Mahmoudi AH, Hoffmann F, Peters B, Application of XDEM as a Novel Approach to Predict Drying of a Packed Bed, International Journal of Thermal Sciences 75 (2014) 65–75.

[28] Hoffmann F, Modelling Heteregeneous Reactions in Packed Beds and its Application to the Upper Shaft of a Blast Furnace, Dissertation, University of Luxembourg (2014).

[29] Mahmoudi AH, Hoffmann F, Peters B, Detailed Numerical Modeling of Pyrolysis in a Heterogeneous Packed Bed Using XDEM, Journal of Analytical and Applied Pyrolysis 106 (2014) 9–20.

[30] Peters B, Validation of a Numerical Approach to Model Pyrolysis of Biomass and Assessment of Kinetic Data, Fuel 90 (6) (2011) 2301–2314.

[31] Peters B, Thermal Conversion of Solid Fuels, WIT Press, Southampton, 2003.

[32] Peters B, Smula-Ostaszewska J, A Numerical Approach to Predict Sulphur Dioxide Emissions During Switchgrass Combustion, Chemical and Process Engineering 34 (1) (2013) 121–137.

[33] Martin C, Schneider L, Olmos L, Bouvard D, Discrete Element Modeling of Metallic Powder Sintering, Scripta Materialia 55 (5) (2006) 425–428.

[34] Estupinan Donoso AA, Peters B, Extended Discrete Element Method Used for Predicting Tungsten Oxide Reduction in a Dry-hydrogen Atmosphere, in: IJRMHM (Ed.), 10th International Conference on the Science of Hard Materials (ICSHM10), Vol. 10, Cancun, 2014, p. 2.

[35] Estupinan Donoso AA, Peters B, XDEM Employed to Predict Reduction of Tungsten Oxide in a Dry Hydrogen Atmosphere, International Journal of Refractory Metals and Hard Materials 49 (March) (2015) 88–94.

[36] Copertaro E, Chiariotti P, Estupinan Donoso AA, Peters B, Revel GM, A Discrete-continuous Approach to Describe CaCO3 Decarbonation in Non-steady Thermal Conditions, Powder Technology 275 (2015) 131–138.

[37] Estupinan Donoso AA, Peters B, Predicting Tungsten Oxide Reduction with the Extended Discrete Element Method, Advances in Powder Metallurgy & Particulate Materials (2015) 02.35–02.48.

[38] Estupinan Donoso AA, Peters B, XDEM Used for Predicting Tungsten-Oxide Reduction, in: Prof. Eugeny Kenig (Ed.), Computer Aided Process Engineering (CAPE) Forum 2015, Paderborn, DE, 2015, pp. 43–52.

[39] APMI-International, A Growth Industry Vital to Many Products, Powder Metallurgy Fact Sheet (2015) 1–3.

[40] Ramakrishnan P, History of Powder Metallurgy, Indian Journal of History of Science 18 (1983) 109–114.

[41] Lassner E, Schubert WD, Tungsten Blue Oxide, International Journal of Refractory Metals and Hard Materials 13 (1-3) (1995) 111–117.

[42] Habainy J, Nilsson C, Oxidation of Pure Tungsten in the Temperature Interval 400 C to 900 C, Master thesis, Lund University, Lund (2013).

[43] Dorantes-García V, Díaz-Reyes J, Pérez-Benítez A, Síntesis Sencilla de Oxido de Tungsteno (VI) a Partir del Filamento de un Foco, Educación Quimica (2008) 341–348.

[44] Wahlberg S, Tungsten-Based Nanocomposites by Chemical Methods, Disertation, KTH Royal Institute of Technology, Stockholm, Sweden (2014).

[45] Kobayashi A, Puric J, Microstructure and Hardness of Tungsten Coating Heat Resistant Material Produced by Means of Gas Tunel Type Plasma Spraying, Indian Journal of History of Science 38 (2009) 57–62.

[46] Christian J, Singh Gaur R, Wolfe T, Trasorras JRL, Tungsten Chemicals and their Applications, Tungsten (2011) 1–12.

[47] Seetharaman S (Ed.), Fundamentals of Metallurgy, Woodhead Publishing in Materials, 2005.

[48] Schubert WD, Lassner E, Production and Characterization of Hydrogen- Reduced Submicron Tungsten Powders - Part I: State of the Art in Research , Production and Characterization of Raw Materials and Tungsten Powders, International Journal of Refractory Metals and Hard Materials 10 (1991) 133–141.

[49] Lunk H, Ziemer B, Salmen M, Heidemann D, What is Behind 'Tungsten Blue Oxides'?, International Journal of Refractory Metals and Hard Materials 12 (1993) 17–26.

[50] Zhengji T, Investigation of Hydrogen Reduction Process for Blue Tungsten Oxide, International Journal of Refractory Metals and Hard Materials 4 (September 1989) (1989) 179–184.

[51] Colombié M, Matériaux Métalliques, 2nd Edition, Dunod, 2012.

[52] Autler SH, Hulm JK, Kemper RS, Superconducting Technetium-Tungsten Alloys, Phys. Rev. 140 (4A) (1965) A1177—-A1180.

[53] Stwertka A, A Guide to the Elements, Oxford University Press, 1996.

[54] Schubert WD, Lassner E, Production and Characterization of Hydrogen-Reduced Submicron Tungsten Powders. Part II: Controlled Decomposition of APT and Hydrogen Reduction of the Oxides, International Journal of Refractory Metals and Hard Materials 10 (1991) (1991) 171–183.

[55] Wendel J, Thermodynamics and Kinetics of Tungsten Oxidation and Tungsten Oxide Sublimation in the Temperature Interval 2001100C, Diploma work, Lund University (2014).

[56] Warren A, Nylund A, Olefjord I, Oxidation of Tungsten and Tungsten Carbide in Dry and Humid Atmospheres, Journal of Refractory Metals and Hard Materials 14 (5-6) (1996) 345–353.

[57] Sabourin JL, Yetter RA, Kinetic Mechanisms of High Temperature Tungsten Oxidation : Experimental Evaluation with Modeling, in: 45th AIAA/ASME/SAE/ASEE Joint Propulsion Conference & Exhibit, American Institute of Aeronautics and Astronautics, Denver, 2009, pp. 1–15.

[58] Greene GA, Finfrock CC, Vaporization of Tungsten in Flowing Steam at High Temperatures, Experimental thermal and fluid science 25 (2001) 87–99.

[59] Sabourin JL, Yetter RA, High-temperature Oxidation Kinetics of Tungsten-water Reaction with Hydrogen Inhibition, Journal of Propulsion and Power.

[60] Kilpatrick M, K. Lott S, Reaction of Flowing Steam with Refractory Metals III. Tungsten (1000-1700 C), Journal of the Electrochemical Society 113 (1966) 17–18.

[61] Unal C, Bohl WR, Pasamehmetoglu KO, Modeling of Heat and Mass Transfer in Accelerator Targets During Postulated Accidents, Nuclear Engineering and Design 196 (2000) 185–200.

[62] Aspinall SR, Principles Governing the Behavior of Solid Materials in Severe High Temperature Environments, Union Carbide Research Inst Tarrytown, NY, 1965.

[63] Haubner R, Schubert WD, Lassner E, Schreiner M, Mechanism of Technical Reduction of Tungsten: Part 1 Literature Review, International Journal of Refractory Metals and Hard Materials 2 (September 1983) (1983) 108–115.

[64] Haubner R, Schubert WD, Hellmer H, Lassner E, Mechanism of Technical Reduction of Tungsten: Part 2 Hydrogen Reduction of Tungsten Blue Oxide to Tungsten Powder, International Journal of Refractory Metals and Hard Materials 2 (December 1963) (1983) 156–163.

[65] Haubner R, Untersuchung der Einflüsse von geringen Konzentrationen an Alkalimetallen, Aluminium, Eisen, Nickel, Phosphor, und Silizium auf die Reduktion von WO3 zu Wolfram mit Wasserstoff, Dissertation, Technische Universität Wien, Vienna (1984).

[66] Kim S, Kim D, Seo Y, Kim YD, Chemical Vapor Transport Process in Hydrogen Reduction of Ball-milled Molybdenum and Tungsten Oxide Powders, Reviews on advanced materials science 28 (2011) 141–144.

[67] Cifuentes S, Monge M, Pérez P, On the Oxidation Mechanism of Pure Tungsten in the Temperature Range 600-800 C, Corrosion Science 57 (2012) 114–121.

[68] Schulmeyer WV, Ortner HM, Mechanisms of the Hydrogen Reduction of Molybdenum Oxides, International Journal of Refractory Metals and Hard Materials 20 (4) (2002) 261–269.

[69] Ardestani M, Arabi H, Razavizadeh H, Rezaie H, Jankovic B, Mentus S, An Investigation About the Activation Energies of the Reduction Transitions of Fine Dispersed CuWO4x/WO3x Oxide Powders, International Journal of Refractory Metals and Hard Materials 28 (3) (2010) 383–387.

[70] Matviichuk OO, Bondarenko VP, Galkov AV, Ievdokymova OV, Kinetics of Transport of WO_3 Via Gas Phase, in: Materials Science of Refractory Compounds, At Kyiv, Ukraine, National Technical University of Ukraine PI of NASU, Vol. 4, Kyiv, 2014, p. 1.

[71] Glemser VO, Haeseler RV, Uber gasförmige Hydroxide des Molybdäns und Wolframs, Zeitschrift für anorganische Chemie 3-4 (1962) 167–181.

[72] Belton G, McCarron R, The Volatilization of Tungsten in the Presence of Water Vapor, The Journal of Physical Chemistry (1964) 1852–1856.

[73] Zhengji T, Production of Submicron Tungsten Powder by Hydrogen Reduction of Tungsten Trioxide, International Journal of Refractory Metals and Hard Materials (1986) 108–112.

[74] Wilken TR, Morcom WR, Wert CA, Woodhouse JB, Reduction of Tungsten Oxide to Tungsten Metal, Metallurgical Transactions 7B (December 1976).

[75] Szekely J, Evans JW, Yong Sohn H, Gas-Solid Reactions, Academic Press Inc., London, 1975.

[76] ANSYS Inc. (US), ANSYS Fluent Theory Guide (2013).

[77] Liu S, Qiu ZJ, Thermodynamic Calculation on Reduction of Tungsten Oxide in H2 Atmosphere, International Journal of Refractory Metals and Hard Materials 26 (4) (2008) 362–366.

[78] Turkdogan ET, Olsson RG, Vinters JV, Gaseous Reduction of Iron Oxides: Part II. Pore Characteristics of Iron Reduced from Hematite in Hydrogen, Metallurgical and Materials Transactions B 2 (11) (1971) 3189–3196.

[79] Peters B, Besseron X, Estupinan Donoso AA, Hoffmann F, Michael M, Mouhadi A, The Extended Discrete Element Method (XDEM) for Multi-Physics Applications, in: Finnish-Swedish Flame Days 2013, Jyväkylä, Finnland, April 17-18, 2013, 2013, p. 9.

[80] Wikipedia, Extended discrete element method (2016).

[81] Michael M, Peters B, Vogel F, Resolution of Different Length Scales by an Efficient Combination of the Finite Element Method and the Discrete Element Method, in: Topping BHV (Ed.), Proceedings of the Eleventh International Conference on Computational Structures Technology, Civil-Comp Press, Stirlingshire, United Kingdom, 2012, p. 18.

[82] Ashraf Ali B, Borner M, Peglow M, Janiga G, Thevenin D, Coupled Computational Fluid Dynamics Discrete Element Method Simulations of a Pilot-Scale Batch Crystallizer, Crystal Growth and Design 15 (1) (2014) 145–155.

[83] Anca-Couce A, Multi-scale Approach to Describe Fixed-bed Thermo-chemical Processes of Biomass, Ph.D. thesis, Technischen Universität Berlin (2012).

[84] Man YH, Byeong RC, A Numerical Study on the Combustion of a Single Carbon Particle Entrained in a Steady Flow, Combust Flame 97 (1994) 1–16.

[85] Jiqiao L, Baiyun H, Zhiqiang Z, Determination of Physical Characterization of Tungsten Oxides, International Journal of Refractory Metals and Hard Materials 19 (2) (2001) 79–84.

[86] Faghri A, Zhang Y, Transport Phenomena in Multiphase Systems, Elsevier, 2006.

[87] Lage JL, Lemos MJSD, Nield DA, Modelling Turbulence in Porous Media, in: Ingham DB, Pop I (Eds.), Transport Phenomena in Porous Media II, 1st Edition, Pergamon, 2002, Ch. 8, pp. 198–230.

[88] Bird RB, Stewart WE, Lightfoot EN, Transport Phenomena, revised 2n Edition, John Wiley & Sons, 2007.

[89] Kansa EJ, Perlee HE, Chaiken RF, Mathematical Model of Wood Pyrolysis Including Internal Forced Convection (1977).

[90] Wakao N, Kaguei S, Heat and Mass Transfer in Packed Beds, Vol. 1, Gordon and Breach Science Publishers, New York, 1982.

[91] Achenbach E, Heat and Flow Characteristics of Packed Beds, Review, Experimental Thermal and Fluid Science 10 (1995) 17–27.

[92] Barrow GM, Physical Chemistry, 6th Edition, McGraw-Hill, Boston, 1996.

[93] Fouad NE, Impacts of Hydrogen Spillover on the Reduction Behavior of Tungsten Oxide: Isothermal and Non-isothermal Approaches, Journal of Analytical and Applied Pyrolysis 44 (1) (1997) 13–28.

[94] Hellmer H, Technische Wolframoxidreduktion: Untersuchung der Reduktionskinetik; Einfluß der Reduktionsparameter auf die Pulvereigenschaften, Dissertation, Technischen Universität Wien (1986).

[95] Fouad NE, Attyia K, Zaki MI, Thermogravimetry of WO3 Reduction in Hydrogen: Kinetic Characterization of Autocatalytic Effects, Powder Technology 74 (1) (1993) 31–37.

[96] Zaki MI, Fouad NE, Mansour S, Muftah AI, Temperature-programmed and X-ray Diffractometry Studies of Hydrogen-Reduction Course and Products of WO3 Powder: Influence of Reduction Parameters, Thermochimica Acta 523 (1-2) (2011) 90–96.

[97] Wrobel RJ, Arabczyk W, Narkiewicz U, Nucleation in a Gas-solid State Reaction, Crystal Research and Technology 47 (11) (2012) 1164–1171.

[98] Kim BS, Kim Ey, Jeon HS, Lee HI, Lee JC, Study on the Reduction of Molybdenum Dioxide by Hydrogen, Materials Transactions 49 (9) (2008) 2147–2152.

[99] González V, Guerrero C, Aguilar J, Nucleacion y Crecimiento Unidimensional. Parte I El Modelo y su Validacion, Ingenierías 5 (2002) 38–43.

[100] German RM, Grain Size Evolution and Grain Size Distribution in Sintered Materials, in: Proceedings of the Seventeenth Plansee Seminar, Plansee Seminar 2009, 2009, pp. PL5.1–PL5.12.

[101] Liu X, Song M, Wang S, He Y, Structure and Field-emission Properties of W/WO2.72 Heterostructures Fabricated by Vapor Deposition, Physica E: Low-dimensional Systems and Nanostructures 53 (2013) 260–265.

[102] Avrami M, Kinetics of Phase Change. I General Theory, The Journal of Chemical Physics 7 (12) (1939) 1103.

[103] Foundation of Computational Thermodynamics, TC-PRISMA Users Guide, Tech. rep., STT Foundation, Stockholm, Sweden (2011).

[104] Masuda H, Higashitani K, Yoshida H (Eds.), Powder Technology. Fundamentals of Particles, Powder Beds, and Particle Generation, Taylor & Francis Group, 2007.

[105] Mullin JW, Crystalization, 4th Edition, Reed Educational, 2001.

[106] Moosbrugger C (Ed.), Fundamentals of Modeling for Metals Processing, Vol. 22, ASM International, 2009.

[107] Vetter T, Iggland M, Ochsenbein DR, Hanseler FS, Mazzotti M, Modelling Nucleation, Growth and Ostwald Ripening in Crystallization Processes: A Comparison Between Population Balance and Kinetic Rate Equation, Crystal Growth and Design (2013) 4890–4903.

[108] Zobel N, The Representative Particle Model, Phd. dissertation, Technischen Universität Berlin (2007).

[109] Peters B, Besseron X, Estupinan Donoso AA, Hoffmann F, Michael M, Mahmoudi AH, Application of the Extended Discrete Element Method (XDEM) in Computer-Aided Process Engineering, in: CAPE Forum 2013 Computer Aided Process Engineering, Graz University of Technology, 2013, p. 12.

[110] Peters B, Džiugys A, Navakas R, Simulation of Thermal Conversion of Solid Fuel by the Discrete Particle Method, Lithuanian Journal of Physics 51 (2) (2011) 91–105.

[111] Langtangen H, Huston R, Computational Partial Differential Equations: Numerical Methods and Diffpack Programming, Second Edition, Applied Mechanics Reviews 56 (6) (2003) B77.

[112] OpenFoam, OpenFoam Documentation (2014).

[113] Michael M, A Discrete Approach to Describe the Kinematics between Snow and a Tire Tread, Dissertation, University of Luxembourg, Luxembourg (2014).

[114] Carslaw HS, Jaeger JC, Morral JE, Conduction of Heat in Solids, 2nd Edition, Oxford University Press, 1986.

[115] Srivastava S, Yazdchi K, Luding S, Meso-scale Coupling of FEM/DEM for Fluid-particle Interactions, Philosophical Transactions of the Royal Society 272 (2021) (2014) 1–30.

[116] Marshall JS, Li S, Adhesive Particle Flow: A Discrete-Element Approach, Cambridge Univeristy Press, 2014.

[117] Besseron X, Hoffmann F, Michael M, Peters B, Unified Design for Parallel Execution of Coupled Simulations Using the Discrete Particle Method, in: Topping B, Iványi P (Eds.), Proceedings of the Third International Conference on Parallel, Distributed, Grid and Cloud Computing for Engineering, Stirlingshire, 2013, p. 16.

[118] Gieorgieva V, Vlaev L, Gyurova K, Non-Isothermal Degradation Kinetics of CaCO3 from Different Origin, Journal of Chemistry (2013) 12.

[119] Peters B, Bruch C, Schröder E, Nussbaumer T, Measurements and Particle Resolved Modelling of Heat-up and Drying of a Packed Bed, Biomass & Bioenergy 23 (2002) 291–306.

[120] Peters B, Bruch C, Drying and Pyrolysis of Wood Particles: Experiments and Simulation, Journal of Applied and Analytical Pyrolysis 70 (2003) 233–250.

[121] Cutillas-Lozano JM, Giménez D, Determination of the Kinetic Constants of a Chemical Reaction in Heterogeneous Phase Using Parameterized Metaheuristics, Procedia Computer Science 18 (2013) 787–796.

[122] Puxty G, Maeder M, Hungerbühler K, Tutorial on the Fitting of Kinetics Models to Multivariate Spectroscopic Measurements with Non-linear Least-squares Regression, Chemometrics and Intelligent Laboratory Systems 81 (2) (2006) 149–164.

[123] Mantel T, Egolfopoulos FN, Bowman CT, A New Methodology to Determine Kinetic Parameters for 1- and 2-Step Chemical Models, Proceedings of the Summer Program (1996) 149–166.

[124] Lagarias JC, Reeds Ja, Wright MH, Wright PE, Convergence Properties of the Nelder–Mead Simplex Method in Low Dimensions, SIAM Journal on Optimization 9 (1) (1998) 112–147.

[125] Soleyn K, Dew Point Measurement in Metal Heat Treating, Heat Treating Progress 5 (2005) 54–61.

[126] MESA Electronics GmbH, Personal Communication (2016).

[127] Jiqiao L, Baiyun H, Particle Size Characterization of Ultra Fine Tungsten Powder, International Journal of Refractory Metals and Hard Materials 19 (2001) 89–99.

[128] Vollath D, Nanomaterials. An Introduction to Synthesis, Properties and Aplications, Wiley-VCH Verlag GmbH & Co. KGaA, 2008.

[129] Sarin V, Morphological Changes Occurring During Reduction of WO3, Journal of Materials Science 0 (1975) 593–598.

[130] Hirsch C, Numerical Computation of Internal and External Flows: : Fundamentals of Numerical Discretization, 1st Edition, John Wiley & Sons, 1988.

[131] Versteeg HK, Malalaskekera W, An Introduction to Computational Fluid Dynamics, 2nd Edition, Vol. M, Prentice Hall, 2007.

[132] Patankar S, Numerical Heat Transfer and Fluid Flow, in: Series in coputational methods in mechanics and thermal sciences, 1st Edition, CRC Press, 1980, pp. 1–197.

[133] Whitaker S, Transport Processes with Heterogeneous Reaction, in: Whitaker S, Cassano AE (Eds.), Concepts and Design of Chemical Reactors, Gordon and Breach,New York, 1986, pp. 1–94.

[134] Yang J, Wang J, Bu S, M.Zeng, Wang Q, Nakayama A, Experimental Analysis of Forced Convective Heat Transfer in Novel Structured Packed Beds of Particles, Chemical Engineering Science 71 (2012) 126–137.

[135] Baker MJ, CFD Simulation of Flow Through Packed Beds Using the Finite Volume Technique, Ph.D. thesis, University of Exeter (2011).

[136] Peters B, Bruch C, Schröder E, Measurements and Particle Resolved Modelling of the Thermo and Fluid Dynamics of a Packed Bed, Journal of Analytical and Applied Pyrolysis 70 (2003) 211–231.

[137] Schröder E, Experiments on the Pyrolysis of Large Beechwood Particles in Fixed Beds, Analytical and Applied Pyrolysis 71 (2004) 669–694.

Appendix A

Characterization of tungsten powders

A.1 Introduction

Within this section the aim is to review the characterisation of the different phases occurring during tungsten oxide to tungsten metal reduction process. The reduction steps are not only characterized by colour changes, but main changes in crystal morphology are also reviewed.

Precise material characterization is important to connect simulation software to the real quality of the used material in industry. Properties of all materials are influenced by their composition, structure and micro-structure and therefore, its correct characterization is extremely important for a particular preparation, study of properties, and/or for reproduction of the material.

A.2 Common PM methods of powder characterization

A.2.1 Fisher sub-sieve sizer

The Fisher sub-sieve sizer (FSSS) is generally called Average Particle Size Analysis, "Blaine" Fineness Test or "Blaine" Air Permeability Test. This is one of the most used method for characterizing the average particle size in various powder applications, such as hardmetals industry.

FSSS value is designated in two types: "as-supplied" and "laboratory-milled". The former term has no direct meaning for W agglomerated powders. However, compared to lab milled values, it may be an indicator of the agglomeration-degree. Only at a constant agglomerate size distribution the "as-supplied" value can indicate differences in the micro-morphology e.g. internal porosity.

The FSSS value is commonly used for characterizing yellow or blue oxide as well as for intermediate oxides occurring during reduction. However, according to Schubert et al. [48], for these materials the FSSS values are not really indicative of the real particle or grain sizes since the micro-porosity of the particles enables a gas flow not only between the particles, but also through particles via cracks and pores. Comparatively, Jiqiao and Baiyun [127] proved that this technique produces misleading information during ultra-fine powder characterization.

A.2.2 Laser scattering

Laser scattering is used to measure in a broadband particle sizes, ranging from 10 nm up to a few mm. Particles are irradiated by a laser beam. Subsequently, the sizes are determined from the angular intensity distribution of the observed light scattering.

Laser scattering not only exposes particle size distribution, but also the average particle size of the porous oxides. A shortcoming of this method is a partial disintegration occurring during measurement for brittle particles, because of the ultrasonic energy applied for de-agglomeration purposes.

A.2.3 Scanning Electron Microscopy (SEM) imaging

During SEM imaging, a beam of high energy electrons is addressed to a point and scanned in a "raster pattern" across the surface of the particles to be measured. The difference of energies between the collided electrons are collected and separated by different detectors to produce different signals/images of the particles being studied.

The method is considered to be the best-suited to study the shape, size and structure of fine- to nano-particles [128] and the only trustworthy one for determining the actual particle size and size distribution of tungsten oxides derived from APT [54].

A.2.4 Specific surface area method

This method is generally called BET from Brunauer, Emmett and Teller, who were the first to describe a method to measure the specific surface of powders by gas adsorption at the surface. This technique is used as standard procedure to determine specific surfaces [85].

A.2.5 Apparent density

The Apparent density is also called Scott Density. The goal is to measure the bulk density meaning the density of a weight of a certain volume of powder. The procedure requires the powder to flow freely and gently into a container of a known volume. Contrary to that, to measure the tap density, the powder is settled or packed until no further volume change is observed before weighting it.

A.2.6 Oxygen content

Schubert et al. [48] found a high correlation between BET and the oxygen content measures. Hence, for very fine grains size, the oxygen content is a consequence of surface saturation after reduction and represents the specific surface of the particles.

A.2.7 Other techniques

Others techniques not commonly found in literature are: Thermo-gravimetric analysis is used to identify the composition of the sub-oxides during reduction processes, Boer's t-method to estimate micro-pore volume, MP method for micro-pore size distribution and BJH method for meso-pore analysis.

A.3 Characterization of raw materials

The BET of a tungsten oxide depends mainly on the micro-porosity and it changes with the reduction conditions. Previous researches, done by Zhengji [73], indicated that a higher WO_X porosity was always linked to a small mean particle size of the reduced W, conversely, it depends on the production conditions. Later on, Zhengji [50] confirmed that the changes of FSSS and BET values of the oxide powders became smaller and smaller successively.

Scott density mainly depends on the particle size as on the apparent density of the agglomerated particles. Therefore, the micromorphology has a distinct influence on the Scott density and consequently on reduction behavior.

TBO is characterized chemically by impurities content, the oxygen index, the ammonia content residue as well as the homogeneity regarding the different compounds. TBO's physical characterization consists of particle size, size distribution and specific surface area measurement. Thus, due to the broad product combinations, many companies prefer to buy APT instead of buying TBO. Performing the calcination, or "blueing" process, in-house allows to ensure the uniform quality of end products, since every company has its own ideas about the optimal chemical as well as physical characteristics of TBO and such characteristics are reproducible by keeping the APT quality and calcination conditions constants [41].

TVO ($WO_{2.72}$) is characterized by presenting the largest meso-pore volume, lowest fractal dimension value, smoother surface [85]. Thus, it is much more favourable for the reduction since more reacting gas can flow through it.

Porosity The degree of porosity of TBO is influenced by the calcination parameters during the "blueing" process. The specific surface area in commercial TBOs varies between 1-15 m^2/g.

Colour characterisation APT is a white crystal powder. When roasted, the obtained tungsten oxide colour ranges from greenish-yellow through deep blue to violet. Figure A.3.1 shows the different stages of tungsten oxide reduction, from APT to tungsten metal, as well as its colour characteristics.

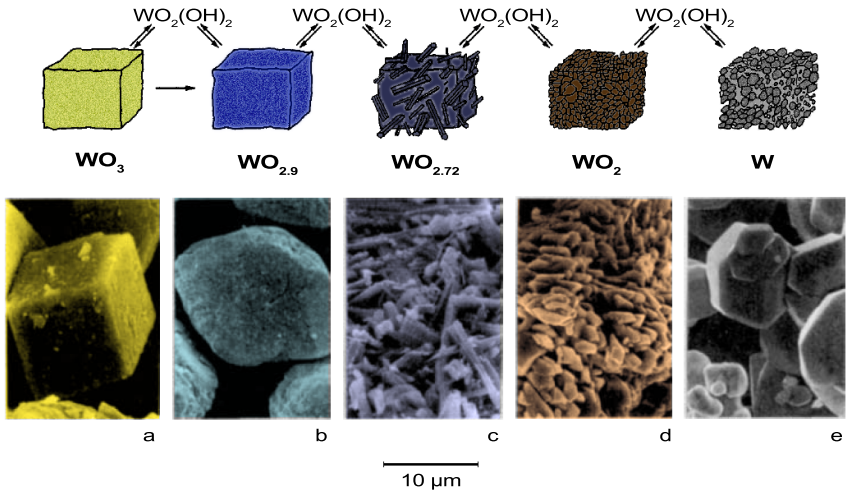

Figure A.3.1: Common morphological changes observed during tungsten production at 1000 °C. Source: [1].

Morphology The first steps during the reduction sequence do not present major changes in particle macro-morphology, except for occasional fractures and particle splitting [50].

Sarin [129] investigated the morphological changes occurring during reduction of tungsten trioxide, where a temperature of 900 °C and hydrogen with a dew point of -60 °C was used in all his cases. Similarly to other authors' researches, he observed that the reduction of WO_3 to $WO_{2.72}$ resulted in "large plate-like whiskers (figs. A.3.1 and A.3.2) of TVO of two morphologies, randomly oriented whiskers and clusters of whiskers". The whiskers formation is attributed to the volatile $WO_2(OH)_2$ presence. During the final reduction of WO_2 to W no further morphological variations are present. Therefore, the transformation of whiskers from TVO to WO_2 determines the final grain shapes of the metallic tungsten powder [129, 14].

Wilken et al. [74] found five different patterns of morphological evolution occurring during the reduction sequence. However, the morphological changes could not be correlated in all cases, but, they were found to fit into a hierarchy.

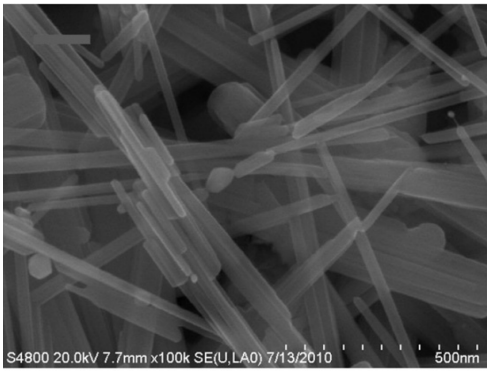

Figure A.3.2: Micro-morphology of $WO_{2.72}$ [14].

A.4 Characterization of W powders

The lower the powder grain sizes, the higher the difficulties for characterization. This is due mainly to the strong tendency of particles to agglomerate and to the limitations of the existing characterization methods[48]. Thus, it is of crucial importance to de-agglomerate the powders before making measurements such as FSSS, sedimentation, laser scattering, and even SEM. Nevertheless, in the case of ultra-fine powders, the results may be erroneous due to the high resistance of oxide pseudo-morphic agglomerates.

W powder derived from APT exists as highly agglomerated particles. Schubert et al. affirmed that *"the finer the grain size, the higher the percentage of oxide pseudo-morphic particles will be" [48]*. They studied the characterization of ultra-fine tungsten powder (below 1 μm). In their findings, coarse particles were still present after 1 h milling time, but, they were de-agglomerated during further milling. FSSS analysis gave misleadingly high results. BET measurements gave a better insight into the differences in fineness of the powders, but, were not found to be an accurate way to "judge" the suitability of ultra-fine powders for hardmetals production, whereas, SEM allowed a more precise description of such powders.

During an industrial analysis, FSSS, sedimentary methods and laser scattering are the highest employed practices, whereas BET and/or SEM imaging are rarely used.

Jiqiao and Baiyun [127] investigated the particle size measurement of as-supplied and lab-milled ultra-fine tungsten powders. The experiments were carried out in a multi-tube push-type furnace, under "dry" reduction conditions, co-current hydrogen flow, low temperature and low humidity, in order to reduce $WO_2(OH)_2$ formation and in order to obtain ultra-fine tungsten powder from pure WO_3. The final W powder was separated into four samples, to be milled, before characterization. They concluded: a) in all the cases "laser diffraction method and FSSS method both gave misleading size values" (fig. A.4.1), b) BET values were smaller than SEM values, thus, they proposed a

modification in the BET particle diameter formula for ultra-fine powder characterization ($d_{\mathrm{BET}} = k(D/2)(S_{\mathrm{BET}}\,\mathrm{density})$, where D is the fractal dimension, S is the surface of pores and k is function of pore surface).

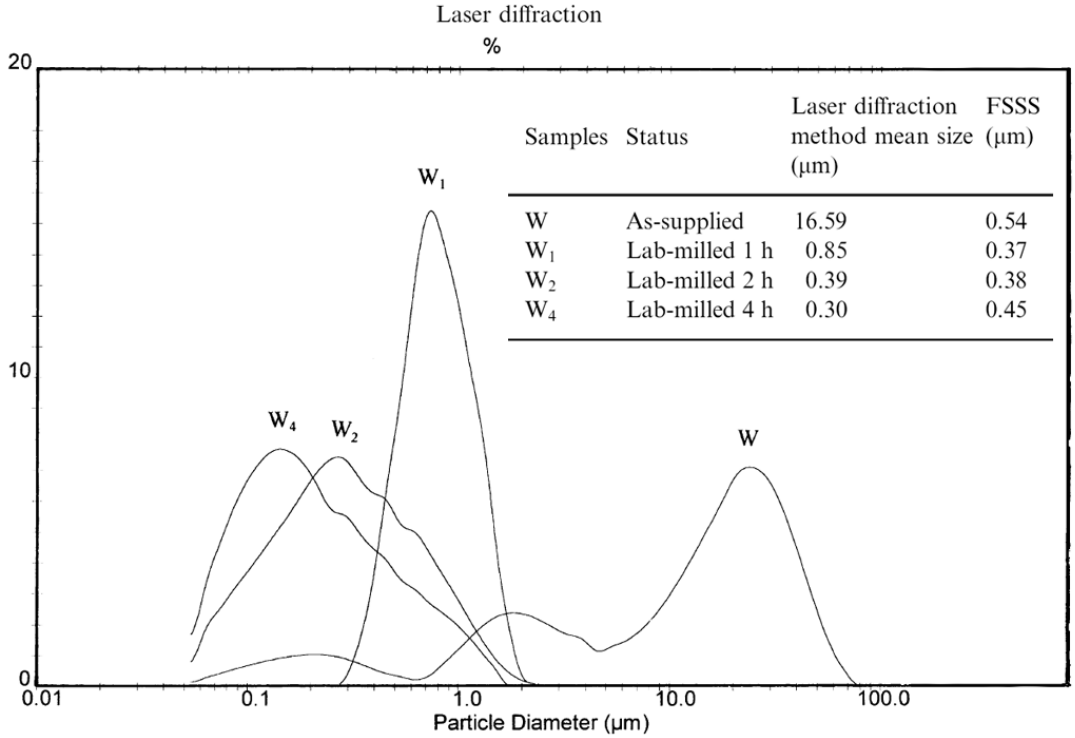

Figure A.4.1: Laser diffraction particle size distributions and measured mean particle sizes of as-supplied and lab-milled tungsten powders. Source: [127].

Characterization of hydrogen-reduced sub-micron tungsten powders was carried out by Schubert and Lassner (1991) [54]. Their focus was on the decomposition of the raw APT and the consecutive WO_X reduction process. In Schubert and Lassner's study, eight different tungsten blue and yellow oxides were prepared by affecting the calcination conditions during pure APT (Na, K, Fe, P, Si $<$ 5 ppm) processing [54]. The full review, as well as complementary information is documented in [54] and in [1].

Appendix B

Mathematical foundations to describe transport phenomena in porous media

B.1 Introduction

This appendix presents the mathematical foundations of multiphase transport following Hoffmann's work [28]. First, the general form of differential conservation equations describing the transport phenomena in a single phase is presented. Consecutively, the multiphase transport model is described.

Two common methods to treat transport phenomena in multiphase systems are distinguished:

1. *The interface tracking method* combines local differential equations for each phase with appropriate jump conditions at the interfaces. This allows explicit tracking of location and shape of interfaces [28].

2. *The averaging techniques* obtains mean values of flow and thermal properties. This treatment captures macroscopic transport aspects of the multiphase system but omits explicit tracking of interfaces and local instance fluctuations of properties [28].

The first method is rarely feasible because of the required amount of computation; that make advantageous to use averaged quantities to express the conservation equations. Thus, spatial averaging techniques (volume averaging) are introduced in order to extend the single phase formulation to a multiphase transport model, and finally, to a multiphase transport model for porous systems.

B.2 General conservation equations

Mathematical conservation equations express the fact that an extensive property like mass, momentum or will remain constant over time in a closed system. A transformation to an analogous intensive fluid property (e.g. density, velocity or specific enthalpy), denoted by ϕ, leads to a formulation in which the rate of change of ϕ, inside a given control volume (CV), corresponds to the sum of volumetric or surface sources or sinks [130, 131]. Thus, each term in the differential equations represents an influence on a unit-volume basis [132].

The flux, defined as the amount of ϕ traversing a surface per time, can be divided into two different quantities, namely, an advective and a diffusive contributions. The first, $\vec{F}_{\phi}^{C}$, characterizes the transport of the quantity ϕ by bulk fluid motion represented by the velocity field $\vec{v}$ as

$$\vec{F}_{\phi}^{C} = \rho \vec{v} \phi \tag{B.2.1}$$

The second, $\vec{F}_\phi^D$, accounts for diffusion processes caused by molecular agitation such as mass transfer according to law of Fick or heat transfer according to Fourier's law [130]

$$\vec{F}_\phi^D = -\Gamma_\phi \nabla \phi \tag{B.2.2}$$

where Γ_ϕ is a diffusion coefficient.

From this, the general transport equation[130], eq. (B.2.3), may be derived.

$$\underbrace{\frac{\partial \rho\phi}{\partial t}}_{\text{transient}} + \underbrace{\nabla \cdot (\rho \vec{v} \phi)}_{\text{advection}} = \underbrace{-\nabla \cdot \vec{F}_\phi^D}_{\text{diffusion}} + \underbrace{Q_V}_{\text{volumetric source/sink}} + \underbrace{\nabla \cdot \vec{Q}_S}_{\text{surface source/sink}} \tag{B.2.3}$$

which leads to the following conservation expressions:

Conservation of mass (continuity equation), $\phi = 1$

$$\frac{\partial \rho}{\partial t} + \nabla \cdot (\rho \vec{v}) = Q_V \tag{B.2.4}$$

Conservation of species i $\phi = \xi_i$ **or** $\rho_i = \rho \xi_i$

In this formulation ξ_i represents the mass fraction and ρ_i denotes the partial density of species i.

$$\frac{\partial \rho_i}{\partial t} + \nabla \cdot (\rho_i \vec{v}) = -\nabla \cdot \vec{j}_i + Q_{V,i} \tag{B.2.5}$$

where the source term $Q_{V,i}$ accounts for species production or consumption by chemical reactions and $\vec{j}_i = -D \nabla \rho_i$ represents the diffusive mass flux according to Fick's law and D denotes a diffusion coefficient.

Conservation of linear momentum, $\phi = \vec{v}$

The conservation of linear momentum accounting for pressure gradient ∇p, viscous shear forces at the surface of the control volume $\nabla \cdot \vec{\tau}$ and body forces $\vec{F}_B$ is computed as [28]

$$\frac{\partial \rho \vec{v}}{\partial t} + \nabla \cdot (\rho \vec{v} \vec{v}) = -\nabla p + \nabla \cdot \vec{\tau} + \vec{F}_B \tag{B.2.6}$$

Conservation of energy, $\phi = h$

The conservation of energy, where h denotes enthalpy, accounts for the work done on the control volume by pressure and shear forces.

$$\frac{\partial \rho h}{\partial t} + \nabla \cdot (\rho \vec{v} h) = -\nabla \cdot \vec{q}'' + \vec{v} \cdot \nabla p + \nabla \cdot (\vec{v} \cdot \vec{\tau}) + Q_V \tag{B.2.7}$$

where the source term Q_V accounts for energy released or consumed by chemical reaction, $\vec{q}'' = -\lambda \nabla T$ is the heat flux vector according to the conduction heat law and λ is the thermal conductivity.

B.3 Volume averaging for multiphase systems

Equations (B.2.4) to (B.2.7) represent the single phase transport phenomena. Near two-thirds of industrial process undergo phase change. Hence, the physical understanding and development of physical models accounting for multiple phases are needed for a more accurate and reliable design of industrial processes.

In this section the averaging process is described according to Eulerian volumetric averaging techniques [28]; for which, an appropriate control volume or representative elementary volume (REV),V_{REV}, is introduced.

Extinsic and *intrinsic* phase average values are defined for any property ϕ_k associated with a given phase k [86].
For a REV the *extrinsic* average of ϕ_k is defined as

$$\langle \phi_k \rangle = \frac{1}{V_{\text{REV}}} \int_{V_k} \phi_k dV \tag{B.3.1}$$

If the average is performed over the volume held by the phase k only, then the *intrinsic* phase average $\langle \phi_k \rangle^k$ is

$$\langle \phi_k \rangle^k = \frac{1}{V_k} \int_{V_k} \phi dV \tag{B.3.2}$$

Both quantities are related by a quantity that characterizes the volume occupied by the phase k, namely the volume fraction ϵ. T of the phase k is the ratio between the volume occupied by phase k and the total volume of the REV ($\epsilon_k = \frac{V_k}{V_{\text{REV}}}$). Thus the volume relation adopts the form

$$\langle \phi_k \rangle = \epsilon_k \langle \phi_k \rangle^k \tag{B.3.3}$$

The spacial average of all phases, of a fluid property ϕ, is defined by the sum of the extrinsic phase averages for all phases; thus, the *Eulerian volume average* writes as

$$\langle \phi \rangle = \sum_{k=1}^{N} \langle \phi_k \rangle = \sum_{k=1}^{N} \epsilon_k \langle \phi_k \rangle^k = \frac{1}{V_{\text{REV}}} \sum_{k=1}^{N} \int_{V_k} \phi_k dV \tag{B.3.4}$$

It can be assumed that a fluid property ϕ is composed of two parts: a volume averaged quantity and a term related to its spacial variations ϕ'_k, as represented by eq. (B.3.5).

$$\phi_k = \langle \phi_k \rangle^k + \phi'_k \tag{B.3.5}$$

From eqs. (B.3.3) to (B.3.5) the next mathematical expressions can be derived for the phase average.

The product of two properties ϕ and ψ,

$$\langle \phi_k \psi_k \rangle = \epsilon_k \langle \phi_k \rangle^k \langle \psi_k \rangle^k + \langle \phi'_k \psi'_k \rangle \tag{B.3.6}$$

$$\langle \phi_k \psi_k \rangle^k = \langle \phi_k \rangle^k \langle \psi_k \rangle^k + \langle \phi'_k \psi'_k \rangle^k \tag{B.3.7}$$

The volumetric average of a time derivative

$$\left\langle \frac{\partial \phi_k}{\partial t} \right\rangle = \frac{\partial \langle \phi_k \rangle}{\partial t} - \frac{1}{V_{\text{REV}}} \int_{S_k} \phi_k \vec{v}_I \cdot d\vec{S}_k \tag{B.3.8}$$

where S_k, $\vec{S}$ and $\vec{v}_I$ denote the interfacial area surrounding the phase k within the averaging volume, the area vector of the interface pointing outward from phase k and the interfacial velocity, respectively.

The theorem of local volumetric average by Whitaker [133] establish a required relation between the volumetric average of a derivative and a derivative of a volumetric averaged quantity

$$\langle \nabla \phi_k \rangle = \nabla \langle \phi_k \rangle + \frac{1}{V_{\text{REV}}} \int_{S_k} \phi_k d\vec{S}_k \tag{B.3.9}$$

The volume average of the general conservation equation of phase property ϕ_k is obtained by applying the definition of the extrinsic phase average to eq. (B.2.3).

$$\left\langle \frac{\partial \rho_k \phi_k}{\partial t} \right\rangle + \langle \nabla \cdot (\rho_k \vec{v}_k \phi_k) \rangle = - \left\langle \nabla \cdot \vec{F}^D_{\phi_k} \right\rangle + \langle Q_{V,k} \rangle + \langle \nabla \cdot Q_{S,k} \rangle \tag{B.3.10}$$

From the before described mathematical formulation and neglecting any products of spatial fluctuations $\left\langle \rho_k' \vec{\phi}_k' \right\rangle$ and rewriting in terms of intrinsic values it is obtained:

$$\begin{aligned}
&\frac{\partial}{\partial t}\left(\epsilon_k \langle \rho_k \rangle^k \langle \phi_k \rangle^k\right) + \nabla \cdot \left(\epsilon_k \left\langle \rho_k \right\rangle^k \left\langle \vec{v}_k \phi_k \right\rangle^k\right) \\
&= -\nabla \cdot \left\langle \vec{F}^D_{\phi_k} \right\rangle + \langle Q_{V,k} \rangle + \nabla \cdot \left(\epsilon_k \left\langle Q_{S,k} \right\rangle^k\right) \\
&\quad - \frac{1}{V_{\text{REV}}} \int_{S_k} \vec{F}^D_{\phi_k} \cdot d\vec{S} \\
&\quad + \frac{1}{V_{\text{REV}}} \int_{S_k} Q_{S,k} \cdot d\vec{S} \\
&\quad - \frac{1}{V_{\text{REV}}} \int_{S_k} \rho_k \phi_k (\vec{v}_k - \vec{v}_I) \cdot d\vec{S}
\end{aligned} \tag{B.3.11}$$

where the last three terms on the right hand side of eq. (B.3.11) represent interfacial exchange terms. This means that they account for the quantities transported at or through the interface of phase k with any another phase.

Depending on the number of phases involved in the averaging, Faghri and Zhang [86] classified the macroscopic equations for multiphase systems in two groups:

- The first, the *homogeneous model*, is represented by a single set of equations, resulting from the averaging over all phases present in a multiphase control volume.
- The second, the *multi-fluid model*, yields a set of conservation equations for each phase, performing spatial averaging for each phase separately.

B.3.1 Multi-fluid model

The spatial average of the governing equations, and considering eqs. (B.3.1) and (B.3.2), for each phase leads into the herein described multi-fluid model.

Continuity equation Considering that the intrinsic phase-averaged density is equal to the phase's density ρ_k, the conservation of mass for the phase k according to B.3.11 takes the form

$$\begin{aligned}
\frac{\partial}{\partial t}\left(\epsilon_k \langle \rho_k \rangle^k\right) + \nabla \cdot \left(\epsilon_k \left\langle \rho_k \right\rangle^k \left\langle \vec{v}_k \right\rangle^k\right) &= -\frac{1}{V_{\text{REV}}} \int_{S_k} \rho_k \left(\vec{v}_k - \vec{v}_I\right) \cdot d\vec{S} \\
&= \sum_{j=1, j\neq k}^{N} \dot{m}'''_{jk}
\end{aligned} \tag{B.3.12}$$

Species equation The conservation of a species i advective and diffusive transport as well as species production or consumption by chemical reactions, within phase k, is accounted for by

$$\begin{aligned} &\frac{\partial}{\partial t}\left(\epsilon_k \langle \rho_{k,i} \rangle^k\right) + \nabla \cdot \left(\epsilon_k \langle \rho_{k,i} \rangle^k \langle \vec{v}_k \rangle^k\right) = \\ &- \nabla \cdot \left\langle \vec{j}_{k,i} \right\rangle + \langle Q_{V,k} \rangle + \sum_{j=1, j\neq k}^{N} \dot{m}'''_{jk,i} \end{aligned} \tag{B.3.13}$$

where

$$\sum_{j=1, j\neq k}^{N} \dot{m}'''_{jk,i} = -\frac{1}{V_{\text{REV}}} \int_{S_k} \vec{j}_{k,i} \cdot d\vec{S} - \frac{1}{V_{\text{REV}}} \int_{S_k} \rho_{k,i} \left(\vec{v}_k - \vec{v}_I\right) \cdot d\vec{S} \tag{B.3.14}$$

Momentum equation Following eq. (B.3.11), the momentum for phase k writes as:

$$\begin{aligned} &\frac{\partial}{\partial t}\left(\epsilon_k \langle \rho_k \rangle^k \langle \vec{v}_k \rangle^k\right) + \nabla \cdot \left(\epsilon_k \langle \rho_k \rangle^k \langle \vec{v}_k \vec{v}_k \rangle^k\right) \\ &= \nabla \cdot \left(\epsilon_k \langle \vec{\tau}'_k \rangle^k\right) + \epsilon_k \langle \rho_k \rangle^k \vec{F}_k + \sum_{j=1, j\neq k}^{N} \left(\left\langle \vec{F}_{jk} \right\rangle + \left\langle \dot{m}'''_{jk} \right\rangle \langle \vec{v}_{k,I} \rangle^k\right) \end{aligned} \tag{B.3.15}$$

with

$$\sum_{j=1, j\neq k}^{N} \left\langle \dot{m}'''_{jk} \right\rangle \langle \vec{v}_{k,I} \rangle^k = -\frac{1}{V_{\text{REV}}} \int_{S_k} \rho_k \vec{v}_k \left(\vec{v}_k - \vec{v}_I\right) \cdot d\vec{S} \tag{B.3.16}$$

$$\sum_{j=1, j\neq k}^{N} \left\langle \vec{F}_{jk} \right\rangle = \frac{1}{V_{\text{REV}}} \int_{S_k} \vec{\tau}' \cdot d\vec{S} \tag{B.3.17}$$

$$\langle \vec{\tau}'_k \rangle^k = -\langle p_k \rangle^k I + \mu_k \left[\nabla \cdot \langle \vec{v}_k \rangle^k + \left(\nabla \cdot \langle \vec{v}_k \rangle^k\right)^T\right] - \frac{2}{3}\mu_k \left(\nabla \cdot \langle \vec{v}_k \rangle^k\right) I \tag{B.3.18}$$

where $\langle \vec{\tau}'_k \rangle^k$ is the phase-averaged stress tensor accounting for viscous shear and pressure [86]. $\langle \vec{v}_{k,I} \rangle^k$ is the intrinsic phase-averaged velocity at the interface of phase k and phase j. $\left\langle \vec{F}_{jk} \right\rangle$ is an interactive force between phase k and j representing friction, pressure and cohesion forces.

Energy Equation Following eq. (B.3.11), the energy equation for phase k writes as:

$$\begin{aligned}
&\frac{\partial}{\partial t}\left(\epsilon_k \langle\rho_k\rangle^k \langle h_k\rangle^k\right) + \left(\epsilon_k \langle\rho_k\rangle^k \langle\vec{v}_k h_k\rangle^k\right) \\
&= -\nabla\cdot\langle\vec{q}_k{}''\rangle + \frac{\partial p_k}{\partial t} + \langle\vec{v}_k\rangle\cdot\nabla\langle p_k\rangle + \nabla\cdot\left(\vec{v}_k\cdot\vec{\tau}_k\right) + \langle Q_{V,k}\rangle \\
&\quad + \sum_{j=1,j\neq k}^{N}\left(\langle q'''_{jk}\rangle + \langle\dot{m}'''_{jk}\rangle\langle h_{k,I}\rangle^k\right)
\end{aligned} \tag{B.3.19}$$

where the heat transfer from all other phases to the k^{th} phase at the interface is

$$\sum_{j=1,j\neq k}^{N}\langle\dot{m}'''_{jk}\rangle\langle h_{k,I}\rangle^k = -\frac{1}{V_{\text{REV}}}\int_{S_k}\rho_k h_k\left(\vec{v}_k-\vec{v}_I\right)\cdot d\vec{S} \tag{B.3.20}$$

Finally, the intensity of heat exchange $\langle q'''_{jk}\rangle$ between phase j and phase k writes

$$\sum_{j=1,j\neq k}^{N}\langle q'''_{jk}\rangle = -\frac{1}{V_{\text{REV}}}\int_{S_k}\vec{q}_k{}''\cdot d\vec{S} \tag{B.3.21}$$

B.3.2 Homogeneous model

The spatial averaging over all phases within a control volume of a multiphase system results in the herein presented homogeneous model. The relationship between individual phase averages and the Eulerian volume average is stabliched by eq. (B.3.4); where the homogeneous model is obtained by summing the individual phase equations of the multi fluid model [86].

Continuity equation Summing the equation for mass conservation eq. (B.3.12) over all phases, introducing a volume-averaged density ($\langle\rho\rangle = \sum_{k=1}^{N}\epsilon_k\langle\rho_k\rangle^k$) and rearranging the homogeneous continuity equation writes

$$\frac{\partial\langle\rho\rangle}{\partial t} + \nabla\cdot\langle\rho\rangle\vec{v} = \langle Q_V\rangle \tag{B.3.22}$$

where the bulk velocity $\vec{v}$ of the multiphase mixture represents the average of individual phase velocities by phase mass fractions and result in

$$\vec{v} = \frac{1}{\langle\rho\rangle}\sum_{k=1}^{N}\epsilon_k\langle\rho_k\rangle^k\langle\vec{v}_k\rangle^k \tag{B.3.23}$$

Species equation Summing the multi fluid equations of all phases for the species i yield into the homogeneous equation for conservation of species. Thus, applying the above described averaged density and mass averaged velocity, it is obtained as

$$\frac{\partial}{\partial t}\langle \rho_i \rangle + \nabla \cdot \langle \rho_i \rangle \langle \vec{v} \rangle = -\nabla \cdot \vec{j}_i + Q_V \tag{B.3.24}$$

Momentum equation The homogeneous momentum equation is calculated as

$$\frac{\partial \langle \rho \rangle \vec{v}}{\partial t} + \nabla \cdot \left(\sum_{k=1}^{N} \epsilon_k \langle \rho_k \rangle^k \langle \vec{v}\vec{v} \rangle^k \right) = \nabla \cdot \langle \vec{\tau}' \rangle + \langle \rho \rangle \vec{F} + \dot{M}_I''' \tag{B.3.25}$$

The more detailed description of eq. (B.3.25) derivation is documented in [28].

Energy equation Summing the energy equations over all phases of the multiphase mixture leads to the homogeneous energy equation

$$\begin{aligned} &\frac{\partial}{\partial t}\left(\langle \rho \rangle h\right) + \nabla \cdot \left(\sum_{k=1}^{N} \epsilon_k \langle \rho_k \rangle^k \langle \vec{v}_k h_k \rangle^k \right) \\ &= -\nabla \cdot \langle \vec{q}'' \rangle + \frac{\partial \langle p \rangle}{\partial t} + \vec{v} \cdot \nabla \langle p \rangle + \nabla \cdot \left(\vec{v} \cdot \langle \vec{\tau} \rangle \right) + Q_V \end{aligned} \tag{B.3.26}$$

where h is the mass averaged enthalpy of the multiphase mixture, defined by Faghri and Zhang [86] as

$$h = \frac{1}{\langle \rho \rangle} \sum_{k=1}^{N} \epsilon_k \langle \rho_k \rangle^k \langle h_k \rangle^k \tag{B.3.27}$$

and Q_V accounts for energy released or consumed due to phase changes and the chemical reactions.

B.3.3 Fluid flow on porous media

An important quantity representing porous media is the porosity or void fraction ϵ. ϵ is defined as the ratio of the "empty" volume, which may be occupied by a gas phase. *Void fraction* term is commonly used to represent the "porosity" at a bed scale while the term *porosity* is preferred to characterize pores within particles [28, 31]. Thus, the voidage between the bed layers and the particles are calculated as

$$\epsilon_p = \frac{V_g}{V_p} \qquad \text{porosity of a single porous particle} \tag{B.3.28}$$

$$\epsilon_b = \frac{V_g}{V_b} \qquad \text{void fraction of a PPB} \tag{B.3.29}$$

Assuming that the porous medium is saturated with a single fluid phase and that the solid matrix is stationary and considering the flow as a flow passing the REV, the homogeneous model for the flow through a porous media is characterized by:

Continuity equation The continuity equation of the fluid phase f is obtained as

$$\frac{\partial}{\partial t}\left(\epsilon_f \langle \rho_f \rangle^f\right) + \nabla \cdot \left(\epsilon_f \langle \rho_f \rangle^f \langle \vec{v}_f \rangle^f\right) = \dot{m}'''_{s,f} \tag{B.3.30}$$

where $\dot{m}'''_{s,f}$ accounts for mass transfer between the fluid and the solid phase by chemical reactions.

Momentum equation Following Hoffmann [28] derivation the momentum equation for porous media writes

$$\begin{aligned} &\frac{\partial}{\partial t}\left(\epsilon_f \langle \rho_f \rangle^k \langle \vec{v}_f \rangle^f\right) + \nabla \cdot \left(\epsilon_f \langle \rho_f \rangle^f \langle \vec{v}_f \vec{v}_f \rangle^f\right) \\ &= \nabla \cdot \left(\epsilon_f \langle \vec{\tau}'_f \rangle^f\right) - \frac{\mu_f}{K}\epsilon_f^2 \langle \vec{v}_f \rangle^f - C \langle \rho_f \rangle^f \epsilon_f^3 | \langle \vec{v}_f \rangle^f | \langle \vec{v}_f \rangle^f \end{aligned} \tag{B.3.31}$$

where K denotes the permeability of the bed and C represents a dimensionless drag coefficient. These parameters can be obtained from empirical relations tabulated for various types of porous media. For a packed bed composed of spherical particles with diameter D_p the following relations have been proposed [86, 31]

$$K = \frac{D_p^2 \epsilon_f^3}{150(1-\epsilon_f)^2} \tag{B.3.32}$$

$$C = \frac{1.75(1-\epsilon_f)}{D_p \epsilon_f^3} \tag{B.3.33}$$

Energy equation According to eq. (B.3.19)), the conservation of energy in a porous medium consisting of a fluid and a solid phase may be expressed as

$$(\rho c_p)_{\text{eff}} \frac{\partial T}{\partial t} + (\rho c_p)_f \nabla T = \nabla \cdot \lambda_{\text{eff}} \nabla T + Q_V \tag{B.3.34}$$

where $(\rho c_p)_{\text{eff}}$ represents an effective thermal mass and λ_{eff} represents an effective thermal conductivity.

To derive the previous eq. (B.3.34), a stationary and incompressible solid phase advection as well as compressibility terms have been neglected following [86]. In addition, it was assumed that *i)* the fluid's thermal mass (ρc_p) is negligible compared to the one of the solid phase, *ii)* local thermal equilibrium between solid and fluid phase, *iii)* enthalpy is only a function of temperature and *iv)* the specific heat coefficient is constant.

Appendix C

Predicting heat transfer in packed beds by XDEM

C.1 Introduction

In this section, results from numerical predictions obtained by the proposed XDEM numerical approach as well as its validation are presented. The rigorous process started with analytical validation of the model for the gas and solid phases independently. Continuing with the validation process, packed-beds presenting an ordered arrangement of particles were selected. Finally a more general packed bed reactor with randomly distributed particles was simulated and validated.

C.2 Analytical validation of numerical model

In order to evaluate analytically the current approach, a single conductive sphere suspended in a fluid was selected. The proposed case can be seen as one dimensional flow, in which a control "volume" containing only one particle (fig. C.2.1) has been chosen. Consequently, considering pertinent assumptions, analytical expressions for fluid and particle temperature evolution may be obtained.

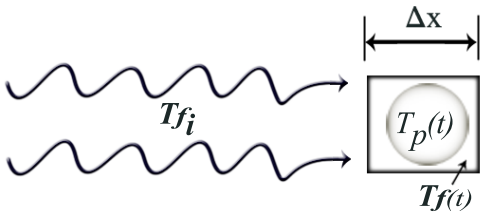

Figure C.2.1: Analytical validation case. Sphere suspended in a fluid.

C.2.1 Intra-particle temperature profile validation

The heat transfer to the solid phase when the particle is immersed in a medium at constant temperature T_{fo} is due to convection. However, heat transfer within the particle takes place by conduction. Hence, the one dimensional governing equation for a single spherical particle is:

$$\frac{\partial T_p}{\partial t} = \kappa \left(\frac{\partial^2 T_p}{\partial r^2} + \frac{2}{r} \frac{\partial T_p}{\partial r} \right) \tag{C.2.1}$$

with initial and boundary conditions:

$$
\begin{aligned}
T(t=0) &= T_0 \\
\frac{\partial T}{\partial r} &= 0 \quad \text{for} \quad r = 0 \\
\frac{\partial T}{\partial r} &= \frac{-h}{\lambda}\left(T_{fo} - T_p\right) \quad \text{for} \quad r = R
\end{aligned}
$$

In a detailed manner Carslaw [114] presented the solution for such a problems. Therefore, Carslaw's exact solution for a solid sphere immersed in a medium constant temperature was used in this study.

Table C.2.1 includes the properties used during this first validation.

Table C.2.1: Properties of gas and solid phases for the intra-particle analytical validation case.

Gas Phase: Air			
T_{fi} =	500	K	Gas temperature
Solid Phase: Fir wood particle			
d =	10	mm	Particle diameter
T_{p_o} =	300	K	Particle initial temperature
C_{p_p} =	1733	J/kgK	Specific heat
λ_p =	0.2	W/mK	Heat Conductivity
ρ_p =	350	kg/m^3	Density

Figure C.2.2 shows the spatial and temporal temperature for the model and the analytical temperature profile prediction. The symbols correspond to the model predictions and the continuous line represent the analytical solution. The different curves from bottom to top represent the particle temperature profile evolution in time, $t = 0\,s$ to $t = 600\,s$ respectively. The highest observed error was 0.4%. The maximum error appears at the first minutes when the heat flux between the fluid and the particle is the highest, then progressively tends to zero when steady state is reached. Thereby, the numerical prediction accurately represents the analytical description of the problem.

C.2.2 Fluid temperature validation

Continuing the proposed problem in fig. C.2.1, where a particle is placed in a control volume Δx with air flowing to it, an analytical solution describing the evolution of the cell temperature was obtained. For the case, the particle conserves a constant temperature

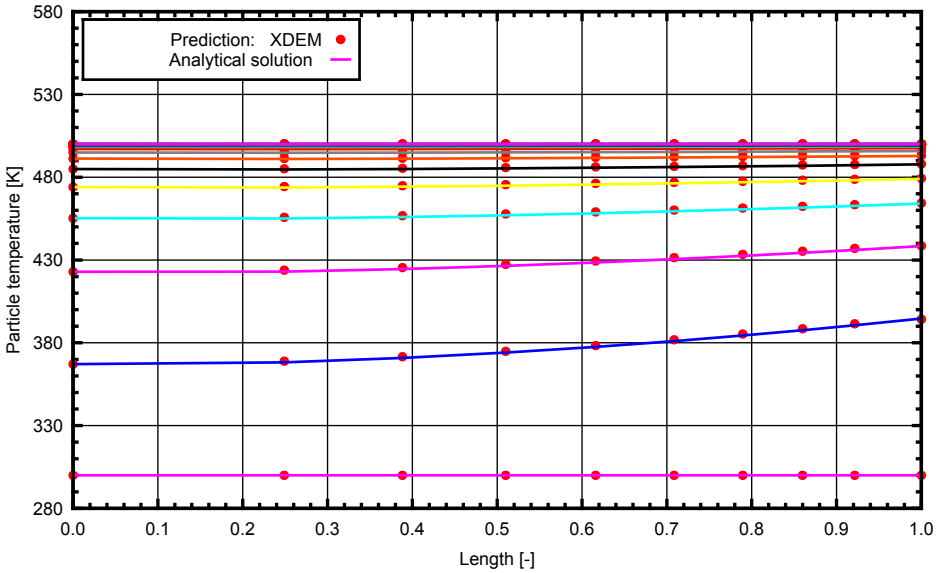

Figure C.2.2: Temperature profile comparison between analytical and XDEM predictions for a single particle.

Table C.2.2: Properties of gas and solid phases for the fluid analytical validation case.

Gas Phase: Air		
$U_{fi} = 0.2$	m/s	Gas inlet velocity
$T_{fi} = 293$	K	Gas inlet temperature
Solid Phase: Aluminium particles		
$d = 7$	mm	Particle diameter
$T_{p_o} = 573$	K	Particle initial temperature

$T_p = T_{p_o}$ during the prediction. Similarly, fluid inlet properties such as density, velocity and temperature were assumed to be constant. Thus, the obtained analytical conservation expression for the air temperature in the cell

$$\frac{dT_f}{dt}\rho_f c_{p_f} + \left(T_f - T_{f_i}\right)\frac{U_{f_i}\rho_f c_{p_f}}{\Delta x} = -\frac{hA_f}{V_f}\left(T_f - T_p\right) \tag{C.2.2}$$

has an unique solution by applying the initial condition: $T_f(t=0) = T_{p_o}$. Where the convective heat transfer coefficient ($h = Nu\lambda_f/L$) was calculated by using the Nusselt number (Nu) semi-empirical relation proposed by Achenbach [91] ((4.1.22))

The parameters chosen for this verification are presented in the table C.2.2.

Figure C.2.3 shows the obtained analytical solution for the fluid temperature with the XDEM prediction for the current case. As expected, the model prediction follow accurately the analytical solution until the quasi steady state is achieved. However it has to be pointed that the lumped analytical solution restricts its use to cases with low temperature variation. Even if the mass flow rate is constant, density acting on the transient

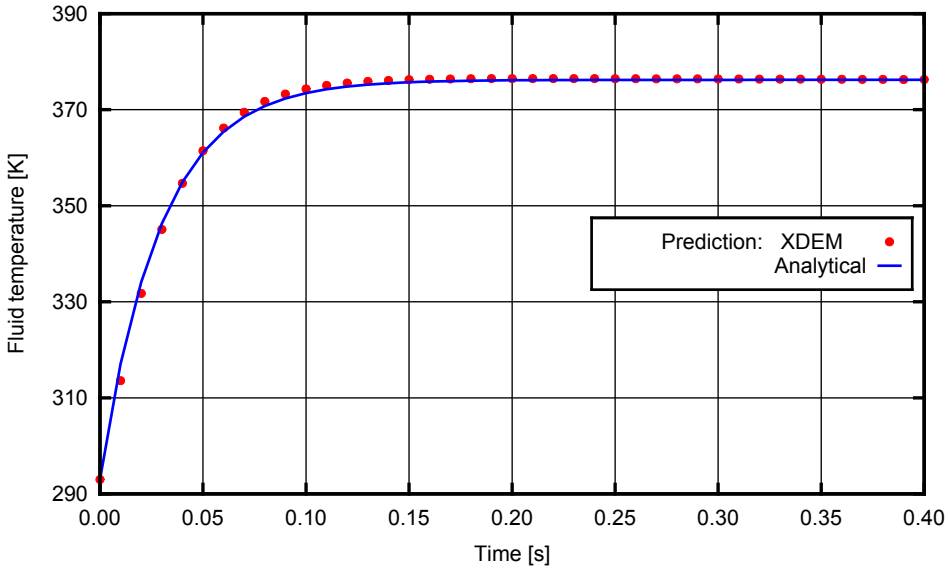

Figure C.2.3: Results of the fluid temperature prediction for the verification case.

term of eq. (C.2.2) is actually affected by the changes in temperature, a fact which is not considered by the analytical solution. Therefore, the accuracy when such variation is present has to be observed by comparison with experimental data.

C.3 Characteristics of flow in packed beds

Heat transfer between granular material and the gas streaming between the particles dominate a broad range of engineering applications. In such applications, the fluid phase is coupled to the surface of particles via heat transfer [21]. For a classical continuous representation granular media experimental data or empirical correlations are used to determine the the distribution of porosity and total surface of the particles. This is omitted by XDEM [21]; the approach allows computing the available surface for heat transfer and void space affecting the flow distribution. In the following case, represented in fig. C.3.1, the porosity is predicted after filling a reactor container by gravity deposition with bi-disperse particles.

"For a spherical particle or any other given geometry of a particle its surface is known to determine heat transfer conditions." [21] Moreover, the local velocity, which also depends on the distribution porosity, influences heat transfer significantly. An accurate representation of the positioning of particles is of high importance for local porosity and total surface of particles calculation. Thus, particles positions are predicted according to DEM techniques as documented by Michael [113]. With known positions and size of particles the porosity distribution is readily determined of which two cross-sectional distributions for the larger and smaller spheres is shown in fig. C.3.2.

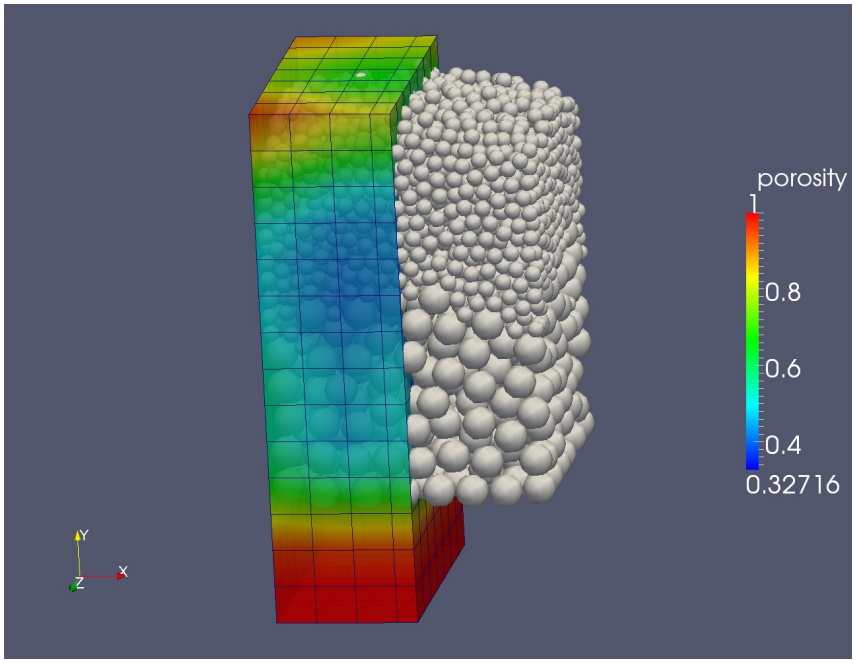

Figure C.3.1: Predicted arrangement of particles in a rectangular reactor [21, 25, 28].

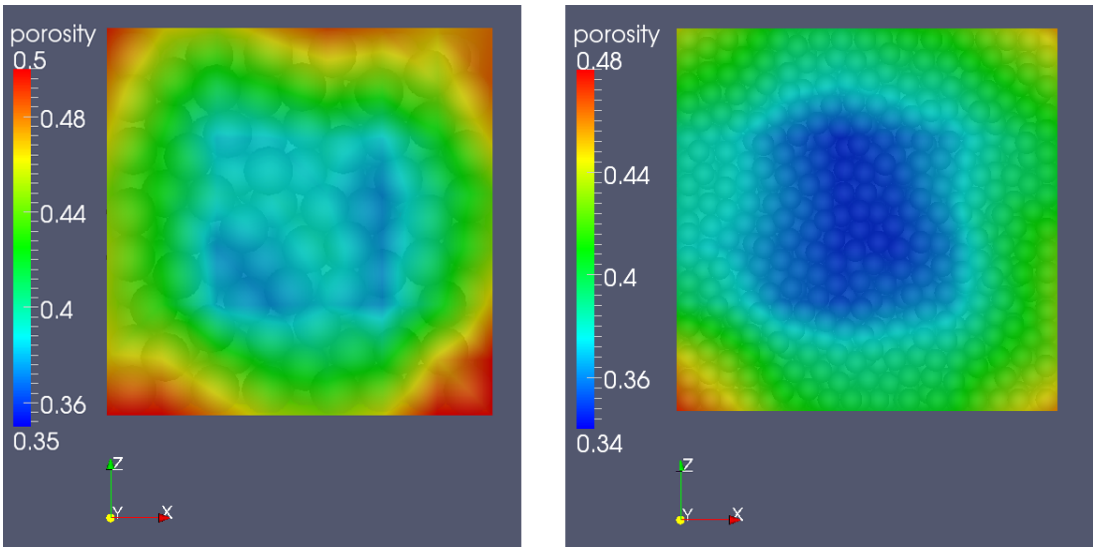

Figure C.3.2: Distribution of porosity in two cross-sectional surfaces in the lower (large spheres, D = 0.1 m) and upper part (small spheres, D = 0.05 m) of a packed bed reactor [21, 25, 28].

Figure C.3.2 highlights two obvious characteristics of packed beds: Different levels of porosity for arrangements of differently sized spherical particles and the wall effect. The latter is manifested by an increased porosity around the inner walls. In these regions the gas flow experiences less drag that results in an increased flow velocity. Consequently, as described in fig. C.3.1, heat transfer to the walls is increased. This may also enhance energy losses through the walls of the reactor. Since both porosity and flow velocity near the walls are predicted adequately heat loss for packed-bed reactors may be determined without further experiments or near wall correlations.

Furthermore, from fig. C.3.2a and fig. C.3.2b the void space predictions are evaluated different size of particles. An arrangement of smaller particles usually yields lower levels of porosity than found for larger particles positioned in a packed bed. Thus, porosities for the arrangement of particles in fig. C.3.2a and fig. C.3.2b are computed as ~ 0.42 and ~ 0.34, respectively. The vertical velocity component of the flow is influenced by the porosity in the lower and upper part of the bed(fig. C.3.3a and fig. C.3.3b). Since the larger porosity is located at the lower part of the packed bed, lower velocities are prescribed; while velocity increases in the upper part of the reactor due to a reduced porosity [21]. Thus, an increase of ~ 50 % on the bulk velocity is observed compared to that one on the vicinity of the walls and the corners in particular.

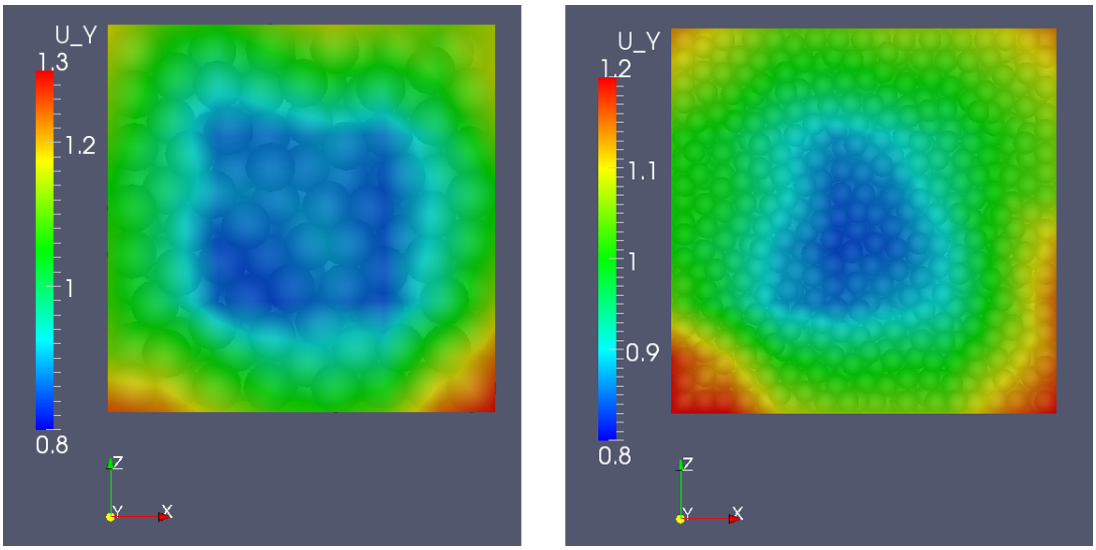

Figure C.3.3: Vertical velocity distribution in two cross-sectional areas in the lower (large spheres, D = 0.1 m) and upper part (small spheres, D = 0.05 m) of a packed bed reactor [21, 25, 28].

C.4 Validation for structured (ordered) packed-beds

In this study, the effect of packing arrangements on flow and heat transfer of different types of structured packed beds was taken into account by using the cases studied by Yang et al [134]. Yang et al [134] compare their continuous heat transfer model with experimental results from various artificially arranged packed beds. Two such ordered arrangements (SC arrangement and BCC arrangement) of monodisperse Bearing-steel spheres which yield a uniform porosity distribution were chosen for the validation of the coupling model.

Yang et al [134] suggest adjusting coefficients for the semi-empirical relation of Nusselt number obtained by Wakao & Kaguei (1982) [90], which seem to suit better in artificial configurations of particles in a packed bed. Therefore the following definition for calculation of the CHTC (Convective Heat Transfer Coefficient) was employed in the XDEM model during this validation.

$$Nu \;=\; a_1 + a_2\, Pr^{1/3}\, Re^{n} \tag{C.4.1}$$

where a_1, a_2, n are the model coefficients.

For the experiment thermocouples have been positioned along the center of the packed bed. The position of the thermocouples as well as the symmetry of the bed allow a simplification of the original case into a simple case characterized by "the central packed channel" [134]. As consequence, non desirable effects caused by the walls are avoided [135].

Due to the above exposed symmetry and thermocouple positions of the experiments [134] the XDEM simulation was ran as a one dimensional flow case. The initial and boundary conditions as well as the numerical properties used in this validation are summarized in table C.4.1.

Table C.4.1: Numerical properties. SC and BCC validation

Solid Phase: Bearing-steel			
d =	12	mm	
T_{p_o} =	335	K	
Gas Phase: Air			
T_{fi} =	299	K	
U_{fi} =	1.25	m/s	(SC configuration)
U_{fi} =	1.49	m/s	(BCC configuration)

The error plots (figs. C.4.1 and C.4.2) show the degree of accuracy of the fluid temperature predictions. The experimental data representation was obtained by converting the dimensionless measurements data, in which the same values used during the XDEM simulation were adopted as reference to represent the central point of the bars. The deviation on the error bars represent the bandwidth of the measurements. An average error (XDEM prediction Vs experiment) of 0.7% and 0.8% for the SC case and the BCC case respectively was obtained.

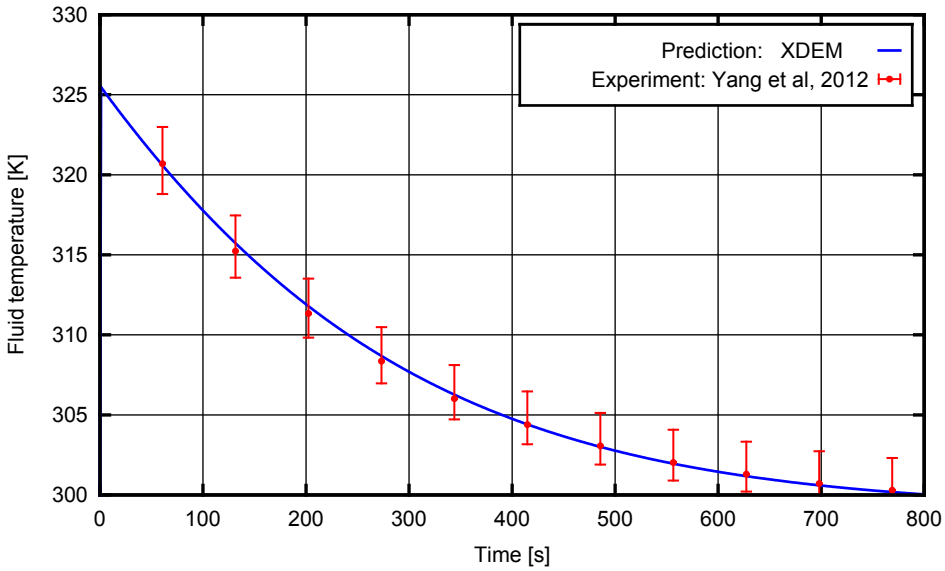

Figure C.4.1: Comparison between fluid temperature prediction and measurements of Yang's SC experiment [134].

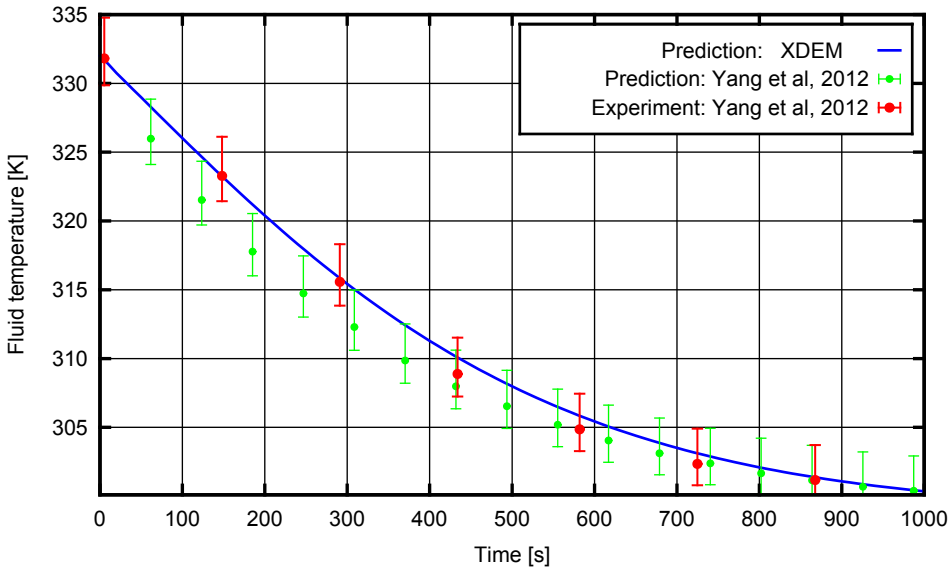

Figure C.4.2: Comparison between fluid temperature prediction and measurements of Yang's BCC experiment [134].

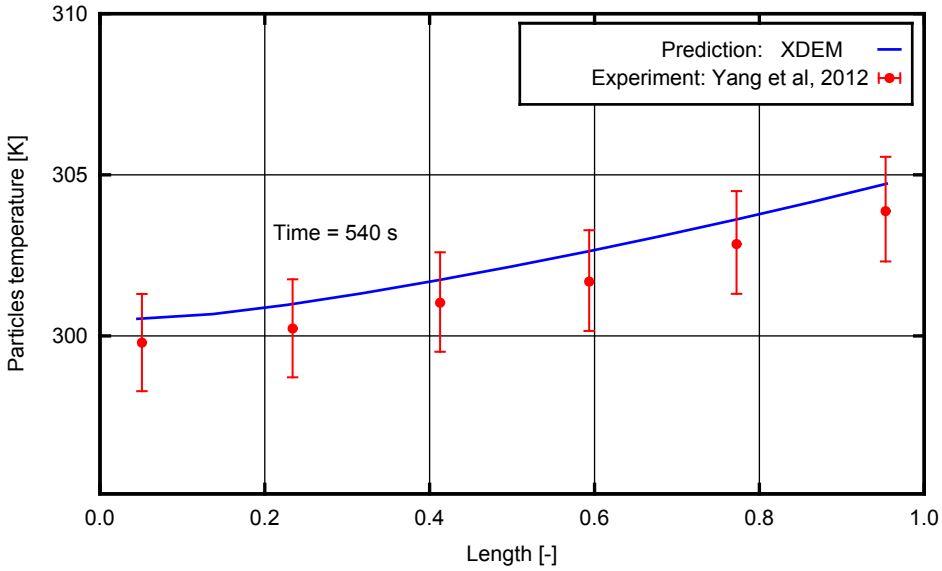

Figure C.4.3: Comparison between the measured particle temperature and the predictions at different locations within the experimental SC sample.

The temperature of the particles prediction were also validated by two different methods. The first one provides experimental data for the particles at a specific point in time, comparing between the measured particle temperature and the predictions at different locations within the sample (fig. C.4.3). The second one was performed by using Newton's law of cooling (appendix C.4) on the first particle of the channel.

$$\frac{dT_p}{dt} = \frac{hA_p}{V_p\,\rho_p\,c_{p_p}}\left(T_p - T_{f_i}\right) \tag{C.4.2}$$

According to the calculated Bi number ($Bi \approx 0.01$), the spatial variation of temperature within the particle at any given time is smaller than the temperature difference between the body surface and the fluid, that means to be uniform at any time and it decreases or increases uniformly until steady state is reached with the surrounding fluid temperature. Furthermore, constant fluid temperature at the first cell (equals to inlet temperature) was assumed. Consequently a unique solution by setting $T_p(t=0) = T_{fo}$ was found. Hence the result from this particle validation is shown in fig. C.4.4.

The continuous model presented by Yang et al [134] had shown a certain degree of accuracy for cases with low difference between particle and gas temperature ($\|T_p - T_f\| < 50\ K$); however, figs. C.4.2 to C.4.4, and the maximum error of 0.7% obtained on this validation shows that the coupling model improves the prediction of their continuous model. Thus the presumption is that the "Wakao's" correlation coefficients obtained by Yang et al [134] may be improved by using a XDEM approach.

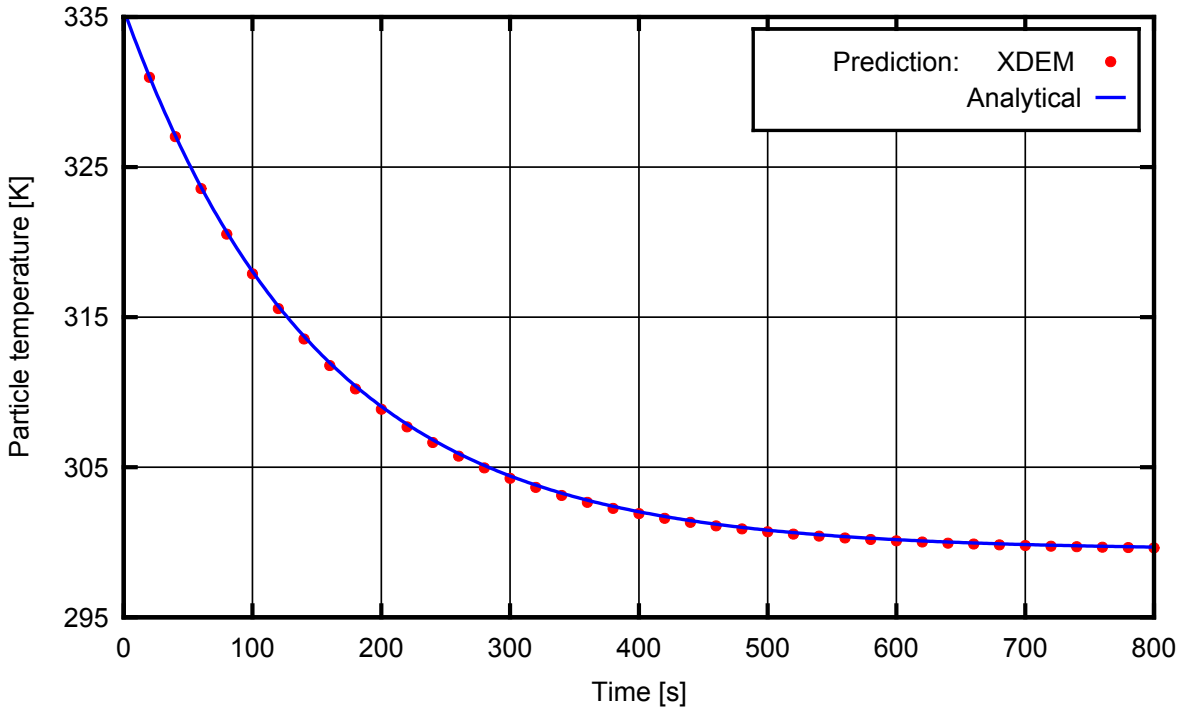

Figure C.4.4: Comparison between analytical and XDEM predictions for a single particle in a SC arranged packed bed.

C.5 Validation for non-structured (randomly) packed beds

While the previous section emphasised structured conditions, the following results of heat transfer in packed beds were obtained with non-structured ones. In reality, packed beds present a random distribution of particles. This type of packed-beds present different characteristics for flow and porosity as mentioned in chapter 4. Thus, in this section the XDEM model is validated for such a random arrangements.

The experimental data used for this validation was obtained by Peters et al [136] at the test reactor Pantha. The reactor was set-up to investigate heating up, drying and pyrolysis of particles in packed beds. Among the experiments performed by Peters et al [136] and Schröder [137], heat-up of Aluminium particles was chosen for this validation.

Due to the vanishing radial temperature gradients [137] in the experiment, a representation of the core of the Pantha reactor was chosen. Hence in a similar way as it was done on the previous validation (section C.4) the case was simplified into a case without non-desirable wall effects [135] and less computational expensive.

Table C.5.1 summarizes the aluminum particles heating-up case [136], including the material properties as well as the initial and boundary conditions used during the prediction.

Table C.5.1: Numerical properties, initial and boundary conditions used during Pantha Experiment

Gas Phase: Air		
$U_{f_i} = 0.1025$	m/s	Inlet velocity
$T_{fi_{max}} = 573$	K	Maximal Inlet Temperature
Solid Phase: Aluminium particles		
See table C.2.2		
$T_{p_o} = 298$	K	Initial temperature of particles
$r = 3.5$	mm	Particle radius
Reactor's core characteristics		
$D = 40$	mm	Diameter
$H = 210$	mm	Height
$No_p = 1254$		Number of particles

The figs. C.5.1 and C.5.2 depict the results of the XDEM simulation for gas and solid phases respectively. Figure C.5.3 shows a comparison between the measured temperature (dotted lines) and the predictions (continue lines) at different axial locations within the sample. A steady state is appreciated from the experimental data, and a non-negligible axial temperature gradient is observed. Thereby it can be inferred that the Pantha experiment presented heat losses, a fact pointed by Peters et al. [136]). The employed model assumed adiabatic walls. Thus, predictions are deviated from the measurements at the end of the simulation. Heat losses can be included into the model by adding an extra heat source representing, for instance, a "wall loss contribution" to the energy equation. Nevertheless, there is no information to characterize the heat losses of the treated case.

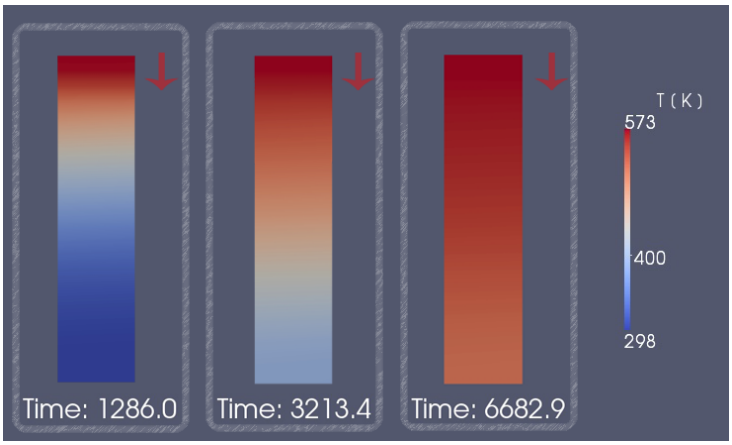

Figure C.5.1: XDEM fluid temperature prediction at different time steps of Pantha heating-up case.

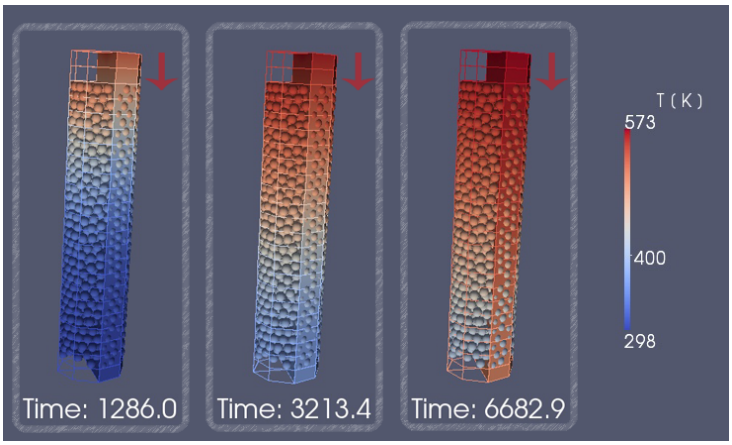

Figure C.5.2: XDEM particles temperature prediction at different time steps of Pantha heating-up case.

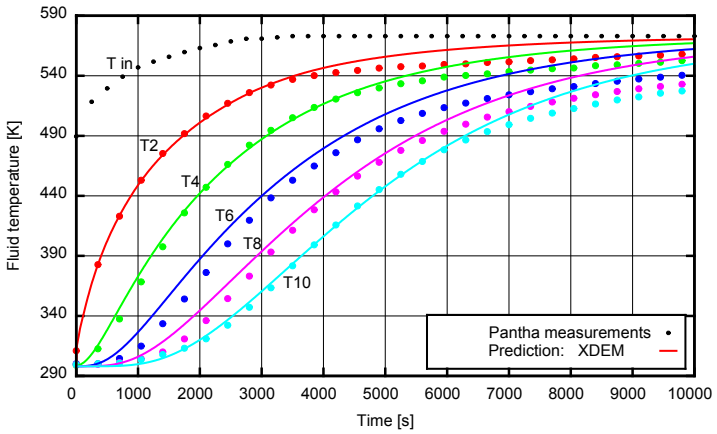

Figure C.5.3: Comparison beteen XDEM fluid temperature prediction and heating-up experiment measurements [136].